COMPUTER MODELLING AND EXAFS STUDIES OF MIXED

METAL FLUORITES

By

Thomas Tendani Netshisaulu

A Thesis Submitted to the Faculty of Sciences, Health and Agriculture, University of the North, SOVENGA, for the Degree of Doctor of Philosophy.

SOVENGA

August 2003

ACKNOWLEDGEMENTS

the execution of this work.

DECLARATION

I declare that except where specifically acknowledged, this thesis is my own, unaided work. It is being submitted to the degree of Doctor of Philosophy at the University of the North, SOVENGA. It has not been submitted before for any degree or examination at any other University.

TT NETSHISAULU

(Name of Candidate)

[signature]

(Signature)

31st day of *August*, 2003

In memory of my late parents

Charlie and Tshinakaho (née Livhalani) Netshisaulu.

CONTENTS

LIST OF FIGURES

LIST OF TABLES

ABSTRACT

The fluorite structured mixed-metal fluorides $CdF_2(xPbF_2)$ for 0 mol % $\leq x \leq$ 100 mol % PbF_2 are exceptionally good F^- ion conductors, a property, which is related to the mixed nature of the cation sub-lattice. Hence, from the technological viewpoint, these materials have important applications as electrolytes in solid state batteries. In this research project, we have used a combination of experiment and theory (classical simulations) to gain some insights into structural and dynamical properties of these materials. For this study, the highly conducting materials are best suited because they are experimentally amenable and have simple structures.

The validity of the model was first assessed by performing a number of preliminary perfect lattice calculations. In general, the calculated values of elastic and dielectric constants agreed with those from available experimental data, in particular those for the pure components of the solid solutions. The experimentally determined variation of the static dielectric constant as a function of composition was reasonably reproduced by the present calculations. It was observed that the dielectric constant increases when the mixed system evolves from CdF_2 to PbF_2. The results also suggest that linear variations (curves with no anomaly) of elastic constants with composition between the two pure components are only due to composition change of the mixed systems. Defect properties of the pure components of the solid solutions under study were determined using a two-region approach. In pure systems, the vacancy activation energy for fluorine migration in the bulk is found to be lower than the interstitial energy for fluorine migration. This suggests that vacancy mode of migration is predominant in the pure alkaline earth fluorides.

Molecular dynamics (MD) technique has been used to yield useful information on fluorine diffusion within $CdF_2(xPbF_2)$ mixed systems. These systems were modelled at temperatures ranging from liquid nitrogen temperature (77 K) to 800 K at a series of dopant concentrations. The plots of the anion species in these materials are seen to increase linearly with time, a clear evidence of migration on the anion sub-lattice, whilst the plots of ionic motion on the cation-sublattice rapidly evolved to a constant value, invariant with time, suggesting that cations do not participate in the diffusion process. The $x = 60$ mol % PbF_2 sample in $CdF_2(xPbF_2)$ mixed systems exhibits the highest magnitude of the fluorine diffusion coefficient (in the temperature range 77 – 800 K) whilst the lowest magnitudes of the fluorine diffusion coefficients were noted for Pb-deficient solid solutions ($x \leq 20$ mol % PbF_2). Furthermore, useful insight can be gained from the study of variation in ionic conductivity (σ) with Pb concentration (x). This study shows an initial rise in σ as x increases from zero (i.e. pure CdF_2). After reaching a peak at $x \sim 60$ mol % PbF_2, σ falls at $x > 80$ mol % PbF_2. In essence, the $x = 60$ mol % PbF_2 sample has the maximum ionic conductivity and correspondingly the lowest activation energy (E_{act}) in the entire series of $CdF_2(xPbF_2)$ samples in agreement with previous experimental results. Hence, we propose that the initial rise in σ is due to an increase in concentration of charge carriers and the subsequent fall is due to a decrease in their mobility.

The analysis of the element-specific pair radial distribution functions to determine if the trends reported for pure compounds continue in the mixed solutions reveals that cation radial distribution functions (RDFs) are typical to those found in solids. Hence, the cubic structure remains preserved in mixed systems (even at high temperatures), suggesting that these materials are solid electrolytes. However, anion RDFs were typical to those found in liquids, indicating that the

fluorine ions formed a weakly correlated sub-system. In addition the extent of disorder in the radial distribution of mixed systems are far complex than that in pure compounds – a feature associated with the evolution of the system from CdF_2 to PbF_2.

Complementary structural studies have been performed at the SERC Daresbury laboratory SRS. EXAFS spectroscopy has been used to probe local environments around cations in $CdF_2(xPbF_2)$ systems. The cation-fluorine peak shows reduced amplitude as a function of increase in dopant concentration. This behaviour is typical of stoichiometric compounds. A high degree of disorder is shown around the Pb cations in the entire series of solid solutions, with the highest disorder noted for the $x = 60$ mol % PbF_2 sample – a feature already alluded to using theoretical techniques. Temperature induced structures revealed that vacancies are preferentially sited adjacent to Pb ions in these systems. A similar study by Cox and co-workers on $PbSnF_4$ showed that vacancies are sited next to Pb ions of the fluorite structure. This suggests that anion (i.e. fluorine) vacancies are nearest-neighbours to host cation when the divalent dopant cation is smaller than the host cation and are nearest neighbours to the dopant when it is larger than the host. EXAFS has also been used to detect the effect of composition variation on the local structure of the two types of cations in $CdF_2(xPbF_2)$. The results reveal differences for the local environments of Cd^{2+} and Pb^{2+} cations. On the basis of this work we are able to predict design of new solid materials and of solids in which useful properties are optimized to support fast ion conduction.

CHAPTER I

GENERAL INTRODUCTION

1.1   SUPERIONIC CONDUCTORS

The present study is based on an experimental and theoretical study of the structure of mixed metal fluorides. Interest in these materials emanated from their potential use as solid electrolytes in high-energy storage devices such as batteries for vehicles, gas sensors and liquid-crystal displays. Solid electrolytes, superionics or fast-ion conductors, represent an interesting example of highly anharmonic and distorted structure, bridging the gap between solids and liquids. These materials exhibit unusually high ionic conductivities, σ (10^{-4}-10^{-1} $\Omega^{-1}cm^{-1}$), comparable to that found in molten salts, but at temperatures well below their melting points (Derrington and O'Keefe 1973). These features led to an interest in understanding the mechanisms behind fast-ion conduction and this spurred basic research into a variety of materials.

Other properties of superionic conductors include: small electronic conductivity, low activation energy, ions are principally charge carriers and number of available empty sites is far greater than the number of ions (Chandra 1981).

Comprehensive reviews on superionic conductors are given by Boyce and Huberman (1979), Catlow et al. (1978, 1983, 1996), Chadwick (1983), Comins et al. (1990), Cox et al. (1994), Wang and Grey (1995, 1997), Rammutla et al. (2001, 2002). Interest in the transition from order

to disordering state goes back to the 1830's when Faraday carried out the first study. However, it was only in the 1960's that more interest was focussed on this field. At the time silver- and copper- based compounds such as $RbAg_4I_5$, AgI and CuI in which the disorder occurs in the silver and copper sublattices were discovered as superionic conductors and there was a realization that there were many potential technological applications. Furthermore, hexagonal compounds with the β–alumina structure, Na-β-alumina ($Na_{1.67}Mg_{0.67}Al_{10.33}O_{17}$), were added to the list followed by fluorites (e.g. CaF_2 etc.), defect stabilized ceramic oxides ($CaO:AO_2$ (A=Zr, Hf, Th, Ce)) and fluorides with the tysonite structure (e.g. AF_3 (A=Y, Lu, Re)) (Ngoepe et al. 1990 and Wang and Grey 1997). However, the full understanding of fast-ion behaviour of these materials requires a detailed knowledge of the nature of defect structures, crystal properties such as elastic and dielectric constants, structural properties such as radial distribution functions, dynamical properties like diffusion coefficients and ion-migration mechanisms. Hence, the objective of the work described in this thesis was to gain such information. An important feature has been combined use of theory and experiment.

This Chapter is broken up as follows: in section 1.1 we present a discussion on superionic conductors; section 1.2 is devoted to a classification of superionic conductors followed by sections on the review of stoichiometric fluorides and solid solutions (section 1.3) and on point defects in solids, diffusion mechanisms and ionic conductivity (sections 1.4 to 1.7) on fluorite lattices. Finally a summary on the objectives of the present study is presented (section 1.8).

1.2   CLASSIFICATION OF SUPERIONIC CONDUCTORS

Superionic conductors are classified according to the nature of phase transition to the superionic

state (Boyce et al. 1979). Types of phase transitions are: transition from one crystal structure to another, where there is no evidence for soft mode transitions; phase transition that extend over few hundred degrees below the melting point. The phase transformation often marks the onset, with increasing temperature, of sudden large-scale disorder. A brief review of various types of superionic conductors of this type is given below.

1.2.1 Type I

Materials of this type are characterised by the transition to the superionic state which is abrupt (Figure 1.1a). This type of transition is regarded as a first order phase transition. Here there is a rearrangement of immobile ion sublattice at the transition temperature in addition to the disordering of the mobile ion sublattice. This process is accompanied by a discontinuous increase in the ionic conductivity (Figure 1.1d). The discontinuity is attributed to the rapid increase in the number of ions available for diffusion. Materials such as $RbAg_4I_5$, AgI and CuI exhibit this type of disorder (Boyce and Huberman 1979). In this class of materials cations are structurally disordered and the cation sublattice is 'liquid-like'. Consequently, cations move from one site to another with a low activation energy.

1.2.2 Type II

In this class the transition temperature T_c to the superionic state is associated with the development of extensive disorder on either anion or cation sub-lattice (Figure 1.1b). The disorder gives rise to a progressive increase in the ionic conductivity over a relatively wide temperature range to values typical of ionic melts, but remains continuous through such transition
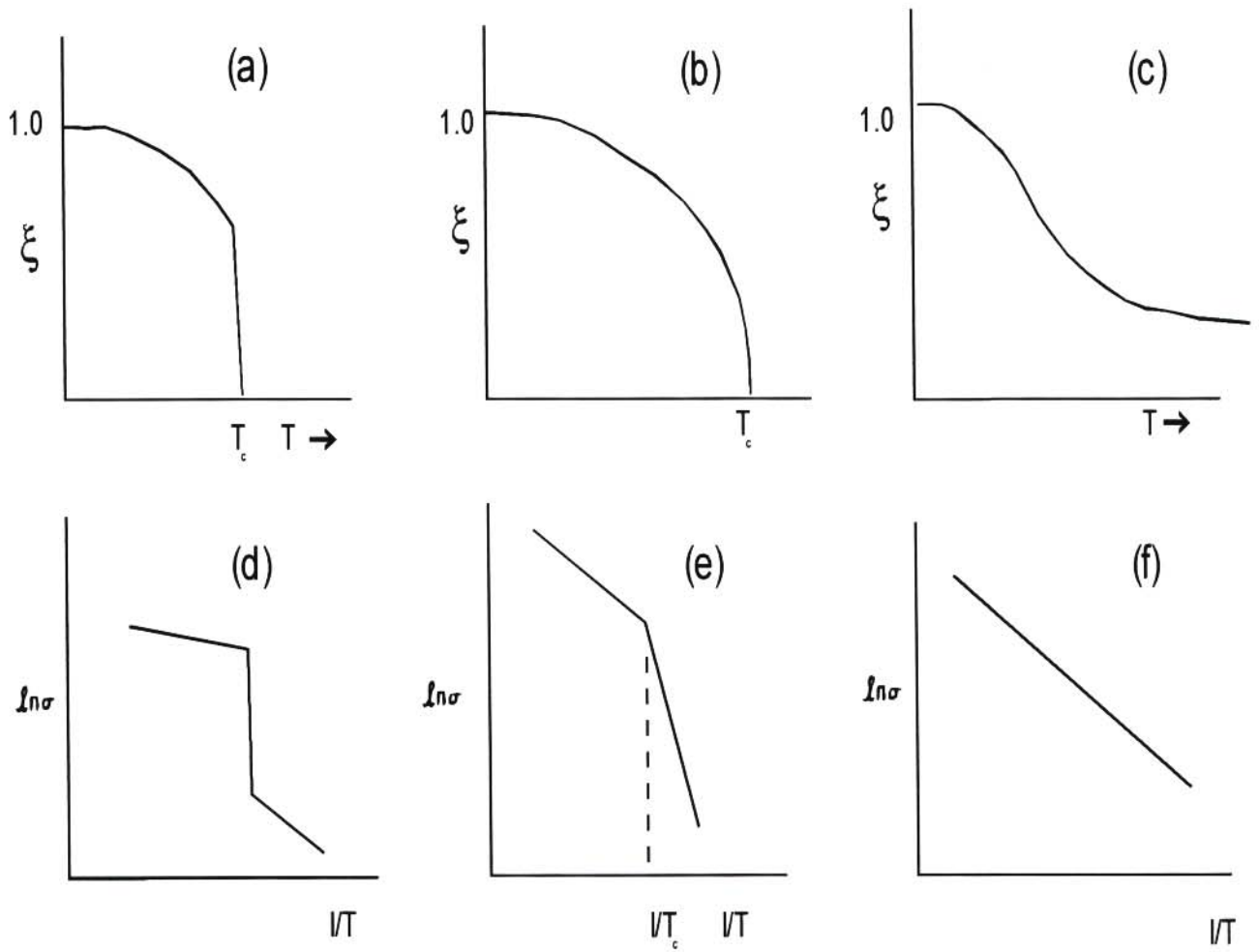
Figure 1.1 The temperature dependent order parameter (a) a first order phase transition, (b) a second order phase transition, (c) a gradual disordering with no phase transition, (d), (e) and (f) show the corresponding ionic conductivity

(Derrington and O'Keefe 1973, Derrington et al. 1975)(Figure 1.1e). Furthermore, this type of superionic conductors exhibits broad specific heat anomalies at temperatures T_c well below the melting temperatures T_m (Catlow et al. 1978). The anomalies in the specific heat are associated with the development of limited disorder on the anion sublattice of fluorites (Catlow et al. 1978) contrary to massive disorder (Rice et al. 1974, Huberman 1974).

Systems in which the phase transitions are apparently second order include fluorite type intrinsic anion conductors such as CaF_2, PbF_2, BaF_2, LaF_3, $ZrO_2(xy_2O_3)$ and anti-fluorite cation conductors like Na_2S Li_4SiO_4 and K_2S. These materials possess low melting temperatures and are predominantly ionic in nature and good electrolytic conductors at high temperatures. In the case of fluorites, T_c is given by $0.8T_m$, where T_m is the melting temperature / point.

The current investigation is concerned with type II superionic conductors.

1.2.3 Type III

In this class of materials, the order-disorder parameter gradually drops to zero, with increasing temperature, with either no "nonconducting-conducting transformation" nor specific heat anomaly, as shown in Figure 1.1c). Certain alkali halides such as $PbCl_2$, $CaBr_2$, YCl_3 and $MgCl_2$ exhibit this type of phenomenon. This usually occurs when there are significant energy differences between two lattice sites. This class of materials simply becomes highly conducting upon melting. Furthermore, the ionic conductivity (typically from $10^{-3} \ \Omega^{-1} \ cm^{-1}$ to $1 \ \Omega^{-1} \ cm^{-1}$) shows Arrhenius behaviour, with no discontinuities or shape changes (Whittingham and Huggins 1971).

1.3   REVIEW OF STOICHIOMETRIC FLUORIDES AND SOLID SOLUTIONS

1.3.1   Introduction

Experimental and computational techniques have been used to study superionic behaviour in numerous compounds and the effects of dopants on both the transition temperature and the extent of disorder. In this section we will particularly pay attention to fluorites and their mixed compounds.

The structure of the fluorite lattice (Fm3m) is shown in Figure 1.2. It is of considerable importance in the discussion of type II superionic conductors. Figure 1.2 shows that in a perfect lattice, each ion occupies the site assigned to it on the basis of the crystal structure. The lattice consists of a simple cubic array of anions, with alternate cube-centres occupied by cations (Baker 1974). Consequently, half of the cube centre sites are empty. A significant aspect of such empty cube centre sites is the provision for the accommodation of fluorine interstitials.

1.3.2   Pure Stoichiometric Halides

Much work has been carried on the pure alkaline-earth fluorides such as CaF_2, BaF_2, PbF_2, etc. (Catlow et al. 1978, Brass 1989, Comins et al. 1990, Cox et al. 1994, Netshisaulu et al. 1993, 1996). In a fluorite structure as shown in Figure 1.2, fluorine ions occupy normal lattice positions with cations occupying alternate cube center-sites, while the other alternate cube centre sites are vacant. Low and high temperature measurements on these compounds revealed that they behave in an essentially the same way. The degree of disorder is negligible at temperatures below the
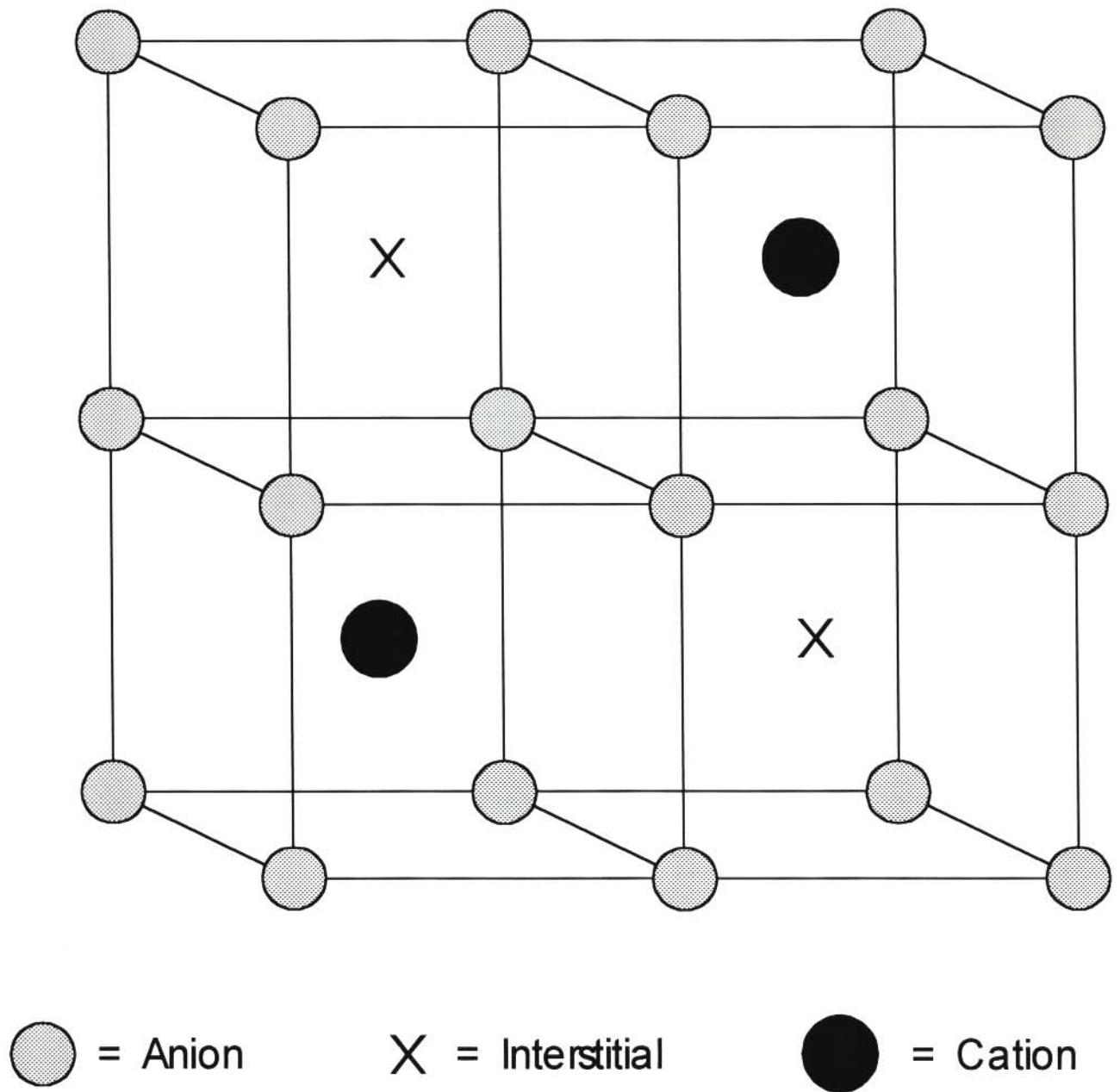
Figure 1.2 The fluorite crystal structure.

fast-ion regime, but with increasing temperature, fluorine ion displacements occur along <100> directions (Shapiro 1976 and Vlieg 1986). Above the critical temperature T_c the disorder is enormous and the material becomes superionic (Brass 1989). During this transition the cations remain at their normal lattice (tetrahedral) sites. In short, the results from statics and molecular dynamics computer simulation techniques on pure fluorites reveal that: anion – Frenkel disorder dominates (i.e. ions occupying cube centre sites leaving anion vacancies); activation energies for vacancy migration are relatively low, i.e., anion vacancy is highly mobile; activation energies for interstitial migration are substantially higher; conductivity is enhanced, disorder on the cation sub-lattice is negligible, etc.

Early theories on the properties of fluorites at high temperatures were based on the assumption that interstitials would contribute effectively to the anion disorder (Shapiro 1976, Dickens et al. 1976a). However, recent computer modelling studies and detailed examination of neutron scattering data have indicated that cube-centre sites are not appreciably occupied for any length of time in the superionic phase (Catlow 1996). In fact a large number of vacancies (on the lattice sites) is due to the relaxation of ions.

1.3.3 Doped Fluorides

1.3.3.1 Trivalent impurity doped fluorides

The rare-earth ions enter the fluorite crystal lattice as trivalent cation substitutionals, with charge compensation being provided by excess fluoride interstitials (Kjems, Andersen and Schoonman 1983). Trivalent impurity cations replace divalent host cations of the fluorite lattice and charge-compensation is provided by the incorporation of fluoride ions (F) (excess anions) in interstitial

8

sites (Baker 1974). Thus the M^{3+} impurities occupy cation sites and are compensated by interstitial fluorine ions. Hence the predominant defect in the alkaline earth fluorites is the Frenkel type. This is also supported by theoretical calculations of point defects (Catlow 1974).

In trivalent doped fluorites, the main focus of interest has been on the nature of the dopant interstitial clusters at low and high dopant concentrations. At low dopant concentrations (<1 mol %), there is a good evidence for the formation of nearest-neighbour (nn) and next-nearest neighbour (nnn) substitutional cation-anion interstitial pairs (Catlow et al. 1973, 1978; Comins et al. 1990). Furthermore, at these concentrations, the ENDOR work (Baker et al. 1968) also indicated that the anion interstitial is not significantly distorted from the cube interstitial site as verified by Catlow and Norgett (1973). It has, however, been well established that at higher dopant concentrations (> 5 mol %), complex defect clusters are formed with interstitials not located at cube-centre sites (Cheetham et al. 1970, 1971). These impurity-stabilized clusters are considered to bind interstitials leading to reduction in the transition temperature T_c to the superionic phase (Catlow et al. 1981, Chadwick et al. 1983, Comins et al. 1990, Mjwara et al. 1991, Ngoepe and Catlow 1991 and Rammutla et al. 2002). These striking features have been primarily ascribed to an effective reduction in energy of formation on anion Frenkel pairs, caused by trapping of interstitial ions by impurity-interstitial complexes.

Theoretical evidence (Catlow et al. 1973) has been put forward in connection with the existence of the 2:2:2 cluster as a basic structure in the more heavily doped fluorites. These dopant-interstitial clustering (in anion-excess alkaline-earth fluorites) has also been studied by extended X-ray absorption fine structure (EXAFS) (Catlow et al. 1985).

Experimental measurements and estimates based on computer modelling techniques suggest that cation impurity-interstitial complexes and charge compensating interstitial anions act as traps for thermally-generated anion interstitials, reducing both the energy of formation of anion Frenkel pairs and T_c.

1.3.3.2 Divalent doped fluorides

The fluorite structured solid solutions $RbBiF_4$ and $PbSnF_4$ are exceptionally good F^- ion conductors (Catlow et al. 1985 and Cox et al. 1994). This is due to the mixed nature of the cation sub-lattice. EXAFS studies on local structures of the two cations, Rb and Bi in $RbBiF_4$, as a function of temperature, showed marked differences (Catlow et al. 1985, 1989 and Cox et al. 1994). The most fascinating insight into this material is that the Rb edge EXAFS displays a marked reduction in both amplitude and frequency with an increase in temperature, whereas in the case of Bi no change in the amplitude or frequency was observed. This suggests that the Bi ions 'dictate' the structure by drawing the F^- ions to form tight co-ordination shell at a short distance. This leaves the Rb-F shell co-ordination comparatively disordered. The larger change in the Rb-F distance as function of temperature was attributed to the fact that the thermally induced F^- ions vacancies were preferentially located next to Rb ions (with larger ionic radii and lower charges). Molecular dynamics (MD) has been used to yield complementary information on structural properties in these materials (Catlow et al. 1989). Ion transport occurs via a non-collinear interstitialcy mechanism. A similar study on $PbSnF_4$, where both cations have a charge of 2+ so that no electrostatic advantage is possible for the formation of vacancies at sites with a surplus of either Pb or Sn nearest neighbours, shows that vacancies are sited next to Pb ions (Cox et al. 1994). This finding has been attributed to the larger ionic radius of Pb cations and a highly

active lone pair on Pb cations.

Information from our previous EXAFS experimental study on CdF_2(60 mol % PbF_2) has provided evidence for an anomalous disorder around Pb cations (Netshisaulu et al. 1995, Netshisaulu 1996). This result is in accord with arguments based on ion size, in which a small ion allows the lattice to relax around it, whereas the larger ion causes a slight distortion in the local structure (Catlow et al. 1989). Complementary molecular dynamics technique has also shown a relatively low value of the transition temperature T_c to the fast-ion phase. It has been found that no diffusion of fluorine ions occur below T_c, in pure fluorites (Netshisaulu et al. 1993, Netshisaulu et al. 1999). However, a feature of primary interest is the mobility of fluorine ions in this system which occurs below T_c and that its T_c is significantly low compared to that of trivalent doped fluorides. Furthermore, a significantly low F^- ion interstitial activation energy suggests that interstitialcy mechanism is a more prevalent mode of transport in CdF_2(60 mol % PbF_2). Such an interstitialcy mechanism was also depicted from the single ion trajectories obtained from our previous MD calculations (Netshisaulu et al. 1999). These factors are more ideal for construction of efficient reversible electrochemical cells.

1.4   POINT DEFECTS IN IONIC SOLIDS

Ionic crystals consist of arrays of different charged ions. A stable crystal structure is formed when Coulombic attractive forces of oppositely charged ions reach equilibrium with repulsive forces of the outer of the electron clouds (like ions). The lattice of a fluorite crystal can be described as a simple cubic array of anions with a cation at every alternate cube centre. In a perfect lattice, i.e. at $T \approx 0$ K, each ion occupies the site assigned to it on the basis of the crystal structure.

11

However, in real crystals the lattice will deviate to some extent from the ideal lattice due to either thermal atomic vibrations (thermal defects) or impurity-induced defects. The existence of crystal defects causes matter transport in ionic solids. There are two major types of thermal (intrinsic) point defects (imperfections which are localised over a few atom sites) that are responsible for ionic transport. These are the Schottky and Frenkel defects. Schottky and Frenkel defects are discussed below as they play a leading role in determining most of the physical properties of the crystals.

1.4.1 Schottky Defects

A Schottky defect is formed when corresponding cation and anion sites in the lattice are vacant (see Figure 1.3a). So ions/atoms move from their normal lattice sites within the crystal structure to the lattice sites on the surface of the crystal leaving behind a vacancy. This disorder is dominant in closed-packed solids/structures, where the energy required to insert an interstitial defect into the structure is very large. It is mostly noted in rare-gas solids (e.g. Krypton and Xe), where only one type of vacancy occurs and also in most pure alkali halides (e.g. rocksalt (NaCl) and KCl), where both cation and anion vacancies occur in equal numbers.

In a pure fluorite crystal of composition MF_2 (Figure 1.2), containing Schottky defects, $n(F^-)$ and $n(M^{2+})$ are the number of F^- anions and M^{2+} cations, respectively. $n(F^-)$ and $2n(M^{2+})$ are each constant with $n(F^-) = 2n(M^{2+})$. For a lattice site to be vacant, the probability for creating

12
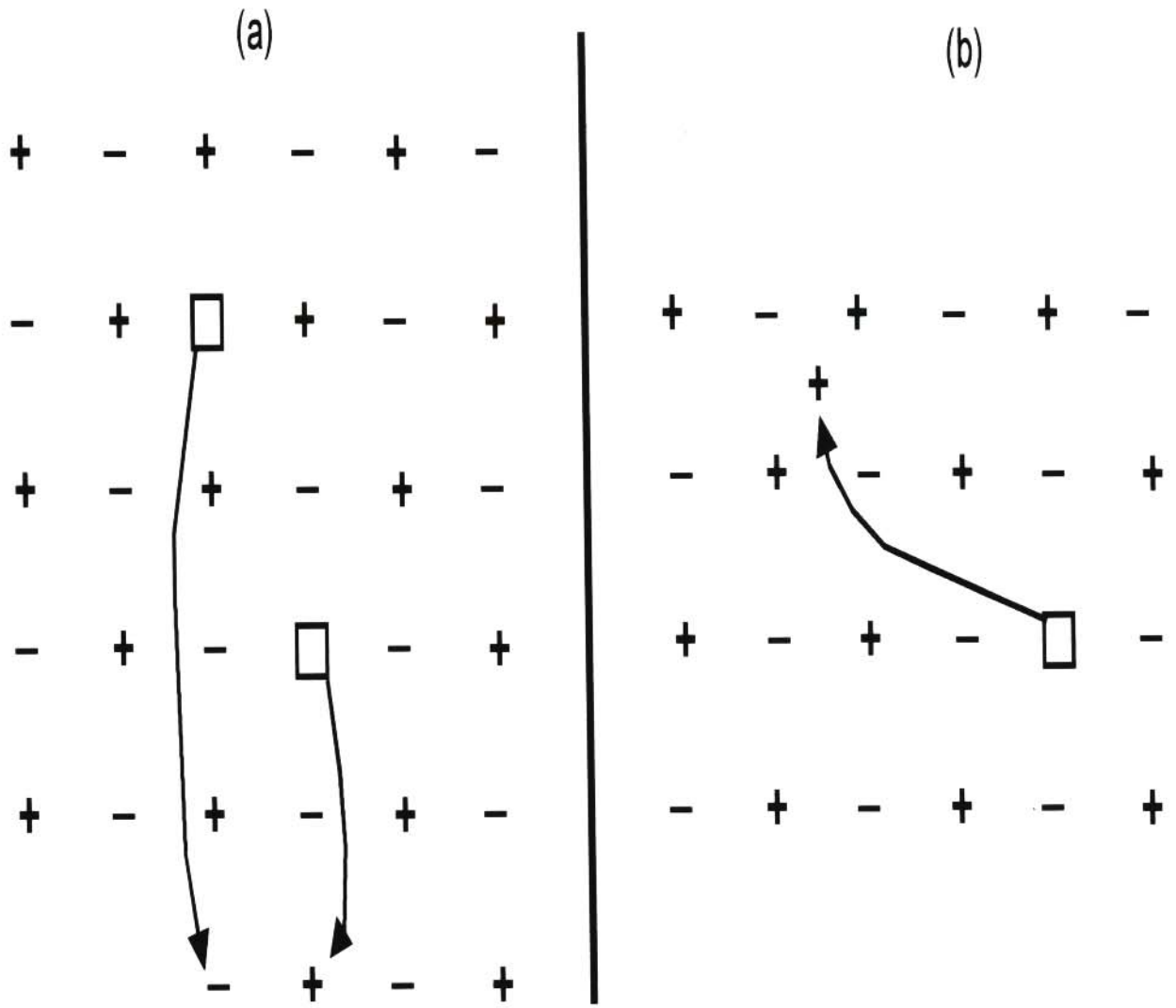
Figure 1.3 (a) Schottky defect (b) Frenkel defect

13

a Schottky defect is given by

$$P = \exp\left[\frac{-E_s}{k_B T}\right]$$ 1.1

where k_B is the Botzmann's constant, T is the absolute temperature and the Schottky free energy $E_s = h_s - TS_s$, with h_s and S_s the enthalpy and entropy of the energy per defect. If the crystal contains N ions and n Schottky defects, then N-n lattice sites are occupied. Hence, the probability P (the number of ways of creating n defects and placing them among N ions) may be obtained from

$$P = \frac{N!}{(N-n)!n!}$$ 1.2

At thermal equilibrium, the total number of vacancies created, n, can be obtained from

$$P = \frac{N!}{(N-n)!n!} = \exp\left[\frac{-E_s}{k_B T}\right]$$ 1.3

If the number of vacancies is much smaller than the total number of atoms, i.e., if $n \ll N$, then

$$n \approx N \exp\left[\frac{-E_s}{k_B T}\right]$$ 1.4

14

1.4.2 Frenkel Defects

A Frenkel defect occurs when an ion moves from its regular site to a cube-centre (interstitial) site, thus leaving a vacancy (see Figure 1.3b) at its normal position (i.e. at the regular cube corner) (Hayes and Stoneham 1985). These defects are prevalent in open structures such as those of silver halides (e.g. AgBr, AgCl, etc), where they are formed on the cation sublattice and those of fluorite structures where they form on the anion sub-lattice. The probability/number of different ways of creating/producing 'n' Frenkel defects and distribute them among N lattice and N' interstitial sites is written in the form

$$P = \frac{n!}{(N - n)!(N'-n)!}$$

$$= \exp\left[\frac{-E_f}{k_B T}\right] \qquad\qquad 1.5$$

where E_f is the Frenkel free energy or the energy required to displace an anion from its normal lattice position to an interstitial.

If the number n of Frenkel defects is much smaller than the total number of atoms and interstitials, respectively, i.e., if $n << N$ and N', then

$$n \approx (NN') \exp\left[\frac{-E_f}{k_B T}\right] \qquad\qquad 1.6$$

where $E_f(= h_f - TS_f$, with h_f and S_f being corresponding enthalpy and entropy) is the Frenkel free

energy necessary to remove an ion from a lattice site to an interstitial position. For a Frenkel pair equation 1.6 becomes

$$n \approx (NN')^{1/2} \exp\left[\frac{-E_f}{k_B T}\right]$$ 1.7

In most solids the crystal formation of Frenkel and Schottky defects are significantly different that one type is dominant. However, calculations on Schottky defects suggest that the energy needed to create a Schottky pair in fluorite-structured materials such as CaF_2 is ≥ 5 eV and to produce a cation Frenkel pair is ≈ 6 eV (Hayes and Stoneham 1985). It is apparent from these large values that the concentration of Schottky defects is fairly low even at high temperatures. In contrast, anion Frenkel defects are most common in pure fluorites MF_2 (M = Ca, Sr, Ba, Pb) where F^- interstitials occur in equal numbers.

1.5   DIFFUSION MECHANISMS IN FLUORIDE SOLIDS

In a perfect crystal, the atoms occupy the sites assigned to them on the basis of the crystal structure and diffusion cannot easily occur. However, atoms in a crystal structure oscillate around their equilibrium positions. Occasionally, these jumps become large enough to allow an atom to change sites. Hence, diffusion (a macroscopic quantity/phenomenon relating to ensembles of atoms) in solids is simply the movement of atoms through a crystal lattice. However, the crystal itself remains fixed/retains its shape. During the diffusion process, the lattice site dwelling time is several orders of magnitude greater than the time spent between lattice sites. Ionic crystals

have simple structures that allow for the straightforward determination of diffusion coefficients. Much of the interest in diffusion process in the fluorites with large divalent cations (e.g. Ca^{2+}, Sr^{2+}, Pb^{2+}, Ba^{2+}, etc) is due to their potential use as solid electrolytes in future battery systems.

Experimental techniques such as Radio-tracer experiments (Hood and Morrison 1967 and Binier et al. 1979) have, in principle, provided useful information on the disordered sub-lattice in ionic solids. In essence, these experiments showed that the cations are relatively immobile, whilst the anions are highly mobile. However, information on diffusion coefficients is not accessible at high temperatures via tracer experiments. NMR experiments become useful in this regard (see Chadwick 1983(b)).

Different types of defects give rise to different mechanisms of diffusion (mass transport) as shown schematically in Figure 1.4 for the fluorine motions in fluorite lattices. This process gives rise to ionic conductivity (i.e. charge transport).

1.5.1   The Vacancy Mechanism

In all crystals some of the lattice sites are unoccupied. Vacancy diffusion mechanism occurs when an ion in a lattice site adjacent to a vacancy (empty lattice site) jumps into a vacancy (at a nearest neighbour (NN) site). The vacancy migrates/diffuses into the bulk of the crystal, displacing the mobile ion by one lattice step in the process. In most fluorite-type crystals diffusion proceeds by vacancy motion along the <100> direction (Figure 1.4a) (Catlow et al. 1989 and Ngoepe and Catlow 1991).

17
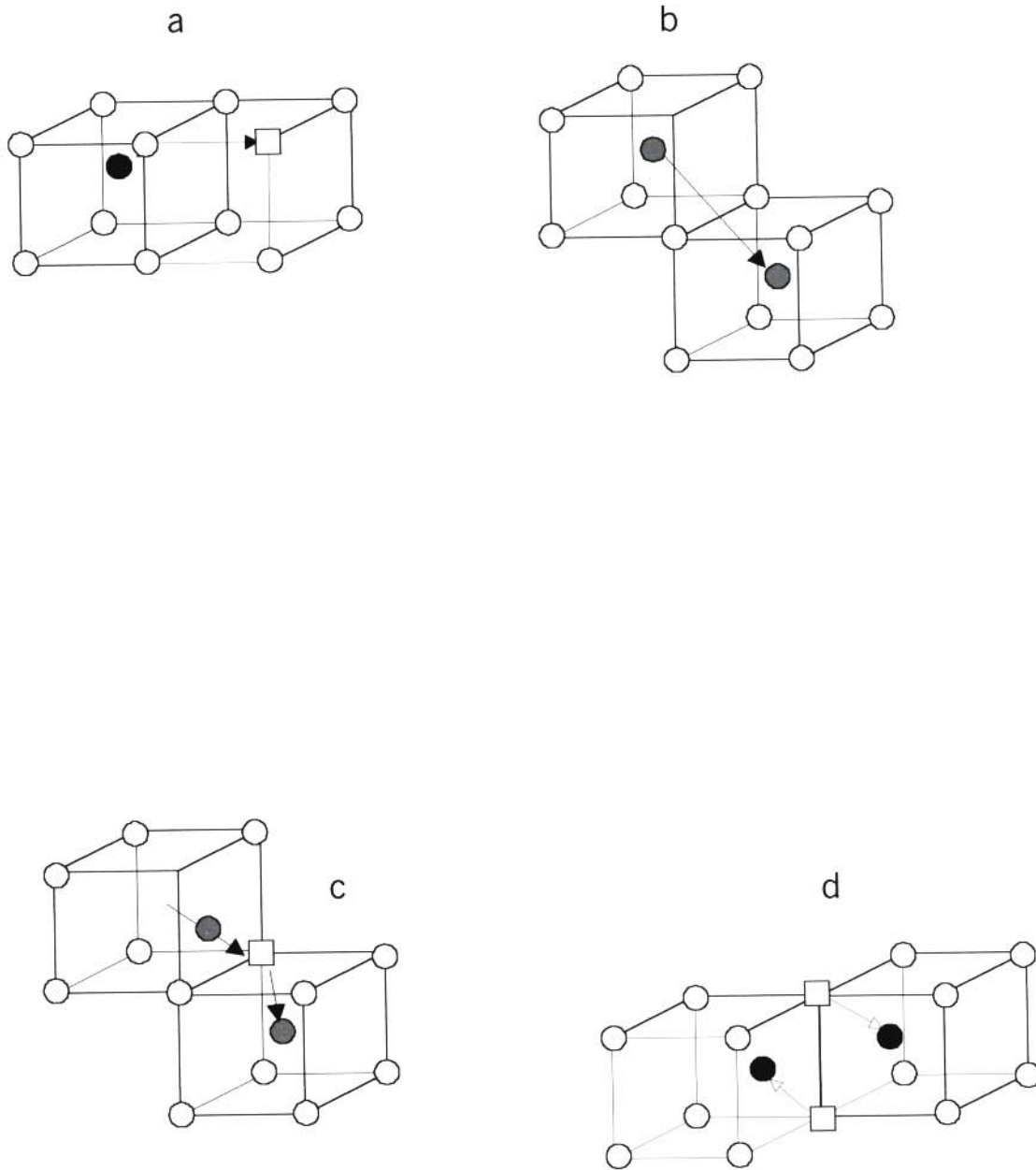
Figure 1.4 Diffusion mechanisms for anions in the fluorite lattice (a) Vacancy mechanism (<100>

jumps), (b) Direct interstitial migration (<110> jumps), (c) Interstitialcy mechanism (non-

collinear) and (d) Exchange mechanism. (Closed circles represent cations, open circles the anions

and open squares the anion vacancies).

1.5.2   The Interstitial Mechanism

In this mechanism an interstitial ion (an ion occupying sites other than those of the perfect lattice) migrates to anyone of the neighbouring interstitial sites by means of the shortest available route (Figure 1.4b). This mechanism is also called a direct interstitial mechanism. Furthermore, it is very unlikely to occur in a fluorite lattice because the lattice distortion would become large enough to make it inoperative. Hence, this diffusion mechanism does not permanently displace any of the matrix ions.

1.5.3   The Interstitialcy Mechanism

This type of diffusion mechanism is mostly common in mixed systems. If an ion gets into the interstitial site, it cannot jump/move from one interstitial position to another since it could cause a large distortion on the structure. Hence, for less distortion, it would simply push/displace one of its NN lattice atoms to the next available (matrix) site (Figure 1.4c). If the displaced ion moves in the direction different from that of an interstitial ion, then the jump is termed non-collinear. The interstitialcy motion takes place along a <111> direction. The path taken depends on the occupancy of the cubes. In the salt structure all cubes are vacant whereas in the fluorite structure alternate cubes are occupied by the ions of the other sublattice, so that only the non-collinear intersitialcy mechanism is operative.

1.5.4   The Exchange Mechanism

This method of migration occurs when two neighbouring ions on normal lattice sites exchange

19

positions via two adjacent interstitial sites (Figure 1.4d). However this mechanism is energetically unfavourable in crystals with close packed structures because each ion is surrounded by its neighbours.

1.6   IONIC CONDUCTIVITY IN SOLIDS

Ionic conductivity is a macroscopic quantity and is a measure of a drift in the random motion of defects due to the applied electric field on the ionic crystal. In superionic conductors conduction occurs by means of ions only and the presence of point defects at higher temperatures enables some species of ions, mostly anions, to transport current under applied electric field. The contribution of the highly mobile defect species to the specific conductivity of the crystal is obtained from Ohm's law:

$$J_i = \sigma_i E \tag{1.8}$$

where J_i is the electrical current density of ion species of type i, σ_i is the conductivity and E is the field.

However, the electrical current density J_i is given by

$$J_i = q_i n_i v_{drift} \tag{1.9}$$

But

$$v_{drift} = \mu E \tag{1.10}$$

Using equations 1.8, 1.9 and 1.10 gives the total conductivity as

$$\sigma = nq\mu \hspace{6cm} 1.11$$

where n_i is the number of mobile species of type i per unit volume or density of charge carriers/mobile species, q_i is the charge of mobile species i and μ is the mobility of mobile species.

From equations 1.8 and 1.11

$$J = (nq\mu)E \hspace{6cm} 1.12$$

However, Fick derived equations to explain the transport of matter in materials as follows:

$$J \propto \frac{dn}{dx}$$

or

$$J = -D \left[\frac{dn}{dx} \right] \hspace{5cm} 1.13$$

where the proportionality constant D is the diffusion coefficient, J the flux density (the flow of matter per unit cross sectional area per unit time), x is the direction of flow of matter due to the presence of a concentration gradient and n is the number of mobile species per unit volume. The negative sign in this equation (i.e. equation 1.13) shows that diffusion occurs in the direction

opposite to increasing concentration or it is down the concentration gradient. This mathematical statement is generally applicable for an isotropic medium, i.e. a medium which has uniform physical properties in all directions about any point in the medium.

It can be shown that, at equilibrium, the flow/transfer of ions is opposed by the diffusion current, i.e. the two current densities are equal.

Hence,

$$-q \, D \left[\frac{dn}{dx} \right] = (nq\mu)E \qquad\qquad 1.14$$

where q represents the electron charge (e = 1.6 x 10^{-19} C)

So that rearranging equation 1.14 gives

$$\frac{dn}{n} = \left[-\frac{\mu Ex}{D} \right] dx \qquad\qquad 1.15$$

On integrating, we obtain

$$n = A \exp \left[\frac{\mu Ex}{D} \right] dx \qquad\qquad 1.16$$

where A is a constant.

However, from Boltzmann statistics,

$$n = B \exp\left[-\frac{qEx}{k_BT}\right]dx \qquad\qquad 1.17$$

where k_B is the Boltzmann's constant: $k = 1.38 \times 10^{-23}$ J/K

Equating equations 1.16 and 1.17 yields the microscopic Nernst-Einstein equation/relation which in terms of the conductivity is

$$\frac{\sigma}{D} = \frac{nq^2}{k_BT}$$

or

$$\sigma = n\left[\frac{Dq^2}{k_BT}\right] \qquad\qquad 1.18$$

This equation finds extensive application in ionic systems. However, it is often much easier to measure the ionic conductivity, which is a nondestructive experiment, than to measure D. From equation 1.18 we can determine D from a measurement of σ. The diffusion coefficient which is measured experimentally is usually the tracer diffusion coefficient (D_t) and is different from D. So, with D_t, equation 1.18 changes to

$$\frac{\sigma}{D_t} = \frac{nq^2}{f_Tk_BT} \qquad\qquad 1.19$$

where f_T is termed the correlation factor for tracer diffusion. Correlation effects for diffusion in solids should be taken into account because each atom follows a correlated walk (i.e. not a truly random walk) during diffusion. The value of f_T is characteristic of the lattice geometry and of the

23

diffusion/jumping mechanism. When the jumps take place completely at random, $f_T = 1$. For cases of correlated jumps, $f_T \neq 1$, the determination of f_T could lead to the definition of a diffusion mechanism and hence the predominant point defect. The topic of correlation effects in tracer diffusion is reviewed comprehensively by Catlow (1982).

So equation 1.19 becomes

$$\sigma = \frac{n}{f_T} \left[\frac{D_t q^2}{kT} \right] \qquad\qquad 1.20$$

where the units (in the present study) for nf_T^{-1} are in cm^{-3}, q in Coulombs (C), k in JK^{-1}, T in Kelvin (K), D in $cm^2 s^{-1}$ and σ in $\Omega^{-1} cm^{-1}$ (or $C^2 J^{-1}.s \times cm^{-1}$)

1.7   COMPARISON OF SELF-DIFFUSION AND IONIC CONDUCTIVITY

The two transport coefficients, ionic diffusion and ionic conductivity, are caused by the jumping of defects through the crystal. Diffusion represents a mixing up of the ions in a crystal caused by the thermally induced random motion of the defects, whereas the ionic conductivity experiment measures a drift superimposed on this motion by an applied electric field (E). The connection between these two phenomena can be obtained from the very general Nernst-Einstein relation (equation 1.18).

24

1.8   MOTIVATION OF THIS RESEARCH

There is theoretical and experimental evidence that ionic motion in superionics is substantially enhanced by monovalent, divalent or trivalent doping (Kosacki et al. 1989, Comins et al. 1990, Cox et al. 1994). Hence, this study forms part of a continuing investigation of fast-ion conduction in fluorite-type materials doped with either trivalent or divalent substitutional cation impurities (Catlow et al. 1985, Comins et al. 1990, Cox et al. 1994). Most of these materials show order-disorder phase transition at high temperatures (i.e., close to T_c, where a substantial Frenkel disorder occurs on the anion sub-lattice). This phenomenon is accompanied by a substantial rise in ionic conductivity, a broad specific heat anomaly and a significant reduction in certain elastic constants (Catlow et al. 1978, Comins et al. 1990 and Rammutla et al. 2001). High ionic conductivity is important so that the ohmic polarization across the electrolyte does not lower the operating cell voltage appreciably. Furthermore, the activation energy should also be low in order to maintain a steady output performance when changes in environmental temperatures takes place.

Previous studies undertaken on trivalent-doped fluorites have shown that the extra positive charge carried by an M^{3+} dopant cation can be compensated by an introduction of a fluorine interstitial ion if a divalent cation is to be replaced in order to maintain electrical neutrality. However, substitutional divalent cations need no charge compensation.

This work was stimulated by the Raman scattering experimental work of Kosacki et al.(1989) on $CdF_2(xPbF_2)$ (0 mol % $\leq x \leq$ 100 mol % PbF_2) mixed metal fluorides, which revealed that there is a high mobility of fluorine anions in these systems (Kosacki et al. 1989) and the operation temperature is drastically reduced, bringing it closer to room temperature. The latter property

has generated the current interest in the computational study of $CdF_2(xPbF_2)$ mixed systems. In addition, it has been shown using experimental methods that CdF_2(60 mol % PbF_2) is the most favourable material for reversible operation battery construction which operates at room temperature (Kosacki et al. 1989). In addition, we have already shown, in our earlier work on these systems, via computational methods that ionic motion in CdF_2(60 mol % PbF_2) is substantially enhanced as compared to those of the two binary compounds, namely, CdF_2 and PbF_2 (see Netshisaulu 1996). The results also agree with our previous EXAFS experiment at concentration $x = 60$ mol % PbF_2. Furthermore, a significantly low F^- ion interstitial activation energy calculated using statics simulations suggested that interstitialcy mechanism is a more prevalent mode of transport in CdF_2(60 mol % PbF_2). Such an interstitialcy mechanism was greatly validated by information obtained from molecular dynamics (using the rigid ion model) which displayed a window through which one can observe the ion trajectories of a simulated system.

However, despite reports elaborated above, there is limited information on the nature of defect structures giving rise to the superionic motion in the entire range of $CdF_2(xPbF_2)$ mixed systems. Furthermore, the local environments of Cd and Pb cations as a function of concentration x and temperature in these systems are not yet fully understood. Hence, the present study focuses on extensive computational and EXAFS studies on the whole series of $CdF_2(xPbF_2)$ mixed crystals. Effects of randomly doping alkaline earth fluorides with divalent ions (over the cation sublattice) on bulk data, transport properties (such as diffusion rates, conductivity and activation energies) and structural properties are also the subject of the present study. Furthermore, the extent of disorder in these systems will be clarified. These properties will be optimized for use as electrolytes in microbatteries. EXAFS measurements were employed to provide complementary

information on the local environments of the cation sites.

It is hoped that a better understanding of the fast-ion phase of the mixed-metal fluorides under study will pave a way for manufacturing other mixed crystals, which could serve as better electrolytes in batteries. Hence, this study seeks to add value to the search/synthesis for/of new mixed-metal fluorites with enhanced conductivities.

CHAPTER 2

COMPUTER MODELLING TECHNIQUES

2.1   INTRODUCTION

With the advent of powerful contemporary computers with rapid access memory, there were several attempts to model the properties of materials, with commercial importance (see for example Catlow, 1997). Computer modelling involves representing physical systems by models, which are constructed to make computations feasible. The models are then simulated on ultrafast computers, with a view to predict the properties of real systems/crystals. The motivation to study real world systems using computer simulation is that the approach expedites the ability to probe systems that could be experimentally inaccessible. These methods are also used as an aid to the analysis of experiments.

There are two basic types of computer modelling methods used in computational physics (concerned with the behaviour of atoms in solids) and chemistry (concerned with the structures of various species in solids). These are classical atomistic modelling and quantum mechanical modelling (Hayes and Stoneham 1985, Catlow 1986, Wimmer 1996, Catlow 1997). These techniques have been used to study bulk, defect and surface properties of condensed matter. Atomistic simulation methods are based on the variation of forces between atoms with interatomic separation. Hence, it is essential that reliable interatomic potential models be obtained since they represent the fundamental physics of the system under investigation. In the present work,

atomistic modelling methods are used to predict the following properties of real systems:

- Structure and lattice energy

- Bulk phenomenon such as elastic and dielectric constants

- Defect properties such as formation and activation energies

- Detailed transport phenomena in disordered solids.

In this chapter an outline of the form of interatomic potential models used to simulate the forces acting between ions/atoms in solids will be presented, followed by an account of the theory of the modelling methods used in this work will be given. Lastly, particular emphasis is given to their applications to fast-ion conductors.

2.2   SUMMARY OF WORK ON POTENTIAL MODELS

In atomistic modelling, the reliability of the simulations depends heavily on the quality of the interatomic potentials used in the calculations. The potentials are used to predict the structural and dynamical properties of solids. The interaction between a pair of ions in an ionic crystal is expressed in two parts, namely, the long-range Coulomb (i.e. electrostatic due to the ionic charges q_i and q_j) and the non-Coulomb short-range part $\phi(r_{ij})$ between the ions. Their sum yields the lattice energy of the crystal:

$$V(r_{ij}) = \frac{q_i q_j}{r_{ij}} + \phi(r_{ij})$$ 2.1

where r_{ij} is the distance between ions i and j. For strongly ionic solids in which interactions between atoms are non-directional, q is assigned the full charge of the ion located at the nucleus (e.g. for NiO: Ni=2; O=-2) (Catlow and Stoneham, 1983). However, for semi-ionic and heteropolar materials, covalence is often marked with directionality to the bonding. In such instances, the use of partial charges is more realistic.

The second derivative of equation (2.1) with respect to strain and displacement yields statics properties such as dielectric and elastic constants, respectively. A number of standard analytical functions are available for $\phi(r_{ij})$, e.g. the Buckingham and Leonard Jones forms which are more suitable for non-bonded interactions. The short-range interatomic forces are described by the Buckingham form (for ionic and semi-ionic systems):

$$\phi\left(r_{ij}\right) = A \exp\left[\frac{-r_{ij}}{\rho}\right] - \frac{C}{r_{ij}^{6}} \qquad\qquad 2.2$$

where r is the interionic separation, $A_{ij}\exp(-r/\rho_{ij})$ denotes repulsion (Born-Mayer potential for cation-fluorine and fluorine-fluorine pairs) when two neighbouring clouds overlap and $C_{ij}r^{-6}$ represents a Van der Waals attraction for fluorine-fluorine pairs. Thus, the Born Mayer form is supplemented by an attractive r^{-6} term for the anion-anion interactions. ρ is the hardness factor/parameter. Generally these calculations are computationally inexpensive due to the exclusion of ionic polarizability.

30

A considerable improvement of the static lattice results obtained from rigid ion potentials has been made using the shell model (Dick and Overhauser 1958). In this model, an ion is simulated by a mass-less shell (external electrons) and a massive core (into which the mass of the ion is concentrated). In this model, the shell is attached to a core by means of a harmonic spring of force constant, k (see Figure 2.1). Polarisation is described in terms of the displacement of the shell relative to the core and is coupled to the short-range repulsion (Catlow et al. 1986) by allowing repulsive forces to act entirely between shells. The net ionic charge is represented by the sum of the core (X) and the shell (Y). Hence, the expression for the polarisability of the free ion is as follows:

$$\alpha = \frac{Y_i^2 e^2}{k_i} \qquad\qquad 2.3$$

where $Y_i e$ is the shell charge and k_i the harmonic spring constant coupling the core and the shell of the ion. The reliability of computer-modelling techniques in calculating defect energetics and thermodynamic properties in solid state materials largely depends on the appropriate determination of the three interaction parameters in equation (2.2) and the shell model constants, i.e. Y_i and k_i. However, in most cases, the increase in the already enormous computational requirements prevents the use of such shell model potentials in molecular dynamical cases. In addition, numerous static and dynamical simulation studies have shown that ionic two-body potential interactions are sufficient for studies of fluorite structured materials; whose structure is simple.

Variables of the interatomic potentials in equations (2.2) and (2.3) must be parameterised. This
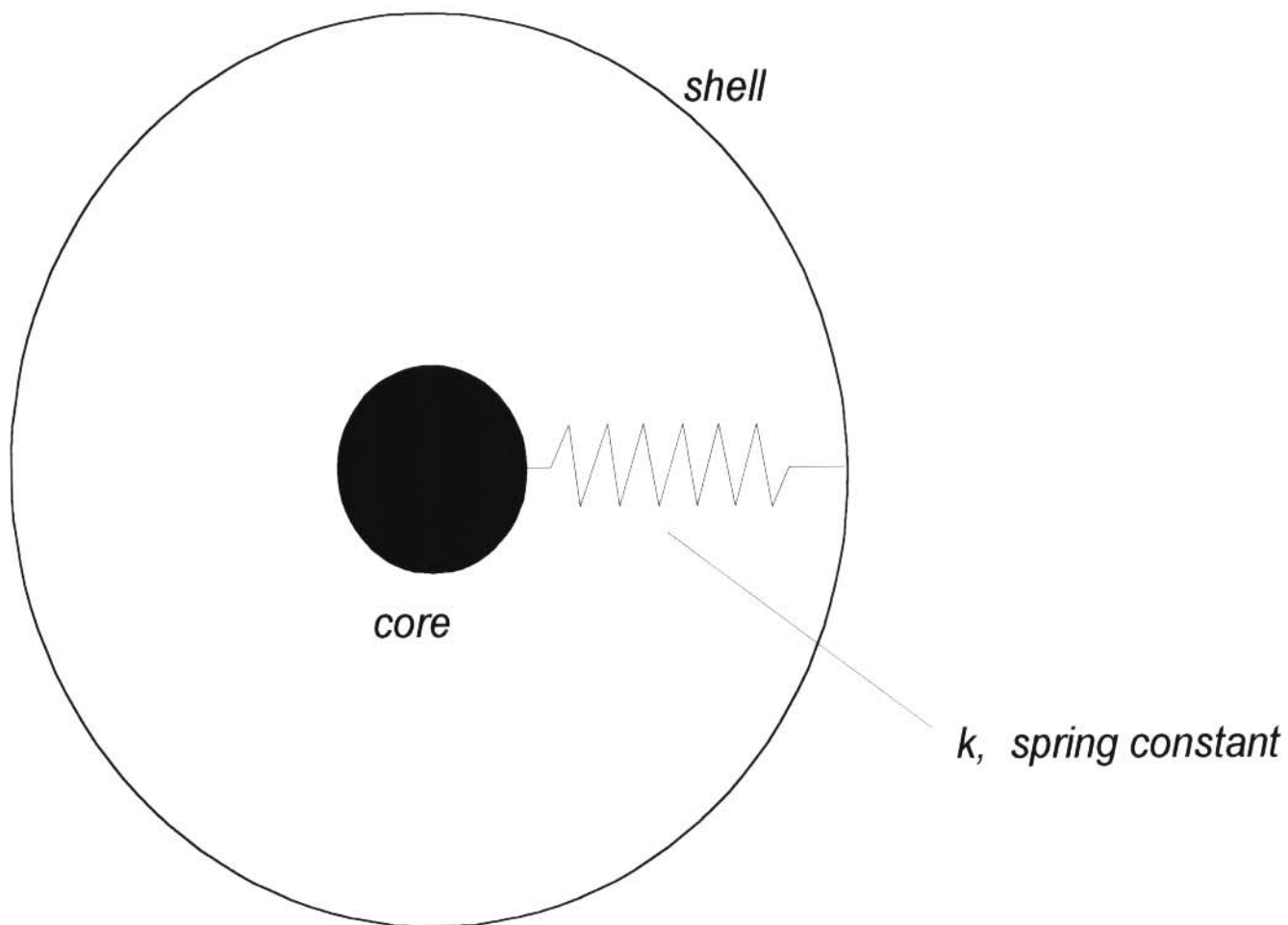
Figure 2.1 Schematic representation of a polarisable model

may be achieved by using either empirical or theoretical (or direct) methods. In empirical procedures, parameters (starting with an initial guess of parameters) in the analytical function describing the potentials are fitted to the experimentally observed properties (e.g., the structure, dielectric, elastic constants, etc.) of a model compound or crystal where they are adjusted via a least squares fitting procedure (in order to minimise the differences between the calculated and the experimental structure). This process is repeated until optimal agreement is obtained. However, there are some drawbacks with this approach:

- The empirical approach only yields information on potentials at interatomic distances close to those in the model compounds.

- Good crystal data (elastic and dielectric constants) must be available for suitable model compounds

- Experimental data is required for the calculations

- The derived potentials are only accurate at internuclear separations, which are close to those of the perfect lattice.

The theoretical approach is based on quantum mechanics. This process involves deriving potentials by calculating the short-range interaction energy between two ions for a series of interatomic separations. The resulting energy surface is then fitted to potential functions. The most accurate approach is likely to be via Hatree-Fock quantum mechanical methods (see for example Gale et al. 1992). Short-range potentials have also been developed from electron gas methods (see for example Mackrodt et al. 1979) and local density methods. Some weaknesses of this approach are:

- Experimental data is required

- Care of environmental factors must be taken into account correctly during the calculations

2.3 Lattice Statics

Static simulations may be subdivided into two categories, perfect lattice and defect lattice calculations. Both methods are based on energy minimization procedures. Structure and lattice energy properties could be calculated using static simulation procedures. These methods take no explicit account of thermal motions of atoms in the materials. However, to obtain detailed information on migration mechanisms requires the explicit inclusion of kinetic energy terms. Most applications of static lattice techniques have been concerned with the study of the defect behaviour in ionic solids. However, the calculation of the energetics for a crystal should always be preceded by a valid test of interionic potentials, which should reproduce a wide variety of perfect crystal properties well.

2.3.1 Lattice Energy Minimization

Energy minimization involves the determination of the minimum energy configuration of the crystal (Catlow 1997). These methods are restricted to the prediction of static structures and of those properties, which can be described within the harmonic (or quasi-harmonic) approximation where there is no explicit inclusion of atomic motions/vibrations.

A crystal structure (initial configuration) must be input as a trial model. However, the choice of a suitable starting configuration may pose serious difficulties for the study of superionics (where structures are often highly disordered and therefore poorly characterized). The 'unit cell' is then

repeated periodically in 3-dimensions/directions in order to generate an infinite system (which is non-defective). The atomic co-ordinates or bond-lengths are then iteratively adjusted until the forces acting between them are reduced to a minimum. This may be carried out at a constant pressure, where lattice parameters are also adjusted or at constant volume where they remain fixed. The latter is the simplest and most commonly used approach (Catlow 1997).

A wide variety of energy minimization algorithms are available. They are classified according to the order of the derivative of the total energy function that is used in the calculations (Catlow 1997). Methods that employ second derivatives of the energy with respect to atomic positions are more rapidly convergent than 1st derivative techniques. The former is more efficient than the latter. The most widely used minimization procedure is the Newton-Raphson method (Norgett and Fletcher 1970). A configuration closer to the minimum energy can be obtained when the updated co-ordinates [in the vector $r_{(n+1)}$] for the $(n+1)$th iteration are related to those in the nth iteration by:

$$\delta \mathbf{r} = \mathbf{r}_n - \mathbf{r}_{n+1} = \mathbf{g}_n . \mathbf{H}_n \qquad\qquad 2.4$$

where g_n is a vector of the first derivatives of the internal energy function with respect to particle co-ordinates and H_n is the Hersian matrix i.e. W_{n-1}, in which the elements of W_n are second derivatives of energy with respect to atomic co-ordinates or positions r.

Two computational problems:

- Inversion of the matrix W_n requires large amounts of computer time. The second problem concerns storage of the Hessian matrix, which may, for complex structures, be close to

the CPU memory limit even of modern day supercomputers. In these cases, conjugate gradient methods, which make use of only first derivatives, are used. These require less CPU memory but converge much less rapidly (see Parker, 1982).

2.3.2 Calculation of Bulk Properties

Once the equilibrium condition has been established, bulk lattice properties can be calculated. Such calculations may be used to test the validity of a particular potential function, or to test a set of potential parameters. Calculations of elastic and dielectric constants require the evaluation of specific terms in the g and W, matrices. Their calculation is straightforward (computationally) although the derivation of the appropriate equations is complex (see Catlow and Norgett, 1976).

Perfect lattice simulation techniques involve generating a non-defective Born model lattice with suitable boundary conditions and adjusting ion co-ordinates until the internal basis strains are completely eliminated (Catlow 1982, Dwivedi and Cormack 1990). Lattice energies associated with resulting structures (equilibrium configurations) are calculated. Knowledge of the lattice energy is of considerable value in predicting the stability of the structure. In this study, the procedure followed is closely related to that given by Catlow (1997). In a lattice containing N atoms per unit cell near its equilibrium configuration, the lattice energy can be written as:

$$U_L(\mathbf{R}') = U_L(\mathbf{R}) + \mathbf{g}^T.\delta + \delta^T.\mathbf{W}.\delta \qquad 2.5$$

where δ is a generalized *(3s + 6)* - dimensional matrix consisting of a 3s dimensional vector of displacements, δr, and 6 bulk components, $\delta \varepsilon$, thus:

36

$$\delta = \begin{bmatrix} \delta r \\ \delta \varepsilon \end{bmatrix}$$

2.6

g is a vector of the first-derivatives of energy

$$\mathbf{g} = \begin{bmatrix} \dfrac{\partial U_L}{\partial r} & \dfrac{\partial U_L}{\partial \varepsilon} \end{bmatrix}$$

2.7

and W denotes the second matrix of second derivatives and is of order 3N+6 by 3N+6

$$\mathbf{W} = \begin{bmatrix} \dfrac{\partial^2 U_L}{\partial r \partial r} & \dfrac{\partial^2 U_L}{\partial r \partial \varepsilon} \\ \\ \dfrac{\partial^2 U_L}{\partial \varepsilon \partial r} & \dfrac{\partial^2 U_L}{\partial \varepsilon \partial \varepsilon} \end{bmatrix} = \begin{bmatrix} Wrr & Wr\varepsilon \\ W\varepsilon r & W\varepsilon\varepsilon \end{bmatrix}$$

2.8

where W_{rr} is the coordinate second derivative matrix (*3N by 3N*), $W_{\varepsilon r}$ and $W_{\varepsilon r}$ are the mixed coordinate and strain second derivative matrices (*6 by 3N* and *3N by 6*) and $W_{\varepsilon\varepsilon}$ is the strain second derivative matrix.

The configuration R′ = {r′ₛ}, is related to R by the transformation

$$r'_s = \Delta\varepsilon \cdot (r_s + \delta r_s)$$

2.9

37

in which $\Delta\varepsilon$ is the symmetric strain matrix formed from the components of $\delta\varepsilon$. In the absence of external fields it is possible to calculate the minimum configuration. This is accomplished by calculating the various derivatives, i.e., the coordinate derivatives $\left(\dfrac{\partial^2 U}{\partial^2 r}\right)$, the mixed derivatives $\left(\dfrac{\partial^2 U}{\partial\varepsilon\partial r}\right)$ and the strain derivatives $\left(\dfrac{\partial^2 U}{\partial^2\varepsilon}\right)$ in equation (2.11) using a lattice model based on the appropriate form of pair potentials. Furthermore, on employing equilibrium conditions that $g = 0$ (which assumes the crystal is at zero strain), $\dfrac{\partial U_L}{\partial\delta r} = 0$ and differentiating with respect to δr gives

$$U_L(R) = U_L[R_e] + \tfrac{1}{2}\delta\varepsilon.W_{\varepsilon\varepsilon} - \tfrac{1}{2}\delta\varepsilon[W_{rr}^{-1} - W_{\varepsilon r}.W_{r\varepsilon}].\delta\varepsilon \qquad 2.10$$

where R_e denotes the field-free equilibrium configuration. Finding the lattice constants involves calculating the second derivatives of the evaluated total lattice energy with respect to changes of atomic co-ordinates within the unit cell. Hence, the elastic constraint tensor C can immediately be obtained as

$$C = \frac{1}{V_c}[W_{\varepsilon\varepsilon} - W_{\varepsilon r}.W_{rr}^{-1}.W_{r\varepsilon}] \qquad 2.11$$

The variations of elastic constants with temperature are then simulated from the change of the lattice parameter of the material with temperature. V_c represents the volume of the crystal.

2.3.3 Defect Energy Calculations

Once the perfect lattice has been modelled satisfactorily, defect energies may be calculated. The basis of the calculation is to introduce a defect (or defects) into the perfect lattice and then to relax the surrounding particles to a new (stable) minimum energy configuration. The lattice energy of the perfect lattice is then subtracted from that of the defect lattice in order to obtain the defect energy.

In ionic or semi-ionic crystals the relaxations arising from a charged defect extend over a wide range owing to the long-range of the Coulomb forces. This makes the exact calculation of the new configuration prohibitively time consuming if large number of particles are included.

The approach developed to overcome this problem is known as the 'two-region' method (Norgett 1974). The defect is surrounded by a spherical region I (inner region) which contains all defects (Figure 2.2). In this region, where the defect forces are strongest, the ions are relaxed to zero force using energy minimization routines (e.g. the Newton-Raphson interactive procedure). Around this an outer region II, which extends to infinity, is placed where, owing to greater distance, the defect forces are weaker and the ionic relaxation (or the response of region II to the defect) is calculated/treated using the Mott-Littleton approach (1938) (a continuum approximation for calculating the displacement of the ions incorporated in the GULP computer code). The total energy of the defective lattice E is written as

$$E = E_1(x) + E_2(x,\alpha) + E_3(\alpha) \qquad\qquad 2.12$$
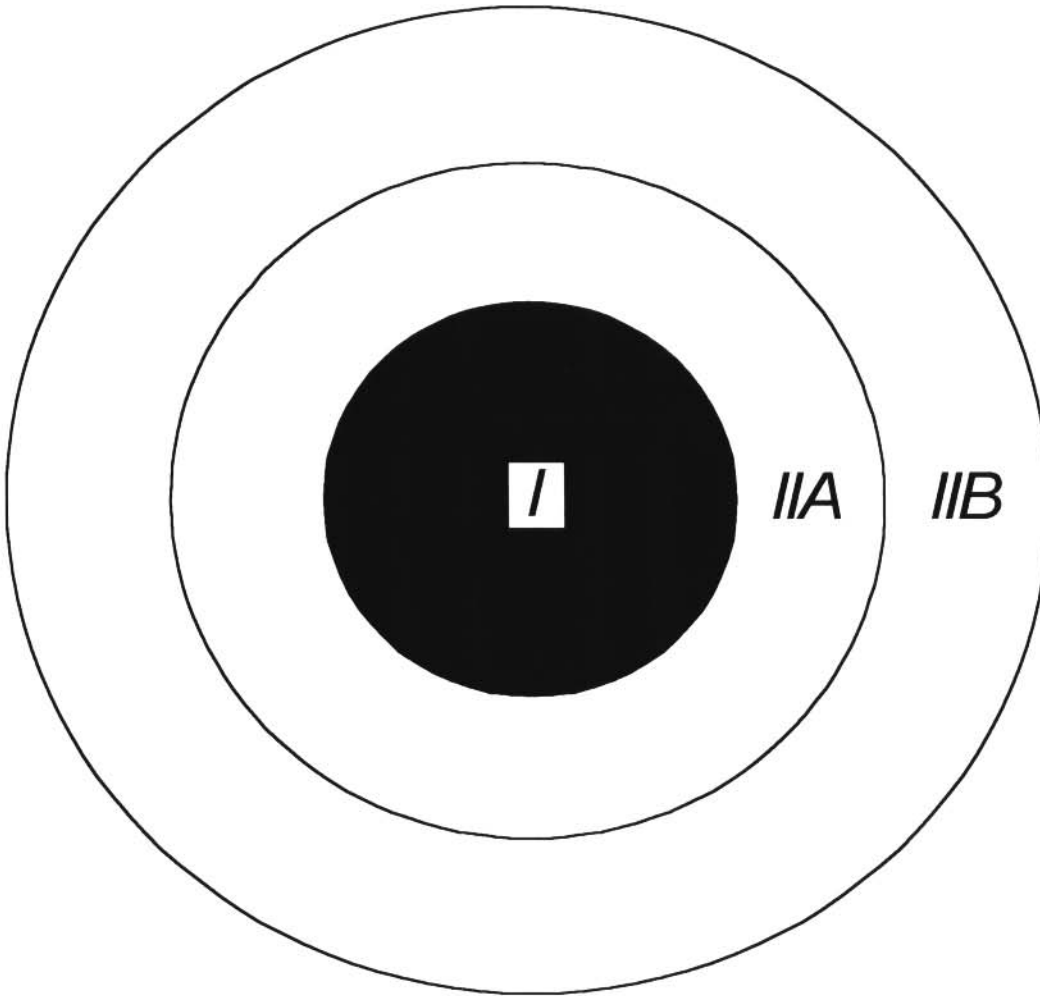
Figure 2.2 Schematic diagram of Mott-Littleton model

where $E_1(x)$ denotes the energy of the inner region, $E_3(x)$ the energy of the outer region and $E_2(x)$ the interaction energy between the two regions, I and II. x are the displacements of the ions in the inner region from the defect position while α are for those in the outer regions. For small values of α, i.e. where the outer region constitutes a perfect crystal, the harmonic approximation holds

$$E_3(\alpha) = -\frac{1}{2}\left[\frac{\partial \varepsilon_2(x,\alpha)}{\partial \alpha}\right]_{\alpha = \bar{\alpha}} . \bar{\alpha} \qquad 2.13$$

in which $\bar{\alpha}$ are the equilibrium values for α corresponding to arbitrary values of x. Defect energies can be determined by direct minimization with respect to x, followed by the determination of $E_1(x)$ using direct simulation. An expression for the defect energy in (2.13) becomes

$$E = E_1(x) + E_2(x,\alpha) = -\frac{1}{2}\left[\frac{\partial \varepsilon_2(x,\alpha)}{\partial \alpha}\right]_{\alpha = \bar{\alpha}} . \bar{\alpha} \qquad 2.14$$

Now that $\bar{\alpha}$ is an implicit function of the inner region, then E can be evaluated by minimizing the energy directly, i.e. by solving equations

$$\left[\frac{\partial \varepsilon}{\partial x}\right]_{\alpha = \bar{\alpha}} = 0 \qquad 2.15$$

41

2.4 MOLECULAR DYNAMICS SIMULATIONS

2.4.1 Introduction

Molecular dynamics (MD) technique is used for studying the structural and dynamical properties of the system. Most molecular dynamics calculations are performed using a DL_POLY program developed by Smith et al. (1997). Unlike the energy minimisation procedures discussed above, molecular dynamics includes effects of thermal motion explicitly. These simulations are based on the first derivative of potential functions to describe the variation in forces between atoms with interatomic separation. However, it is essential that reliable crystal potentials be obtained since they represent the fundamental physics of the system under investigation.

2.4.2 Setting Up an MD and Running MD Simulations

An MD simulation is set-up and run as follows:

(a) **Establishment of an initial configuration**: First it is necessary to establish an initial configuration of the system/crystal under study. Hence, a simulation box of 100–several thousands atoms is specified. These atoms are arranged initially on a fcc lattice in a cubic box. Periodic boundary conditions (pbcs) are applied to the simulation box in order to generate an infinite system in three dimensions, i.e. the box is surrounded by images of itself

such that if a particle leaves the box, it re-enters on the opposite face with the same trajectory in order to eliminate surface effects (limitations by the edges of the periodic box). For adequate statistics, a supercell of the basic unit cell is normally used. The initial configuration may be obtained from experimental data, from a theoretical model or from a combination of the two, while velocities (as the simulations are dynamical) are chosen in accordance with the target temperature for the simulation.

(b) **Calculation of forces from potential energy**: The net force, F_i, acting on each ion is obtained by summing the forces (pair-wise interactions are considered) exerted on it by all the ions in the N-particle system. So the net force, F_i, acting on the ith particle at each time step are calculated from the derivatives of the interatomic potentials as follows:

$$F_i(t) = \nabla V(r_{ij}) \hspace{6cm} 2.15$$

where $V(r_{ij})$ is a pair potential between ions i and j separated by a distance r_{ij} ($r_{ij} = r_j - r_i$).

(c) **Mathematical algorithms**: The system is made to evolve in time, with the motion of each ion being governed by classical (Newtonian) equations of motion in an iterative fashion. This is achieved by specifying a time step, Δt, shorter than the period of any important dynamical process in the system at atomic level (e.g. a period of atomic vibrations). For this reason, values of 10^{-15}-10^{-14} s (i.e. 0.01 ps-0.001 ps) are commonly used [Allen and Tildesley (1987), Jacobs and Rycerz, 1997]. The shorter the Δt, the more accurate is the numerical integration of the equations of motion. After the system has evolved for a successive timestep the co-

43

ordinates (x_i) and velocities (v_i) of the particles are updated. For an infinitely small value of Δt, the positions (x_i) and velocities (v_i) of an arbitrary ith particle can be written as

$$x_i(t + \Delta t) = x_i(t) + v_i(t)\Delta t \qquad\qquad 2.16$$

$$v_i(t + \Delta t) = v_i(t) + \frac{F_i(t)\Delta t}{m_i} \qquad\qquad 2.17$$

where $x_i(t + \Delta t)$ and $v_i(t + \Delta t)$ are the values of x_i and v_i after the lapse of time Δt and m_i refers to the mass of the ith particle with F_i being the total force acting upon the ith particle. However, using (in practice) finite timesteps, Δt, these expressions are inadequate and so updating formulae (complex updating algorithms for x_i and v_i) must include higher powers of Δt. The Beeman algorithms (Beeman 1976) are commonly used. Hence equations (2.20) and (2.21) can be rewritten as

$$x_i(t + \Delta t) = x_i(t) + v_i(t)\Delta t + \left[\frac{[4a_i(t) - a_i(t - \Delta t)]\Delta t^2}{6} \right] \qquad\qquad 2.18$$

$$v_i(t + \Delta t) = v_i(t) + \left[\frac{[2a_i(t + \Delta t) + 5a_i(t) - a_i(t - \Delta t)]\Delta t^2}{6} \right] \qquad\qquad 2.19$$

where a_i is the acceleration of the ith particle at time t.

(d)   **Equilibrating and production run**: The above procedure is repeated for several thousand timesteps to enable the system to reach equilibrium at the appropriate temperature. Once

44

equilibrium is attained, the simulation is run for several thousand timesteps during which data is collected. Data is then sent to a file for subsequent analysis and processing (i.e. details of the structure and dynamics of the system may be calculated).

2.4.3 Calculation of Physical Properties from Molecular Dynamics (MD) Simulations

Simulation by the MD method makes it possible to monitor the system of particles over a number of timesteps. Features of interest such as transport properties (e.g. diffusion coefficients) and structural properties, in particular, the radial distribution functions (RDFs) can be obtained.

2.4.4 Transport Coefficients

Transport refers to a phenomenon that gives rise to a flow (movement) of material from one region to another. The (very) presence of transport implies that the system is not in equilibrium. So most of the MD simulations are on calculations of non-equilibrium properties from equilibrium simulations. Estimates of the magnitude of the diffusion constants D_i of ions i can be obtained from the dependence of the mean-square displacement $<r_i^2(t)>$ of particles i on time t using the Nernst-Einstein relation/equation (Einstein 1905):

$$D_i = \left[\frac{<r_i^2(t)> - B_i}{6t} \right], t \rightarrow \infty \qquad\qquad 2.20$$

where B_i is a thermal factor arising from thermal vibrations.

Plots of mean-square displacements $<r^2(t)>$ as a function of time t provide a means to establish whether diffusion is occurring and whether a solid has melted (Figure 2.3). If diffusion is occurring then the mean-square displacements gradually increase with time and the diffusion coefficient D_i becomes the gradient of the plot of the MSD with time. If diffusion is not occurring (or $D_i = 0$) or the atoms are merely vibrating about the mean values (mean lattice sites), a line parallel to the horizontal axis is obtained with a value equal to the mean-square amplitude of thermal motions (B_i).

In the case where the plots of MSD versus t are not perfectly linear whereas the other conditions concerning stability of the simulation have been satisfactorily met (short enough Δt, constant T, sufficiently long run) then the ensemble average has not sampled a sufficient number of initial times (Catlow 1997). It is generally known that for a sufficiently long run, initial times starting at every 10th timestep, with t extending over half the run, may be sufficient.

2.4.5 Radial Distribution Functions (RDFs)

Structural information can be extracted from MD studies via calculated RDFs ($g(r)$) which can be compared directly with experiment. Radial distribution functions yield information on the probability of finding an atom/molecule a distance r from another atom/molecule compared to the ideal gas distribution. Thus g(r) is dimensionless. Hence, the probability of finding an ion of type i at a point
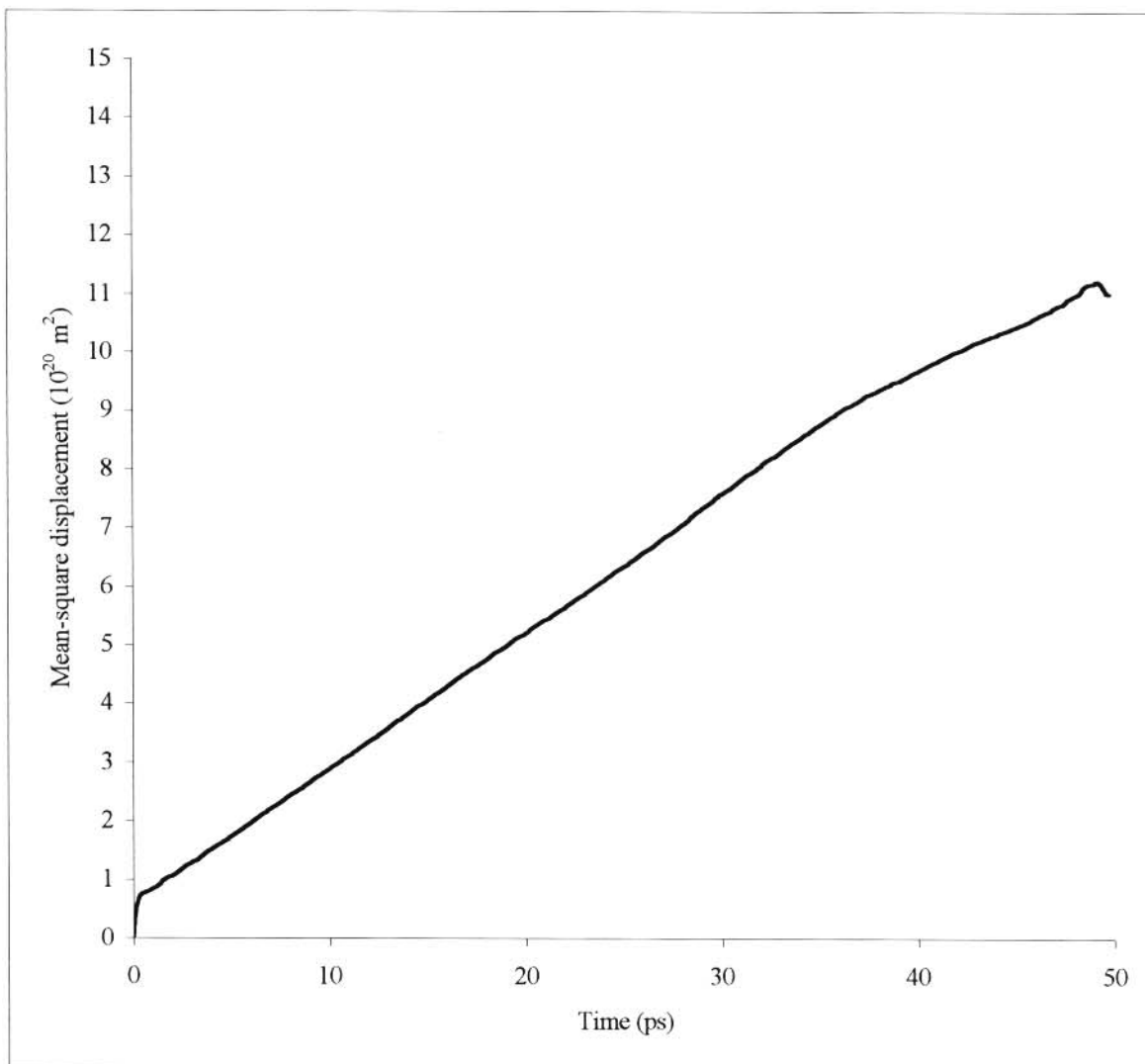
Figure 2.3 Variation in mean square displacement of the mobile species.

r from another ion j is given by

$$\rho_i(r) = \left\langle \sum_{i=1}^{N_j} f(r - r_{ij}) \right\rangle \qquad\qquad 2.21$$

where the position of the ith ion of type i is r_{ij} and the sum goes over the entire simulation or all such ions in the system, i.e. N_j.

In a crystal, g(r) has an infinite number of (sharp) peaks whose separations and heights are characteristics of the lattice structure. Figure 2.4 shows the RDF calculated from a molecular dynamics simulation for liquid argon. The first (and largest peak) occurs at about 3.7 Å with g(r) having a value of ~ 3. This means that it is three times more likely that a pair of molecules (two molecules) would have this separation than in the ideal gas. For short distances (less than the atomic diameter) g(r) is zero. This is attributed to strong repulsive forces. The RDF then falls and passes through a minimum value r ~ 5.4 Å. The likelihood of finding a pair of atoms atoms with this separation is less than for the ideal gas. However, at long distances, g(r) tends to the ideal gas value, indicating that there is no long-range order, i.e. after long time intervals individual ion-trajectories become continuous ion density distribution, which represent less probability of finding a group of ions in different regions of the unit cell.

To calculate the pair distribution function, the neighbours around each atom or molecule are divided/sorted into histograms (distance 'bins'/small discrete 'bins'). The number of neighbours
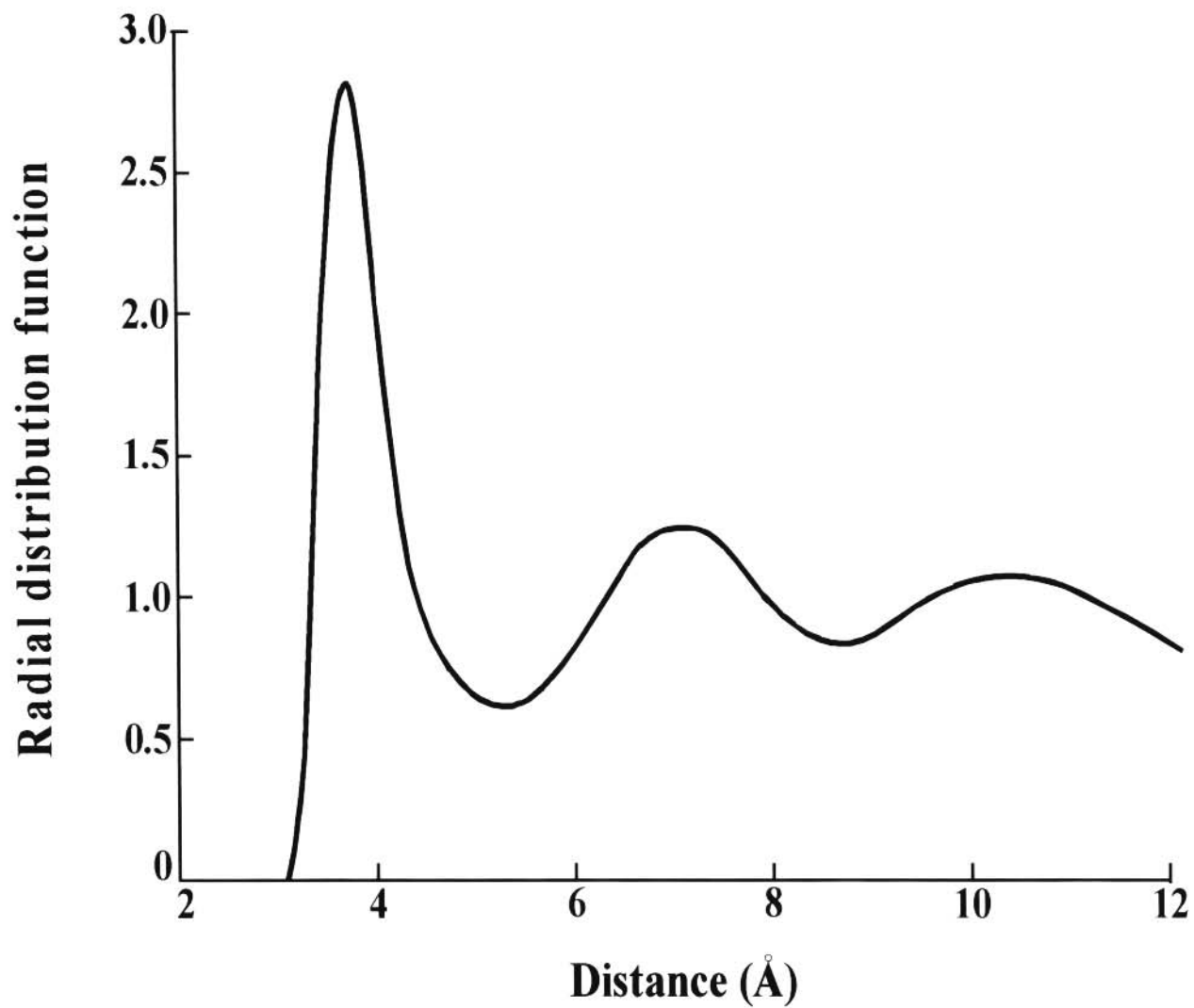
Figure 2.4 Radial distribution function from molecular dynamics simulation of a liquid material.

around each atom in each bin is then averaged over the entire simulation. For an example, a count is made between 2.5 Å and 2.75 Å, 2.75 Å and 3.0 Å and so on for every atom in the simulation. This count can be performed during the simulation itself or by analysing the configurations that are generated (Leach 1996). $g(r)$ can also be used to monitor the progress of the equilibration. Furthermore, this function is useful for detecting the presence of two phases (where larger than expected first peak appears and by the fact that $g(r)$ does not decay towards a value of 1 at long distances.

2.4.6 Limitations of the MD Method

The following constraints are common to the MD method:

(a)   MD simulations are computationally expensive in terms of CPU time and memory as compared to energy minimization methods. However, computationally faster methods now permit the inclusion of larger systems (i.e. systems which involve several thousand particles) in MD simulations.

(b)   Diffusion must be rapid (i.e. $D > 10^{-7}$ cm^{2}s^{-1}) if we are to observe any during the simulation.

(c)   A further consequence of (a) above is that the inclusion of polarizability leads to very large amounts of computer time. However, the omission of polarizability may be a serious one particularly in massively doped electrolytes having a very high concentration of defects, e.g., oxides.

(d)   Surface effects are excluded from the simulation due to the application of periodic boundary conditions. So Schottcky disorder cannot be spontaneously formed.

(e)   The finite-size of the simulation box plays a major drawback in the world of computer

modelling, since the number of mobile species must be large.

2.5 COMPUTER SIMULATION CODES

Ionic materials are modelled using interatomic potentials, which are embodied in general, purpose computer programs. Atomistic computer modelling codes employed in the current study are as follows:

- DL_POLY: This is a molecular dynamics program which is used for calculating details of both structural and transport properties of mobile sub-lattices in fast-ion conductors. Data collected using this MD code are cast into pictorial forms which provides a window through which one can observe the behaviour of a simulation model. The DL_POLY program is comprised of five (5) sub-directories as shown below:

  - Data: Standard test cases for DL_POLY are stored in the 'data' sub-directory. Each test case has its own sub-directory. Input files for running DL_POLY are copied into the execute sub-directory using the 'select' macro.

  - Build: A master copy (back-up) of the DL_POLY makefile sits in this sub-directory. The makefile is copied to the 'source' sub-directory in order to facilitate the compilation of the DL_POLY program.

  - Utility: This directory stores utility routines for adapting data to suit different circumstances.

  - Source: A DL_POLY program is compiled in this sub-directory. A sample makefile is edited (in this sub-directory) before being used. Before compilation, dl_params.inc file should be

51

edited to adjust the DL_POLY array dimensions for their systems.

- Execute: The executable, DLPOLY.X (a program for carrying out a routine function), will be placed/deposited in the executable sub-directory. Hence, this is regarded as a 'working' sub-directory from which jobs are submitted for execution and data files manipulated. Typing DL_POLY begins the execution. However, before running DL_POLY, ensure input files [i.e. *Control* (This file contains job control information, i.e. the amount of data to be gathered), *Config* (This file contains information on positions and velocities of the atoms of the system under investigation) and *Field* (This file describes the system in terms of atom types and intermolecular forces i.e. number of atoms and interatomic potentials are present in the execute sub-directory)] are present in the execute sub-directory. Output data files are returned to execute sub-directory. The DLPOLY output files are as follows:

- *History* – This file is not human readable. It contains information on atomic coordinates, mean square displacements (MSDs), etc.

- *Output* – This file is human readable and contains information on radial distribution functions (rdfs).

- *After* – This file is used for data crunching. It facilitates the identification of coordinates for the trajectories for MSDs.

- GULP: This program is essential for deriving interatomic potentials in a crystal. The process involves adjustment of variable parameters to known structural properties of the compounds, namely, dielectric and elastic constants, etc. Furthermore, this program performs calculations for perfect and defect crystal lattice.

2.6 SOME EXAMPLES OF COMPUTER MODELLING APPLICATIONS

Rahman (1976) and Vashishta (1979) investigated fast-ion properties of BaF_2 and AgI, respectively, using molecular dynamics techniques. Structural properties obtained were in good agreement with experimental results. Their studies were conducted using rigid ion potentials which successfully described fast-ion properties of these materials.

Comprehensive MD simulations of high temperature fast-ion conductors were conducted by Dixon and Gillan (1980), Gillan and Dixon (1980a,b, 1981) on $Srcl_2$. Their results strongly indicated that fast-ion phase interstitials simply skirt past the cube-centre sites. These results were supported by neutron diffraction studies carried out by Hutchings et al. (1983).

Studies on $SrCl_2$ revealed that there was no evidence for the occupation of cube-centre sites. Movement of the anions was by a solid-jump process in which the flight time was several orders of magnitude less than the residence time. These 'hops' took place along the <100> cube-edge direction. There is substantial disorder on the anion sub-lattice. It is however, complex and dynamical in nature.

Several studies of mixed-metal fluorides (e.g. $RbBiF_4$, $PbSnF_4$, etc.) have provided evidence that these systems are good F^- ion conductors – considerably better than for example pure PbF_2 (see Cox 1988). In these materials it is easy to excite F^- ions into interstitial sites from lattice positions surrounding which there is a local excess of Rb^+. Hence, interstitials are the mobile species. MD

studies on these systems have shown that interstitial migration mechanism (movement of ions between lattice and interstitial sites) is a more prevalent mode of transport.

2.7 EQUIPMENT USED FOR THIS PROJECT

The equipment listed below were used for computer modelling calculations and experiments:

- Hardware:
  Silicon Graphics workstations

  Silicon Graphics Origin 2000 Server

  Silicon Graphics Power Challenge XL Server

  Pentium Pro Desktop computer

- Software:
  Classical calculations: DL_POLY and Gulp codes

  Data Software: Microsoft Word, Microsoft Excel, SigmaPlot and Corel Draw packages

- Printing facilities:
  HP LaserJet 6MP, HP ColorLaserJet 5, HP DeskJet 930C and HP DeskJet 870C*xi*, HP ScanJet 3200C

- Daresbury Synchroton Radiation facilities in the UK

CHAPTER 3

EXPERIMENTAL METHODS FOR MEASURING STRUCTURAL

PROPERTIES OF SOLIDS

3.1   INTRODUCTION

X-ray diffraction and Extended X-ray Absorption Fine Structure (EXAFS) are valuable techniques in the study physical and chemical properties for a wide variety of solids. The former was the first method for studying the internal structure of crystals. X-ray diffraction reflects long range-order (order over many interatomic distances) (particularly in single crystals), within solids whereas EXAFS reveals short-range order/local structural information around a particular atomic species within condensed materials. There is a link between these techniques and computer modelling (Chadwick 1998). Furthermore, there are a number of comparative issues between the two techniques that warrant some discussion.

X-ray diffraction measurements yield diffraction patterns, which contain information about the size and shape of the (entire) unit cell, structures, average atomic positions, thermal motion of atoms and defects. It is also used extensively to study the relationship between ionic arrangement (structure) and ionic transport. In fact, diffraction techniques give information on the solid as a whole (i.e. information is collected simultaneously on a large number of atoms of the system). This technique

is mostly useful in the determination of long-range order in solids. So X-ray diffraction is used to evaluate materials for the purposes of synthesis and control of properties of materials and to determine structural features that promote or hinder conductivity in solids.

EXAFS is a local structural probe (tool) widely used in physics, chemistry, electronic and electrical engineering, biological materials, metallurgy, surface sciences and elsewhere (Hayes and Boyce 1981 and Catlow 1997). It is able to provide a detailed picture (within 3–5 coordination shells, i.e. within a small local environment) of the arrangement of atoms around the one whose x-ray absorption edge is measured (central atom). Hence, EXAFS gives physically meaningful results on coordination number (number of atoms surrounding the excited atom), bond distances/lengths, elements/type of atoms in the coordination shell around the excited atom, a Debye-Waller factor that is a measure of the static and thermal disorder in the system. This information is of great use in resolving many chemical and structural problems in materials science studies.

In this chapter we review these techniques with emphasis on origin of each method, theoretical aspects, strategies of data collection and data analysis, their strengths and limitations, their application to superionics and types of samples (i.e. single or powder).

3.2   X-RAY DIFFRACTION TECHNIQUES

3.2.1   Origin of X-ray Diffraction

X-rays are electromagnetic waves with high energies, and with a wavelength of the order 10^{-10} m (1 Å) and can therefore be diffracted (deviated from the periodic arrangement of atoms in solids) by atoms in solids which have interatomic separations of this order. Visible light has a much larger wavelength ($\lambda \sim 400$ to 700 nm), so it cannot be used to study/resolve molecular structure details, since diffraction occurs when a wave meets a barrier with approximately this wavelength (of about 1 Å). Hence, wavelengths that are comparable to the interatomic spacing are required to probe the arrangement of atoms in a crystal.

When X-rays encounter atoms in a plane/layer of atoms in the crystal, diffraction patterns are formed. Sir Lawrence Bragg first published the theory of X-ray diffraction in 1912. In this theory, the difference between the distance travelled by rays bouncing off two different planes is $2d\sin\theta$. For the rays that interfere in phase (i.e. they have their maximum amplitudes at the same time), the interference is referred to as constructive (add up to give a strong beam), while those that interfere out of phase (i.e. one has its maximum amplitude when the other has a minimum) are called destructive interference (zero resultant sum). Bragg's equation for a bright (intense) X-ray reflection is

$$n\lambda = 2d\sin\theta \qquad\qquad\qquad 3.1$$

where d is the separation between the planes under consideration, θ is the angle at which X-rays enter

the planes, $n\lambda$ is the path difference, n=1 indicates that a first-order reflection occurs, n=2 is for the

occurrence of a second-order reflection, and so on. If the planes are not at an angle θ to the

incoming beam then there will be no diffracted beam due to this set of planes. In most cases,

emphasis is on first order reflections (i.e. when n=1).

3.2.2   Experimental Arrangement

There are two types of X-ray diffraction experiments which are in common use:

3.2.2.1 Single crystal diffraction technique

Single crystals give data of the highest quality as all diffracted beams (rays) give a distinct reflection

which can be recorded as a 'spot' on the photographic film. In this technique, a single crystal is

mounted so that its crystallographic axes are in some known direction in relation to the position of

the photographic film. The mounted single crystal is rotated about the axis. As the crystal oscillates

there will be certain positions in which the relation between the incident X-ray beam and the atom in

a crystal is correct for giving a bright-diffracted X-ray beam. Hence, a series of spots will be formed

on the film corresponding to these reflections. However, there are problems associated with the use

of single crystals in X-ray diffraction measurements. These include, sample availability (growing of single crystals of adequate size and quality) and difficulties with high temperature experiments. Nevertheless, some single crystal experiments have been performed on high temperature fluorite structured crystals. A crystal is distinguished from a glass or an armophous material by possessing long-range order. Most armophous materials and glasses do not possess long-range order. Diffraction effects are only observed from crystalline solids, in the same way as X-rays.

3.2.2.2 Powder diffraction technique

Crystals of the sample to be investigated are ground to a fine powder whose crystallites should be of random orientation (i.e. there is no necessity to find a well-formed specimen of the crystal nor is it necessary to spend a long time setting the specimen accurately in a particular direction). In the original X-ray powder diffraction, a powder sample is packed tightly in a tube made of glass which is not opaque to X-rays and placed in the path of the X-ray beam at the centre of the powder camera. The sample is then rotated about its axis. A set of planes of atoms within the crystal which satisfy the Bragg condition (i.e. have the appropriate λ for the diffraction to condition to occur) will give a reflection. Most research papers published nowadays focus on modern powder diffraction techniques where a detector (ionisation chamber and SSD) is used. Powder diffraction experiments are straightforward and widely applicable although they are riddled with limitations. Information is often lost due to peak overlap. Reducing the peak width using synchrotron X-ray sources can reduce this problem. Other problems arise from preferred orientation which becomes more severe at high pressures.

59

3.2.3 Analysis of X-ray Diffraction Data

Diffraction data refinement in superionics is comprised of two stages: determination of the unit cell dimensions and the positions of the atoms inside each unit cell (forming the basis) from the intensities of the diffracted beams in the pattern. Refinement using diffraction data normally proceed by using least squares fitting methods where structural parameters are varied. These parameters include atomic parameters, the coordinates of the atoms in the unit cell, the occupation numbers of each atomic site and the thermal parameters.

3.2.4 Limitations of X-ray Diffraction Techniques

X –ray diffraction-based techniques, while providing the essential information on the average structure, are not effective as local structure measurements/probes in characterising the differences in the behaviour of the different cations in fluorite structured materials (e.g. stabilized cubic zirconia).

3.2.5 Applications of Powder Diffraction to Superionic Conductors

Powder diffraction has been extensively used as a tool for bulk structure determination in superionic conductors. The technique is also used to identify crystalline phases and impurities as an aid in synthesis and fabrication. The number of independent structure factors that are obtained from

powder techniques may be too small for highly complex systems. Nevertheless structures with many variables are presently solved using powder diffraction methods as profile fitting techniques are used to enhance the extraction of information from complex powder diffraction data whereas overlapping component peaks can be solved using the techniques pioneered by Rietveld (1969) as reviewed by Young and Mackie (1974). Cubic calcia stablized-zirconia is an example of a solid electrolyte in which many aspects of conduction processes have been clarified by powder diffraction technique. Studies of X-ray and Neutron powder diffraction have established features of the structure that results in high ionic conductivity. These studies have also found an order-disorder transformation that results in changes of ionic conductivity. Its X-ray powder intensities have a disordered fluorite arrangement in which Ca and Zr ions are in the cation sites and O_2 and vacancies are in the anion sites (Tien et al. 1965). This defect structure explains high ionic conductivity as a result of oxygen ions exchanging positions between lattice sites and vacancies. However, evidence for ordering of Ca and Zr, which is seen in X-ray patterns and electron micrographs of single crystals, is not observed by powder diffraction, because the changes in intensity are small.

3.3   EXTENDED X-RAY ABSORPTION FINE STRUCTURE SPECTROSCOPY (EXAFS)

3.3.1   Origin of X-ray Absorption Fine Structure (XAFS)

EXAFS are the oscillations in the absorption spectrum of an element in a condensed phase that provides information on local structure. A combination of the X-ray Absorption Near-Edge Structure (XANES) and EXAFS is referred to as XAFS (X-ray Absorption Fine Structure). In fact, XAFS

spectrum is divided into three distinct regions as marked in Figure 3.1: (i) the 'pre-edge region', which spans roughly 10 eV above and below the edge, (ii) the X-ray Absorption Near Edge Structure' region (XANES) which extends approximately 50 eV above the edge, and (iii) the 'EXAFS' region extends beyound the edge up to even 1 keV (finite energy range) (see Teo et al. 1980, Catlow et al. 1990, Chadwick 1998). The three features provide structural information about the target atom (the photoelectron emitter) and are finding increasing applications for studies in both crystalline and armophous materials. XANES yields important chemical information about the excited atom while EXAFS contains structural information. In the EXAFS region the higher photoelectron energies mean that the mean free path of the photoelectrons are much shorter. Thus, the EXAFS features extend out with decreasing amplitude (see Figure 3.1) leading to shorter-range information.

For a model lattice of central atom A (excited or the centre of the outgoing wave excited atom) in a condensed medium (solid or liquid) surrounded by an environment of atoms B (atoms very close to the emitting atom) in an X-ray beam, the photoelectron ejected from atom A and propagating to neighbouring atoms B as a spherical wave is backscattered by these atoms (B) in the medium resulting in the interference with the outgoing wave (Figure 3.2). Thus, depending on the difference in pathlengths (distance between the excited atom and the back scattering atom and the wavelength of the photoelectron), the interference will be constructive or destructive (see Figure 3.3). If the wavelength of the initial outgoing wave from the excited atom is such that the scattered wave is reflected back (backscattered) exactly in phase with the outgoing wave they add up to produce a resultant wave (Figure 3.3). If they are out of phase they subtract to produce a wave with a reduced
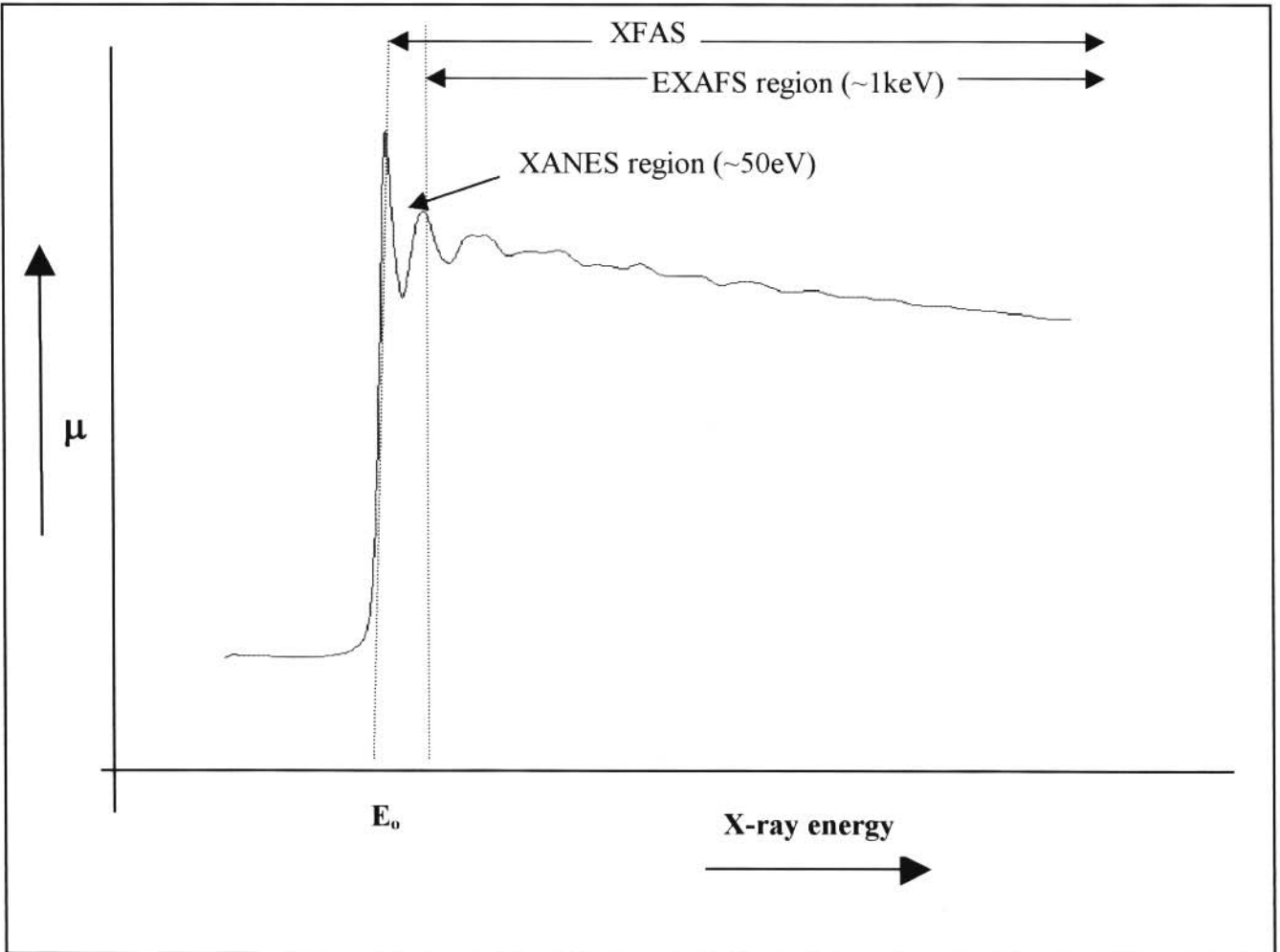
Figure 3.1 The variation of the absorption coefficient as a function of photon energy for an atom in a solid (for a transmission experiment). E_0 denotes the point where the XAFS spectrum starts.
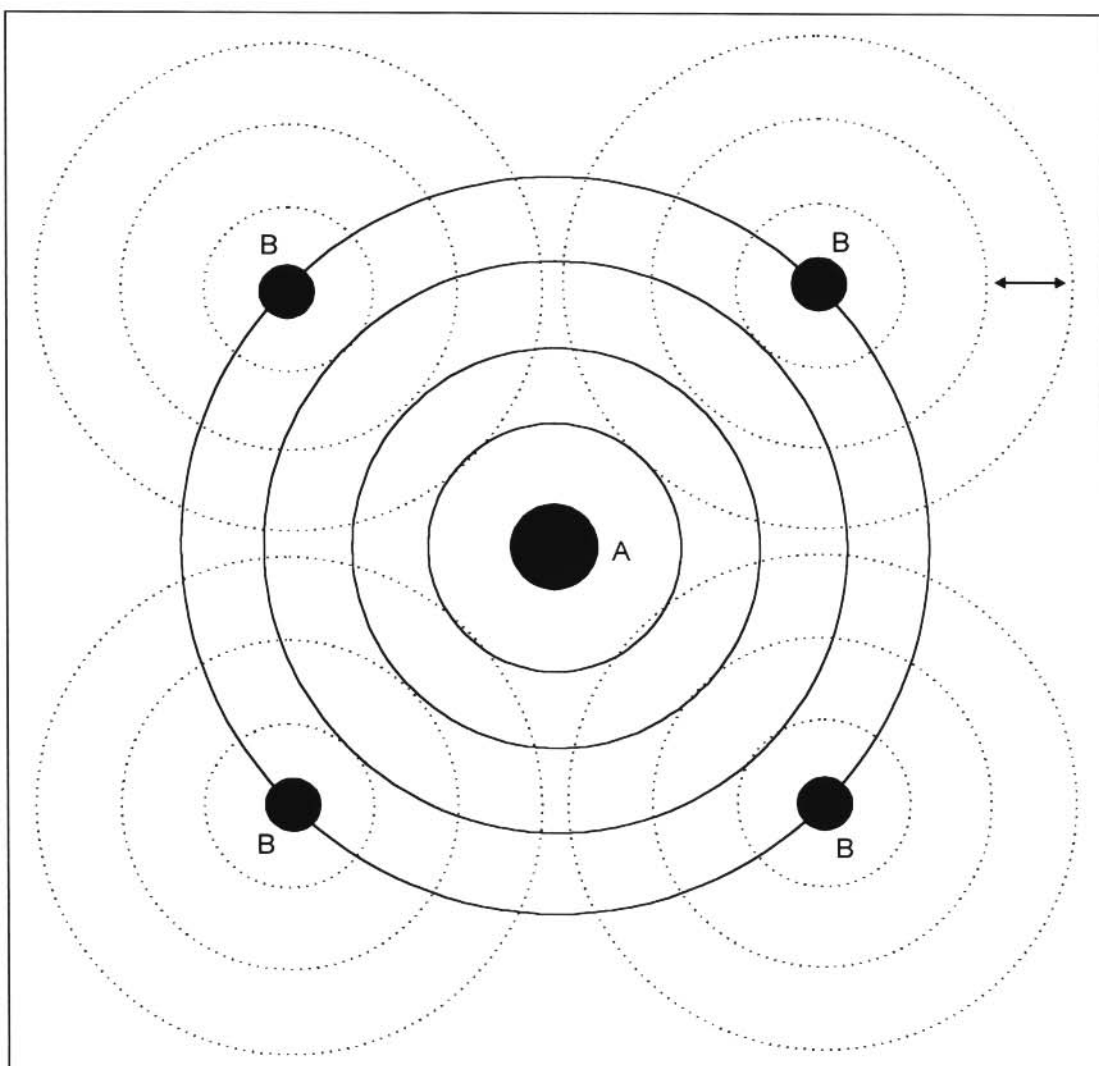
Figure 3.2 A schematic representation (model) of the origin of the EXAFS features. **A** is the central atom, **B** is the neighbouring atom, '———' represents the outgoing photoelectron wave and '······' represents the backscattered wave. The outgoing photoelectron waves propagate to neighbouring atoms. The backscattered waves modify the electron wave at the central atom and give rise to EXAFS as shown in Figure 3.3.
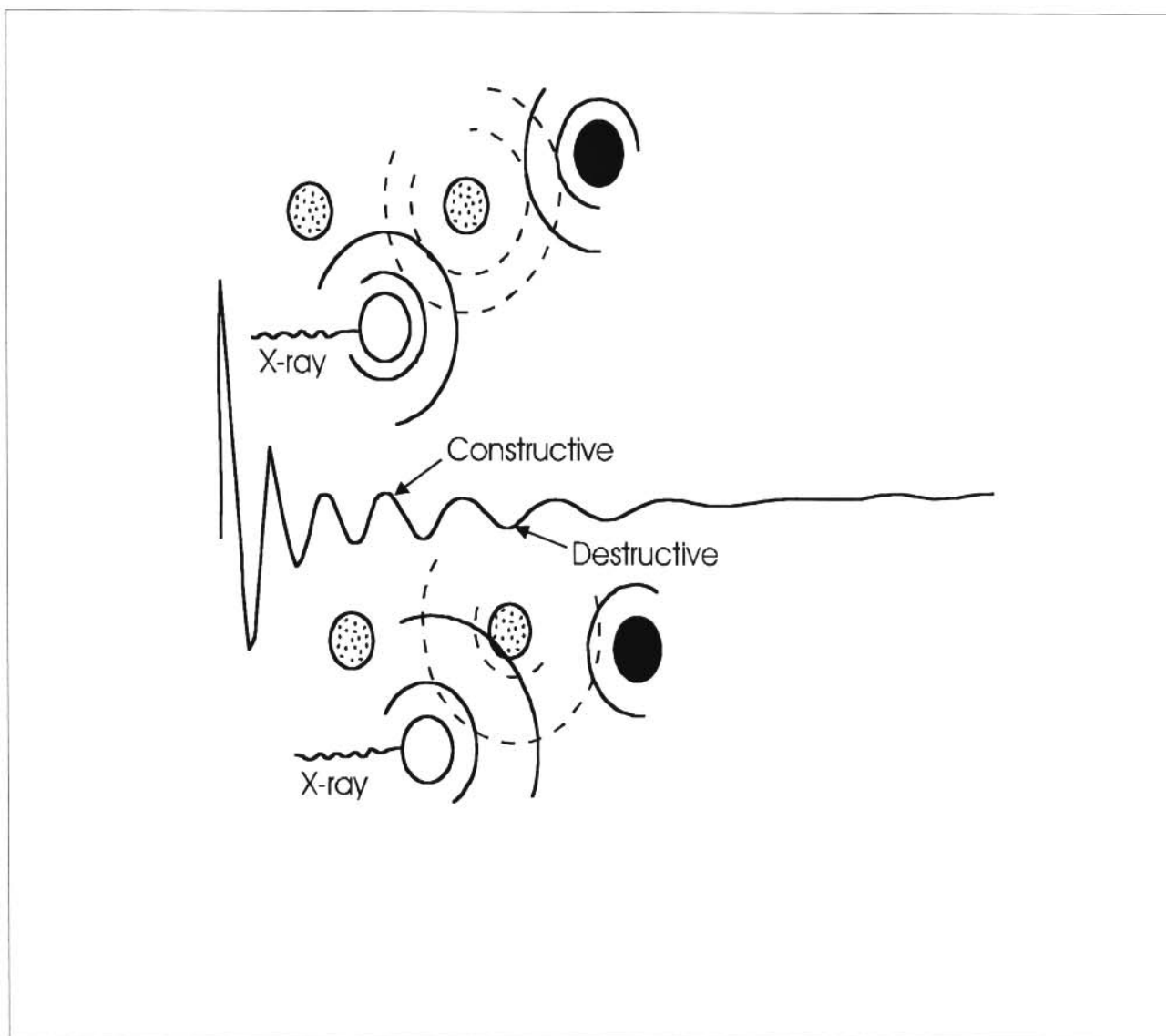
Figure 3.3 The excited electron wavefunction (wavelength λ) propagating away from the atom at which photon absorption occurs, and is being backscattered from surrounding atoms. The interference between the outgoing and backscattered photoelectron wave is demonstrated and gives rise to EXAFS.

amplitude (Figure 3.3). This modification of the electron wave (by backscattered waves) at the central/excited atom gives rise to EXAFS which can be analyzed to give extra information on the structure around the excited atom. Thus EXAFS arises due to the presence of atoms around the core (excited atom) which absorbs a photon.

3.3.2 Data Collection Techniques

EXAFS technique is element specific, and this permits investigation of the local environment of a constituent element in a composite material. The X-ray absorption coefficient of the entire system/ a material as a function of photon energy, in an energy range that is below and above the absorption edge of one of the elements in the material is measured. X-rays are energy selected out using an appropriate crystal monochromator [e.g. Si(111), Si(220), Ge(111), Si(311), etc]. When X-rays encounter any form of matter, they are partly transmitted and partly absorbed.

In a transmission EXAFS experiment, X-rays are passed through an incident reference ion chamber (ion chamber 1) to measure their incident current intensity (I_o). Then, they are passed through the sample and the transmitted intensity (I_t) is measured using ion chamber 2 (see Figure 3.4). (These ion chambers are filled with the correct gases). These intensities are measured simultaneously to allow for cancellation of sudden changes in intensity of the incident photon beam.

66
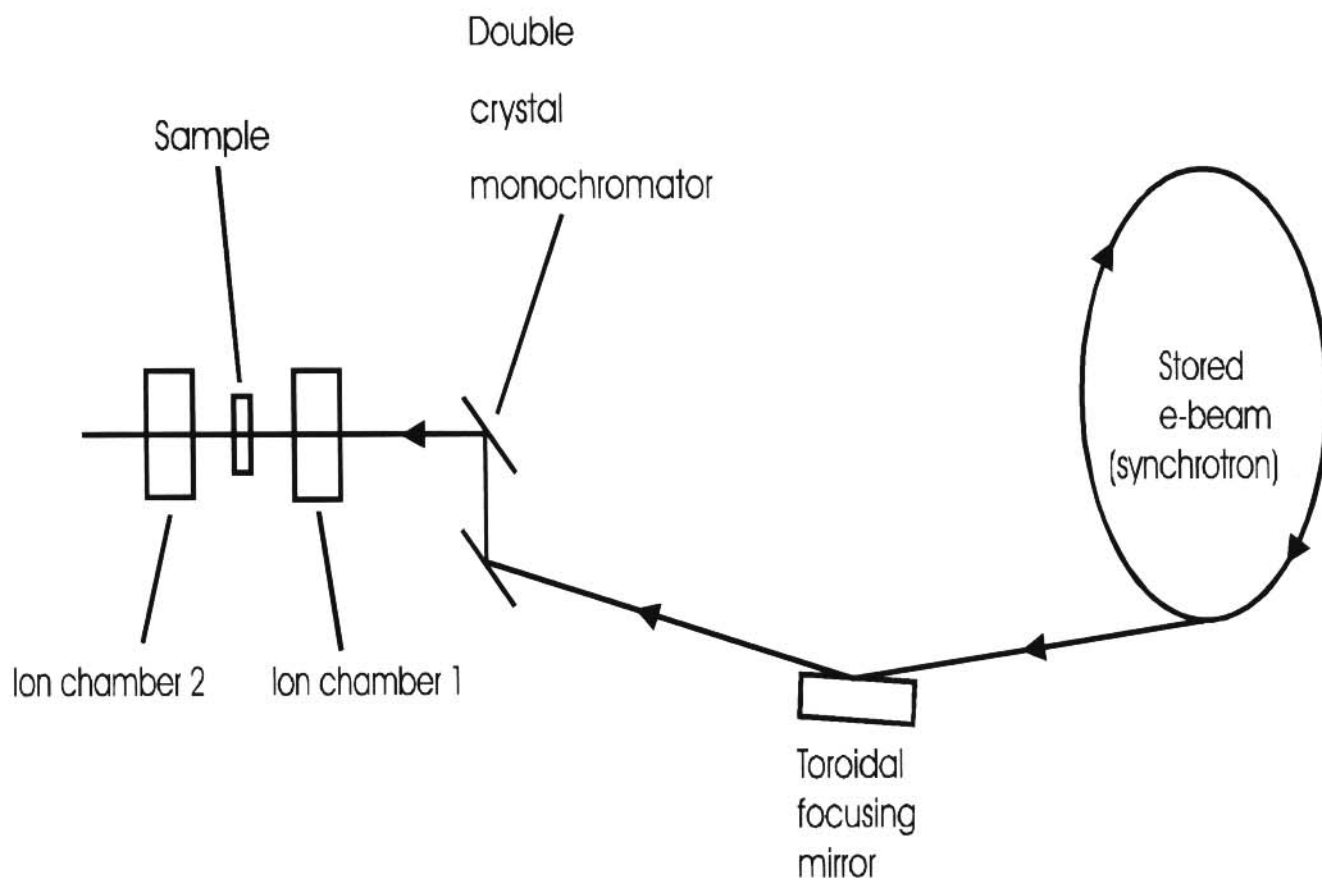
Figure 3.4 Schematic experimental arrangement for transmission EXAFS.

The extent to which X-rays are attenuated or modulated as they pass through a material is expressed by the X-ray absorption coefficient,

$$\mu = \ln\left(\frac{I_o}{I_t}\right)$$ 3.2

From the above equation μ is obtained by plotting $\ln\left(\frac{I_o}{I_t}\right)$ versus the energy of incident X-rays as shown in Figure 3.1. The dependence of μ on the X-ray energy can be evaluated. The process by which X-rays are absorbed by atoms is termed photoelectric effect. As the X-ray energy is increased, first the X-ray photons will pass directly through the sample (at low energy values) and then a point will be reached where the X-ray beam has sufficient energy (in the range 1 to about 40 keV) to 'eject' an electron (a photoelectron) from the atom's shell in the element. The point where there is a sharp rise in μ (i.e. where the new mode of absorption begins) is referred to as the absorption edge (a sharp discontinuity in the absorption curve)(an absorption edge is shown in Figure 3.5).

68

Absorption edge

μ

X-ray Energy
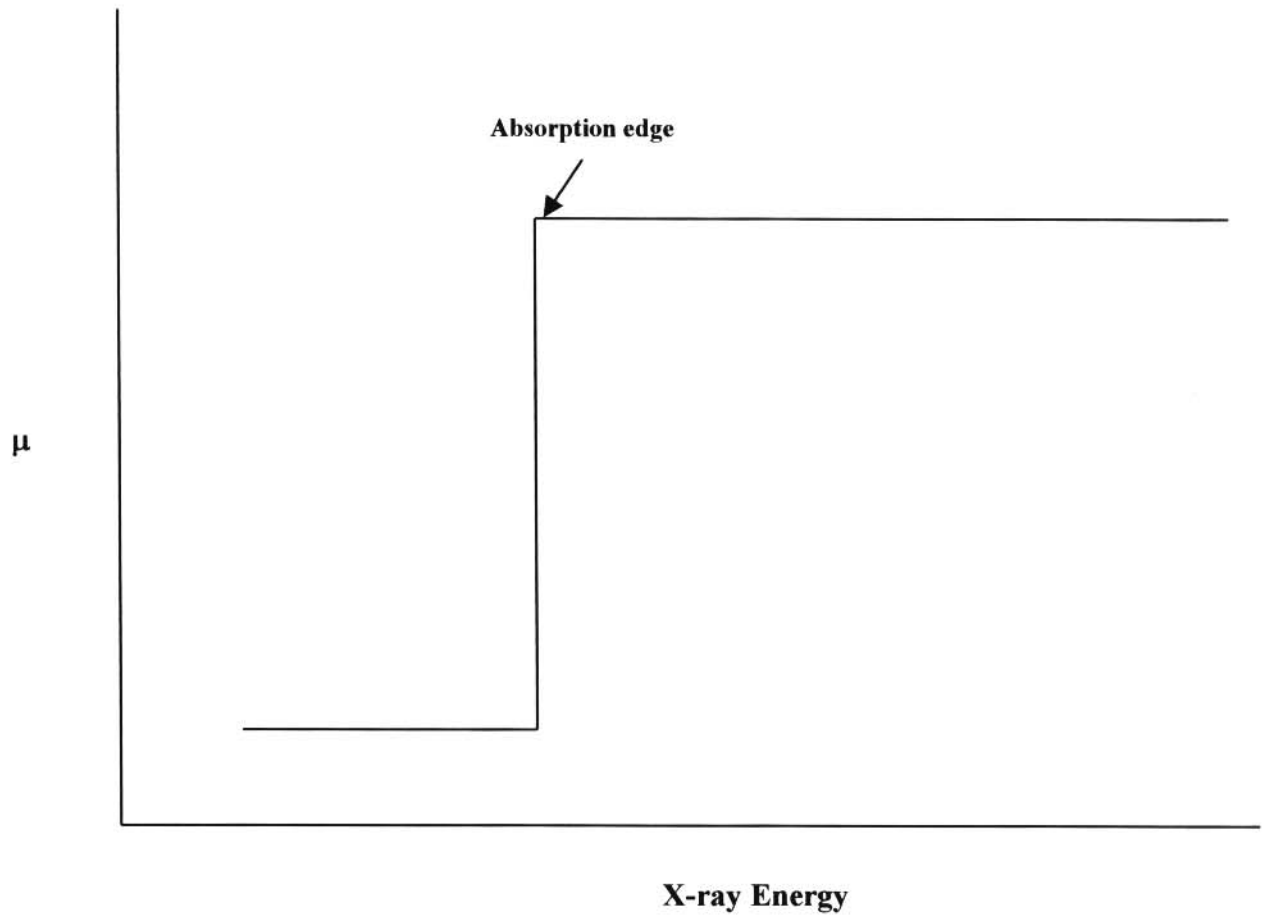
Figure 3.5 Schematic X-ray absorption edge.

An atom consists of a central nucleus surrounded by electrons lying in various shells, where the designation $K, L, M,\ldots$ corresponds to the principal quantum number $n = 1, 2, 3,..$ Absorption edges are named after the core levels from which photoelectrons are ejected such as 1s (K), 2s (L), etc (Rao and Rao 1988), in the order of increasing wavelength. So the energy where a K–edge electron can just be ejected is called the K–edge. This process leaves the atom in an excited, high-energy state. Then, one of the outer electrons immediately falls into the vacancy in the K shell, emitting energy in the process, and the atom is once again in its normal energy state. The energy emitted is in the form of radiation of a definite wavelength and is, in fact, characteristic K radiation. An electron from any one of the outer shells (i.e. L or M shells) can fill the K-shell vacancy. However, it is more probable that a K-shell vacancy will be filled by an L electron than by an M electron. L characteristic (L–edge) originates in a similar way: an electron is knocked out of the L shell and the vacancy is filled by an electron from some outer shell. It requires less energy to remove an L electron than a K electron, since the former is farther from the nucleus. It therefore follows that the L excitation voltage is less than the K and that K characteristic radiation cannot be produced without L, M, etc., radiation accompanying it. There are three types of L–edges, L_1, L_2 and L_3. L_1 corresponds to the ejection of the photoelectron from the $2s^2$ shell, L_2 and L_3 edges correspond to the ejection of an electron from a 2-p level (i.e. $2p_{1/2}(L_2)$ and $2p_{3/2}(L_3)$, respectively). All elements of atomic number above 9 have three L edges. However, in practice measurements are done at either the K or the L_3 edge.

3.3.3 EXAFS Theory

EXAFS describes a spherical wave which comes out from the excited atom, propagates towards another atom, is scattered from it, propagates back towards the excited atom and finally reaches the excited atom, after being scattered again from it. The EXAFS function [$\chi(k)$], based on a single scattering event by the photoelectron (valid at photoelectron energies greater than ~ 30 eV), i.e. assuming no significant multiple scattering contribution, is given by

$$\chi(k) = \sum_{j} -\frac{N_j}{kR_j^2}\left|f_j(k,\pi)\right|\exp(-2\sigma_j^2 k^2)\exp\left(\frac{-2R_j}{\lambda}\right)x\sin(2kRj + 2\delta_i + \psi_j) \qquad 3.3$$

This equation can be reduced to

$$\chi(k) = \sum_{j} -\frac{1}{k}A_j(k)\sin(2kR_j + \psi_j(k)) \qquad 3.4$$

where the sine term represents frequency of the EXAFS oscillations arising from each shell ,j, and A_j represents their amplitude. The amplitude of the oscillations depends on the number and type of atoms surrounding the central/x-ray atom, whilst the frequency depends on distance between the

excited and the neighbouring atoms or distance travelled by the photoelectron wave from the exited atom to the backscattering atoms (Cox et al. 1994). Hence, the equation indicates that the number and type of each (surrounding) atom at a distance R_j from the excited atom can be identified. R_j, N_j, $f(k,\pi)$ and σ_j^2 are the structural parameters of the jth shell, where, N_j is the number of identical atoms around the excited atom, R_j is the distance between the excited atom and the neighbouring atoms, σ_j^2 is the Debye-Waller (DW) term/factor which takes into account the loss in amplitude caused by thermally induced and static displacements within the jth shell atoms (the backscatterer) relative to the emitting atom and $f(k, \pi)$ describes the type of atoms in the jth shell (backscattering atoms). $1/kR_j^2$ and $e^{-2R_j^2/\lambda}$ are the factors which modify the amplitude of the oscillations. In the sine term, $2kR_j$ and $\psi_j(k)$ account for the phase shifts suffered by the photoelectron on interacting with the jth shell atoms (backscattering atoms) and the excited atom, respectively. The phase shifts must be included in the calculations. Typically quantitative structural data are gained up to the third–fourth co-ordination shell, in the luckiest cases since the contribution of the co-ordination shells far from the excited atoms is small. Atoms with low atomic numbers (z) (few electrons) will be weak backscatterers whereas those with high z numbers will be strong backscatterers.

The amplitude and the frequency of the oscillations in $\chi(k)$ from a given shell contains information on the number and type of neighbouring atoms around the excited atom, whilst the frequency of the oscillations gives the distance between the excited and the neighbouring atoms. These neighbours can be considered as being in a series of 'shells' going out from the excited atoms.

3.3.4   Sample Preparations

Samples are ground to a fine powder (<20 μm) using a mortar and prestle. However, these samples must have an absorbance change of $\sim$ 1.5 over the absorption edge.

$$Absorbance = \mu t \qquad\qquad\qquad 3.5$$

where μ denotes the absorption coefficient and t the thickness of the sample. Typical values of t are 5 – 10 μm. Samples are then compressed under high vacuum into thin discs (pellets) (200-400 μm thickness) of uniform thickness using hydraulic pellet press. Samples with high absorption coefficient are diluted with boron nitride (which has a low X-ray absorption coefficient) in order to obtain a disc which can be easily handled. Optimum sample thickness/concentration are found by trial and error. Then, samples are mounted in an evacuable crystal heating furnace with Beryllium windows.

3.3.5   Analysis of the EXAFS Spectrum

3.3.5.1 Introduction

In Daresbury Laboratory, the data analysis procedure requires that the transmission data sets, with pre-suffix '.dat', obtained from the samples are saved on the XRSSERV1 computer database. Before data analysis, the data sets are retrieved from the archives by a telnet link where xrsserv1.dl.ac.uk is used as an i.p. address for the XRSSERV1 operating system. Then, 'nrsget' command in the UNIX machine at Daresbury Laboratory is executed. The directory in which the data sets sit depends on

the station on which the data were collected, e.g. directory '/ex1a/' corresponds with 'station 7.1', directory '/exf9/' corresponds with 'station 9.2', etc. Hence, the command for restoring the files from the station 9.2 takes the following format: 'nrsget exf9 r1234.dat', where 'exf9' and 'r1234.dat' are the station number and filename, respectively.

There are a number of iterative programs (about three or so) which are valuable for the analysis of EXAFS data. These include the Daresbury Laboratory programmes such as EXCALIB, EXBACK and EXCURVE codes (Binsted 1992). Manipulation of the data involves extraction of the EXAFS signal from the x-ray absorption background through several stages (see Figures 3.1 and 3.3-3.6). These include pre-edge subtraction, normalisation of the signal, subtraction of the signal from the background and transformation into k-space and extraction of parameters of interest from the suitably processed data.

3.3.5.2 EXCALIB

EXCALIB converts the raw experimental data collected on the station into a form which is suitable for the background subtraction program EXBACK. Thus EXAFS oscillations are extracted from the spectrum by turning the x-scale into energy and the y-scale into absorption ($\ln\left(\frac{I_o}{I_t}\right)$). This is accomplished by reading into the program information on EXAFS type (e.g. transmission or fluoresence), monochromator type (e.g. Si (111), Si (220), Si (311), Ge (111), etc), inspection and deletion of glitches (offending features which appear as sharp structure of narrow width and are due

74

to spurious reflections from the crystal monochromator) and specification of the reference

chambers'gain ratio $(\ln\left(\frac{I_o}{I_t}\right))$. The plot is then saved into a file with extension '.exc', which is then

read into EXBACK.

3.3.5.3 EXBACK

This program subtracts the X-ray absorption background of an excited atom from the generated

EXAFS spectrum. This process is carried out in several steps as follows:

- **Setting the E_0**: This is defined as the point in the spectrum where the EXAFS spectrum starts and is set by placing the cross hairs on the summit of the largest peak in the spectrum. This point is then set to an arbitrary zero point/energy (E_0) and the spectrum is then rescaled to this value (see Figure 3.1).

- **pre-edge fitting**: Two points are selected in the pre-edge region, i.e. below the absorption edge (an absorption edge is shown in Figure 3.5) as shown in Figure 3.6(a). Then, a polynomial is fitted to these points (one at the start and the other at a position just before the edge). The two points are reset and different degrees of polynomial are used until a line (which is linear for transmission data and quadratic for fluorescence data) can be drawn that matches the slope of the pre-edge part of the spectrum. This will give some confidence that pre-edge absorption effects have been removed (Figure 3.6a).

- **post-edge fitting**: Two points [one at the start of the EXAFS (at about 20–50 eV) and the other at about 200 eV beyound the absorption edge] are chosen above the absorption edge as shown

75
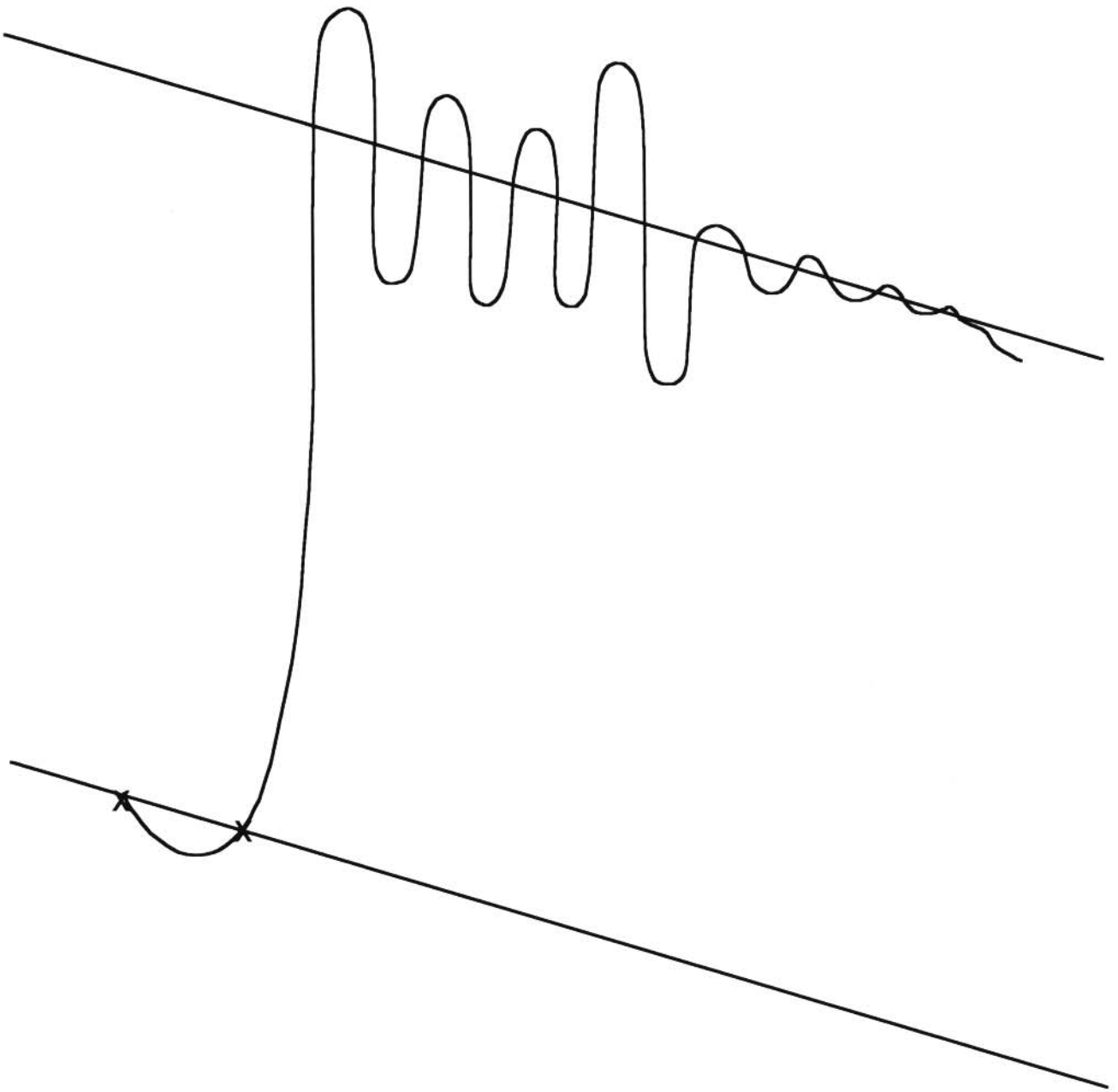
Figure 3.6(a) An example of a polynomial being fitted to the spectrum using two selected points in the pre-edge region
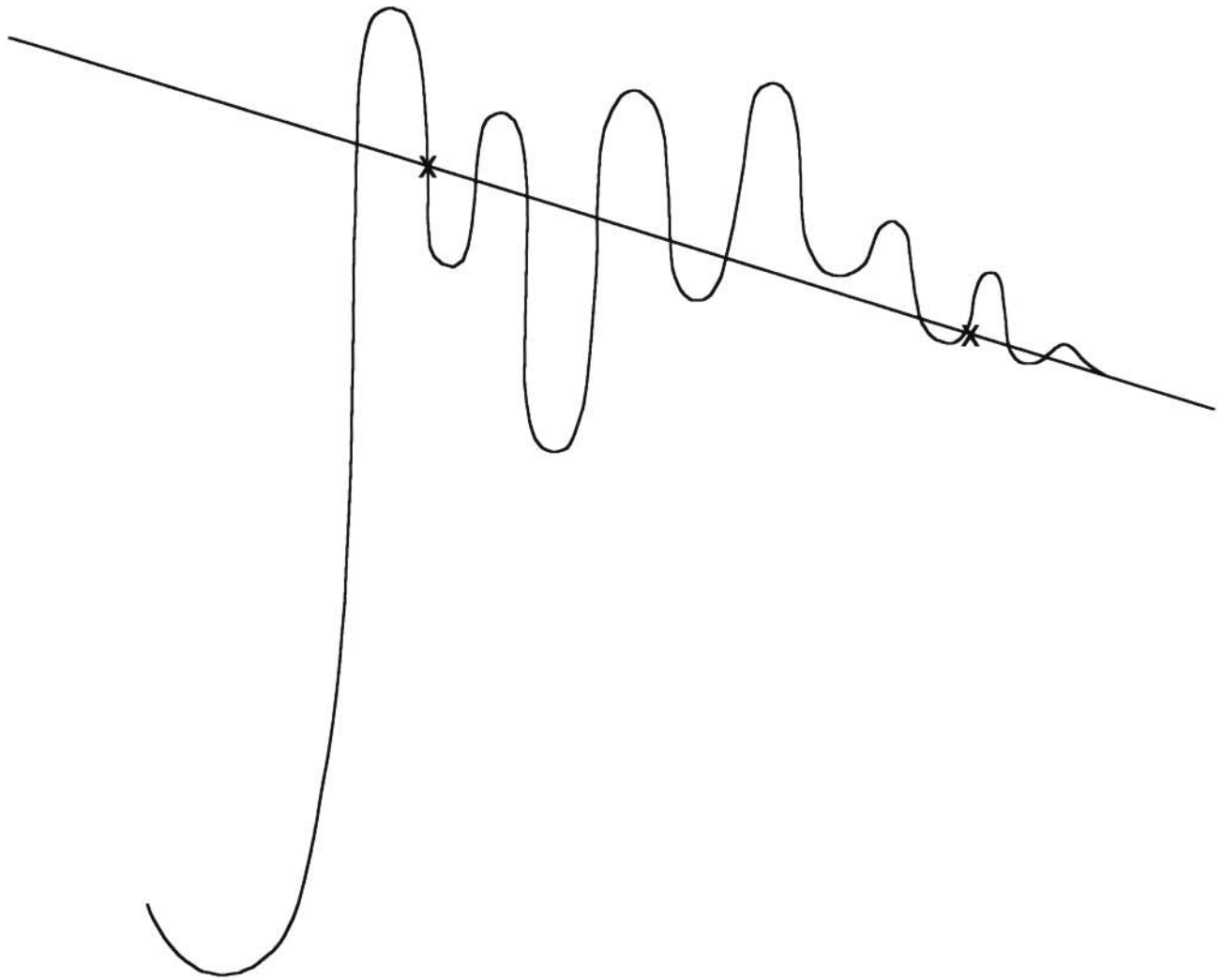
Figure 3.6(b) An example of a polynomial being fitted to the spectrum using two selected points above the absorption edge the EXAFS region.

- in Figure 3.6(b). A polynomial is fitted to the spectrum using the two selected points. This process is repeated until the line of best fit (i.e. a line that cuts through the fine structure/spectrum with equal oscillations on each side/the average of the structural oscillations) is achieved. However, caution must be taken that the EXAFS should not show low frequency oscillations which belong to the background and the background should not exhibit any oscillations due to following the EXAFS too closely. However, in most cases the first point is chosen along the rising part of the first EXAFS peak. Furthermore, there should be no discontinuities on the post-edge when looking at the derivative of the energy function.

- **background subtraction/correction**: The background is then subtracted using the pre and post–edge polynomials and the resultant EXAFS is plotted with the energy scale (*x*-axis) converted into the k-scale (see Figure 3.7a) using the relationship

$$k = \left(\frac{2m}{h^2}\right)^{1/2} \left(E - E_0\right)^{1/2} \qquad\qquad 3.6$$

where E_0 is the edge energy. The oscillations $\chi(k)$ are weighted, commonly cubed, i.e. the k-space weighting is chosen as three, to provide symmetric function in high k-space (see Figure 3.7b). More accurate descriptions of the EXAFS are given in the curved wave theory of Lee and Pendry (1975) and the small atom approximation of Gurman (1988).

- **Fourier Transform (FT)**: Two points are chosen from either end of the back-ground subtracted k (frequency)-dependent spectrum/data to Fourier Transform between them. The spectrum is Fourier Transformed from frequency to distance (*r*) space giving rise to an

78
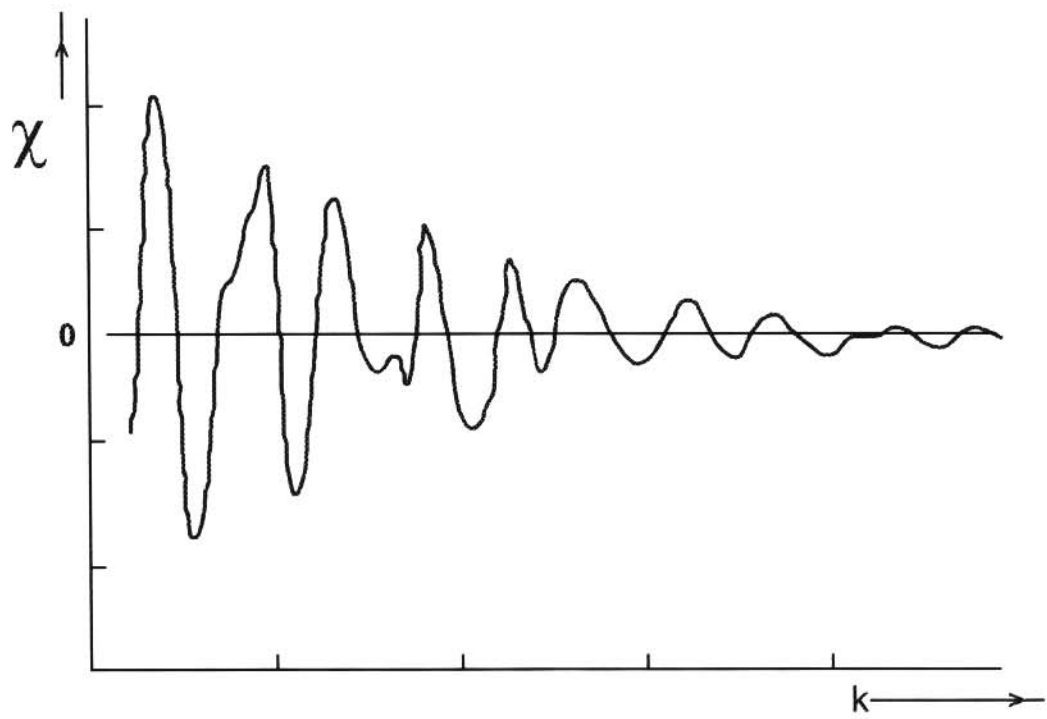
Figure 3.7(a) The normalized EXAFS function $\chi(k)$ plotted as a function of wave vector k.
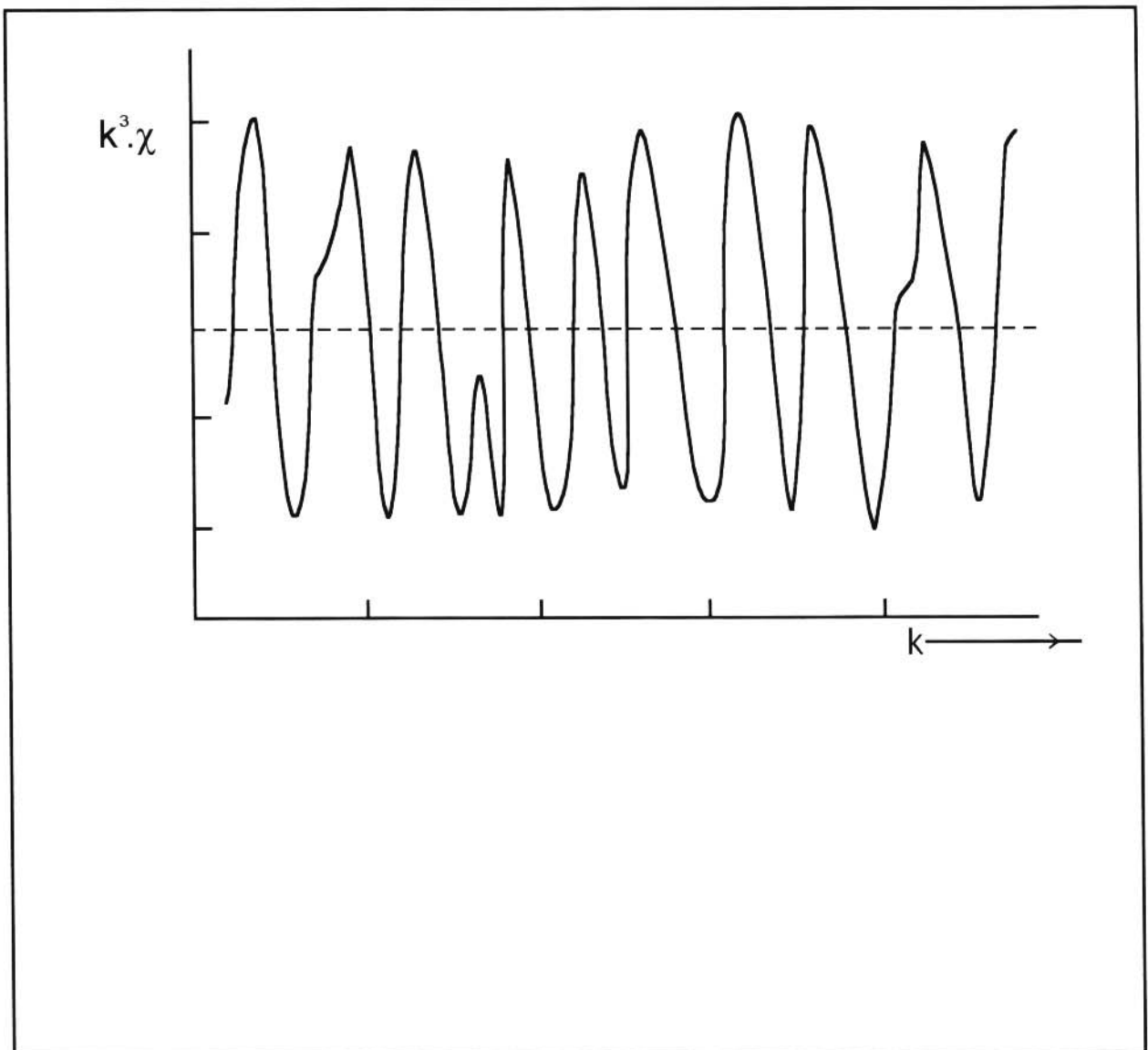
Figure 3.7(b) The EXAFS modulation [data shown in Figure 3.8(a)] replotted as $k^3.\chi(k)$ as

a function of the wave vector k. Note the effect is to bring out the oscillations at high k.
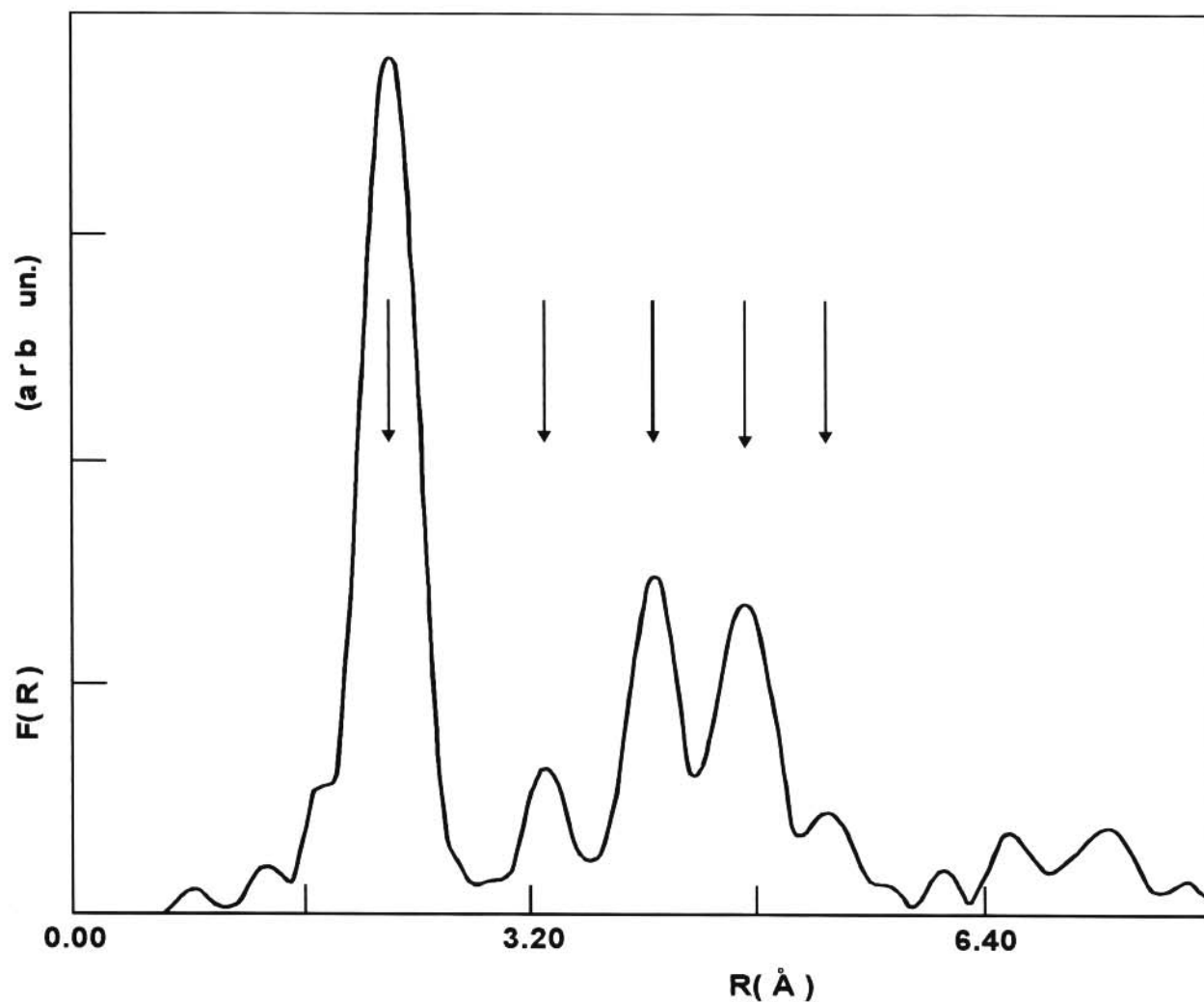
Figure 3.8 Fourier Transform of Figure 3.8(b); the arrows show the real/true nearest-neighbour and second nearest-neighbour (interatomic) distances. The magnitude of this Fourier Transform shows four well separated maxima, which are assigned to the four shells of nearest neighbours surrounding the excited atom. The corresponding number of atoms in each shell can be identified.

approximate radial distribution function (Cox et al. 1994). The *x*-axis of the FT represents distances

in Å and the peaks correspond to the successive neighbouring shells (see Figure 3.8). The inspection

of the FT is a powerful tool in selecting the optimal background subtraction of the data. However,

this Fourier Transformed spectrum is obtained without phase shift corrections. Thus, distances of

the FT are shorter than the real/true distances. Hence, in order to get accurate values of R_j the phase

shifts have to be known. These can be obtained from theoretical calculations or from the EXAFS of

model compounds. A model compound is the one which contains the same central atom and

scattering atom at similar distances to the unknown material but which has exactly known structure

(N_j and r_j are generally known for model compounds). The background-subtracted spectrum is written

out to a file with extension '.exb'. The file is then read into EXCURV92 or EXCURV97.

3.3.5.4 EXCURV92

EXCURV92 is a curve-fitting program. Data analysis is carried out as follows:

• The spectrum is read into EXCURV92 and the point frequency is set to 1 (every point) and

the column combination is set to 32 (where column 3 is the energy and column 2 the

EXAFS). The exchange potentials and ground state are used in EXCURVE to calculate

phaseshifts of the elements involved in the system whose EXAFS is being investigated. First,

the elements involved are specified. The potentials are calculated by inputting information

about a two-atom model, i.e. the atoms' atomic number, the type of edge being measured

(e.g. K- or L-edge) and the excited atoms' nearest neighbours. The value of the potential V_0

should be about −12 eV. This process is followed by the calculation of phaseshifts.

- The EXAFS and its FT are plotted.

- EXAFS is fitted when it has been weighted by k^3 in order to try to fit the entire oscillations and not just those in the low k region.

- The main shell parameters (radius of the shell $1(r_1)$, number of atoms in shell 1 (n_1), Debye-Waller factors in shell 1 (a_1) and the type of atom in shell 1 (t_1)) are entered for the first shell (ns = 1). A number between 1 and 500 is chosen to define the size of the changes the program makes in the parameters while iterating with 1 being the biggest change and 500 the smallest. The parameters are iterated (via a least-squares refinement) until the best fit of the 'theory' to the 'experimental' curve is obtained. Then a new spectrum is drawn to these values.

- Shells are added (from ns = 1 to ns = 5) and trial parameters are iterated as above.

- The output file is written out and printed.

3.3.5.5 Strategies for data analysis

The accuracy of the parameters can be achieved as follows:

- R_j: can be determined within an accuracy of 0.02 Å, the accuracy depending on the accuracy of the phase shifts.

- N_j and σ^2: these are highly correlated in any fitting, and are difficult to separate. Thus values of N_j and σ^2 are normally good to 20% (i.e. they are less accurate). However, σ^2 should always be positive and are normally between 0.001 and 0.025 $Å^2$.

83

- $f(k,\pi)$: the reliability of the calculations is somewhat smaller, since this function is much more sensitive to the details of the potential. Differences in atomic number need to be ~ 5 to 10 for usefulness. Thus EXAFS cannot distinguish between elements in the same row of the Periodic Table such as C, N or O as backscatterers.

3.3.6 Some Applications of the EXAFS Technique

EXAFS spectroscopy does not rely on long-range order within a sample. Hence, it has been extensively used in the study of materials science.

Examples of the applications of the technique are given below:

3.3.6.1 Glasses

EXAFS yield detailed information on the local structure in glasses. A good example is provided by the work on ZrF_4-based glasses, namely, $55ZrF_4.(45\text{-}x)BaF_2.xCsF$ glasses. It has been shown that Zr-F peaks in the Fourier Transform shift to shorter distances with the progressive substitution of CsF for BaF_2. This implies that the F co-ordination environment around Zr, especially the Zr-F bond lengths (Kawamoto et al. (1991)), affects the activation energy for conduction.

Synchrotron radiation and a range of complementary techniques provide information on the

phenomenology of zeolite materials instability (Greaves 1997). These structural instabilities lead to the collapse of the microporous structure when the temperature or pressure is raised sufficiently. In $Na_{11}Al_{12}$-$Si_{12}O_{48}$, the temperature of collapse occurs close to the glass transition T_g (Greaves 2001). At T_g, a supercooled liquid becomes indistinguishable from a solid. Hence, zeolite collapse incorporates the shear typical of a solid but well below the melting point. As a result, the armophised alumino-silicate that is formed is essentially a rigid glass.

3.3.6.2 Disordered systems

Vast studies of solids containing defects have been made (e.g. the local structural environments of Bi^{3+} and dopant cations (Rb^{1+}) in the fluorite structured solid-solutions). These studies showed that that whilst the Rb-F shell is heavily disordered, the first co-ordination shell of the host-fluorine shell is fairly ordered (Catlow et al. 1985). This behaviour was attributed to the fact that thermally-induced vacancies arising from F^- ion conduction are preferentially sited next to Rb ions. The formation of these vacancies as the temperature increases causes the remaining F^- ions in the Rb-F co-ordination sphere to relax to a new minimum energy configuration with a shorter mean Rb-F distance.

Similarly, previous EXAFS work on the local environments of a range of rare-earth doped CaF_2 showed that two types of clusters are formed depending on the radius of the dopant ion. For the smaller rare-earth ions (Tb, Yb, Tm) stable large cubo-octahedral clusters (6'/0'/8'/6') were formed.

However, there is little variation in their structure. For the larger dopant ions (La, Ce, Nd, Pr) the dimeric clusters (2'/0'/2/'2') were dominant. However, there are slight variations in the structure in these clusters. The presence of clusters affect the vibrational properties of the material, affect the transition temperature to the superionic state and the development of disorder.

3.3.6.3 Biological molecules

The local environment of metal ions in biomolecules such as ferritin and haemoglobin may be established using EXAFS. Hence, accurate bond lengths have also been determined for a number of important enzymes and proteins. The precise determination of the Fe-S bond lengths via EXAFS has enabled the crystal structure of the metalloprotein rubredox to be successfully refined via X-ray diffraction (Garner and Halliwell 1986).

3.3.6.4 Amorphous semiconductors

The FT of the EXFAS of a–Ge as well as A-Ge:H shows the presence of a single peak, due to four Ge atoms at a distance of 2.45 Å, confirming that the local structure of the amorphous network is similar to that of a crystal. The absence of any second shells at about 4.0 Å points to a spread in the tetrahedral angle of at least $7°$ rms (see a series of studies pioneered by Evangelisti et al. (1981)).

3.3.7 Strengths and Limitations of EXAFS

The power of EXAFS in examining complex structural problems in heavily defective materials can be considerably enhanced when it is combined with computer modelling studies. EXAFS also compliments X-ray diffraction techniques. The special features of EXAFS technique which have made this possible are:

- Determination of structural information, namely, the local environment (local coordination and interatomic distances) of an excited atom may be established by tuning the absorption edge of an individual atom type. As the EXAFS oscillations are produced only by atoms close to the emitting atoms, EXAFS studies are not limited to single crystals (i.e. systems having long-range order). Even systems which have a well defined coordination around a central atom may be studied. Furthermore, by careful analysis some information may be obtained about the second nearest neighbour coordination shells or sometimes about more distant shells.

- EXAFS is not limited to single materials/crystals. Hence, disordered materials such as glasses, amorphous materials, gels, solutions, polycrystalline, etc can be investigated.

- EXAFS is not very sensitive to pressures and high temperatures. Hence, catalytic materials are studied under real catalytic environments.

- EXAFS data collection (process) is simple and lasts for short periods.

- EXAFS can be sensitive to low concentration of the target atom.

However the following experimental realities offset these advantages (see Cox et al. 1988):

- A high intensity synchrotron light source is required for the collection of high quality data.

- The technique is only suitable for short-range order, i.e. for r up to 5 Å from the central atom since the contribution of the atoms in the coordination shells far from the central atoms (to the EXAFS spectrum) is small.

- Although more Synchrotron sources are being built and access is getting easier, these sources are sparse in other parts of the world (e.g. in Africa) and available time is highly sought after. For instance, the only places so far where SRS are available world-wide are UK (Daresbury Laboratory), USA (The National Light Source, Brookhaven), Japan (the Photon Factory of the National Laboratory for High Energy Physics, Tsukuba), France (LURE, Orsay), Germany (DESY, Hamburg), Germany (BESY, Berlin), EC central facility under construction (European Synchrotron Radiation Facility, Grenoble), Italy (the PULS Synchrotron Radiation Facility, Frascati), etc.

- Co-ordination numbers are difficult to extract from EXAFS spectrum because of the high correlation between co-ordination numbers (CN) and the effects of thermal vibrations. The accuracy on CN is about 20 %.

- It is difficult to distinguish between atom types unless they display marked differences in backscattering powers, e.g. EXAFS cannot distinguish between elements that belong to the same row in the Periodic Table such as C, N, or O as backscatters.

- It is difficult to detect EXAFS oscillations for light atoms (i.e. atoms with low atomic numbers, i.e. below Ca). However, synchrotron light sources are now becoming more

competitive to cater for this drawback.

- The EXAFS theoretical approximation is not valid below 2-3 Å^{-1}, since the limit k_{min} in the FT spectrum cannot be reduced to zero. Thus analysis of the FT spectra for disordered systems in the R space is only limited to low distance determinations (typical accuracy 0.05-0.10Å). However, the diffraction experiment gives the $i(k)$ from practically k=0. On the other hand EXAFS extends up to very high k values (up to 12-20 Å^{-1}) values). Thus it is very much sensitive to short range correlations than x-ray diffraction.

CHAPTER 4

COMPUTER MODELLING OF STRUCTURAL AND DYNAMICAL PROPERTIES OF CdF_2-PbF_2 MIXED METAL-FLUORITES

4.1   INTRODUCTION

Fluorite structured compounds are prime candidates for investigations by experimental and computer modelling techniques. In these materials, wide computational flexibility enables optimization of their solid electrolyte properties such as conductivity, activation energy, etc. through compositional control. This is necessitated by the need for new fast ionic conductors working at substantially low temperatures. Among fast-ion conductors, alkaline-earth fluorides show order–disorder phase transition at high temperatures. The use of the terms order and disorder in this work always refers to regular/perfect lattice sites and random occupancy of the atoms. The structure itself is ordered. The disordering (in most alkaline-earth fluorides) is predominantly on the anion sub-lattice. A substantial rise in ionic conductivity (which often results in good redox stability) to values typical of ionic melts (values ~ 1 Ω^{-1} cm^{-1}), unusually low values of activation energies and anomalous reductions in certain elastic constants (Comins et al. 1990) are the prominent features, which accompany this process. Changes in elastic constants mark the transition temperature region. However, their superionicity is not concomitant with structural phase transition. Furthermore, in

most of the superionic conductors one of the ions is relatively more mobile than the others. For example, in alkaline-earth fluorides, anions are the current-carrying species, while in alkali halides and β-aluminas, cations carry practically all of the current.

In the present study CdF_2 is doped with divalent cations of anomalously high polarisability to form fluorite type solid solutions $CdF_2(xPbF_2)$. There is an ionic size difference between the host and guest cations ($rPb^{2+} = 1.20$ Å and $rCd^{2+} = 0.97$ Å). In $CdF_2(xPbF_2)$ mixed crystals the Pb atoms take the sites of Cd atoms with increasing Pb concentration x. These dopant species are randomly substituted. $CdF_2(xPbF_2)$ mixed systems form a continuous series of substitutional solid solutions with the fluorite structure (Kosacki et al. 1989). Hence, in this study a cubic fluorite structure is assumed for the solid solution at all compositions. There have been several studies on these novel mixed crystals, notably the investigation of their ionic transport using Raman scattering techniques by Kosacki et al. (1989). However, atomic (statics and molecular dynamics) simulations have never been performed at various dopant concentrations and at different temperatures on these systems. Previous work was only performed for the $x = 60$ mol % PbF_2 sample (Netshisaulu et al. 1999). In the present study, particular attention is mainly given to the use of conventional rigid ion potentials in clarifying features that give rise to the fast-ionic motion in the entire range of these 'mixed-conducting' materials. Hence, we modelled mixed $CdF_2(xPbF_2)$ systems using atomistic simulations (facilitated by the use of the GULP (Gale, 1997) and the DL_POLY (Smith and Forrester 1998) codes) in the whole composition range (0 mol %$\leq x \leq$100 mol % PbF_2). This involves calculations of structural and dynamical properties of these solid solutions. First, interionic potentials for $CdF_2(xPbF_2)$ are derived and used in calculations of the bulk crystal data such as the second-order

elastic and dielectric constants. In the absence of experimental data for comparison, the calculations on bulk properties of the mixed systems are based on the experimentally determined trend of the static dielectric constant (ε_s) as a function of temperature. The temperature and concentration (Pb content) dependences of bulk properties of $CdF_2(xPbF_2)$ are investigated. Second, the mean square displacements of the cations and anions in the two end members and in their mixed systems were determined from molecular dynamics (MD) simulations. Transport properties such as diffusion coefficients, activation energies and ionic conductivity are extracted from the mean-square displacement plots of the anions. Furthermore, the temperature and dopant dependences of the ionic conductivity and activation energy are also investigated. These MD calculations have been used to provide complementary (theoretical support) information on structural properties of these systems such as the radial distribution functions for the EXAFS experiments discussed in Chapter 5. This helps to provide a detailed interpretation of the properties of these mixed crystals. These materials could find their industrial application in the form of energy-storage devices, light-emitting devices and light-energy converters. Hence theoretical and experimental treatments of the atomic structure of the novel $CdF_2(xPbF_2)$ are necessary.

4.2   INTERIONIC POTENTIALS FOR CUBIC CdF_2-PbF_2 MIXED SYSTEMS

An interatomic potential model is a representation of the potential energy of the system as a function of particle coordinate system. The pair potential model has serious inadequacies for more covalent materials. However, for most strongly ionic materials the pair potential model is considered to be a

reasonable approximation (Catlow 1986).

The short-range interactions between the ionic species in $CdF_2(xPbF_2)$ are described by interatomic potentials and the polarisability of the ions themselves is described by the shell model. On the one hand, the use of potentials based on shell model potentials in ionic systems is expected to give better estimates of dynamical properties (those due to interactions between ions as their local environments change dynamically) than rigid-ion models, although structural properties, such as dielectric constants and radial distribution functions are modelled more or less equally well by rigid-ion and shell model potentials in ionic materials (Gillan and Lindan 1991). On the other hand, it has been found that the explicit inclusion of polarisation has very little effect on the quantities of interest (see Gillan and Lindan 1991), so long as the rigid-ion potential is suitably constructed. In addition, the use of rigid-ion model results in great saving in computational costs in the execution of MD calculations, because all the shells in the shell model have to be relaxed adiabatically at each time-step.

There has been a concerted effort to model a wide range of related systems, including fluorites such as pure CaF_2 (Bingham 1989, Lindan and Gillan 1995), mixed-metal $RbBiF_4$ (Cox et al. 1994), etc. For these varieties of systems, it has been reported that rigid-ion potentials give reasonable estimates of their static and dynamical properties (Lindan and Gillan 1995). Hence, for these materials, conventional rigid-ion potentials have been employed extensively in molecular dynamics studies. As has already been outlined in Chapter 2.2, the most popularly used expression in simulating ionic solids has the Buckingham form (see equation 2.2).

In the present study, the rigid-ion and shell model short-range interionic parameters of CdF_2 ($xPbF_2$) mixed systems were derived empirically using a GULP code (Gale 1997). However, the shell model F-F potential parameters were taken from Lindan and Gillan's (1993) work on CaF_2. The cation-cation (cation = Cd or Pb) interactions are generally ignored in view of large separations of cations in the fluorite structure. The remaining cation-F interactions for the two potential models were determined by empirically fitting them to the absolute zero temperature lattice parameter, the bulk data (dielectric and second-order elastic constants) and the lattice energy data for mainly pure components of the solid solutions. The validity of both models was assessed by performing a number of preliminary perfect lattice calculations, where crystal properties such as dielectric and elastic constants were compared with available experimental data. In this study the same set of potentials were used for both molecular statics and molecular dynamics calculations on all of the samples (i.e. 0 mol $\%\leq x\leq 100$ mol $\% PbF_2$) under study. Furthermore, in modelling these mixed systems, a single description of F-F interaction terms, which are common to the two pure compounds, were used. Essentially this is the approach adopted by Cox et al. (1994) in modelling mixed systems.

For the fitting, an acceptable range for the sum of squares is considered a variable quantity. Errors in our observable are looked at and a value judgement is made about whether they are acceptable or not. The first three vibrational frequencies are found to be zero for a core only model, but deviate slightly when shells are present due to the numerical precision of matrix inversion. In this case, a value within about 0.5 cm – 1.0 cm of zero is what we consider acceptable.

4.3 COMPUTATIONAL PROCEDURES

4.3.1 Static Modelling of $CdF_2(xPbF_2)$

In this study, perfect lattice and defect simulations are conducted on $CdF_2(xPbF_2)$ mixed systems and pure materials, respectively. These simulations are based on room temperature parameters and are static in nature; that is, thermal motions of the ions are not included explicitly as outlined in Chapter 2. However, the two simulation techniques are based on energy minimisation procedures, where the ionic-coordinates are iteratively adjusted until the forces acting between them are reduced to a minimum (Catlow 1997). In the current study, these simulations are conducted at constant pressure.

4.3.1.1 Perfect fluorite lattice calculations of CdF_2-PbF_2 systems

The perfect lattice is the lattice with all ions being at their original/undisplaced positions and without the impurity. The lattice static calculations were carried out using the standard procedure efficiently coded in the GULP program that is used throughout the work presented in this Chapter. However, it is worth noting that in order to simulate all the compositions of interest, i.e. $x = 0$ mol % to $x = 100$ mol % PbF_2 in $CdF_2(xPbF_2)$, we adopted a mean-field approach/strategy which consists of scaling interaction energies by the product of site occupancies. This allowed the simulation of a randomly distributed solid solution, and was preferred to the usual methodology of setting up large supercells, which unavoidably builds up an ordered system. Elastic constants associated with equilibrium structures were deduced using energy-minimisation techniques as discussed in Chapter 2. In each case, a valid energy minimisation was produced for each composition in a reasonable amount of c.p.u.

95

time. Hence, the fluorite structure for each composition was the actual structure adopted by each material.

4.3.1.2 Defect fluorite lattice calculations of the pure constituents, CdF_2 and PbF_2

The defect lattice simulations for pure compounds (CdF_2 and PbF_2) were performed using the GULP code. The basis of the calculation was to introduce a defect (or defects) into the perfect lattice and then to relax the surrounding particles to a new minimum energy configuration (see Chapter 2 for more details). Thus the calculations involved the division of the crystal lattice into an inner-region I containing all defects, where the energy minimization method is applied, and an outer region II, where defect forces are weaker and the relaxation may be calculated via the Mott-Littleton approximation (Mott and Littleton 1938). The lattice energy of the perfect lattice was then subtracted from that of the defect lattice in order to obtain the defect energy of the pure materials.

4.3.2   Molecular Dynamics (MD) Simulations

MD is a well-established computer modelling technique originally derived to model liquids so as to gain some valuable insight into the physical chemistry underpinning their fast-ion conduction. This technique is based on 'classical' methods where Newton's laws of motion are applied in order to follow the dynamical behaviour of every atom in a system over a given time (see Chapter 2). By real time standards the time-scales are short (i.e. measurements are taken in pico-seconds), but on atomic

scales, these are times in which atoms move randomly in a system, because matter at atomic level is dynamic (atoms are in constant motion). Using Beeman's numerical algorithm, the positions and velocities of all the atoms can be predicted for some future time, i.e. one can locate, unambiguously, the position of each atom and follow its motion as it interacts with its neighbours. Such complex simulations can take several hundred hours of CPU time on most powerful workstations, but it is the only way that such great detail can be resolved.

In the present study, molecular dynamics studies were performed on $CdF_2(xPbF_2)$ using a DL_POLY code (see Chapter 2 for further details), where the rigid-ion potential model (with the same rigid-ion potential parameters as for the static calculations) was employed. Simulation runs were started from the fluorite structure, where a simulation box containing 768 particles (256 cations and 512 anions, i.e. 4 x 4 x 4 unit cells) was set up with each ion at a given velocity in accordance with the target temperature. Periodic boundary conditions were applied and the ensemble used imposes the conditions of constant temperature and volume (NVT). However, cations were randomly distributed over the available cation sites. In fact, the arrangement of the cations in these systems was such that Cd^{2+} ions were put on all tetrahedral positions in the fcc lattice forming CdF_2. No charge compensating fluorine ions were introduced since both cations, i.e. Cd^{2+} and Pb^{2+}, have the same charge (2+). Next, a suitable number of Cd^{2+} ions were replaced by Pb^{2+} ions at random for each composition x. Then, the system was allowed to evolve in time. After each time-step, Δt ($\sim 10^{-15}$ s), coordinates and velocities of each ion were updated using the procedures based on Newton's equations of motion. Each simulation was equilibrated until a constant temperature was obtained (for at least 3 000 Δt). Once the system had equilibrated, it was run for several thousands of time-steps

(for about 50 000 Δt to yield a simulation time of 50 ps – time sufficiently long for noting diffusion in $CdF_2(xPbF_2)$ during which data were collected. A wealth of information (thermal average values of the quantities of interest) on structural and transport properties including the radial distribution functions (RDFs) (they give the full probability distribution of the ions in the immediate environments of the target ion / the probability of finding ions in different regions of the unit cell and are useful comparisons with EXAFS Fourier Transform), transport coefficients (e.g. diffusion coefficients can be deduced from the gradient of the graph of the MSDs of the mobile species with time, conductivity is estimated using the Nernst-Einstein equation), transition temperatures (temperature associated with marked changes in physical properties), the melting point and ion transport mechanisms can be extracted from the subsequent data. The simulations were run on Silicon Graphics servers at the University of the North, in the Materials Modelling Centre.

4.4   RESULTS AND DISCUSSION

4.4.1   Derived Interionic Potentials

The derived rigid-ion and shell model potential parameters for $CdF_2(xPbF_2)$ mixed crystals are listed in Tables 4.1 and 4.2. These potentials were developed by predicting physical properties (e.g. bulk properties of the perfect solid) that are reasonably in agreement with experimental data apart from C_{12}. Consequently, they were used in the statics and molecular dynamics calculations.

It is worth noting from tables 4.1 and 4.2 that cation-cation (cation = Cd or Pb) interactions were not considered in the present calculations because they are, in general, rather weak and consequently can be neglected. It is evident from the tables that short-range forces were taken to act between anions and cations, and between anions and anions. Values of the cation-fluorine (i.e. Cd-F or Pb-F) interactions were found by fitting to the available experimental/crystal data such as elastic and dielectric constants. Furthermore, a single (common to the two nominally pure compounds/materials) description of the interatomic potential for fluorine-fluorine interactions was used, since the second-neighbour interactions do not make very substantial contributions to the elastic or equilibrium properties of alkaline-earth fluorides.

Table 4.1   Rigid-ion potential parameters obtained for $CdF_2(xPbF_2)$ mixed systems.

Buckingham parameters	A(eV)	ρ(Å)	$C(eVÅ^{-6})$
Cd^{2+}-Cd^{2+}	0.00	0.3000	0.00
Cd^{2+}-F^-	420.060	0.3529	0.0280
Pb^{2+}-Pb^{2+}	0.00	0.3000	0.00
Pb^{2+}-F^-	157.339	0.4662	0.9284
F^--F^-	160919.850	0.1758	22.3070

Cut off = 12 Å

Table 4.2   Shell model potential parameters for $CdF_2(xPbF_2)$ mixed systems.

Ion	$Y(|e|)$	$K(eVÅ^{-2})$
Cd^{2+}	6.315	741.40
Pb^{2+}	3.1459	32.35
F^-	-2.8475	101.20

Buckingham parameters	A(eV)	ρ(Å)	$C(eVÅ^{-6})$
Cd^{2+}-Cd^{2+}	0.0	0.300	0.0
Pb^{2+}-Pb^{2+}	0.0	0.300	0.0
Cd^{2+}-F^-	1742.172	0.288	0.0
Pb^{2+}-F^-	1511.692	0.322	0.0
F^--F^-	1808.00	0.293	109.10

Cut off = 12 Å

4.4.2 Crystal Bulk Data

The validity of the rigid-ion and shell models was assessed by carrying out a number of perfect lattice calculations. The accuracy in the determination of elastic constants provides a convenient test for the appropriateness of the derived interionic potentials for a solid. Furthermore, the behaviour of the elastic properties of crystals is of great importance in understanding such properties as structure, composition and phase transitions, etc. in materials. Basically, they are a measure of the energy change when a solid is strained/deformed uniformly and are related to lattice vibrations. The dielectric constant reflects the response of the solid to the application of an electric field.

Following our previous work on pure CdF_2 (Netshisaulu 1996), a full study of the elastic properties on a series of fluoride solutions between PbF_2 and CdF_2 is presented here based on improved potentials (i.e. regarded as superior to those used in the earlier work) derived using the GULP program. In addition, F-F short-range potentials used for the shell model in these calculations were obtained from an extensive study of the alkaline-earth fluorides (see Catlow et al. 1977). The shell model (polarization) parameters (shell charges and spring constants) were fitted to the dielectric constants.

First, the calculated crystal bulk data for pure (CdF_2 and PbF_2) components of the solid solutions that were evaluated using the two potential models given in Tables 4.1 and 4.2 are presented in Table 4.3. Owing to the symmetry of a cubic crystal, there are three independent elements in the elastic constant tensor, namely, C_{11}, C_{12} and C_{44}, in several crystals of $CdF_2(xPbF_2)$. While no direct comparison

Table 4.3   Calculated crystal properties of pure CdF_2 and PbF_2 fluorine ion compounds.

Property	CdF₂			PbF₂		
	Rigid-ion	Shell model	Experiment$^{\pm}$	Rigid-ion	Shell model	Experiment†
Elastic const.						
C_{11}(Gpa)	183.7	182.3	184.0	90.5	105	93.0
C_{12}(Gpa)	28.2	60.2	67.0	11.8	40.8	44.0
C_{44}(Gpa)	27.8	23.0	21.8	7.00	18.2	20.6
Dielectric const.						
ε_o	8.68	8.76	9.00	31.7	35.4	31.7
ε_∞	-----	3.27	2.43	-----	2.00	-----
Lattice par.						
a_0(Å)	5.38	5.38	5.39	5.93	5.93	5.94

†Experimental estimates from Catlow et al. (1978)
$^{\pm}$Experimental estimates from Hart et al. (1971)

could be made for the entire series, it is apparent from Table 4.3 that most of these properties are in fair agreement with the measured values, with the exception of C_{12}, which is poorly estimated, by the rigid-ion model. A similar inconsistency had been found in the case of materials with a similar structure. This discrepancy can be explained in terms of the limitations of the rigid-ion model. It has been shown by Basu et al. (1985) that agreement in C_{12} can be improved by including a three-body interaction term, but this has a tendency to cause a larger discrepancy in the other two elastic constants. However, the latter potentials have been found to be satisfactory in molecular dynamics simulations provided that static dielectric constants are correctly predicted. It is gratifying to note that our potentials correctly reproduce the value of the static dielectric constant for CdF_2, which is essential for adequate representation of defect dependent properties. Moreover, the static dielectric constants are also reproduced fairly well on including the polarizability.

For PbF_2, the rigid-ion model consistently underestimates the values of the elastic constants for a highly polarisable PbF_2 material as compared to CdF_2. Most of the rigid-ion values for the elastic constants of PbF_2, in particular, C_{12} and C_{44} are much too small compared to the experimental values (Catlow et al. 1978). The discrepancy in these elastic constants can be ascribed to the rigid-ion model itself since it assumes that ions are not polarisable and they interact as point charges. A shell model, which assumes ions to be made of charged cores and spherical shells, is more appropriate as shown by the results in Table 4.3. However, it is well known that the Pb^{2+} ion is highly polarisable. The calculated lattice parameters from our rigid-ion and shell model potentials are in excellent agreement with the experimental values. This indicates that our potential models are reliable in the study of fluorite-structured compounds, which gives us confidence in using both potentials in the investigation.

The crystal data of the mixed systems calculated on the basis of the rigid ion potential model are reported in Table 4.4. In the absence of experimental data for comparison, the present investigation

Table 4.4 Calculated crystal properties of $CdF_2(xPbF_2)$ mixed crystals

Property	Material composition x (mol % PbF_2)					
Elastic const.	0	20	40	60	80	100
C_{11} (Gpa)	183.7	158.9	137.3	118.9	103.3	90.5
C_{12} (Gpa)	28.1	23.4	19.4	16.2	13.7	11.8
C_{44} (Gpa)	27.8	22.3	17.4	13.1	9.6	7.0
Diel.Const., ε_0	8.7	10.8	13.9	18.2	24.3	31.7

on these crystal properties have been based on an experimental static dielectric constant of ≈ 16 deduced from conductivity measurements carried out by Kosacki et al. (1985, 1989) on the $CdF_2(60$ mol %PbF_2) material, which compares well with the calculated value, 18.2.

4.4.3   Effects of Temperature on Crystal Bulk Data in Mixed Crystals

It is well known that many of the physical properties of the fast-ion conductors change anomalously at high temperatures (Ngoepe 1987). These include rapid increases in dielectric constants, large decreases in the elastic moduli and continuous curvature in the Arrhenius plots of the diffusion
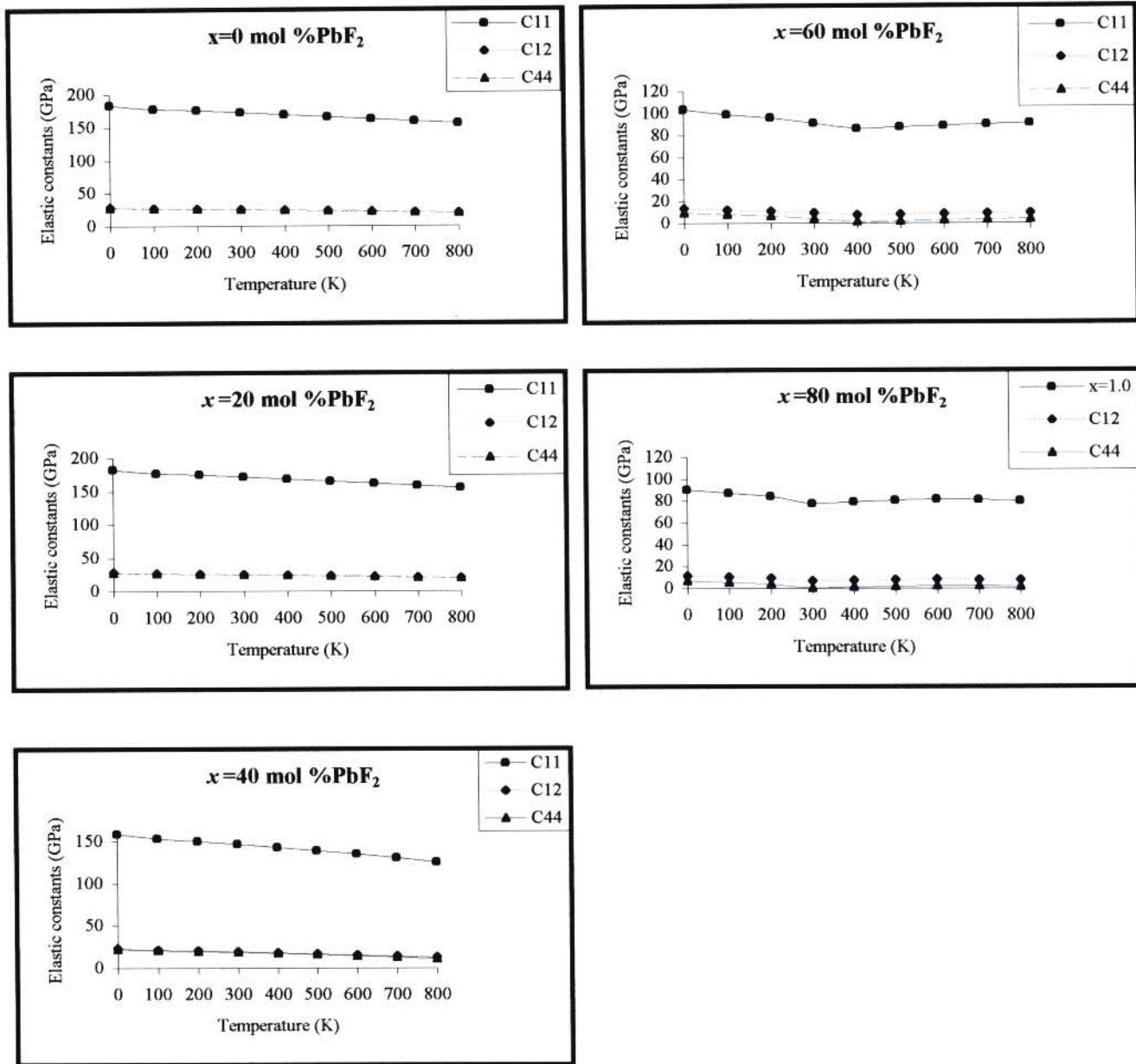
Figure 4.1(a) The temperature variation of the three independent elastic constants in $CdF_2(xPbF_2)$ mixed systems.
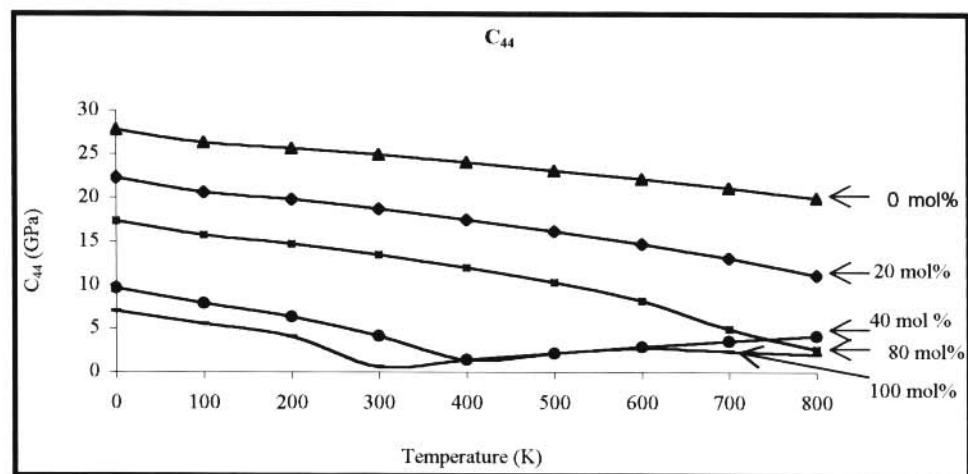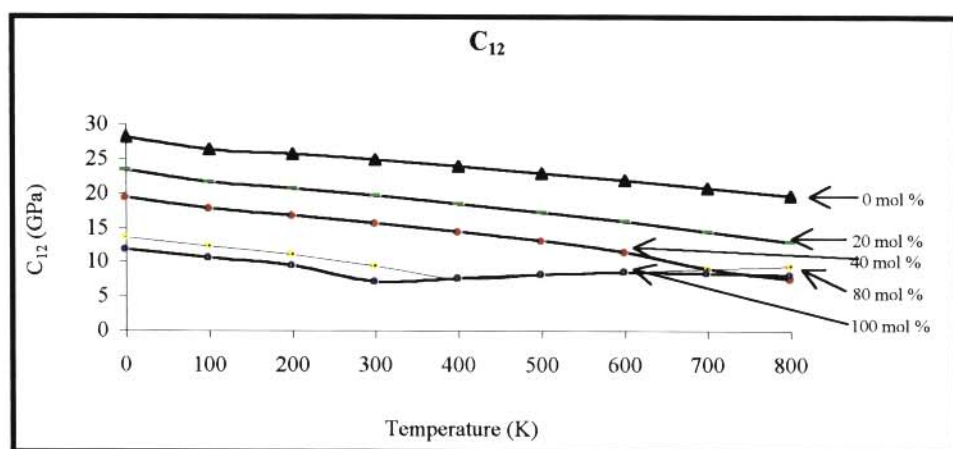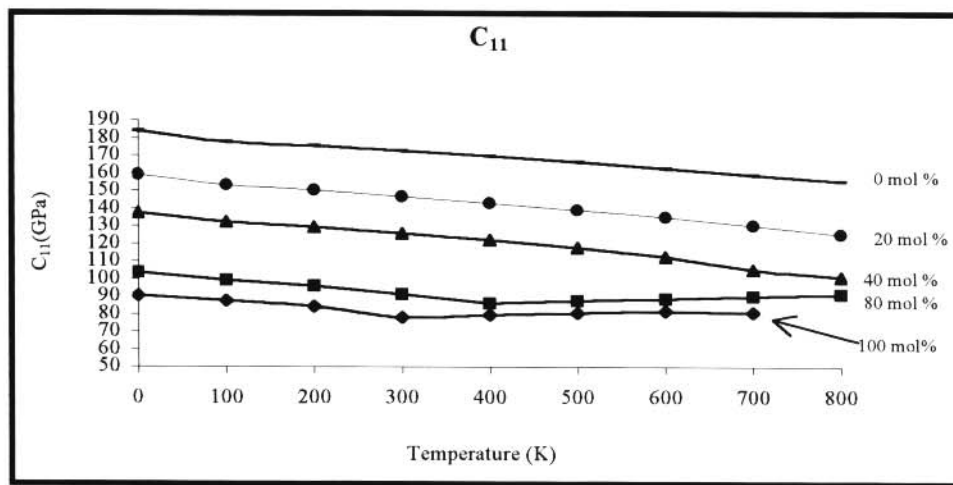
Figure 4.1(b) Temperature dependence of the elastic constants, C_{11}, C_{12} and C_{44} in $CdF_2(xPbF_2)$.

coefficients of these materials. Calculations on the temperature dependences of the second-order elastic constants C_{ij} are derived on the basis of the quasiharmonic approximation. In this part of the study the variations of thermodynamic quantities with temperature are discussed. Hence, extensive calculations on the temperature dependences of elastic moduli were carried out on Pb^{2+} dopant CdF_2 in the temperature range 77 - 800 K. These results were compared with observations from ionic conductivity experiments of Kosacki et al. (1989). Figure 4.1 (a) and (b) gives the temperature dependences of the three independent elastic constants C_{11}, C_{12} and C_{44} in various samples x. In the temperature range 77 - ~ 400 K (see Figure 4.1(a)), all three elastic constants (C_{11}, C_{12} and C_{44}) in mixed samples have the same characteristic temperature - dependent curves as for the pure compounds, i.e. the curves are smooth and show no anomally. This may be attributed to the similarity in the crystal structure throughout the compositions of the six-fluorite samples. In addition, these variations of C_{ij} with temperature in the temperature range 77 - ~ 400 K result from anharmoncity, where long-wavelength acoustical modes are dominant in the low temperature region (Catlow et al. 1978, Ngoepe 1987 and Chaba and Ngoepe 1999). Figure 4.1(a) also shows that the temperature variation of the elastic constants start to deviate from linearity at $x = 60$ mol % PbF_2 in the temperature range 400 – 800 K since the quasi-harmonic approximation does not fully account for changes noted in C_{ij}'s at high temperatures, in particular above T_c. The experimental value for T_c in CdF_2(60 mol % PbF_2) is ~ 485 K. The anomalous behaviour observed in this temperature region also coincides with the reported anomalies in ionic conductivity for the sample $x = 60$ mol % PbF_2 (Kosacki et al. 1989).

107

It is also apparent from Figure 4.1(a) that the elastic constant C_{11} is strongly dependent on temperature whereas the other two, namely, C_{12} and C_{44}, do not change significantly. The elastic constants in most pure fluorite-structured materials are known to exhibit similar features (see Netshisaulu 1996). However, the doped crystals have significantly smaller values of elastic constants than in pure CdF_2 suggesting corresponding reductions in the three elastic constants (C_{11}, C_{12} and C_{44}) with an increase in temperature as shown in Figure 4.1 (b). Furthermore, the temperature variations of C_{44} are smaller than those of other elastic constants.

Our results are in accord with previous reports on doped fluorites (e.g., Catlow et al. 1981, Ngoepe and Catlow 1991, etc.) that deviations from the linear anharmonic decrease occur at a significantly lower temperature than in pure crystals indicating that the transition temperature T_c is lower for doped crystals than for pure crystals, i.e. T_c moves to lower temperatures with increasing doping.

4.4.4 Effects of Concentration on Crystal Bulk Data

Static lattice calculations on fast-ion conductor $CdF_2(xPbF_2)$ in the entire composition range, i.e. from $x = 0$ to 100 mol %PbF_2, were conducted. Calculated and observed dielectric constants were plotted as a function of composition in Figure 4.2. Hence, in the absence of some experimental data, particularly the elastic constants, calculations on the $CdF_2(xPbF_2)$ mixed solid solutions were mainly validated from the experimentally determined behaviour of the static dielectric constant (ε_s) as a function of concentration x which was fairly reproduced by the present study. It was observed that
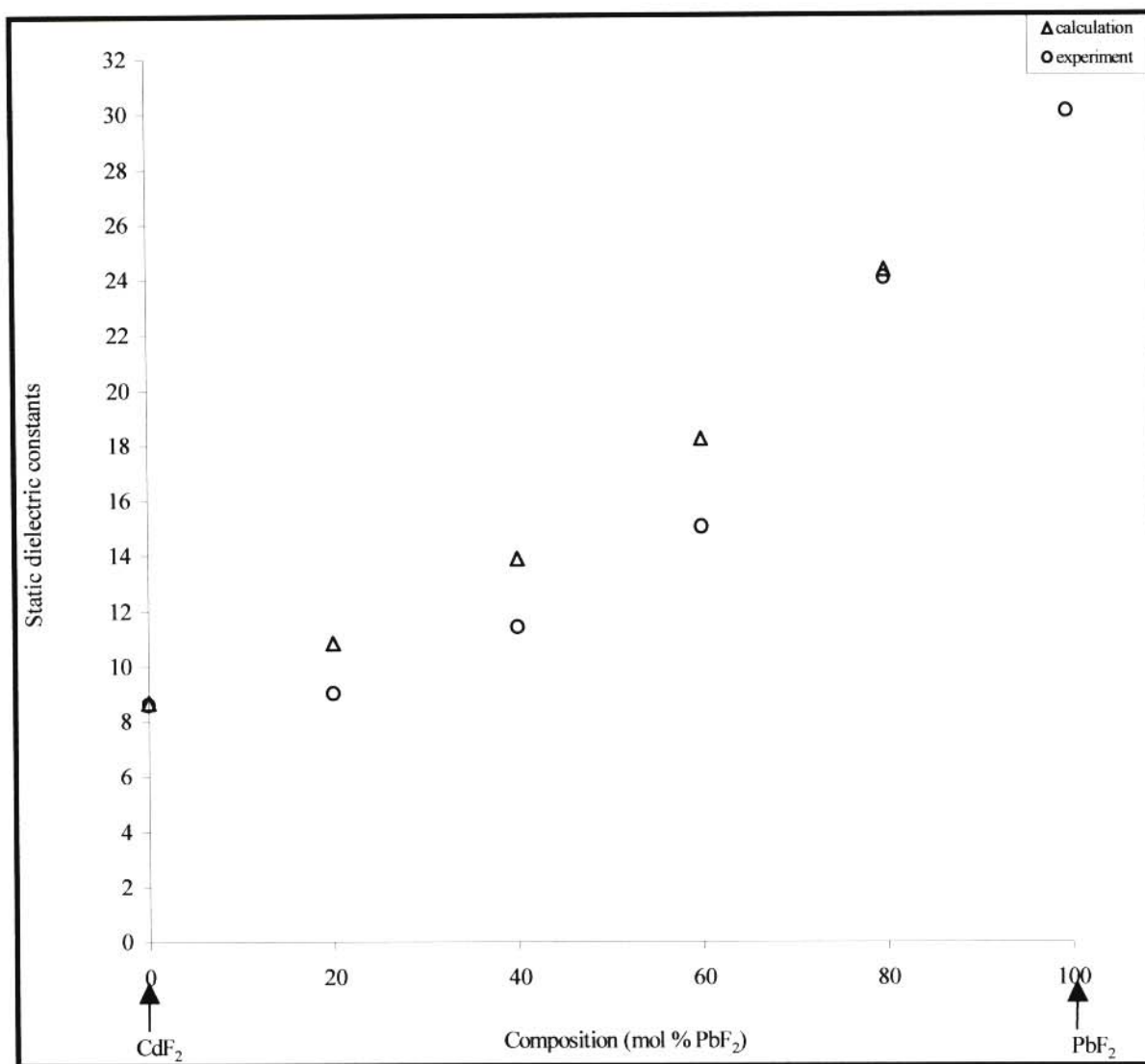
Figure 4.2 Comparison of the calculated and experimental values of the dielectric constants, ε_0, of CdF$_2$(xPbF$_2$) mixed crystals as a function of composition x.

ε_s increases when the mixed system changes from CdF_2 ($x=0$ mol % PbF_2) to PbF_2 ($x=100$ mol % PbF_2). Initially, i.e. for $x<60$ mol %, a steady increase in the dielectric constant, ε_s, with composition, x, is observed, whilst a linear increase is observed beyond $x=60$ mol % PbF_2. The curvature on ε_s vs. x plot commences just below $x=60$ mol % PbF_2. Furthermore, satisfactory reproduction of the experimental composition dependence of the dielectric constant is noted at values close to the end members (i.e. $x=0$ mol % PbF_2 and $x=100$ mol % PbF_2). This is attributable to the complex nature of the mixture in the region 40 mol % $\leq x \leq 80$ mol % PbF_2 and the large polarisablity of the lead ion in mixed-metal fluorites.

Plots of the variations of the elastic constants with composition are shown in Figure 4.3. The most obvious aspect of these plots is the linear decrease with increasing Pb composition x in all the elastic constants C_{ij} in the region between CdF_2 ($x=0$ mol % PbF_2) and PbF_2 ($x=60$ mol %PbF_2). However, all the elastic constants change less rapidly above 60 mol % PbF_2. This behaviour accords well with the composition dependence of the dielectric constant, where the curvature on ε_s vs. x plot commences just below $x = 60$ mol % PbF_2. An important feature of the results is the confirmation of the enhanced ionic conductivity at $x = 60$ mol % PbF_2 (see Kosacki et al. 1989). In addition, the lack of anomaly in the variation of the elastic coefficients C_{ij} with composition for the $CdF_2(xPbF_2)$

110

Figure 4.3 Compositional dependence of the elastic constants C_{ij} of $CdF_2(xPbF_2)$ mixed crystals.

111

crystals (Figure 4.3) is due to the fact that the mixture remains cubic phase (absence of phase transformation) throughout the entire composition and the variation in elastic constants is only due to the concentration of Pb in the mixed crystals (Gasanl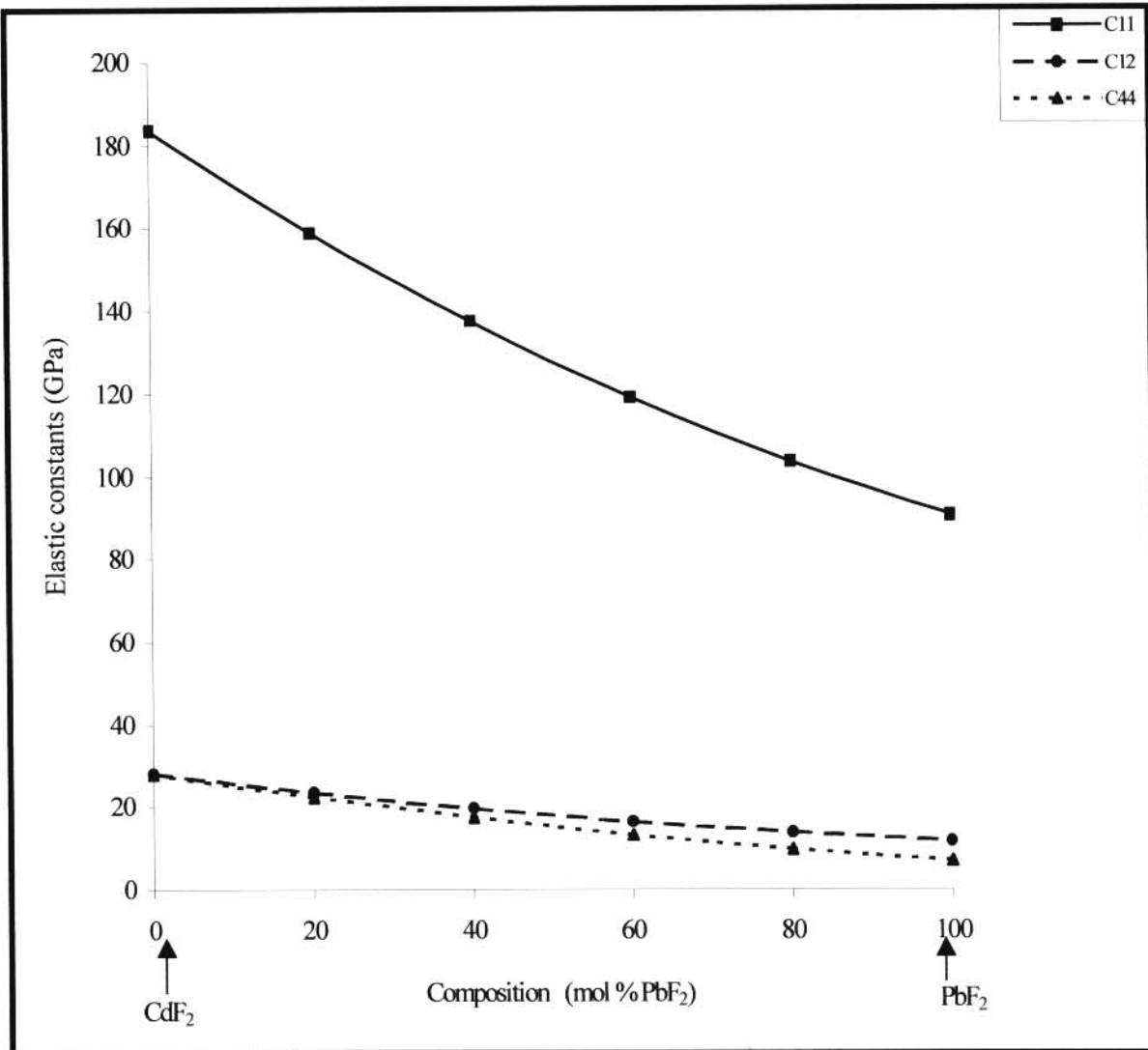y et al. 1993). Hence, the graph shows the usual tendency that elastic constants C_{ij} tend to decrease with increasing bond length. On the basis of changes noted in ε_0, it could be surmised that C_{ij} would correspond to experimental results.

4.4.5 Defect Formation and Migration Energies

We have used our model potentials (rigid-ion and shell) in the calculations of the defect energies for CdF_2 and PbF_2. The results are presented in Tables 4.5 and 4.6 (for pure fluorine ion conductors CdF_2 and PbF_2, respectively). Activation energies can shed some useful insights into the nature of the disorder in these superionic conductors. It can be seen from Table 4.5 that the calculated anion vacancy activation energy (~0.4 eV) for CdF_2, based on the shell model, is in reasonable agreement with the available experimental value of 0.44 eV obtained by Tan et al. (1970). In these calculations, migrating F^- ion in the saddle point is equidistant from two vacant fluorine lattice sites. The activation energy is calculated by subtracting the anion vacancy formation energy (initial configurations) from that of the saddle point/migration energy. This energy is linked to the motion of fluorine vacancies in CdF_2. Furthermore, the value of the anion interstitial activation energy (i.e. the activation energy for interstitial mobility) of 0.48 eV is more than that of the anion vacancy activation of 0.37 eV. This difference suggests that the vacancies are more mobile than interstitials in pure CdF_2. Hence, vacancy mechanism is a more prevalent mode of transport in CdF_2. This is in excellent agreement with the current understanding that for nominally pure fluorites the vacancy mechanism is more favoured,

112

whilst interstitial transport occurs only in the presence of suitable dopants (Catlow et al. 1977). This suggests that the predominant type of disorder is Frenkel disorder. The Frenkel energy is obtained by adding the values for the isolated anion vacancy formation and anion interstitial formation energies (see Table 4.5). It is, however, noted that the rigid ion model tends to underestimate the anion activation energy.

Table 4.5 Calculated defect formation and migration energies for CdF_2

Defect type	Model		
	Shell model (eV)	Rigid ion model (eV)	Experimental (eV)
Anion vacancy formation[†]	5.42	4.05	
Anion interstitial formation[‡]	-3.55	-1.80	
Anion Frenkel pair	0.87	2.25	
Anion vacancy migration (saddle point energy)	5.79	4.17	
Anion interstitial migration (saddle point energy)	-3.07	-1.47	
Anion vacancy activation	0.37	0.12	0.44[°]
Anion interstitial activation	0.48	0.33	

[†]Energy required to remove a lattice anion from the perfect (lattice) site to infinity
[‡]Energy required to introduce an interstitial anion from infinity into the perfect lattice (crystal).
[°]Experimental (Tan et al. 1970)

113

Table 4.6   Calculated defect formation and migration energies for PbF_2

Defect type	Rigid ion model (eV)	Shell model (eV)	Experimental (eV)[‡]
Anion vacancy formation	2.82	3.31	
Anion interstitial formation	-1.80	-2.02	
Anion Frenkel pair	1.02	1.29 (1.12)[†]	0.94
Anion vacancy migration	2.84		
Anion interstitial migration	-2.18		
Anion vacancy activation	0.02	0.235 (0.08)[†]	0.26
Anion interstitial activation	0.38	0.476 (0.08)[†]	0.52

[†]Theoretical estimates from Jacobs et al. (1984), where available, in brackets
[‡]Experimental estimates from Azimi et al. (1984)

In an analogous fashion, defect formation and migration energies for nominally pure PbF_2 were calculated using rigid ion potentials. These energies are presented in Table 4.6. The calculated values are compared with previous estimates and the available experimental data. The calculated anion Frenkel pair energy of 1.0 eV is in reasonable agreement with the experimental value of 0.94 eV. As can be seen, theoretical calculations of the defect energies are more difficult for PbF_2 due to problems in modelling the highly polarizable Pb^{2+} ion. The activation energy ($E_{act} \sim 0.02$ eV) is extremely underestimated by the rigid ion model for PbF_2, a phenomenon that was also observed by Walker et al (1985) ($E_{act} \sim 0.08$ eV). However, these values can be used qualitatively to predict the predominant type of disorder in PbF_2 as Frenkel disorder and the vacancy mechanism as the most favoured mode of migration.

4.4.6   Effects of Temperature on Mean Square Displacements (MSDs) of Ions

This part of the study was carried out using molecular dynamics method in order to investigate the effects of temperature on the mean square displacements (MSDs) of ions in mixed metal fluorites. MSDs plots are helpful in explaining the phenomenon of phase changes such as melting. This fundamental property is determined by choosing a particular F^- ion species and following it over a long period of time as it diffuses from site to site through the lattice. The MSDs are averaged over the particles in the system to reduce the statistical errors. Hence, MSDs is the property of the whole sample rather than individual species. As indicated in equation 2.2, the relationship strictly holds only for the limit as $t \rightarrow \infty$ (so not applicable for short times). This relationship can thus be used to calculate the diffusion coefficients from an equilibrium simulation by plotting the MSDs as a function of time and then attempting to obtain the limiting behaviour as $t \rightarrow \infty$.

In the present study, the simulation runs were made on mixed metal fluorites at temperatures ranging from liquid nitrogen temperature 77 to 700 K. Plots for the variation of MSDs with time for F^- ion species in CdF_2 ($xPbF_2$) mixed solutions are indicated in Figure 4.4. These plots show that diffusion is negligible at liquid nitrogen temperatures. Linear variation of MSDs with t implies diffusion of fluorine ions in mixed metal fluorites, in particular, for concentrations $x = 40$ mol % to 100 mol % PbF_2 at 700 K. The rapid diffusion of the F^- ions is in accordance with the general understanding that smaller ions are expected to diffuse more easily through materials. A similar behaviour is found in other solid electrolytes such as Y/ZrO_2 (Petrolekas and Metcalfe 1995, Chaba and Ngoepe 1998), a number of perovskite-type oxides such as $LaMnO_3$ and $LaCoO_3$ (Islam et al. 1996), fluoride

perovskites (Watson et al. 1992) and most mixed metal fluorites (e.g. RbBiF$_4$) (Cox et al. 1994). However, for concentrations $x = 0$ mol % PbF$_2$ and $x = 20$ mol % PbF$_2$, no fast-ion conduction is predicted at T=700 K, indicated by a constant MSD with time. This observation indicates that the transition temperatures for samples $x = 0$ mol % PbF$_2$ and $x = 20$ mol % PbF$_2$ are well above T = 700 K, a result which is in excellent agreement with our previous results (Netshisaulu, 1996) on the transition temperature T$_c$ of pure CdF$_2$ [T$_c$ (CdF$_2$) ~ 1000 K]. T$_c$ for CdF$_2$ is also well reproduced by our current study (see Figure 4.4 for the diffusion trends in pure CdF$_2$, i.e. $x = 0$ mol % PbF$_2$) and that for CdF$_2$(20 mol %PbF$_2$) is ~ 800 K (see Kosacki et al. 1989). These results also show that the well-documented transition temperature to the fast-ion phase of PbF$_2$ is well above 600 K (i.e. T$_c$(PbF$_2$)>600 K). The transition temperature, T$_c$, for PbF$_2$ is ~ 700 K (see Samara 1978, Dickens and Hutchings 1978, Kosacki et al. 1989, etc). Hence, substantial fluorine diffusion in mixed-metal fluorites takes place below the transition temperature of pure CdF$_2$, which is about 1000 K. In contrast, no diffusion of cation species (both Pb^{2+} and Cd^{2+}ion species) takes place, even at 700 K (see Figures 4.5 and 4.6), indicating that the material is below its melting point since the crystal is considered to have melted when all sub-lattice show an increase in MSDs with time.

Figure 4.4 Mean square displacements of fluorine ions at different temperatures for concentrations x = 0 mol % PbF$_2$ - 40 mol % PbF$_2$.

Figure 4.4 Mean square displacements of fluorine ions at different temperatures for concentrations x = 60 mol % - 100 mol % PbF$_2$.

118

Figure 4.5 Mean square displacements of Cd ions at different temperatures for concentrations $x =$ 0 mol % PbF$_2$, $x =$ 60 mol % PbF$_2$ and $x =$ 80 mol % PbF$_2$.
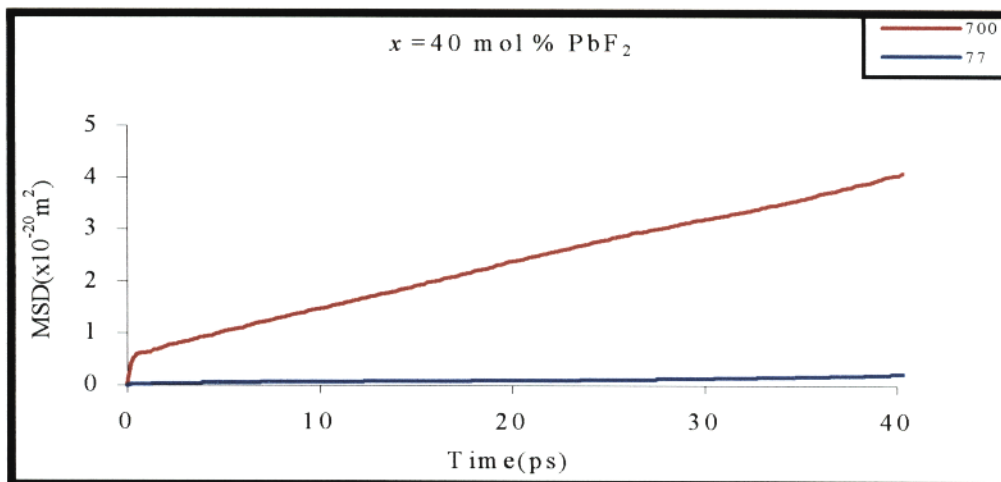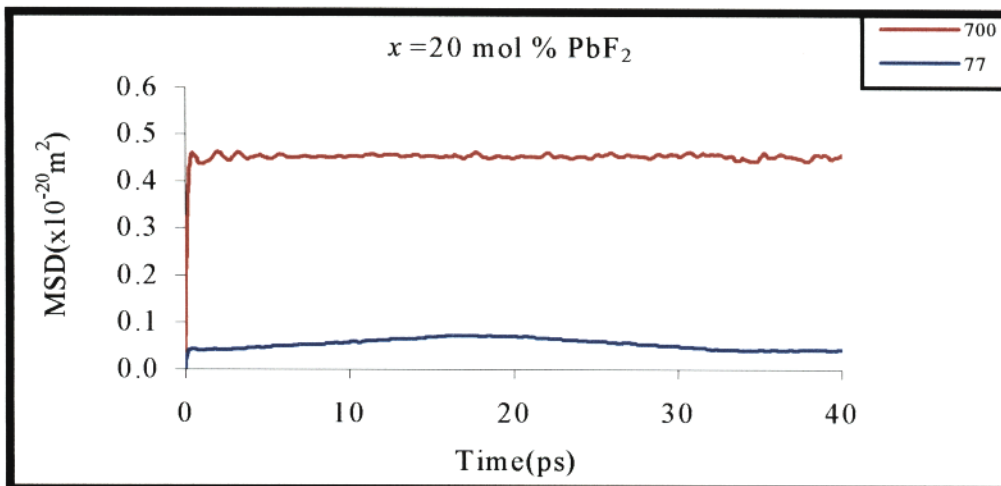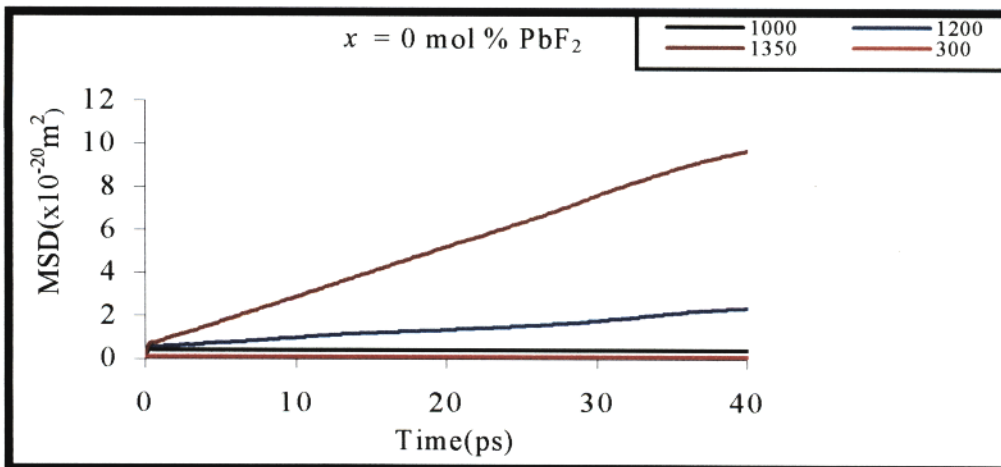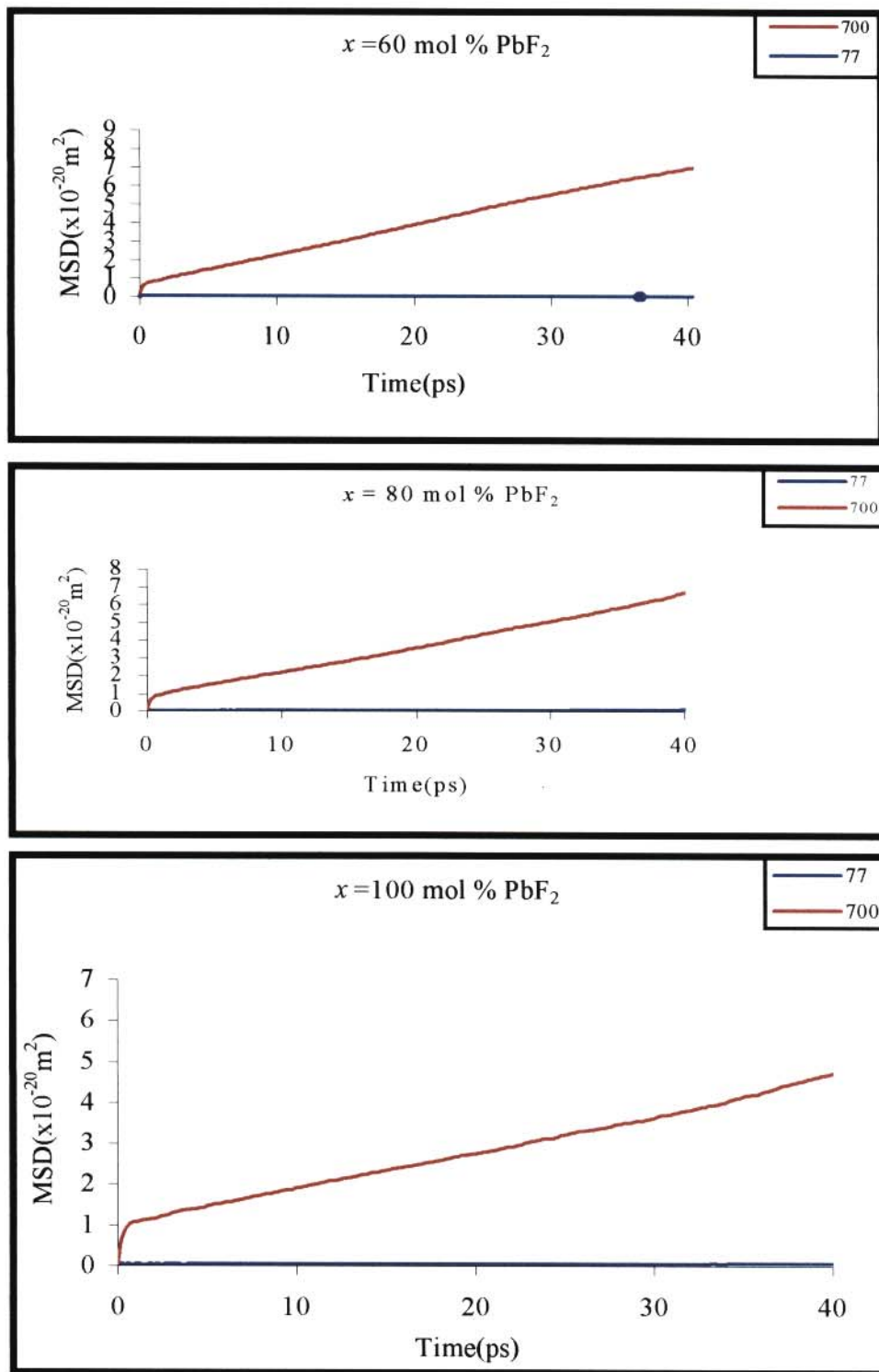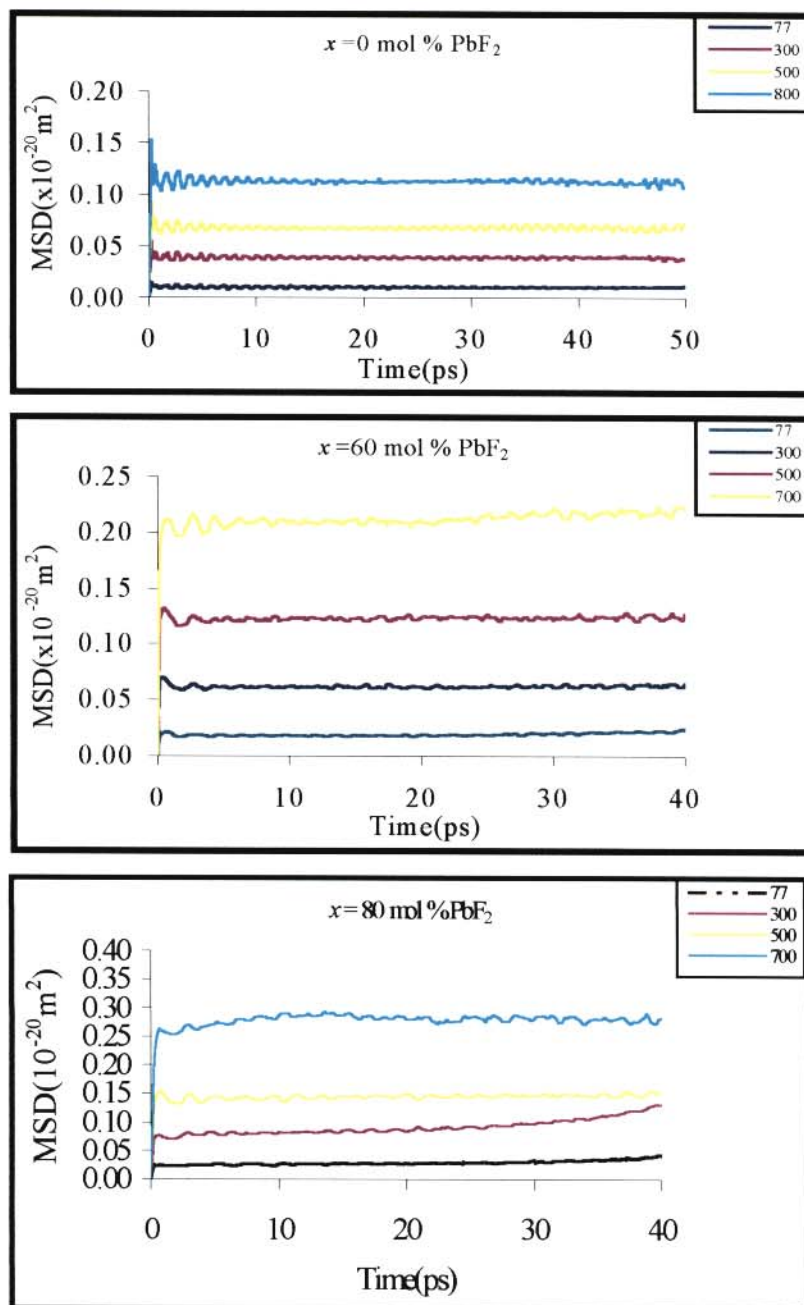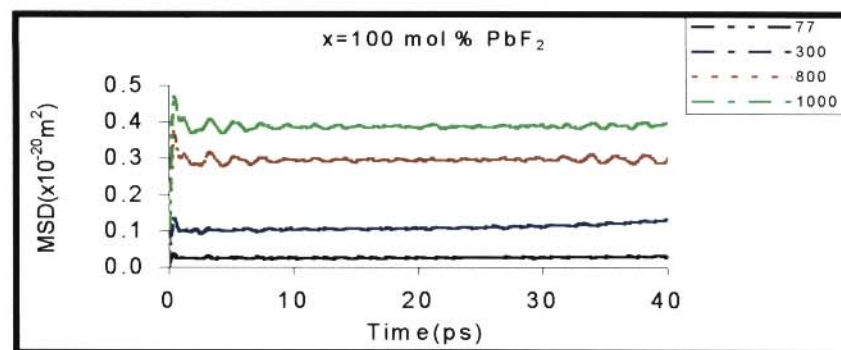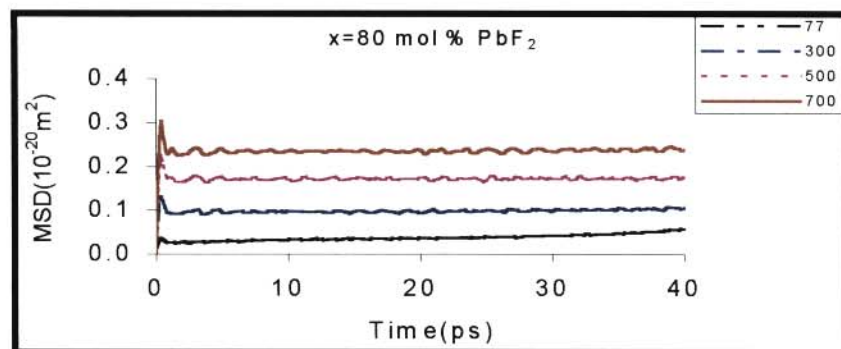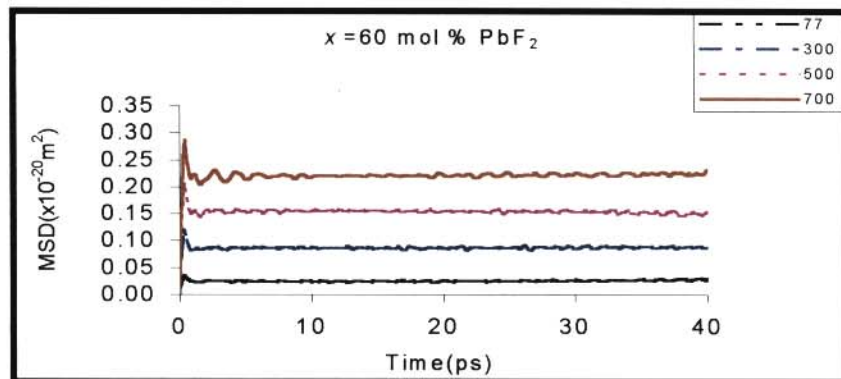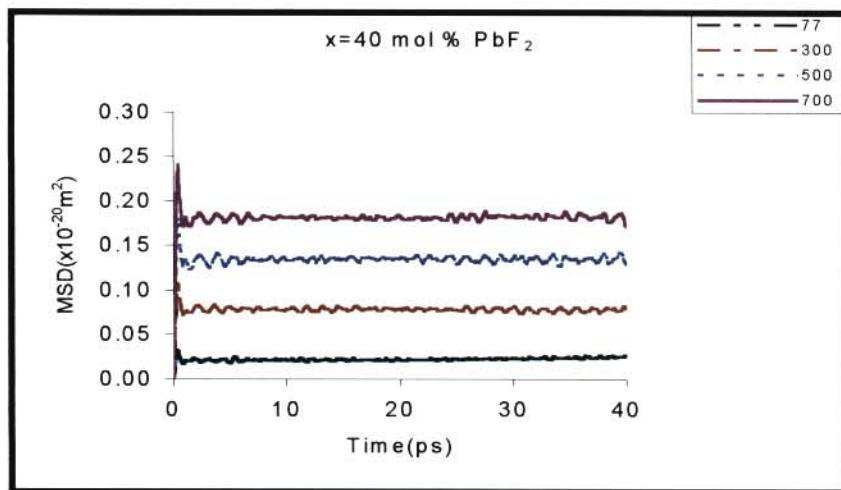
Figure 4.6 Mean square displacements of Pb   ions at different temperatures for concentrations x=0 mol % -100 mol % PbF$_2$.

120

Hence, the presence of the fast-ion phase in mixed metal fluorites is achieved even before the crystal actually melts. A similar behaviour was noted in oxygen (Li and Hafskjold 1995, Khan et al. 1998 and Chaba 2000) and fluorine ion conductors (Netshisaulu et al. 1999) from MD studies.

4.4.7   Effects of Composition on MSDs

MSDs versus time for all dopant concentrations (the six models) at 700 K are presented in Figure 4.7. It is clear from Figure 4.4 that, on the one hand, at low concentrations (i.e. at $x = 0$ mol % PbF_2 – 20 mol % PbF_2 with T = 700 K), no fast-ion conduction is predicted, indicated by a constant MSD with time. Furthermore, the asymptotic time dependence of this quantity, MSDs, in this composition range ($x = 0$ mol % PbF_2 – 20 mol % PbF_2) shows that $D_i = 0$ (diffusion virtually ceases) for anions at T= 700 K. On the other hand, fast-ion conduction is evident through the mobility of the fluorine anions at temperature T=700 K for $x = 40$ mol % PbF_2 – 100 mol % PbF_2. It is interesting to note that the highest value of diffusion is observed on the anion sub-lattice at the composition $x = 60$ mol % PbF_2. However, the diffusion decreases to below that of the $x = 60$ mol % composition for $x \geq 80$ mol % PbF_2. Furthermore, in all solid solutions the cations do not diffuse with increasing concentration x (see Figures 4.5 and 4.6). These cations simply oscillate in the vicinity of the tetrahedral sites. Hence, the fluorite structure is maintained as the system evolves from CdF_2 to PbF_2, with the role of the cation sub-lattice being to maintain long-range order of the materials.
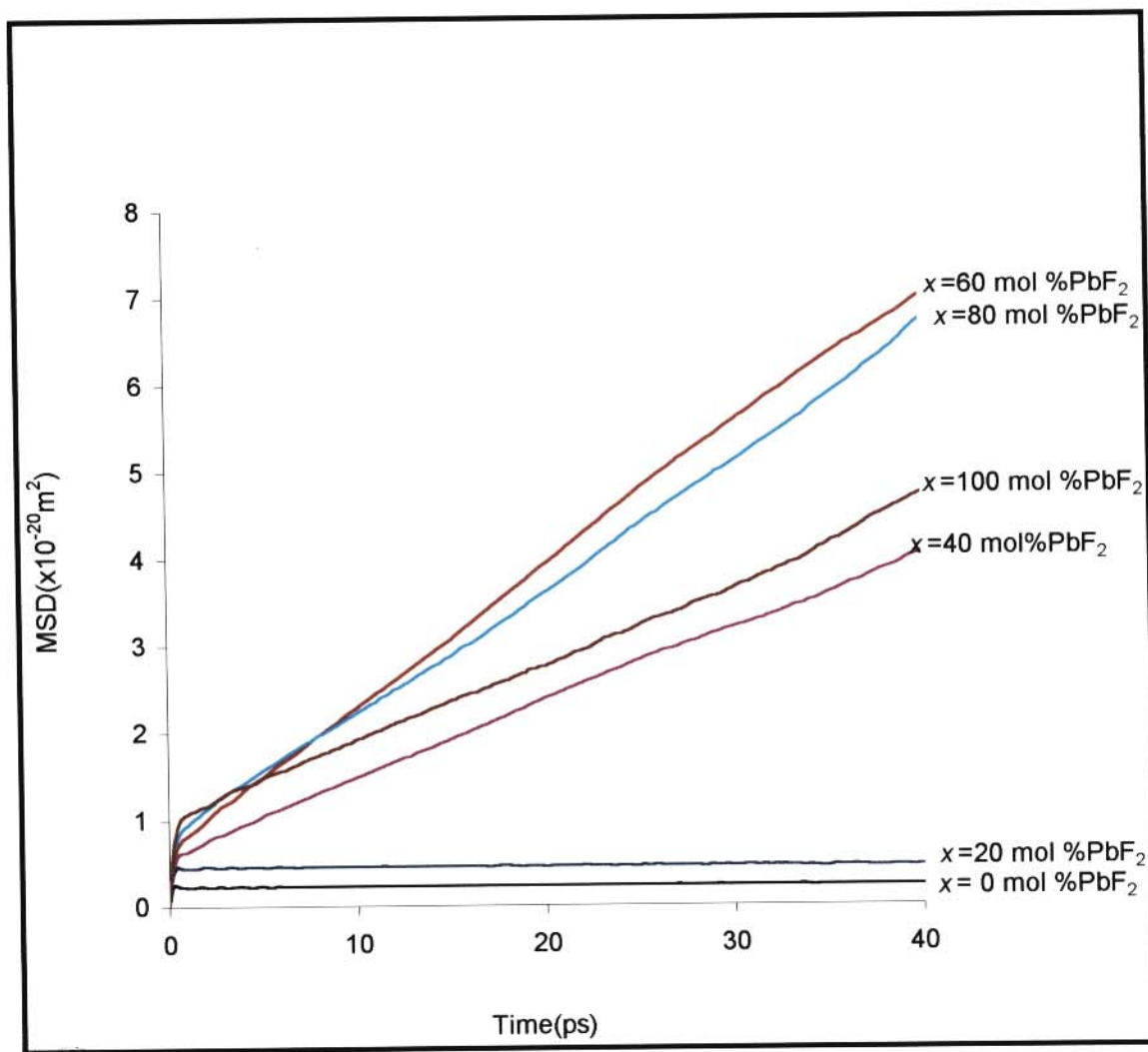
Figure 4.7 Mean square displacements of fluorine ions for various concentrations of PbF$_2$ in CdF$_2$(xPbF$_2$) mixed crystals at T = 700 K.

4.4.8   Effects of Temperature on Transport Properties

The present investigation aims to provide additional data on the ionic conduction of $CdF_2(xPbF_2)$ mixed solid solutions. It is generally known that mixed solid solutions are highly conducting, but they have considerably lower superionic transition temperatures than those of the pure compounds (Kosacki et al. 1989). The self-diffusion constant D_i of the F^- ions is obtained from the slope of the MSDs ($<r^2(t)>$) – time line using equation 4.1.

In the current study, anion diffusion coefficients were extracted from the plots of the MSDs (see Figure 4.4) in the temperature range 77 to 800K. The calculated results are presented in Table 4.7. From the profiles of the anion diffusion coefficients (see Figure 4.8), there is no diffusion until a certain temperature, T_c, is reached.

It is assumed that diffusion and conductivity are manifestations of the same migration process so that the two physical properties are closely related (see Chapter 1.6). Hence, from the profile of the diffusion coefficients, it is possible to use the Nernst-Einstein relation to make the connection between diffusion and conductivity for a single conduction mechanism and to estimate the magnitude of the ionic conductivity. The Nernst-Einstein relation shows that the diffusion coefficient is proportional to the ionic conductivity.

Hence,

$$\sigma = \left(\frac{nq^2}{fkT}\right)D_i$$ 4.1

Table 4.7 Calculated fluorine diffusion coefficients for specimens x = 0 mol % - 100 mol % PbF$_2$ in CdF$_2$(xPbF$_2$) mixed crystals.

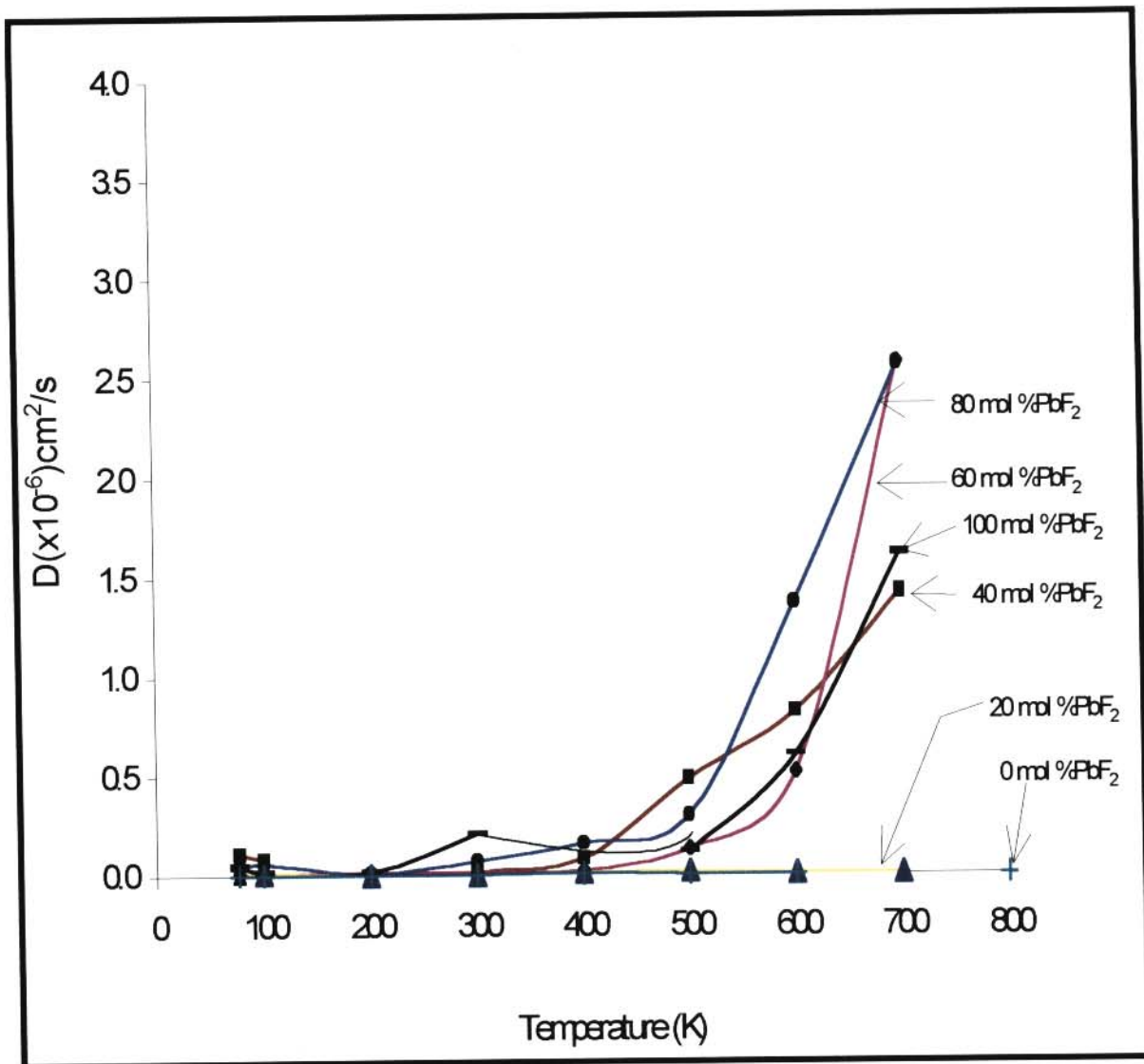| Temperature	D_f x 10^{-9} (cm^2/s) for each composition x (mol % PbF$_2$)					
T(K)	0	20	40	60	80	100
77	0.459	-	10.8	10.8	48.3	46.2
100	-	9.67	8.21	3.22	58.1	14.9
200	0.267	2.35	-	13.6	10	14.9
300	0.645	1.03	14.3	18.1	70.3	206
400	0.559	12.5	81.6	21.7	159	-
500	1.44	14.7	482	13.0	300	116
600	1.40	6.03	818	513	1370	605
700	-	4.97	1420	2580	2570	1620

Figure 4.8 Variation of the fluorine diffusion coefficients of $CdF_2(xPbF_2)$ mixed systems with temperature.

where k is the Boltzmann's constant in eV, q is the charge of the carrier ion, T is the absolute temperature, n is the number of charge carriers per unit volume (density) or simply the concentration of charge carriers and f is the correlation factor (where f is equal to or less than 1) that depends on the type of diffusion mechanism. In the present study the conductivity was calculated from the diffusion coefficients via the Nernst-Einstein relationship by setting f to unity (1) since the main goal of this study is to establish the order of magnitude of diffusion or conductivity as recommended by Watson et al. (1992). The relation in the equation above is only expected to hold accurately when both mass transport (diffusion) and charge transport (conductivity) are effected by the same physical mechanism. Furthermore, in the present work, only anion species, i.e. the fluorine ions, were assumed to participate in both the mass transport and charge transport as shown in the earlier sections above.

The variation of ionic conductivity with temperature and composition is the key to understanding transport phenomena in mixed solid solutions. Hence, we have presented in Figure 4.9 the temperature dependence of the conductivity [$\ell n\,(\sigma T)$ against T^{-1} plot] for several compositions of the $CdF_2(xPbF_2)$ solid solutions. It can be seen that the conductivity of these mixed solutions increases in the temperature range covered upon the incorporation of PbF_2. The conductivity curves observed correspond to an Arrhenius-type law, i.e. the usual conductivity plot of $\ell n\,(\sigma T)$ against T^{-1} is linear. This trend is typical of most of the mixed metal fluorites (Cox et al. 1994). In the present study conduction models are based on random distributions of lead (Pb) cations and it is assumed that transport is effected through the bulk of the solid with the mixed crystals containing one kind of mobile charge carriers, i.e. F species, which leads to a disordering on the anion sub-lattice of these
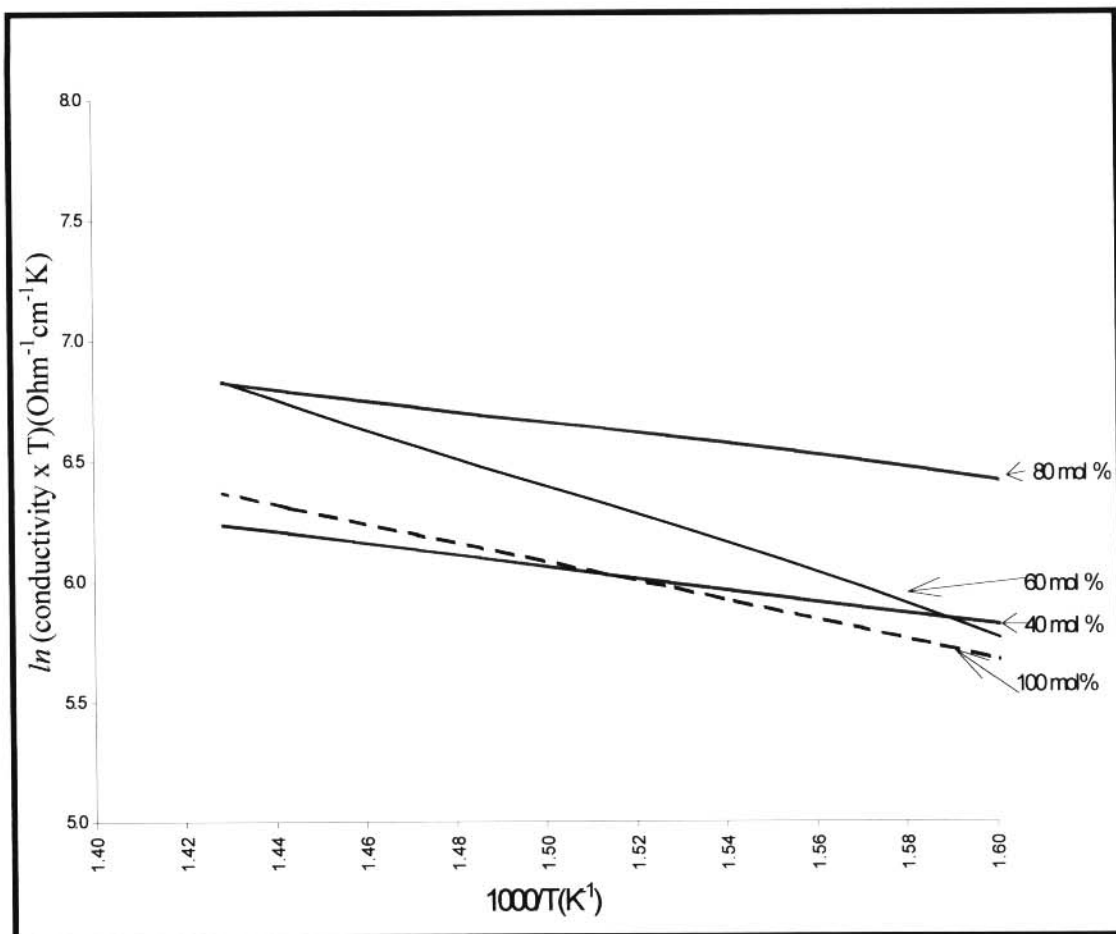
Figure 4.9 Arrhenius plots [ℓn (σT) versus T^{-1}] for samples x = 40 – 100 mol % PbF$_2$ in CdF$_2$(xPbF$_2$) systems.

solid solutions. The cations provide the immobile 'lattice' through which the mobile F^- ions can migrate. It is clear from Figure 4.9 that doped samples had conductivities with values higher than those of the pure ones throughout the temperature range covered (curves for samples $x \leq 40$ mol % PbF_2 are excluded for clarity purposes). Comparing the different materials in Figure 4.9, the slope corresponding to sample $x = 60$ mol % PbF_2 is the steepest. In addition, qualitatively, the trend in the temperature variation of conductivity in the $CdF_2(xPbF_2)$ crystals is similar to those observed in related mixed metal fluorites such as $RbBiF_4$ sand $PbSnF_4$ (Catlow et al.1989 and Cox et al. 1994).

The activation energy has been derived from the Arrhenius-Einstein equation, which relates the ionic conductivity to activation energy E_a:

$$\sigma T = \sigma_0 \exp\left(\frac{-E_a}{kT}\right) \qquad\qquad 4.2$$

Taking ℓn on both sides,

$$\ell n(\sigma T) = \text{constant} - \left(\frac{E_a}{k}\right)\left(\frac{1}{T}\right) \qquad\qquad 4.3$$

Hence

$$E_a = -kT\ell n(\sigma T) \qquad\qquad 4.4$$

where E_a is the activation/ Arrhenius energy for conduction in eV derived from the gradient of the slopes of the conductivity versus the reciprocal temperature (T^{-1}) curves. The plot of $\ell n(\sigma T)$ versus T^{-1} normally yields a straight line with the gradient equal to $-\left(\dfrac{E_a}{k}\right)$. Activation energy is the energy required to overcome a 'barrier' to diffusive motion.

4.4.9 Correlation between ionic conductivity, concentration and activation energy

In this section, we examine the correlation between ionic conductivity (σ), dopant concentration x and activation energy (E_a) in $CdF_2(xPbF_2)$ samples. The variation of ionic conductivity with Pb content x is shown in Figure 4.10(a) for the temperature $T = 700$ K. Experimentally (Kosacki et al. 1989) determined pattern is also shown in Figure 4.10(c). Figure 4.10(a) indicates that incorporation of Pb ions on cadmium (Cd) sites increases the ionic conductivity until a certain dopant level is reached. In essence, the effect on conductivity of varying composition (Pb content) in the $CdF_2(xPbF_2)$ systems leads to a conductivity increase in the composition range 0 mol %$\leq x \leq$60 mol % PbF_2 (in line with the general understanding that diffusion of ions can be accelerated enormously by impurities), whereas for 80 mol %$\leq x \leq$100 mol % PbF_2 the conductivity starts to decrease upon increasing Pb content x. In an earlier work on polymer electrolytes by Bhattacharyya et al. (1999),

129
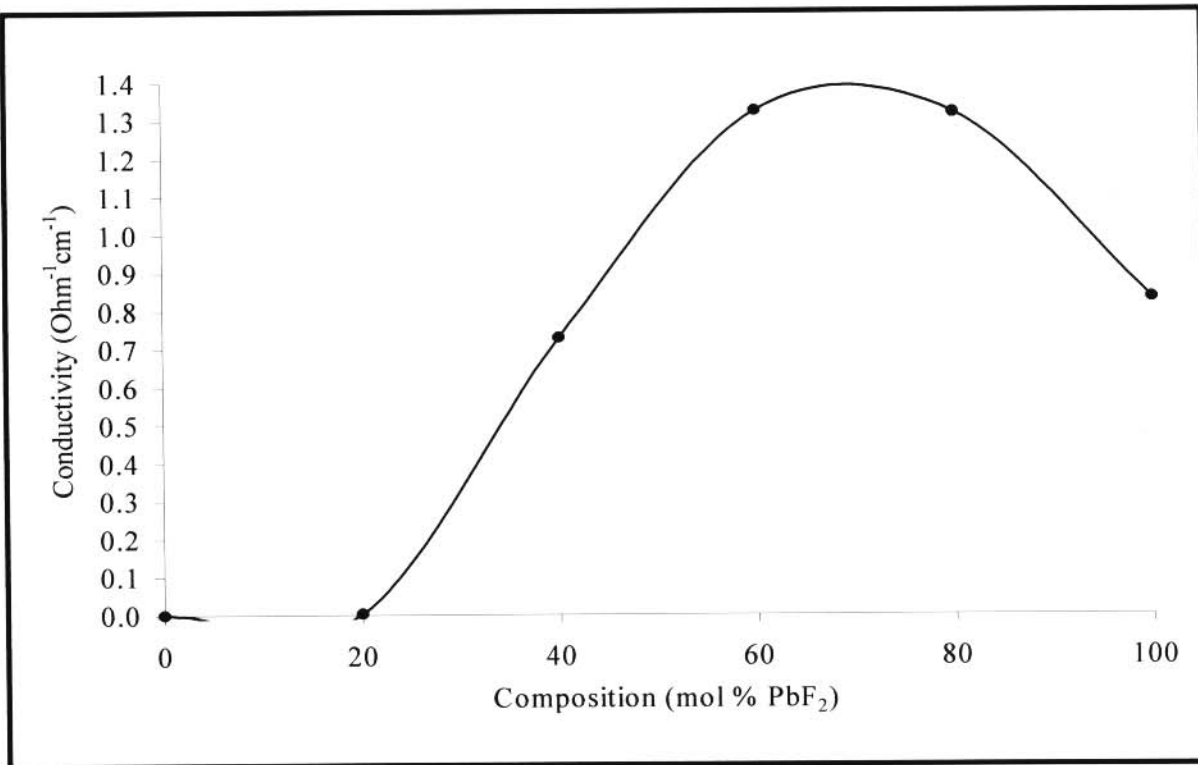
Figure 4.10 (a) Composition dependence of the ionic conductivity in $CdF_2(xPbF_2)$ systems at T = 700 K.
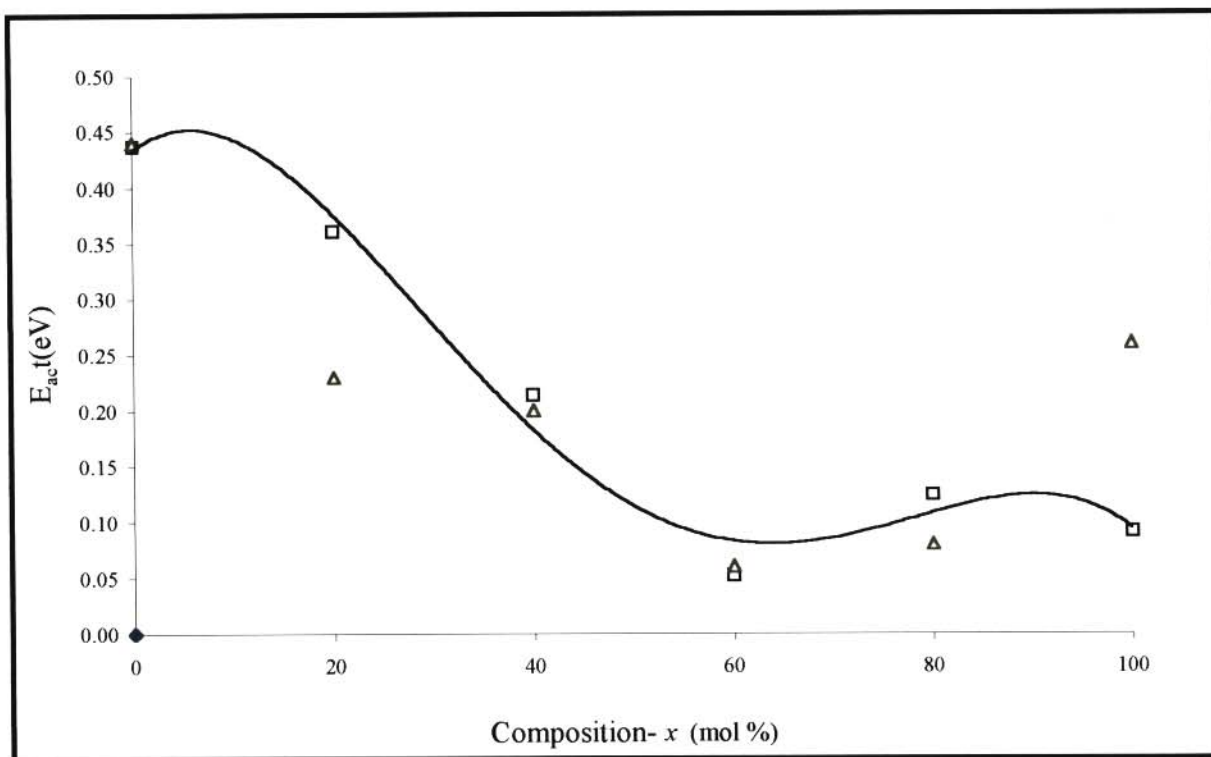
Figure 4.10(b) Composition dependence of activation energy E_{act} in CdF_2-PbF_2 systems. (□: E_{act} from this work; Δ: E_{act} from ionic conductivity measurements (Kosacki et al.'s (1989))
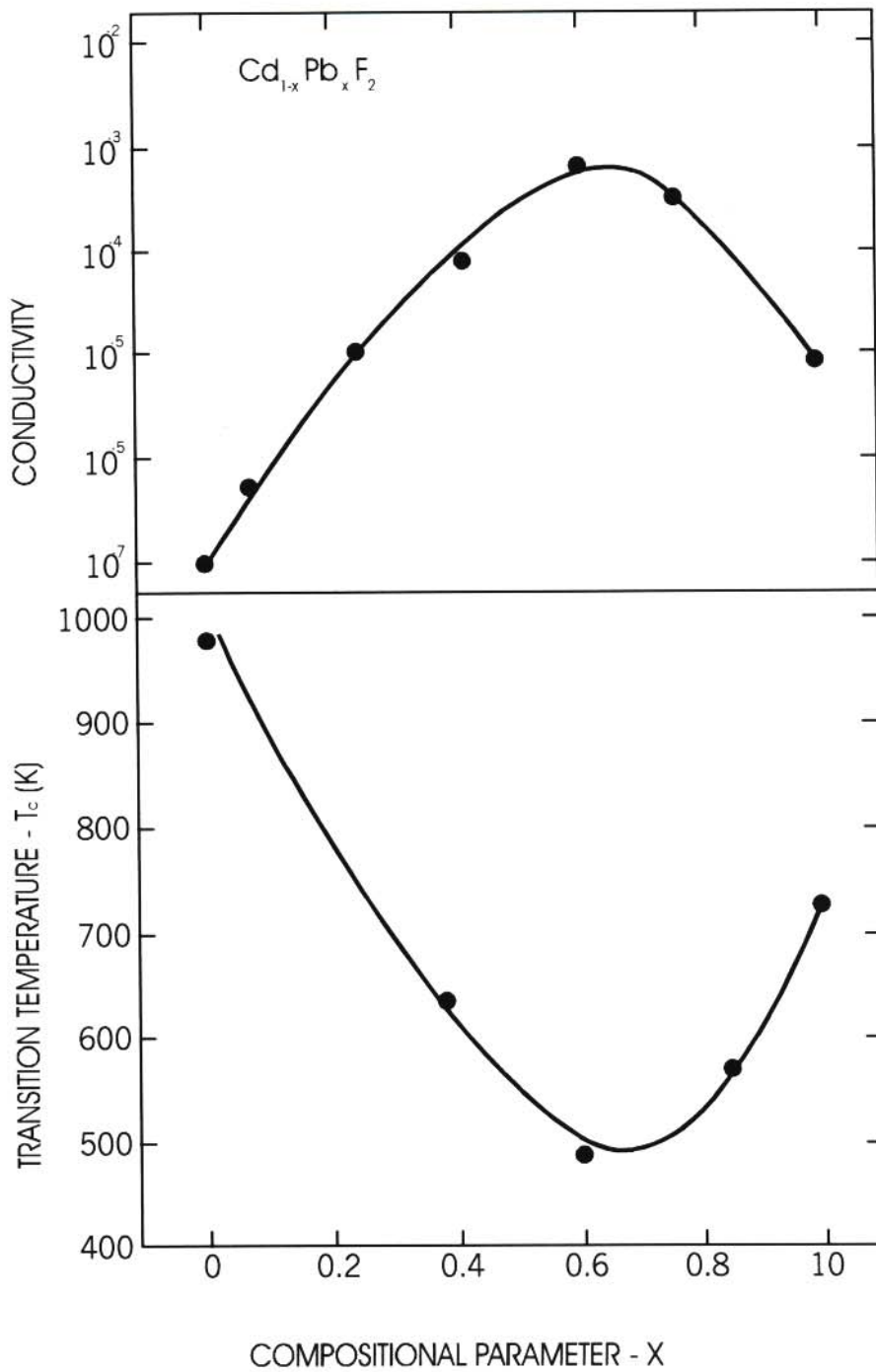
Figure 4.10(c). The compositional dependence of the ionic conductivity and the superionic state transition temperature (T_c) for $CdF_2(xPbF_2)$ crystals (after Kosacki et al. 1989)

131

it was indicated that the initial rise in σ is due to an increase in concentration of charge carriers and the subsequent fall is due to a decrease in their mobility. A notable feature found in the calculation of conductivity is that there is a maximum (peak) in the plot of ionic conductivity versus dopant concentration which occurs at ~ 60 mol % dopant concentration of PbF_2 (see Figure 4.10(a)). This is in reasonable agreement with the composition dependence of the calculated diffusion constant and the experimental σ measurements from Kosacki (1989) et al.'s work (see Figure 4.10(c)). Associated with this enhancement in conductivity for the 60 mol % sample is a reduction in the activation energy for conduction, with the maximum in conductivity corresponding to a minimum (dip) activation energy E_a (see Figure 4.10 (b)). Hence, the conductivity is much higher and the activation energy much lower for the same PbF_2 substitution rates/values of x at T=700 K. Furthermore, Figure 4.10(b) shows there is reasonable agreement between calculated and experimental results for the activation energies.

The exceptional high ionic conductivities and relatively low activation energies in these systems have been found in other mixed cation fluorite structured compounds with a definite composition, e.g. $PbSnF_4$ and $RbBiF_4$ (Catlow et al. 1989 and Cox et al. 1994). In essence, the present study provides evidence that when the Pb content x is less than 60 mol %, migration of F^- ions (from lattice (normal) positions into interstitial ones increases. In this case, F^- ions are easily transferred into interstitial sites from their normal (anionic) sublattices surrounding which there is a local excess of Pb^{2+}. This (process) leads to the creation of supplementary vacancies in the anionic lattice positions. The Cd cations enhance σ by preserving the open-nature of the fluorite. This helps to retain the pathway/route for migration via interstitial sites. Experimental evidence for this proposal has been

132

obtained from EXAFS studies on $RbBiF_4$ by Cox (1988). However, our results also show that the conductivity decreases tremendously after the maximum at $x = 60$ mol % PbF_2 concentration. Thus, for higher concentrations, the migration of fluorine interstitials decreases resulting in a diffusion coefficient decreasing. Alternatively, this decrease in conductivity with dopant concentration at concentration levels beyond $\sim x = 60$ mol % PbF_2 (i.e. for 60 mol %$<x<$100 mol % PbF_2) doping level is attributed to fluorine jumps becoming decreasingly effective in causing bulk ionic conductivity. In this case the fluorine ions increasingly perform 'ineffectively' since they simply oscillate/percolate around an interstitial position. This could be an indication of the presence of extensive short-range order of local ordering which suggests a strengthening of the Cd-F / Pb-F bonding.

The calculated activation energies together with the values derived from ionic conductivity measurements by Kosacki and co-workers (Kosacki et al. 1989) for each concentration formed between CdF_2 and PbF_2 are presented in Table 4.8 (also see Figure 10(b)). The calculated energies compare reasonably well with their observed values. In addition, examination of the table shows that 0.051 eV is the lowest activation energy E_{act} at $x = 60$ mol % PbF_2 and corresponds with the maximum ionic conductivity. The apparent low activation energy (for conduction) for the mixed crystal at $x=60$ mol % PbF_2 clearly indicates a rapid mobility through the bulk. The occurrence of such high ionic conductivities also suggests that the structural properties of the materials and the ion migration mechanisms may show unusual features. This improvement in conduction suggests that the $x = 60$ mol % sample may have randomly disordered structure. Similar dependences of ionic conductivities on dopant content in related materials were also seen (see for example Catlow et al. 1989 and Bhattacharyya et al. 1999).

133

Table 4.8 Calculated and experimental activation energies for specimens $x = 0$ mol % PbF_2, $x = 20$ mol % PbF_2 and $x = 40$ mol % PbF_2, $x = 60$ mol % PbF_2, $x = 80$ mol % PbF_2 and $x = 100$ mol % PbF_2 at T= 400 K and T = 700 K.

	Activation energy (eV)	
Composition x (mol % PbF_2)	Calculated	Experimental
0	0.437	0.44[‡]
20	0.360	0.23[±]
40	0.214	0.2[±]
60	0.051	0.06[±]
80	0.124	0.08[±]
100	0.091	0.26[†]

[‡]Tan et al. (1970)
[†]Azimi et al. (1984)
[±]Kosacki et al. (1989)

The activation energies for the solid solutions shown in Table 4.8 decrease with increasing Pb content x. The current calculations qualitatively reproduce the main features observed experimentally, in particular the observed maximum in the conductivity at $\sim x = 60$ mol % PbF_2 which corresponds to the lowest activation energy E_a. Kosacki et al. (1989) observed a strong non-linear dependence of the superionic transition temperature on mixed metal fluorites, with a minimum occurring at $T_c = 485$ K which corresponds with the $x = 60$ mol % PbF_2. In fact, in the PbF_2 concentration range of 60 mol %$\leq x \leq$100 mol %, there is an increase of the temperature of the transition to the superionic state (T_c). In contrast, in the composition range of 0 mol %$\leq x \leq$60 mol % PbF_2, a decrease of the transition temperature has been observed. The dependence obtained is directly related to similar dependences seen in the ionic transport results and the Raman line half-width (Kosacki et al. 1989).

4.4.10 Combined Effects of Temperature and Concentration on Radial Distribution Functions

In this section, several molecular dynamics studies have been undertaken in order to understand the effect of composition and temperature on structural properties, in particular, radial distribution functions (RDFs) of $CdF_2(xPbF_2)$. These studies were performed on $x = 0$ mol %, 20 mol %, 40 mol %, 60 mol %, 80 mol % and 100 mol % PbF_2 concentrations at various temperatures, i.e. for $T = 77$, 300, 500, 600 and 700 K. However, in this work, results for $T = 77$, 300, and 700 K are presented.

RDFs give the probability of finding ions of a certain species in a particular region of the crystal at a given distance away from a point of reference or even as a function of distance from one species to another. It also provides information about the spatial distribution of the ions and their environments in a shell fashion (see equation 2.1 in Chapter 2). Hence, the degree/nature of (dis)order on the local structure of species in the system could be determined.

The intention of this section is to probe the degree of (dis)order on the Pb, Cd and F sublattices in doped $CdF_2(xPbF_2)$ crystals, and to clarify its nature. Calculations of the RDFs were performed for the entire concentration range of the solid solution, i.e. for compositions $x = 0$ mol % to $x = 100$ mol % PbF_2. First, we consider the RDFs for the two cations, namely, Cd^{2+} ion and Pb^{2-} ion for the whole composition range, i.e. $x = 0$ mol % to $x = 100$ mol %, followed by the $F^- - F^-$ RDFs.

135

4.4.10.1 RDFs of the cations (g(Cd-Cd) and g(Pb-Pb))

The curves for the two cations (g(Cd-Cd) and g(Pb-Pb)), in the whole concentration range $x = 0$ mol % PbF_2 to $x = 100$ mol % PbF_2, at temperature T = 700 K, are calculated and presented in Figures 4.11 and 4.12, respectively. These structures reveal a series of well-defined peaks corresponding to successive nearest-neighbour distances (positions of the first peaks) of the regular lattice, i.e. like that of a normal solid (Islam et al. 1996). The peaks are strongly peaked such that they fall to approximately zero in between. Hence, the cation RDFs of all systems reveal that the extensive long-range order is preserved. The peak intensity increases with composition x for the Cd-Cd peaks and decreases with composition for the Pb-Pb peaks (see Table 4.9). In addition, in all compositions, the distances between the cations (i.e. Cd-Cd and Pb-Pb distances) are greater than the F-F distances/separations (see Table 4.10).

4.4.10.2 RDFs of fluorine ions (g(F-F))

The F-F RDFs for the six compositions at temperature T = 700 K are shown in Figure 4.13. At low PbF_2 concentrations ($x < 20$ mol % PbF_2), the F-F RDF curves are sharply peaked, i.e. they show more structure. With increasing PbF_2 content, the F-F RDF curves become less structured, and the height of all the first peaks are reduced. The F-F RDF curves, for the systems $x > 20$ mol % PbF_2, simulated at T=300 to T=700 K, show that the degree of disorder (shown by decreases in height and broadening of the first peaks) was found to increase with increasing temperature and the locations of the peaks also change with temperature (see Table 4.10). This is also accompanied by the loss of
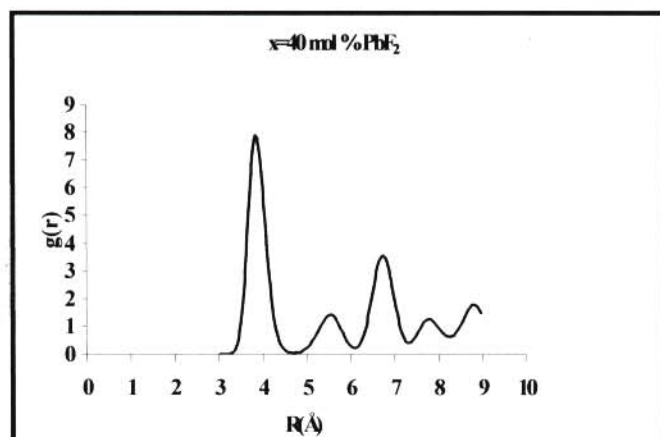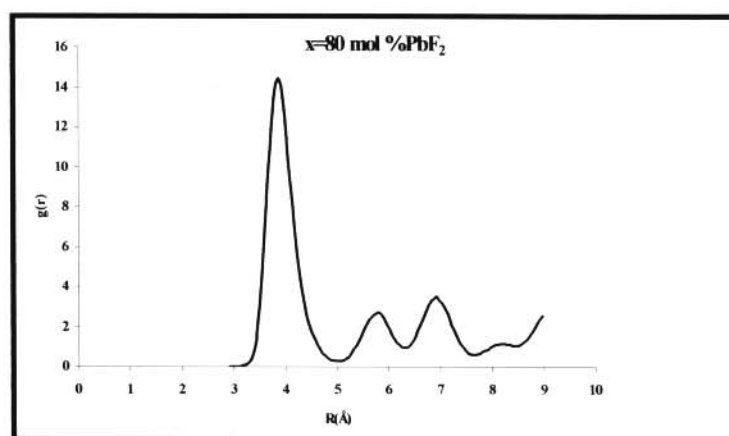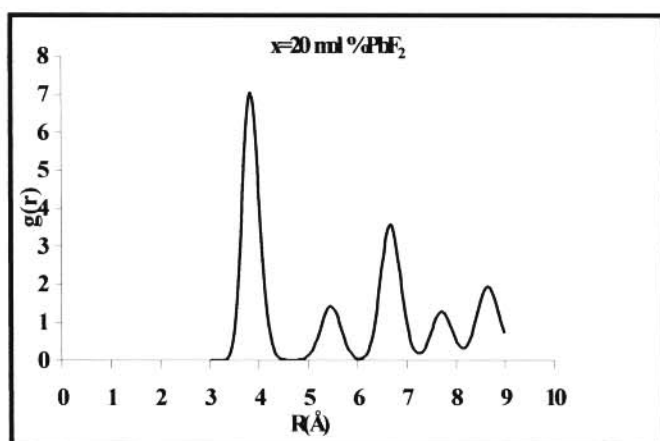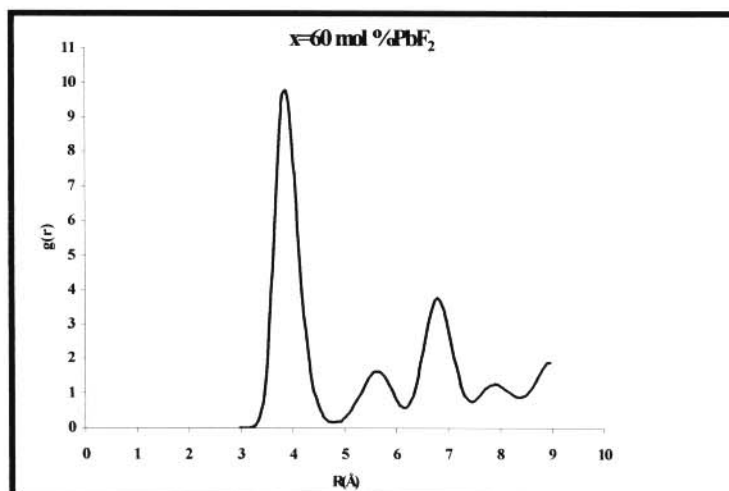
136
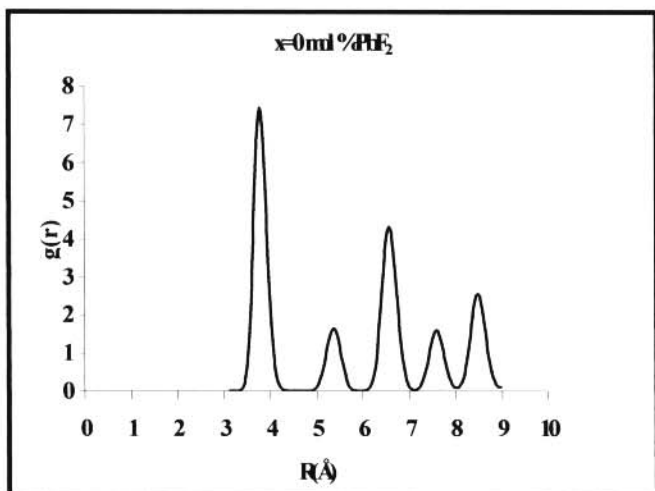
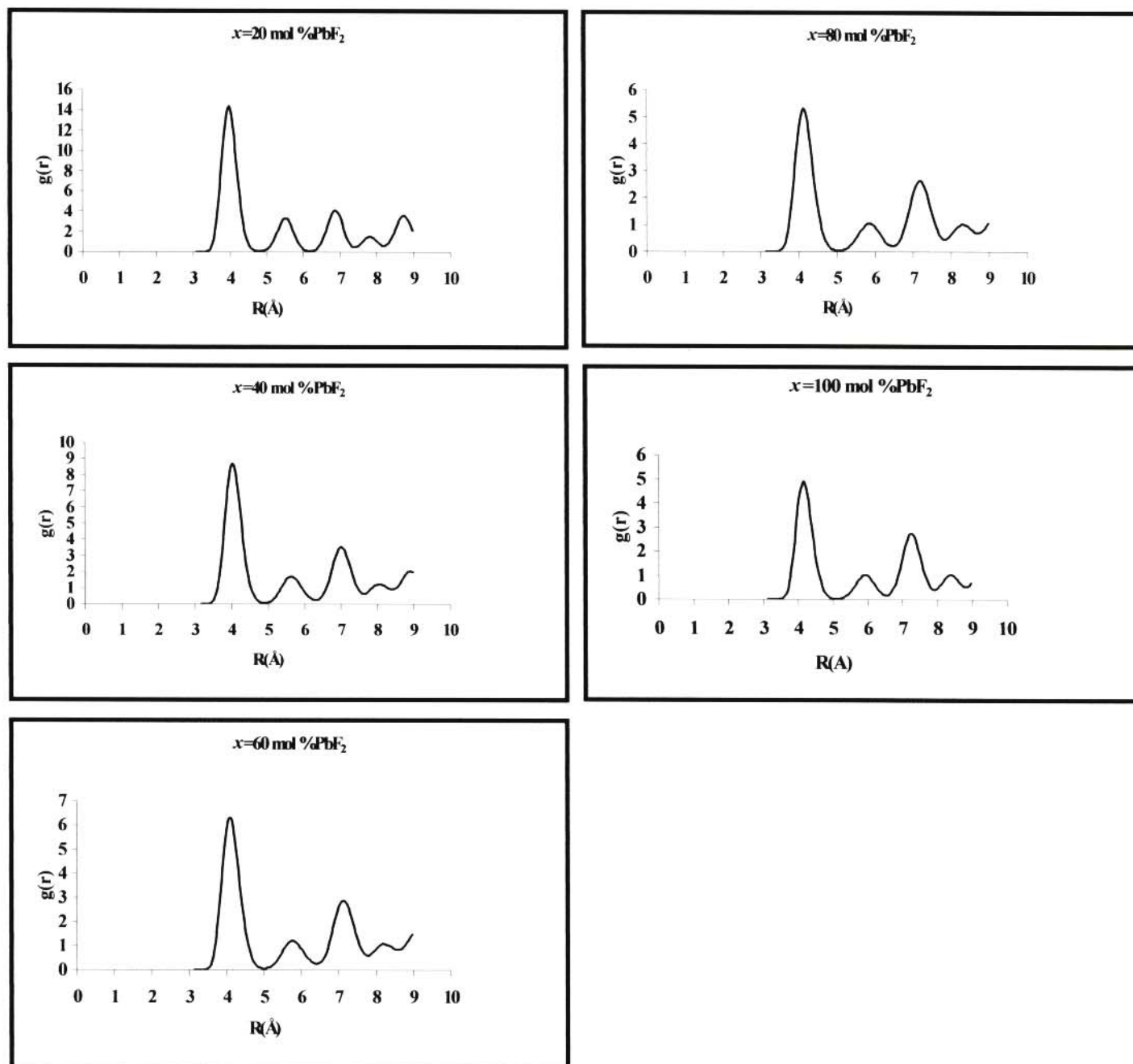Figure 4.11 Cd-Cd Radial distribution functions in CdF$_2$(xPbF$_2$) at T=700 K.

Figure 4.12 Pb-Pb Radial distribution functions in $CdF_2(xPbF_2)$ at T=700 K.

Table 4.9 Cd-Cd and Pb-Pb bond-lengths obtained from molecular dynamics studies on $CdF_2(xPbF_2)$ mixed solutions.

Bond-length	Temp.	Composition $x(PbF_2$ mol %)											
		0		20		40		60		80		100	
	T(K)	r(Å)	height	r(Å)	height	r(Å)	height	r(Å)	height	r(Å)	height	r(Å)	height
Cd-Cd	700	3.825	7.212	3.875	6.849	3.925	7.404	3.925	9.506	3.925	14.10	-	-
Pb-Pb	700	-	-	4.025	13.88	4.075	8.581	4.125	6.284	4.175	5.169	4.175	4.706

Table 4.10 F-F bond-lengths obtained from molecular dynamics studies on $CdF_2(xPbF_2)$ mixed solutions.

Temp.	Composition $x(PbF_2$ mol %)											
	0		20		40		60		80		100	
T(K)	r(Å)	height	r(Å)	height	r(Å)	height	r(Å)	height	r(Å)	height	r(Å)	height
300	2.625	5.230	2.775	3.660	2.825	2.888	3.025	2.607	3.025	2.704	3.075	2.721
700	2.675	3.674	2.775	2.739	2.875	2.427	3.075	2.240	3.125	2.170	3.075	2.167

long-range order on the anion sublattice, i.e. the oscillations in the RDFs die out rapidly with increasing r (and is similar to those in liquids even though the crystal remains unmelted). Hence, the F^--F^- RDFs for these systems resemble the mobile ion–mobile ion RDF of liquids, indicating that they form a weak, diffuse structure (system with less structure) for separations larger than the nearest neighbour. In this respect, doped $CdF_2(x\ PbF_2)$ crystals resemble many superionic conductors so far characterized [e.g. $PbSnF_4$ (by Cox et al. 1994), $RbBiF_4$ (by Catlow et al. 1985), Yttria-doped cubic zirconia (by Shimojo et al. 1992 and Islam and co-workers 1996), etc].

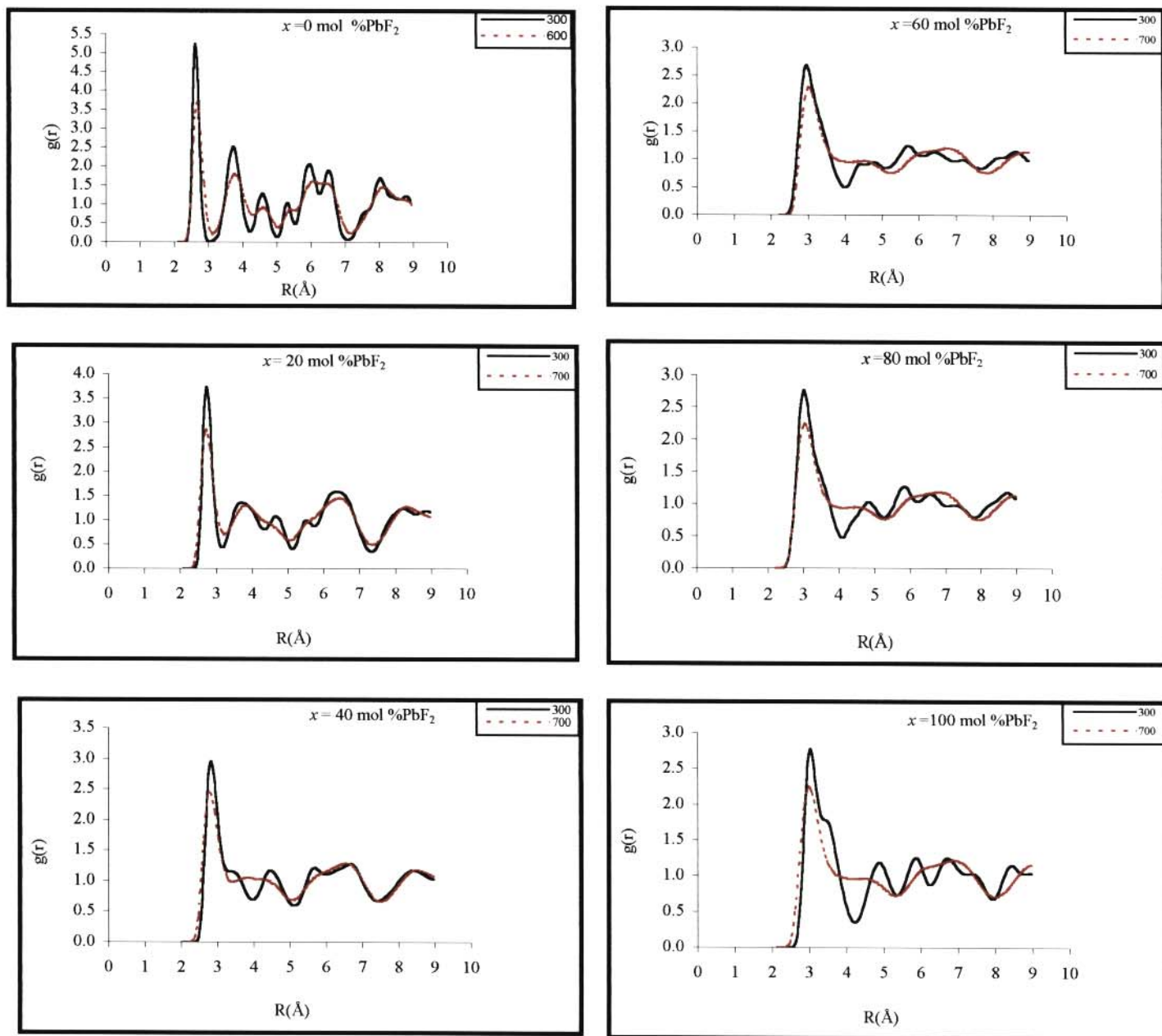Analysis of the general profiles for cation-caction and fluorine-fluorine interactions shows that whilst

Figure 4.13 Radial distribution functions from F-F for samples x = 0 mol % - 100 mol % PbF$_2$ at temperatures T = 300 and 700 K.

the cations retain their original coordinates, the anions form a complex, grossly distorted 'cubic' structure. In particular, the F^--F^- RDFs are much less sharp than the cation-cation RDFs (compare Figures 4.11-13). This shows a more diffuse anion sublattice. Furthermore, in F-F RDFs, a broadening of the general profile is observed with an increase in the concentration of PbF_2 (see Figure 4.13) such that the height of the second peak for the mixed systems rapidly dies out. Hence, the fluorine sublattice is deformed from a simple cubic lattice.

4.4.10.3   RDFs of the cations (g(Cd-F) and g(Pb-F))

The Cd-F and Pb-F RDFs are presented in Figures 4.14 and 4.15, respectively. As expected, these peaks correspond to the cation-fluorine interactions. To study the local environments of the two cations, we will concentrate on the behaviour of the first peaks (cation-fluorine first-neighbour distance) of the cation-fluorine RDFs.

It is remarkable to note that the Cd-F and Pb-F RDFs show no pronounced qualitative changes on raising the concentration from $x = 0$ mol % PbF_2 to $x = 100$ mol % PbF_2. However, the heights of the Cd peaks remain greater than those of the Pb peaks (see Figures 4.14 and 4.15), i.e. the differences in the Cd-F and Pb-F RDFs are greatly shown. This is indicative of the high extent of disorder on the Pb cation sites/sublattices than that on the Cd cation sites. Furthermore, in all compositions the distances between the Pb-F pairs are greater than those between the Cd-F pairs [see Table 4.11(a)-(b)]. This implies that it is energetically more favourable for a fluorine vacancy to be the nearest neighbour of Pb^{2+} ion in the CdF_2-PbF_2 systems. The results accord well with the computational
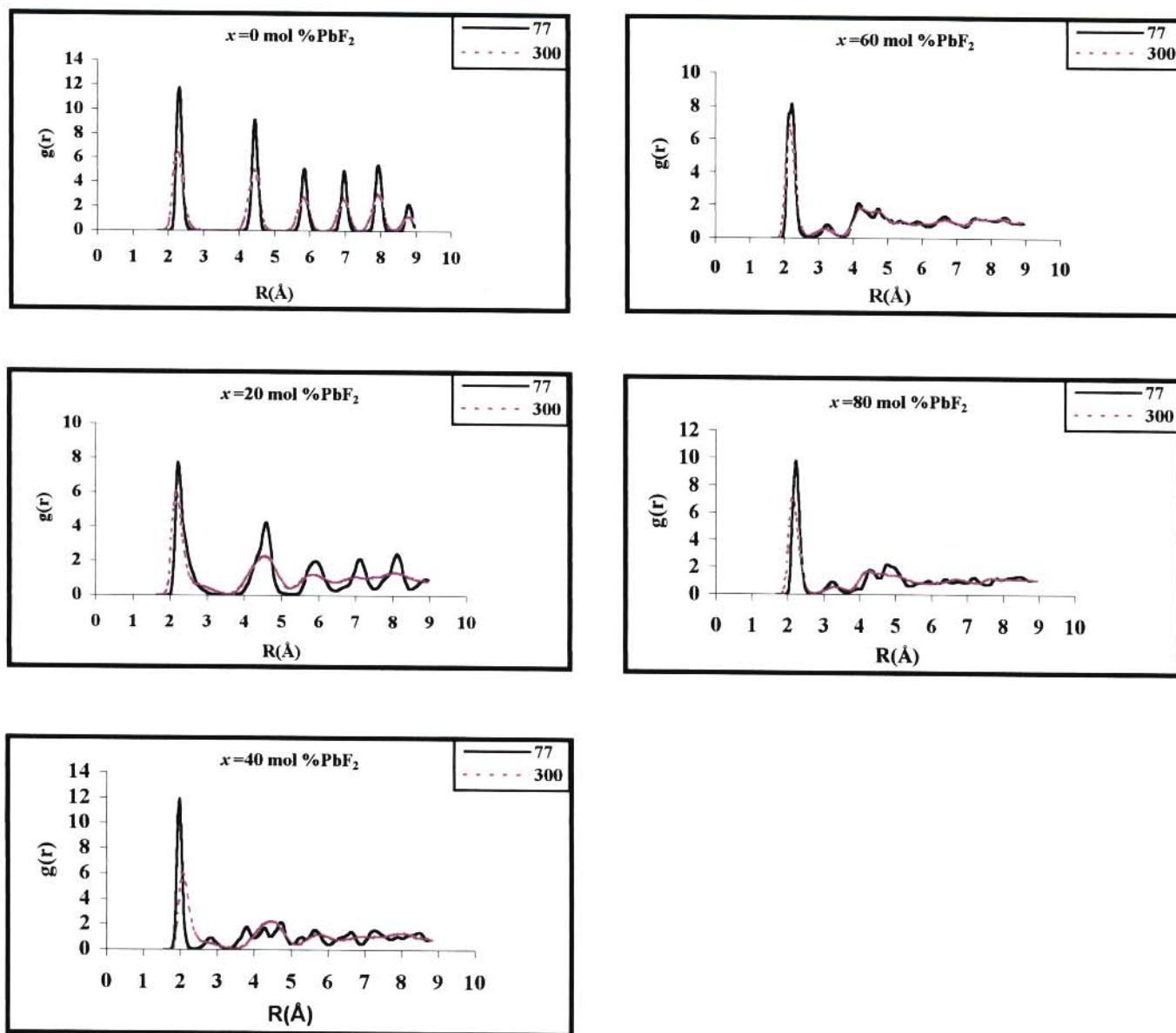
141

Figure 4.14 Radial distribution functions from Cd-F for samples *x*=0 mol % to *x*=80 mol % PbF$_2$ at temperatures T = 77 and 300 K.
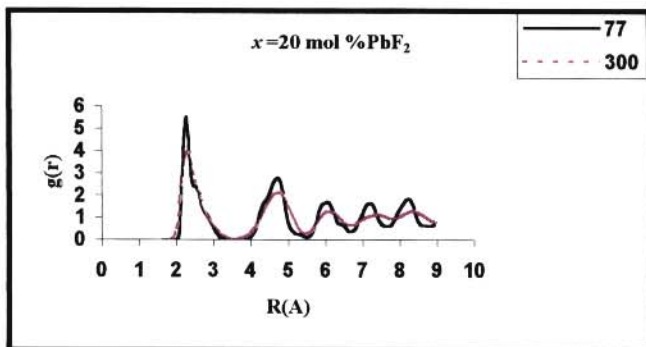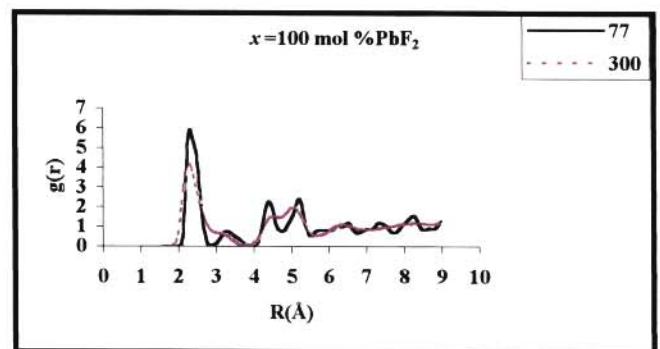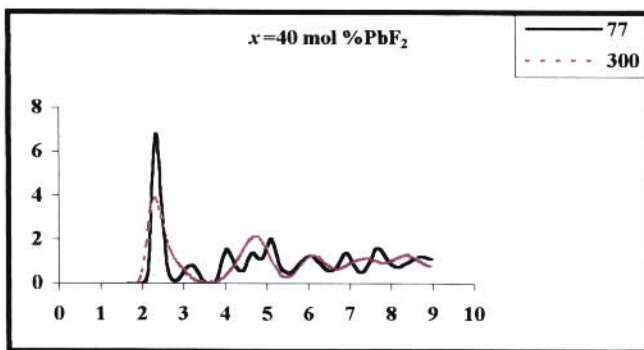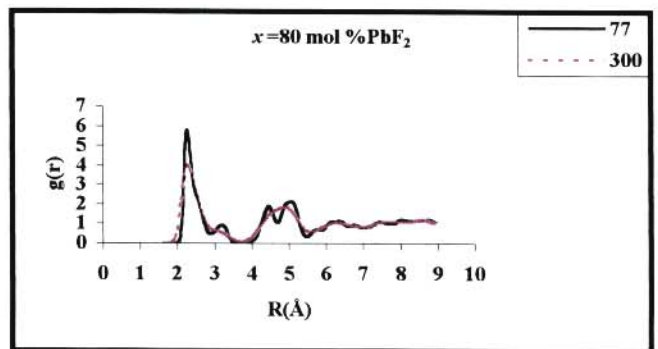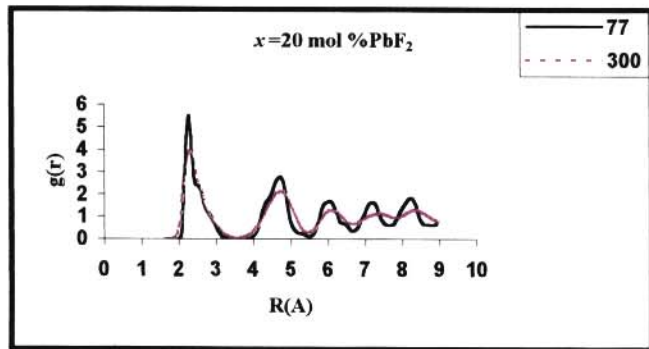
Figure 4.15 Radial distribution functions from Pb-F for samples x=20 mol % - 100 mol % PbF_2 at temperatures T = 77 and 300 K.

Table 4.11(a) Cd-F bond-lengths obtained from molecular dynamics studies on $CdF_2(xPbF_2)$ mixed solutions.

Temp.	Composition x (mol % PbF$_2$)									
	0		20		40		60		80	
T(K)	R(Å)	Height	r(Å)	Height	r(Å)	height	r(Å)	Height	r(Å)	Height
77	2.325	11.73	2.125	7.734	2.225	7.70	2.225	8.123	2.225	9.777
300	2.375	6.405	2.275	5.200	2.325	5.96	2.175	7.172	2.175	7.172

Table 4.11(b) Pb-F bond-lengths obtained from molecular dynamics studies on $CdF_2(xPbF_2)$ mixed solutions.

Temp.	Composition x (mol %PbF$_2$)									
	20		40		60		80		100	
T(K)	r(Å)	Height	r(Å)	Height	r(Å)	height	r(Å)	Height	r(Å)	Height
77	2.275	5.58	2.375	6.685	2.325	4.946	2.125	5.324	2.325	5.893
300	2.325	3.798	2.375	3.798	2.475	3.670	2.325	3.785	2.375	3.999

results of Li and Hafskjold (1995) and Allilla et al. (2001) on Y_2O_2-ZrO_2 systems, which showed that it is energetically more favourable to create an oxygen vacancy in the nearest neighbourhood of the Y^{3+} ions than of the Zr^{4+} ions. In addition, Cox et al. (1994) showed similar results from simulations of PbSnF$_4$ and RbBiF$_4$. Hence, this is a general trend for mixed-metal fluorites. These results are also in accord with arguments based on ion size (see Cox et al. 1994), in which the small ion (Cd in the present study) allows the lattice to relax around it, whereas the large ion causes slight distortion in the local structure.

A further feature of note is that no significant structure is observed in the cation RDF peaks at

distances more remote than the first neighbours (in particular, for $x \geq 40$ mol % PbF_2 samples). This clearly contrasts with the parent materials CdF_2 and PbF_2, which show contributions to the peaks from second neigbours and beyond (see Figures 4.14 for $x = 0$ mol % PbF_2). A possible explanation for the absence of peaks due to cation-fluorine shells in the doped samples could be the high degree of disorder in the mixed systems than in the parent materials.

In summary, Figures 4.14 and 4.15 present the calculated RDFs for the two cations at $T = 77$ and 300 K at various temperatures and at various concentrations. Some similarities/differences can be detected:

- One peak can be well-identified / resolved in the two RDFs for the mixed systems ($x \geq 40$ mol % PbF_2), even though the cations display negligible mobility on the MSD-time scale/line. This is indicative of the loss of long-range order in the mixed systems.

- The peak in the Pb RDF is broader than the peak in the Cd RDF in all samples independent of the temperature, i.e. the static disorder in the Pb-F coordination shell is greater than in the Cd-F one.

- The peak in the Cd RDF is higher than the peak in the Pb RDF, i.e. the Pb-F bond length is longer than the Cd-F bond length.

Reductions in the height of the Pb-F and Cd-F amplitudes with temperature increase are noted. This points to the extent of disorder in complex systems.

CHAPTER 5

EXAFS STUDIES OF STRUCTURAL PROPERTIES OF CdF_2-PbF_2 MIXED SYSTEMS

5.1   INTRODUCTION

EXAFS is a technique that allows one to probe the immediate structural environment of a constituent element in a composite material as outlined in Chapter 3. Thus the technique probes only short-range order within a solid, namely, the nearest-neighbour elements, the number of nearest-neighbours and the location of atoms coordinating the excited element within the material. EXAFS measurements are carried out using a synchrotron as a source for X-ray radiation.

In this study, the local environments of Cd and Pb cations in $CdF_2(xPF_2)$ solid solutions as a function of composition x and temperature have been measured by means of EXAFS. Hence, individual local structural features surrounding both Cd and Pb cations can be directly compared.

Previous EXAFS work on mixed-metal fluorides of the form $ABiF_4$ and $MSnF_4$ (where A=Rb and M=Pb), with very high F^- ion conductivities, successfully revealed the local structural environments of the cations (Catlow et al. 1985 and Cox et al. 1994). The EXAFS profiles and Fourier Transform

146

data obtained for the Rb and Bi edges in $RbBiF_4$ mixed systems showed that local environments of both cations are highly disordered and the Fourier Transform of each cation consists of a single peak. This is in contrast with the results for pure fluorite-structured materials such as CaF_2, CdF_2, etc (Catlow et al. 1984 and Netshisaulu 1996) which show more than one peak in the Fourier Transform profile. The absence of contributions from more distant shells to the Fourier Transform in $RbBiF_4$ was attributed to the large extent of displacements of the atoms from their perfect lattice sites. Hence, backscattering from shells beyond the first nearest neighbours is negligible. Furthermore, the Rb-F bond length is marginally greater than the Bi-F bond length in these materials. On this basis, it was concluded that the Bi ions 'dictate' the structure by drawing F^- ions to form a tight coordination shell at a short distance which leaves the Rb-F shell comparatively disordered (Cox et al. 1994). Further evidence to the observations above was that F^- vacancies were preferentially located in anion sites neighbouring cations having larger ionic radii and lower charges. This intriguing behaviour was attributed to the fact that it is electrostatically easy to remove ions from sites in excess of singly charged ions (e.g. Rb in $RbBiF_4$) (since Rb ions carry a lower charge of +1 as opposed to +3 for Bi ions) than to remove them from sites adjacent to the more highly charged Bi ions. The reasons for the greater ease of removing F^- ions from a site rich in Rb than from a site adjacent to an excess of Bi ions were as follows:

(a)   Electrostatically,.

(b)   Elastically, significant size difference between the involved cations (i.e. $rRb^{1+} = 1.47$ Å $> rBi^{3+} = 0.96$ Å) suggests that Rb promotes vacancy stabilisation in neighbouring sites.

The profile of the EXAFS spectra for the local structure surrounding the two cation edges in $RbBiF_4$

as a function of temperature showed significant differences. In the case of Bi no change in the amplitude or frequency of the oscillations was observed whilst the Rb edge EXAFS displayed a dramatic reduction in both amplitude and frequency as a function of temperature. This implies that local ordering about Bi^{3+} is much greater than about Rb^{1+}. The first peaks in the Fourier Transforms of Rb^+ show reduced amplitudes (with increasing temperature) and are broader than those for Bi. This phenomenon is linked to the decrease in the number of F^- ions in the neighbouring shell of Rb^{1+} as well as an increase in the static component of the Debye-Waller factor. The decrease in frequency of the EXAFS oscillations with increasing temperature is accounted for by a decrease in the Rb-F distance for the shell.

In the present investigation, Cd and Pb cations have the same charge (+2) as in $PbSnF_4$ (Cox et al. 1994) so that no electrostatic advantage exists for the creation of F^- vacancies in anion sites adjacent to the cations with an excess of either Cd or Pb ions. The removal of ions from a site rich in Pb neighbours is more favourable than from a site adjacent to an excess of Sn due to the reasons given below:

(a) there is no electrostatic advantage in $PbSnF_4$ mixed these systems so that removal of F^- ions is equally favourable from either type of site.

(b) Pb^{2+} cation promotes vacancy stabilisation in neighboring sites due to their large ionic radius.

(c) The greater activity of the lone pair on Pb^{2+} favours the stabilisation in the neighbouring sites due to lone pair localisation. This is also evident in the marked loss of higher frequency contribution to the EXAFS at high temperatures. This shows the negligible impact of more distant neighbours on the Pb edge EXAFS.

148

Generally, effects observed on the Sn edge in $PbSnF_4$ are similar to those observed on the Bi edge in $RbBiF_4$. On the other hand, for the Pb edge, effects observed are similar to those observed on the Rb edge. Furthermore, the Sn-F distances are shorter than the Pb-F distances. On the basis of this discussion, Cox et al. (1994) proposed that Rb^{1+} and Pb^{2+} ions transfer F^- ions from normal sites into interstitial ones with the creation of supplementary vacancies in the normal anionic sublattice, whilst Bi and Sn cations enhance the conductivity by preserving the structure (maintaining a temperature-independent local environment), thus helping to preserve the open-nature of the fluorite structure, retaining the pathway for migration via interstitial sites.

$CdF_2(xPbF_2)$ are mixed solid solutions of the $A_{1-x}B_xC$ type for every composition (0 mol %$\leq x \leq$100 mol %PbF_2). Hence, this solid solution is based on the CdF_2 matrix and the lattice parameter varies linearly with temperature (see Figure 5.1). Furthermore, X-ray diffraction analysis shows that the lattice constant of the $CdF_2(xPbF_2)$ mixed crystals varies almost linearly with Pb content (Kosacki and Dynowska, 1980), i.e. it fulfills Vegard's law. These mixed crystals also possess high levels of F^- ion disorder. High temperature studies on these compounds (Kosacki 1986 and Kosacki et al. 1989) have provided strong evidence for a relatively low value of the transition temperature T_c to the fast-ion phase at x=60 mol %. Our previous computer modelling results on $CdF_2(xPbF_2)$ (Netshisaulu, 1996) crystal also revealed that the extent of disorder increases around Pb. However, a detailed study of the structural, dynamical and conductivity properties of $CdF_2(xPbF_2)$ mixed systems in the whole compositional range is still lacking. This chapter is aimed at the examination of the environment around the Cd and Pb atoms and the determination of the extent of structural disorder. For these
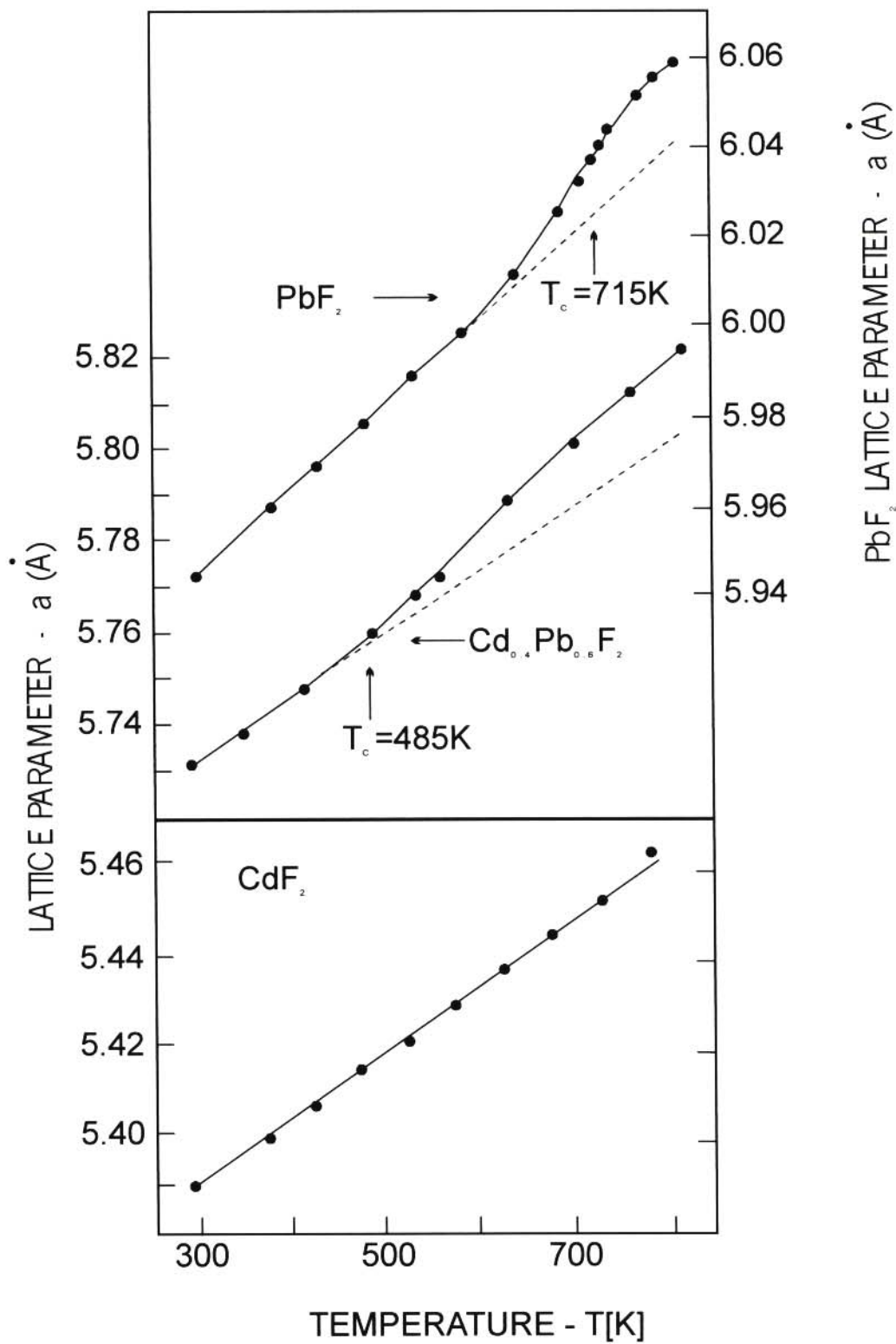
149

Figure 5.1 The temperature dependence of the lattice parameter for CdF_2-PbF_2 crystals. (After Kosacki et al. 1989)

reasons it is necessary to undertake more elaborate EXAFS studies on CdF_2-PbF_2 systems in order to give a qualitatively detailed interpretation of the results.

5.2   EXAFS THEORY

The plane-wave approximate of the EXAFS is described in Chapter 3. However, the plane-wave approximation's application is limited to high photo-electron (emitted on absorption of the x-ray). In this work, the exact, rapid curved-wave (EXCURV) theory is used for EXAFS analysis.

5.3   EXPERIMENTAL DETAILS

5.3.1   Sample Preparations

CdF_2-PbF_2 crystals with 0, 20, 40, 60 80 and 100 mol % PbF_2 were prepared for this study in the Chemical Laboratory of the University of Kent, at Canterbury, in the UK. Weighed quantities of CdF_2 and PbF_2 compounds were thoroughly mixed and melted in graphite containers inside quartz tubes until a uniformly clear melt was obtained under vacuum (10^{-6} torr). These prepared specimens were finely ground (< 20 mm) with a mortar and prestle and well diluted with boron nitride and pressed into thin coherent pellets using a 13-mm die. After preparation the samples were mounted in an evacuable crystal-heating furnace.

5.3.2 The EXAFS Technique

Details on the EXAFS technique have been reported in Chapter 3. X-ray absorption spectroscopy is simply the accurate determination of the X-ray absorption coefficient of a material as a function of photon energy, in an energy range that is below and above the absorption edge of one of the elements in the material. Each element (in this case, Cd or Pb) has a unique absorption edge that corresponds to the binding energy of the inner shell electrons. This work is concerned with K and L_3 absorption edges for the study of the local environments of the neighbours of Cd and Pb elements, respectively. The former results from the photo-electric process in which the energy of the X-ray is absorbed by a 1s core state while the latter results from the corresponding process for the 2p core state.

5.3.3 Experimental Procedure

We have made X-ray absorption measurements on absorption edges of all the cations present in the sample. Thus EXAFS measurements for $CdF_2(xPbF_2)$ mixed systems were taken at the Pb (L_{111}) (13.036 keV) and Cd (K) (26.716 keV) edges using the Science and Engineering Council (SERC) Synchrotron Radiation Source facilities of station 7.1 at Daresbury in the UK. The samples $CdF_2(xPbF_2)$, $x=$ 0 mol %-100 mol % PbF_2, were mounted in an evacuable heating furnace with Beryllium windows. The EXAFS absorption spectra were recorded at various temperatures in the transmission mode using a channel-cut Si(111) crystal monochromator to study the L_3 absorption edge of Pb and the Si(220) one for the Cd edge. Order-sorting monochromators were used to minimise harmonic contamination of the beam. During the data collection, the SRS was operated at

an electron energy of 2.0 GeV with a typical beam current of *ca.* 150 mA.

5.3.4   Data Analysis

The EXAFS were analyzed following a standard procedure using the Daresbury EXAFS programme library (see Chapter 3 for details). Data were fitted using least squares fitting program. Five parameters (i.e. energy E_0, afac, potential V_i, afac, radial distance R_i, Debye-Waller factor $\Delta\sigma^2$) for each of the five nearest-neighbour shells were allowed to vary in order to obtain a good fit to the experimental data. The coordination of the first shell was held fixed at eight fluorines.

In essence, data analysis of the raw EXAFS includes removal of the background level and a Fourier transformation of the EXAFS (experimental data). The result is a series of peaks in the Fourier transform that correspond to the contributions of various coordination shells around the excited atom. The Fourier Transform is similar to a radial distribution function. Further data analysis of the EXAFS gives coordination numbers (N), radial distances (R) and a Debye-Waller factor ($\Delta\sigma^2$) that is a measure of the thermal and static disorder in the $CdF_2(xPbF_2)$ solutions. The amplitude and phase parameters have been obtained from the parent solid samples CdF_2 and PbF_2 for the analysis of the EXAFS of mixtures. Calculated phase shifts should be included in data analysis to ensure that peaks represent shell distances. Furthermore, fluorine coordination around Cd^{2+} and Pb^{2+} ions in the solid solution of the $CdF_2(xPbF_2)$ system are similar to those in the end-members CdF_2 and PbF_2, respectively.

5.4 RESULTS AND DISCUSSION

5.4.1 Introduction

The objective of this study is to examine the effects of increasing concentration and temperature on the local structural environment of the host and dopant cations. Hence, information on local environments of the host Cd and dopant Pb cations in $CdF_2(xPbF_2)$ mixed systems and the extent of structural disorder was obtained from EXAFS measurements as a function of PbF_2 composition x and temperature T. EXAFS technique has also been used to compare the immediate structural environments of the Cd and Pb cations in an attempt to locate the position of anion vacancies in $CdF_2(xPbF_2)$.

5.4.2 Compositional Effects on Fourier Transforms

The EXAFS spectra $\chi(k)$ have been k^3 weighted in the usual manner (see Catlow et al. 1985) so that the Fourier transform amplitude (corresponding to interatomic/radial distances) can be determined more accurately within this weighting. EXAFS data were collected for Cd and Pb edges at both liquid-nitrogen (77 K) and ambient (300 K) temperatures in order to distinguish between the effects of static and thermal disorder. The radial distribution functions RDFs were obtained by Fourier transforming the $k^3 \chi(k)$ data of the Cd K and Pb L_3 edges. Figures 5.2 and 5.3 show the low temperature (77 K) Fourier transform amplitudes [(an 'EXAFS radial distribution function (RDF)'] against r of the Cd (K) (——) and the Pb (L_3) (----) edges in $CdF_2(xPbF_2)$(0 mol %≤ x ≤100 mol %) systems, respectively. The first peaks in the Fourier transforms (Figures 5.2 and 5.3) result from

154
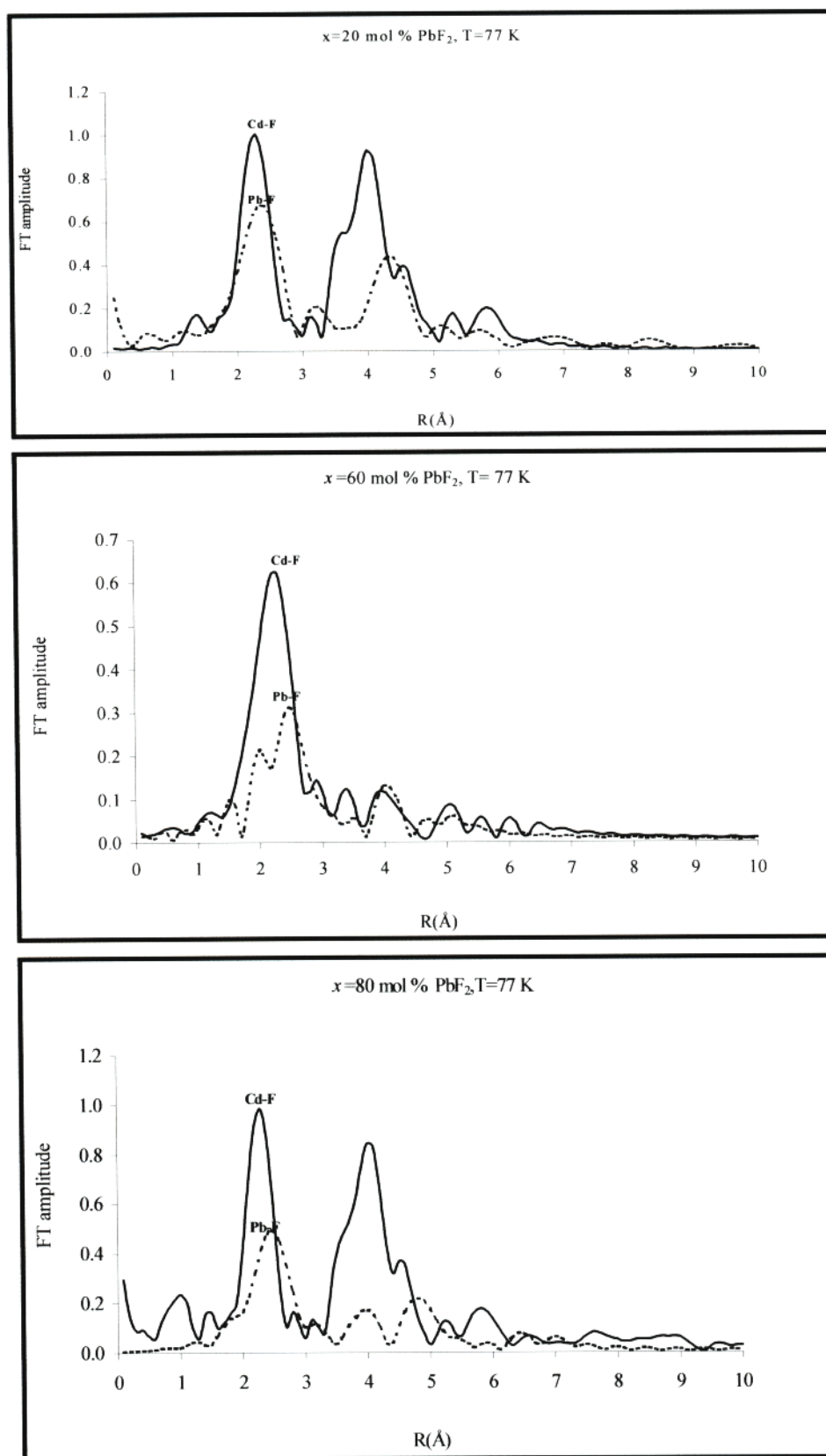
Figure 5.2 Fourier Transforms of the EXAFS function above the Cd(K) edge($-$) and the Pb(L_3) edge ($\cdots\cdots$) for various Pb content x in $CdF_2(xPbF_2)$ crystals.
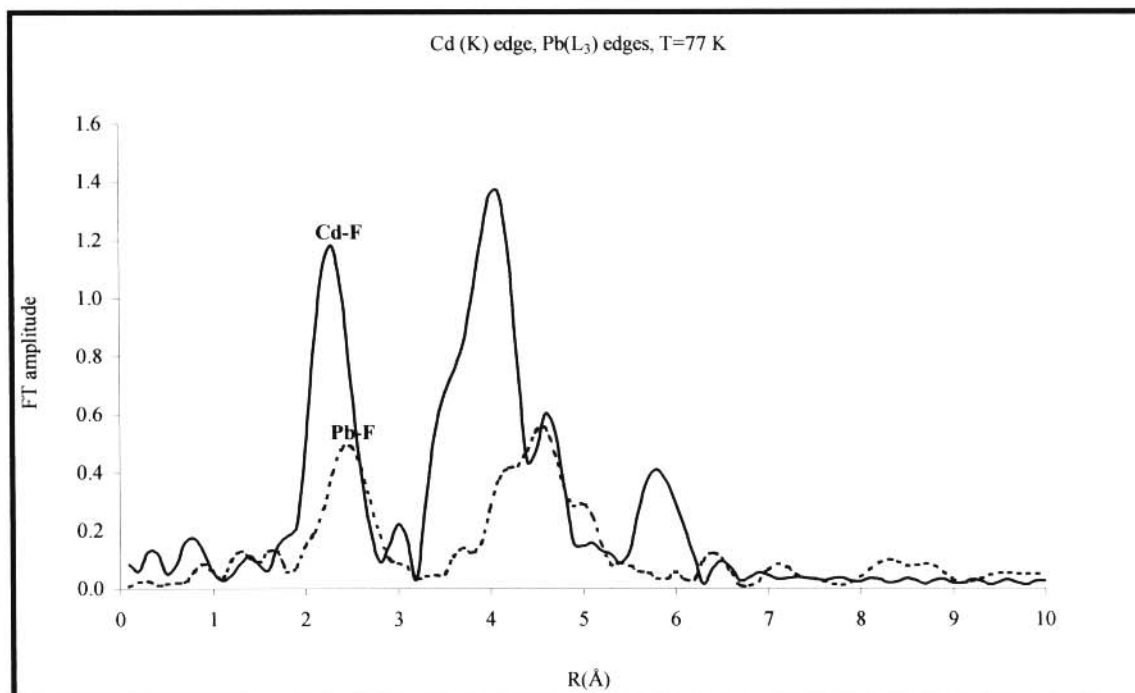
155

Figure 5.3 Fourier Transforms of the EXAFS function above the Cd(K) edge(———) and the Pb(L$_3$) edge (·······) in binary (i.e. CdF$_2$ and PbF$_2$) compounds of CdF$_2$(xPbF$_2$) crystals.
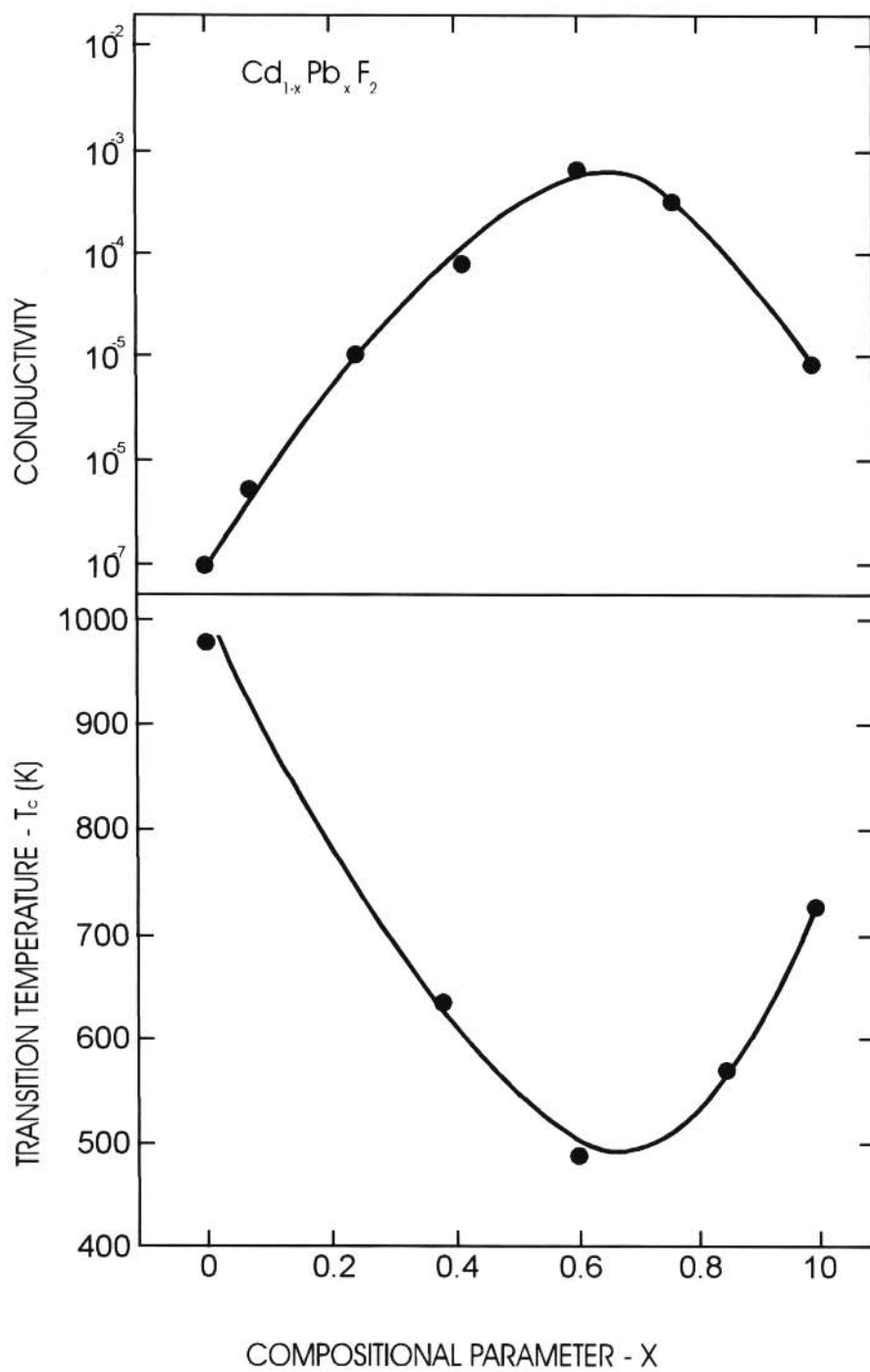
Figure 5.4 The compositional dependence of the ionic conductivity and the superionic state transition temperature (T_c) for $CdF_2(xPbF_2)$ crystals (after Kosacki et al. 1989)

backscattering from the nearest-neighbour shell of fluorine atoms (i.e. nearest neighbour to the central metal atom giving rise to Cd-F or Pb-F distances, while the second peaks correspond to backscattering from the shell of metal atoms [(Cd,Pb)-Cd or (Pb,Cd)-Pb]. A comparative examination of the Cd and Pb spectra in Figures 5.2 and 5.3 reveals the presence of two well-defined peaks (for the composition ranges 0 mol %$\leq x <$60 mol % PbF_2 and 60 mol %$< x \leq$100 mol % PbF_2) with the amplitudes of the second shells (cation-cation / metal-metal peaks, i.e. (Cd,Pb)-Cd or (Pb,Cd)-Pb peaks significantly reduced at x=60 mol % PbF_2 for both edges. Thus the Fourier transforms of the EXAFS spectra are dominated by the first fluorine shell [fluorine-cation (Pb or Cd)] for the composition x=60 mol % PbF_2. This spectrum (for x=60 mol % PbF_2) clearly shows that the EXAFS results from a single fluorine shell and this is typical of most solid solutions (see Catlow et al. 1985 and Cox et al. 1994). This is a manifestation of an extensive static disorder in the CdF_2(60 mol % PbF_2) sample. The disorder tends to increase with composition until the value of $x = 60$ mol % is reached. This is consistent with Kosacki et al.'s (1989) observations (see Figure 5.4) where a decrease in the temperature to the superionic state T_c was noted as the value of x was increased in the range 0 mol %$< x \leq$60 mol % PbF_2. For 60 mol %$\leq x <$100 mol % PbF_2 an increase in T_c was noted. The compositional dependence of T_c attained a minimum at $T = 485$ K for $x = 60$ mol % PbF_2 (see Figure 5.4). However, it is a commonly accepted view that the lack of features from further shells (i.e. lack of long-range order) shows that this system is heavily disordered.

In the same vein it can be concluded that doping in $CdF_2(xPbF_2)$ mixed systems leads to both large local distortions of the structure and lower values of T_c (Kosacki et al. 1989). The amplitudes of the Fourier transforms of the edges of the two cations indicate significant differences in heights as shown in Figure 5.2 and 5.3. Amplitudes in the Fourier transforms of the first shells of the Cd (K) edge spectra are markedly higher than those for Pb (L_3) edge spectra across the entire composition. On the basis of these results, it can be concluded that F vacancies are mainly excluded from the near environment of the Cd ions. Furthermore, in both cases, the first peak is also significantly affected by changes in composition x (see Figure 5.5 and 5.6). The amplitude of the Fourier transform of the first shell for both sites is seen to decrease rapidly with an increase in Pb content until $x \approx 60$ mol %, followed by an increase in amplitude as observed for the Cd-Cd and Pb-Pb profiles in Figures 5.2 and 5.3, respectively. Thus no nearest Cd-Cd nor Pb-Pb pairs are detected for sample $x = 60$ mol % PbF_2. The smearing out of the second shell at $x = 60$ mol % PbF_2 could be due to destructive interference of amplitudes from Pb and Cd. However, to make the picture clear, let us focus on the behaviour of the cation-fluorine peaks since we are interested in the nearest neighbour interactions (i.e. the cation-fluorine interaction). It is immediately obvious by comparing the compositional dependence of the amplitudes of the Fourier transforms of the first shells (Figures 5.5 and 5.6) for 0 mol %$\leq x \leq$100 mol % PbF_2, that Cd sites are less sensitive to the increase in Pb content. Thus there is less disorder associated with the first peak for Cd-F interactions whilst the first shell in the Pb^{2+} cation EXAFS is considerably disordered. Hence, the disorder in the Pb sites is almost certainly due to increase in the DW factor rather than the change in coordination numbers (since the coordination numbers are held fixed). The increase in the DW factor could be linked to a decrease in amplitude for the Fourier Transforms. Furthermore, from previous arguments in the work of Cox et al. (1994) on $PbSnF_4$ that
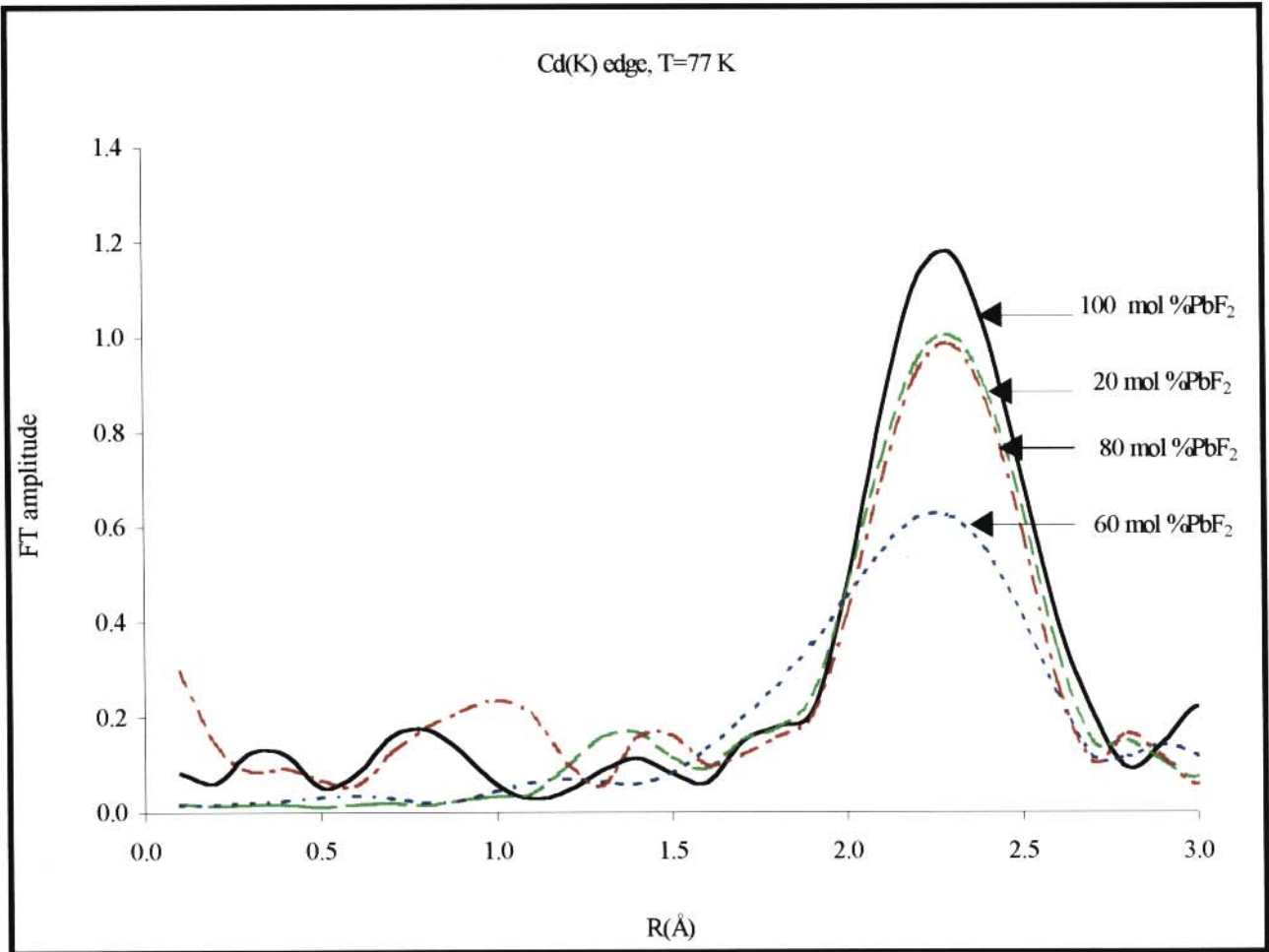
159

Figure 5.5 Fourier Transforms of the EXAFS data above the Cd (K) edge for various specimens x in $CdF_2(xPbF_2)$ crystals.
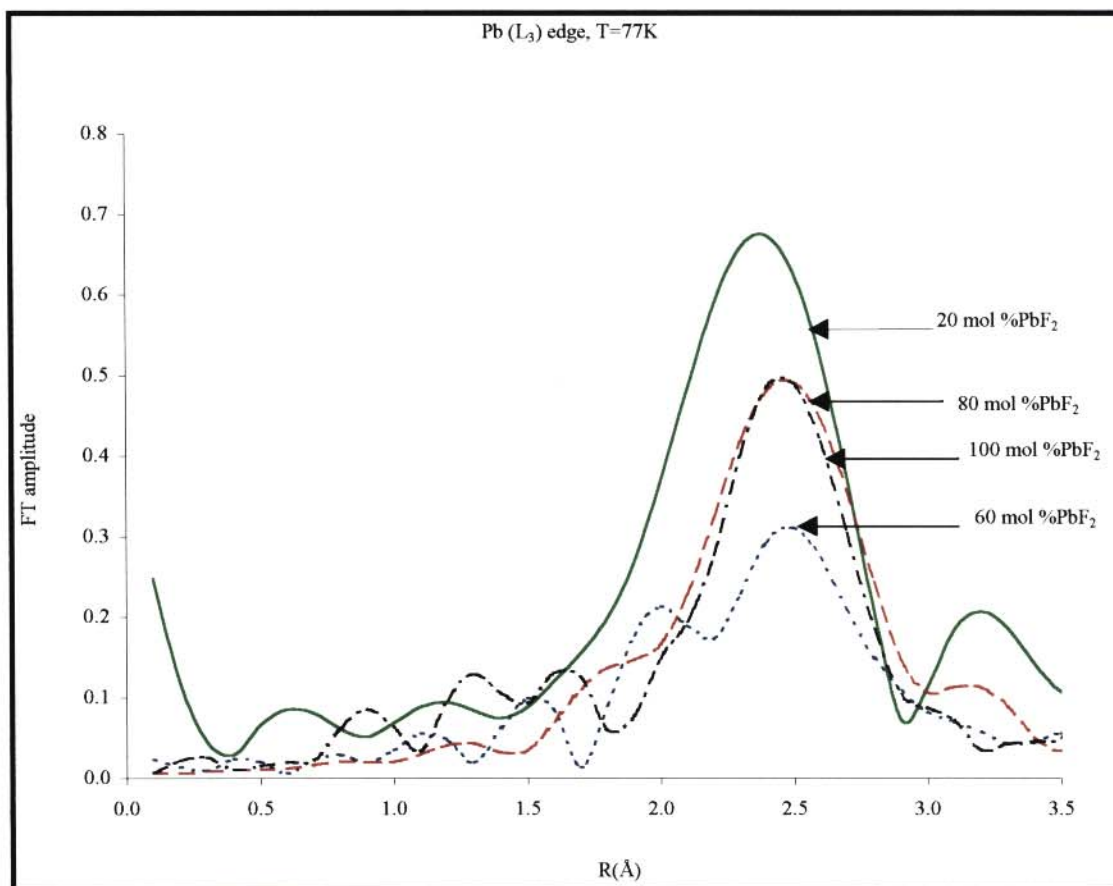
Figure 5.6 Fourier Transforms of the EXAFS data above the Pb (L_3) edge for various specimens x in $CdF_2(xPbF_2)$ crystals.

the larger Pb^{2+} ion is expected to favour the Pb-F sites.

5.4.3 Compositional effects on DW factors

Structural parameters (nearest-neighbour number N, radial distance R and DW factor σ^2) of the first peak give a description of the local environment / structure of the cations in mixed systems and are presented in Tables 5.1 and 5.2, in order to compare the extent of disorder in the entire range of $CdF_2(xPbF_2)$ systems. Since σ^2 and N are highly correlated, we preferred to fit the EXAFS spectra holding N fixed. Hence, in each case, the dopant is surrounded by eight (8) fluorine ions. The high values of the Debye-Waller factors in Tables 5.1 and 5.2 suggest the presence of static disorder in Cd and Pb sites, respectively, in $CdF_2(60\ mol\ \%PbF_2)$ at 77 K. A closer examination of the tables 5.1 and 5.2 reveal that for almost pure CdF_2 and $x \geq 80\ mol\ \%\ PbF_2$ (or $CdF_2(xPbF_2)$ for x close to 0 mol % PbF_2 or 100 mol % PbF_2), the values of the DW factors are low. The value of each DW factor appears to increase with composition for both edges. Least-squares fit with N, R and σ^2 as fitting parameters consistently shows the Pb-fluorine shell to have larger σ^2 than Cd-fluorine shell in the whole composition as shown in Figure 5.7. Thus the DW factors of the Pb-F peaks are consistently larger than those for Cd-F peaks. This implies that the dopant sites are disordered or atoms in fluorine shells surrounding the Pb are more disordered than atoms in fluorine shells surrounding Cd. This is in line with simple elastic arguments which, suggest that vacancies would be sited adjacent to the dopant cation (i.e. Pb promotes vacancy stabilisation in neighbouring sites). In the case where a relatively small dopant cation is used, the vacancies are located in the vicinity of the host cation.

162

Table 5.1 Structural parameters for the first shell of fluorines obtained from EXAFS experiments on $CdF_2(xPbF_2)$ mixed solutions for the Cd (K) edge.

Temp.	Composition x (mol %PbF_2)									
	0		20		40		60		80	
T(K)	R(Å)	σ^2(Å²)	r(Å)	σ^2(Å²)	R(Å)	σ^2(Å²)	r(Å)	σ^2(Å²)	r(Å)	σ^2(Å²)
77	2.310	0.012	2.294	0.014	2.235	0.025	2.275	0.027	2.296	0.015
300	2.295	0.020	2.293	0.021	-	-	2.249	0.025	2.288	0.021
500	2.276	0.021	-	-	-	-	2.235	0.031	-	-
650	2.290	0.027	-	-	2.219	0.031	2.211	0.039	-	-

Table 5.2 Structural parameters for the first shell of fluorines obtained from EXAFS experiments on $CdF_2(xPbF_2)$ mixed solutions for the Pb (L_3) edge.

Temp.	Composition x (mol %PbF_2)									
	20		40		60		80		100	
T(K)	R(Å)	σ^2(Å²)	r(Å)	σ^2(Å²)	r(Å)	σ^2(Å²)	R(Å)	σ^2(Å²)	r(Å)	σ^2(Å²)
77	2.485	0.023	2.275	0.027	2.496	0.042	-	-	2.524	0.027
300	-	-	2.249	0.025	2.438	0.046	-	-	2.500	0.048
450	-	-	2.235	0.028	2.437	0.058	-	-	2.458	0.056
500	-	-	2.383	0.050	-	-	-	-	2.427	0.058
550	-	-	2.411	0.093	-	-	2.460	0.076	2.405	0.058

However, in the situation where a much larger impurity cation is used (as in the present study), the vacancies are situated in the proximity of the dopant cation. The implication of this is that the central Cd^{2+} host cation has less static disorder in the presence of the larger dopant cations. Perhaps this comes as no surprise because it might be expected that large (ionic radius) cations (dopants) would relieve some of the 'steric' strain introduced into the system by accommodating a vacancy in the
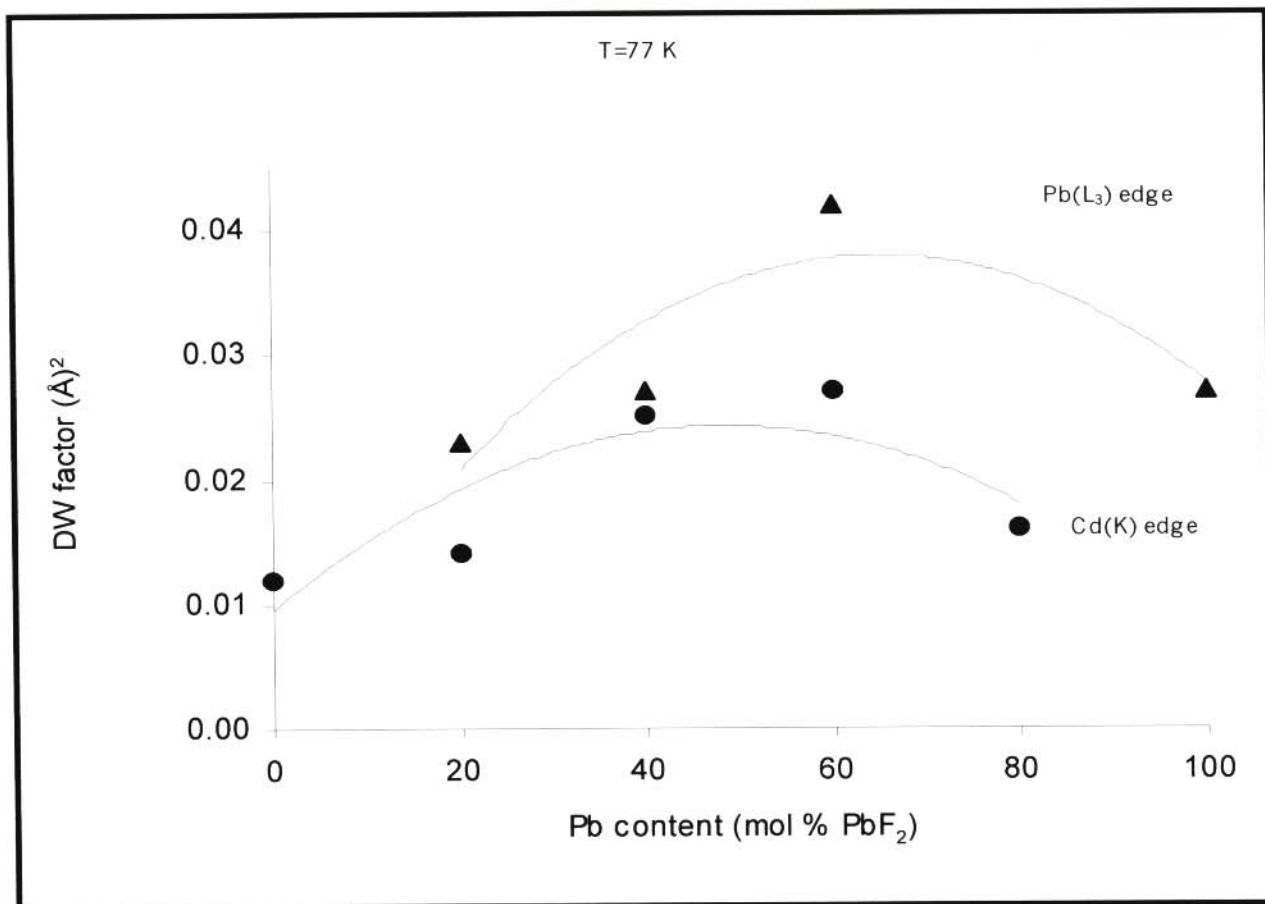
163

Figure 5.7(a) Variation with composition x of the disorder term σ^2 (Debye-Waller parameters) (from EXAFS) of the first neighbour (cation-fluorine) shell in $CdF_2(xPbF_2)$ at temperature T = 77 K. The curves are guides to the eye.
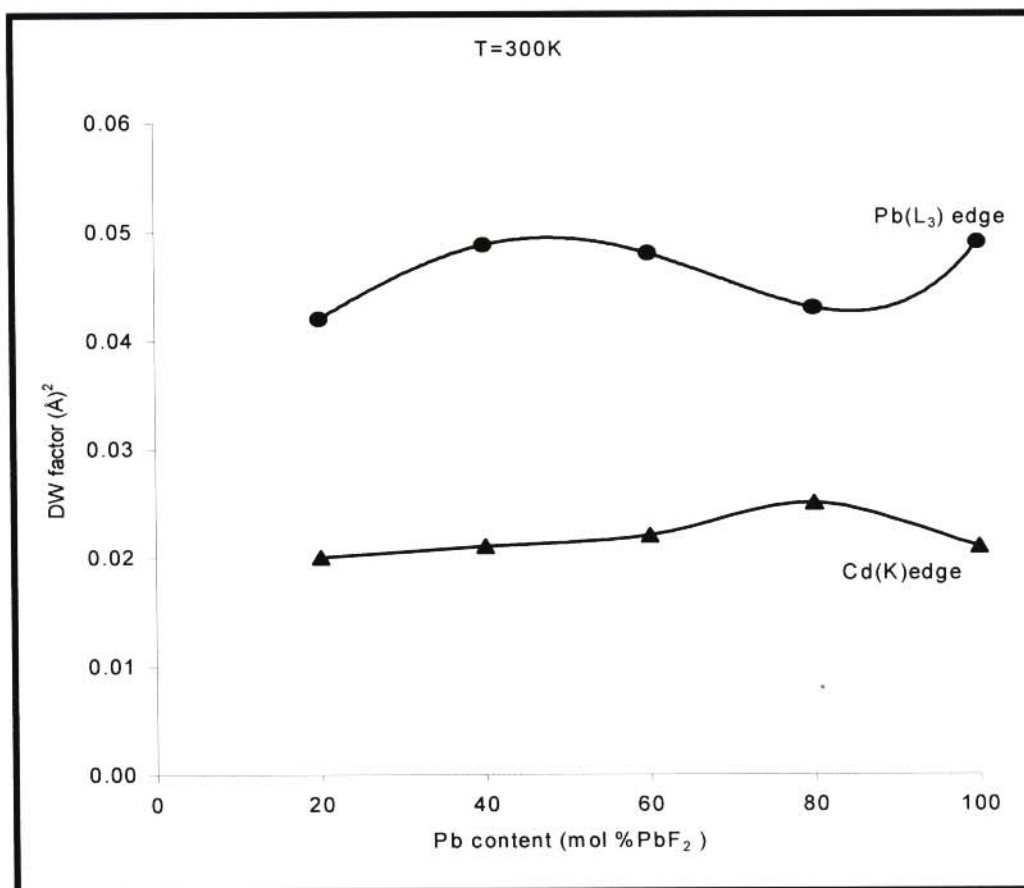
Figure 5.7(b) Variation of the disorder term σ^2 (Debye-Waller factors) from EXAFS of the first neighbour (cation-fluorine) shell as a function of composition in $CdF_2(xPbF_2)$ at temperature T = 300 K.

Figure 5.8(a) Debye-Waller parameters (as determined from EXAFS) of the first neighbour (Pb-F) shell as a function of composition in $CdF_2(xPbF_2)$ at T = 77 and 300 K.
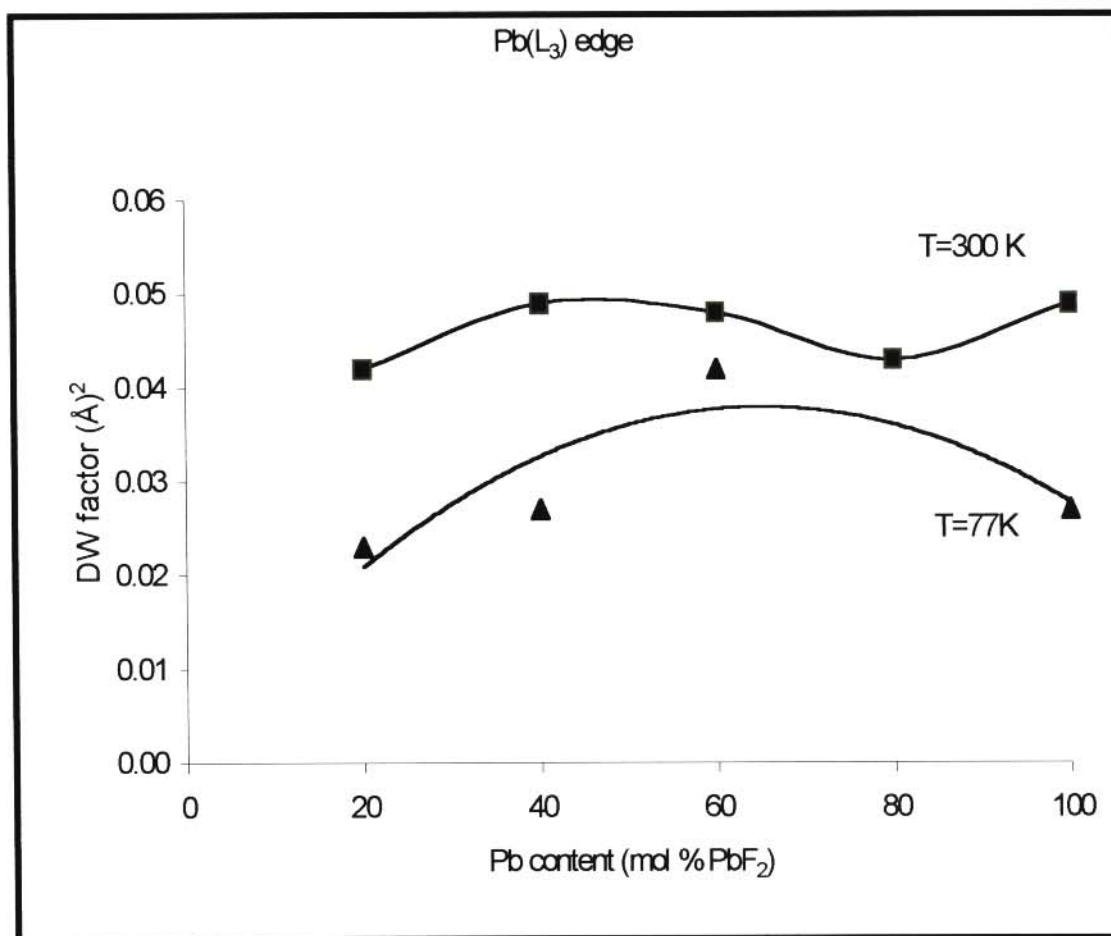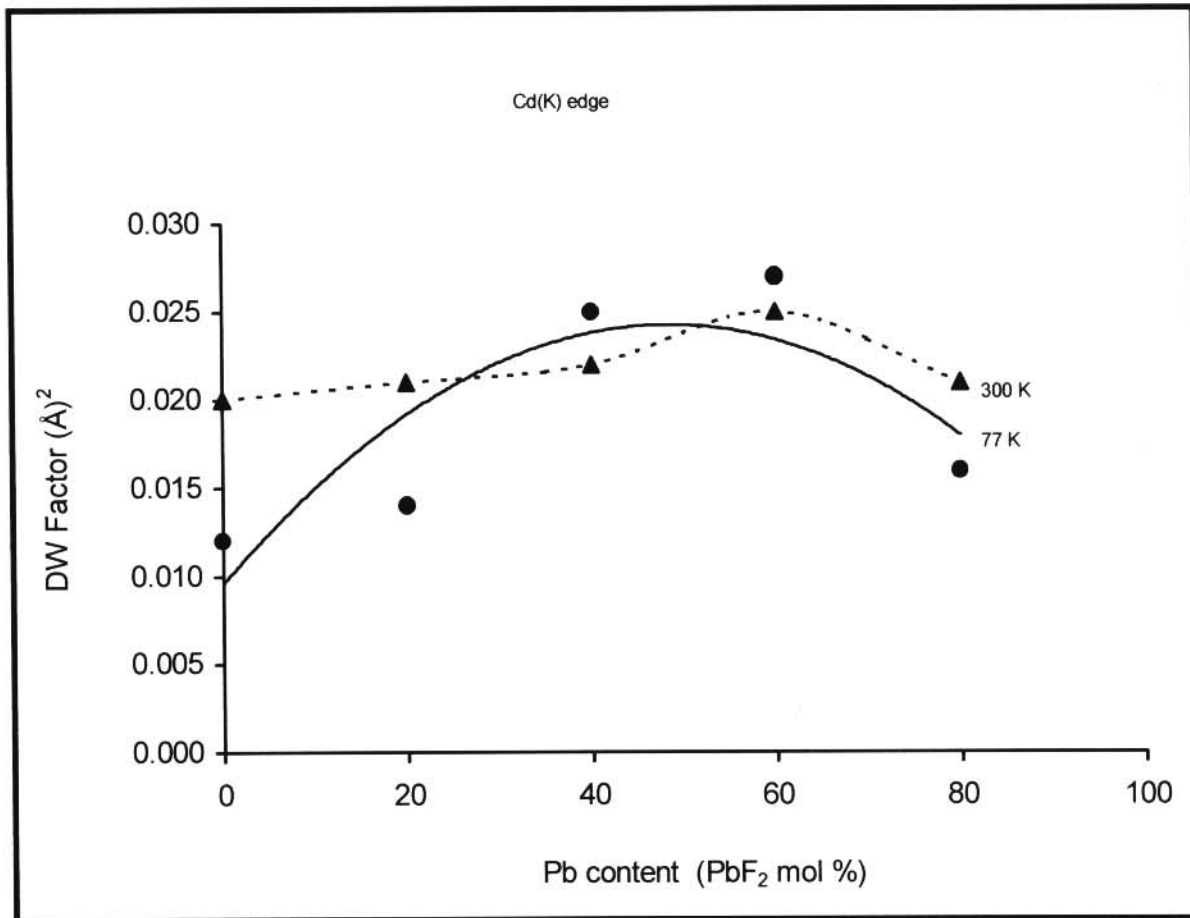
Figure 5.8(b) Debye-Waller parameters (as determined from EXAFS) of the first neighbour (Cd-F) shell as a function of composition in $CdF_2(xPbF_2)$ at temperature T = 77 and 300 K.

nearest-neighbour anion site. A possible explanation of the effects we observe is that in the case of Pb dopants and Cd hosts, the size mismatch could lead to an increase in the number of Cd^{2+} ions without any F^- species in the nearest neighbour cation sites.

Low values of the DW factors for the Cd-F interaction (σ^2 of about 0.02 $\mathring{A}^2$) imply less disorder whilst the high values of the Debye-Waller factors in Pb sites (σ^2 of about 0.04 $\mathring{A}^2$) reflect the extensive disorder around the Pb cations in the entire range of $CdF_2(xPbF_2)$ systems. The plots for the dependence of the DW factors on composition x suggest that the fluorine lattice becomes more disordered as the mix of large ions (Pb) and small ions (Cd) in the fluorine shell becomes more evenly distributed. Maximum disorder occurs when the mixture has approximately equal concentration of Cd and Pb for both sites (Cd and Pb). Thus the most pronounced change in Debye-Waller factor occurs for 40 mol % $<x<$ 80 mol % PbF_2. Such a situation is quite similar to that observed in $PbSnF_4$ and $RbBiF_4$ mixed crystals (see Catlow et al. 1985 and Cox et al. 1989). In $RbBiF_4$ mixed metal fluorides, such behaviour was related to the properties of the cation such as ionic radius. Cations with large ionic radius promote vacancy stabilisation in neighbouring sites.

The large values of the DW factors of the Pb-F interactions in $CdF_2(xPbF_2)$ systems are consistent with low amplitudes of their Fourier transforms (see Figures 5.2 and 5.3). Small values of the DW factors for the Cd-F interactions also indicate a well-defined coordination environment for the Cd-F Fourier transforms. This suggests that the addition of Pb^{2+} to CdF_2 disorders the local environment around the Pb sites. Furthermore, the profiles of the Debye-Waller (DW) factors of the Pb-F interaction as a function of composition in the mixed systems are larger than those in the Cd–F

168

interation, which result in a smaller Pb-F peaks as displayed in Figure 5.2 and 5.3. The amplitude reduction of the Fourier transform can be fully explained by the increase in σ^2.

5.4.4 Compositional effects on bond lengths

Tables 5.1 and 5.2 give radial distances that were determined from the first peaks of the Fourier transforms for the Cd and Pb edges in $CdF_2(xPbF_2)$ mixed systems at 77 K. The actual Cd-F and Pb-F distances / separations are plotted in Figure 5.9 as a function of composition x. Although both EXAFS spectra consist of two major peaks, there are clear differences in the dependences of the radial distances of Cd and Pb cations on composition x. Notably, the Pb-F distances are consistently larger than Cd-F distances, again reflecting the larger Pb ion size and the high state of disorder on the Pb sites, yet the unit cell expands with increasing Pb content x (see Figure 5.1). The net expansion occurs because the smaller Cd ions are increasingly replaced by the much larger Pb ions. The same argument was used by Veal et al. (1988) on their EXAFS study of yttria stabilized cubic zirconia. However, the metal-oxygen distances (i.e. Zr-O and Y-O) in yttria stabilized cubic zirconia systematically decrease with composition x (or vacancy concentration) and the plot of the weighted-average of Y-O and Zr-O distances [or (Zr,Y)-O distance] obtained from EXAFS shows the expected expansion with composition x. The mean (Zr,Y)-O distance was calculated using the lattice constant of the fluorite-type structure where the coordinate of metal is assumed to be (0,0,0) and that of oxygen is (¼,¼,¼). The same behaviour was reported for $ZrO_2-Gd_2O_3$ solid solutions (Uehara et al. 1987). In essence the decrease in the metal-oxygen distance was attributed to the decrease in the

169

coordination numbers around the absorber / target cation.

Examination of the results given in Tables 5.1 and 5.2 and Figure 5.9 shows that the radial distances remain more or less the same over the entire composition range (i.e. 0 mol $\% \leq x \leq 100$ mol % PbF_2) or no appreciable changes in metal-fluorine distances are observed with Pb content. This is reasonably explained by the fact that the coordination number N of both Cd and Pb was kept fixed at eight (8) across the composition beacause the fitting parameters (i.e. N and σ^2) for fluorine shells surrounding the Cd and Pb absorbers are highly correlated in equation 3.3. This behaviour of near constant bond-lengths with concentration is noted at high temperatures.

5.4.5   Temperature effects on Fourier transforms

Fitting high temperature experimental data for mixed systems is more difficult since these materials possess high levels of defects and makes detailed quantitative analysis more complex. However, in this study we are mainly concerned with changes in the local arrangement (structural information) of the neighbours of Cd and Pb cations with temperature. K and L_3 edge spectra of Cd and Pb cations, respectively, were obtained for each concentration in the temperature range 77 to 300 K.

Shown in Figures 5.10 and 5.11 are the Fourier Transforms for the Cd - and Pb – edges obtained for $CdF_2(xPbF_2)$ mixed crystals at T = 77 K and 300 K. Examination of the Fourier transformed data
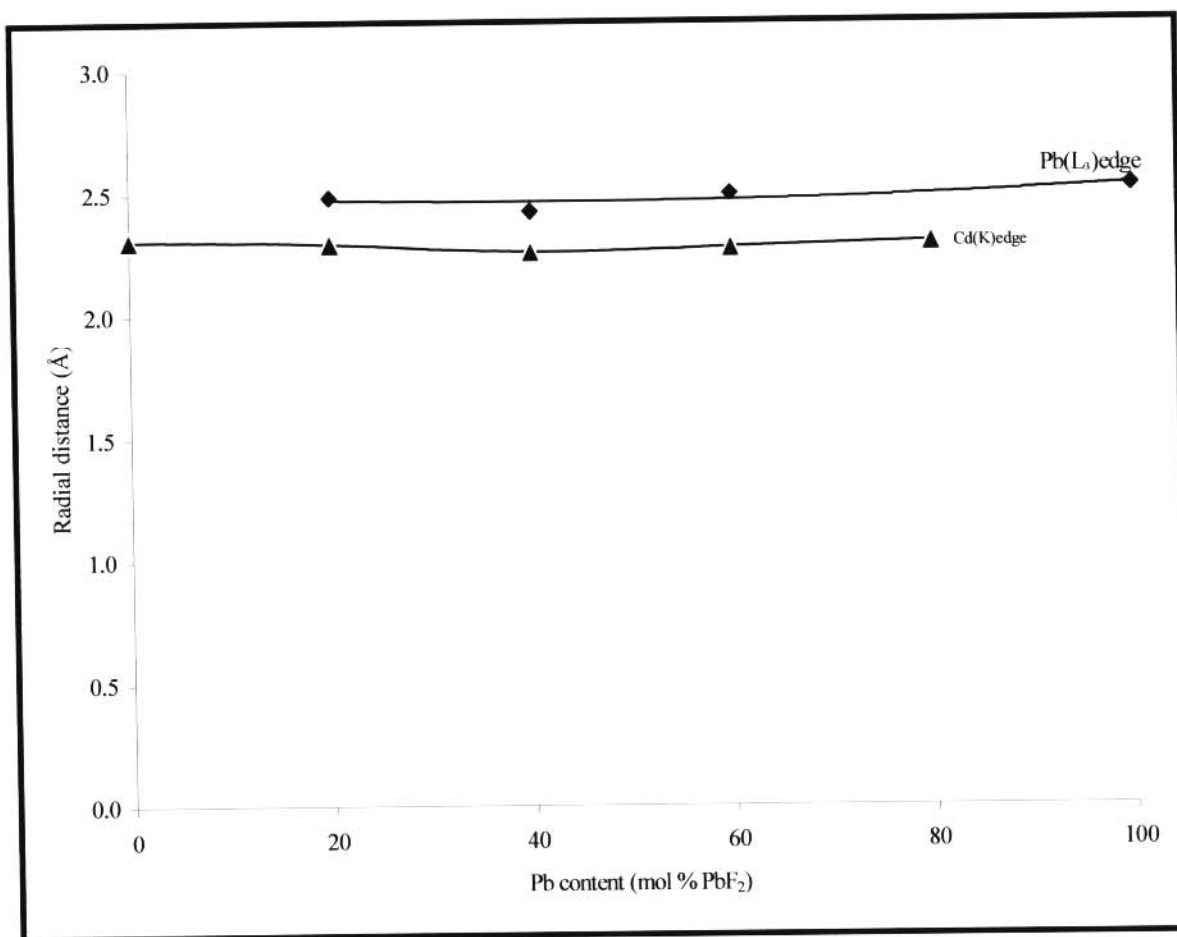
Figure 5.9 Pb-F and Cd-F nearest-neighbour distances as a function of composition *x* in CdF$_2$(*x*PbF$_2$) mixed crystals as measured by EXAFS at temperature T= 77 K.

Figure 5.10 Fourier Transforms of the EXAFS function for various samples x in $CdF_2(xPbF_2)$ crystals above the Cd (K) edge at temperatures T = 77(———) and 300 K (·······).

172
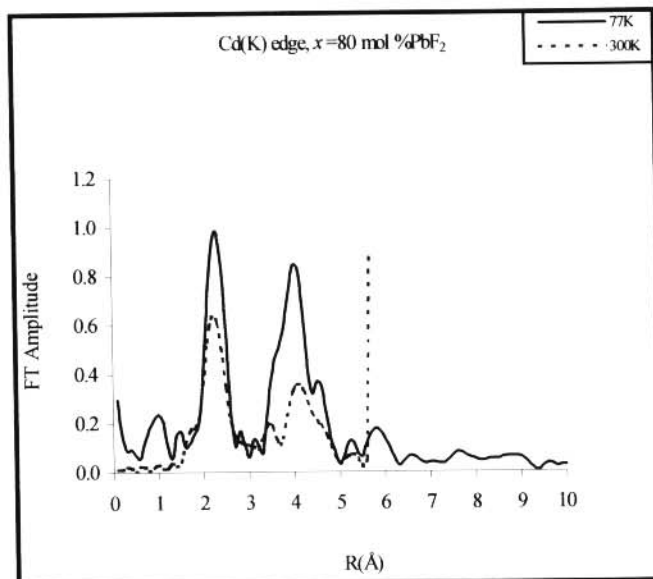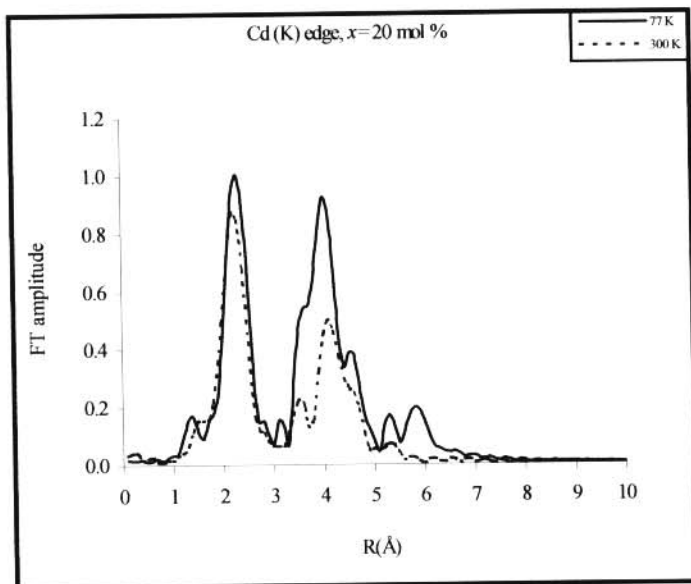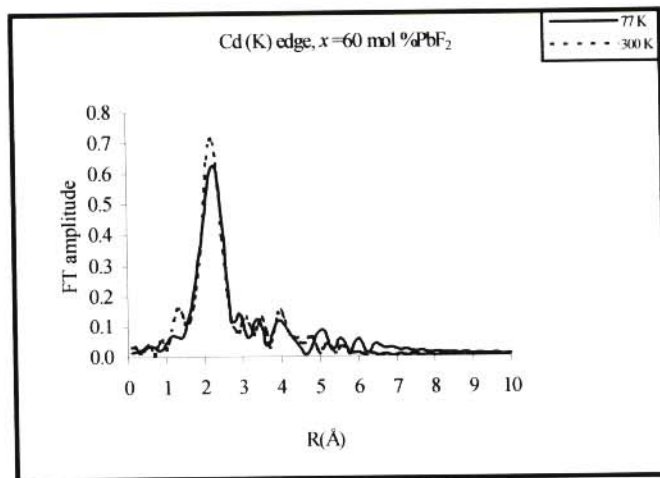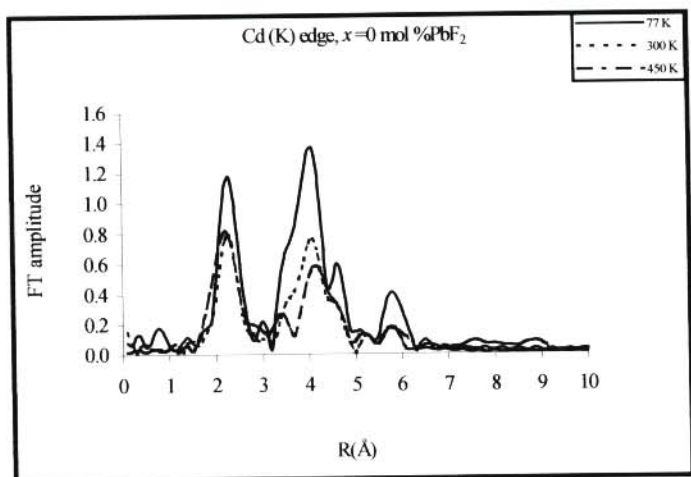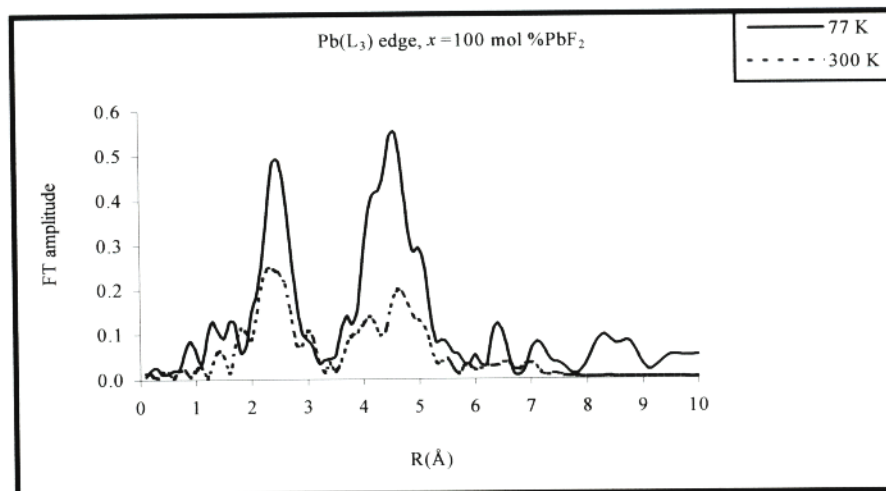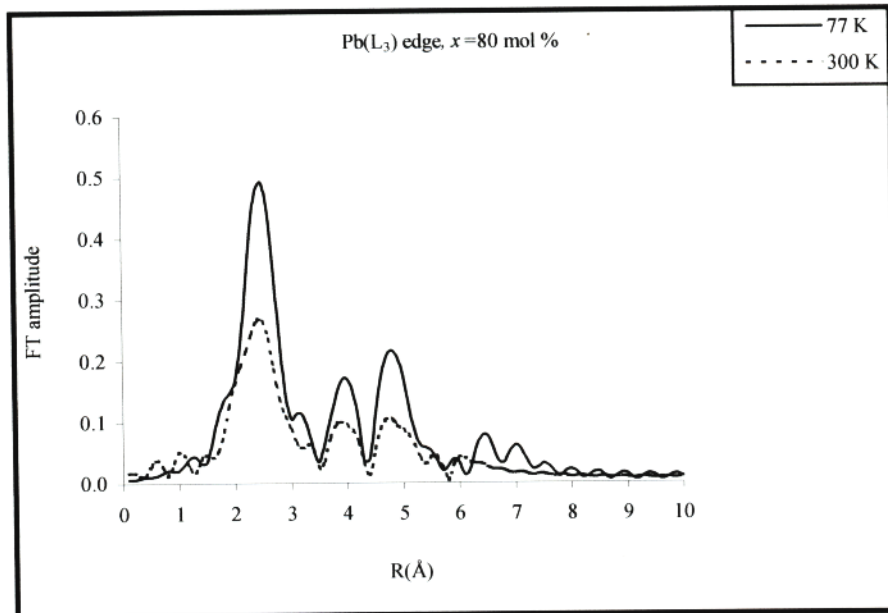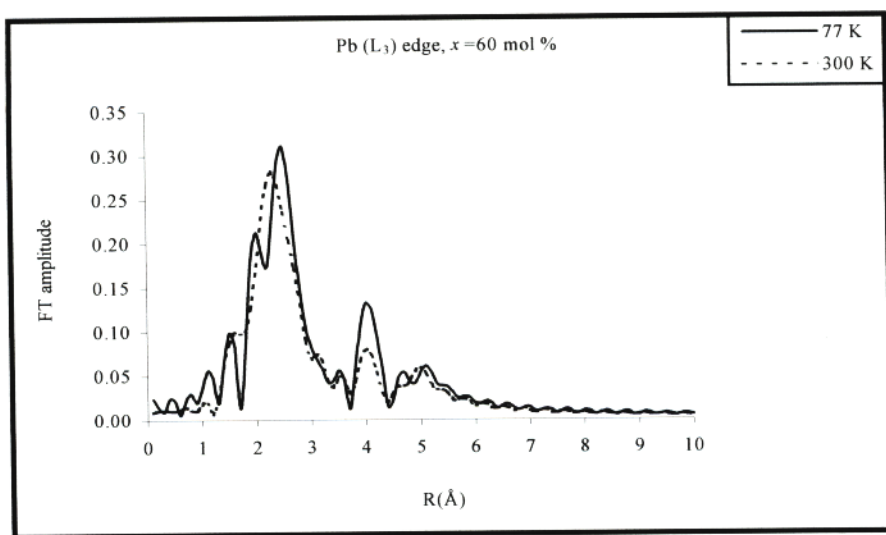
Figure 5.11 Fourier Transforms of the EXAFS function for various samples x in $CdF_2(xPbF_2)$ crystals above the $Pb(L_3)$ edge at temperatures T = 77 (———) and 300 K (·······).

173

(Figure 5.10) reveals that for the pure CdF_2 compound the structure is richer at low temperatures (e.g. at temperature T = 77 K). A two-peak structure was observed for CdF_2. As before, the first peak in Figure 5.10 corresponds to the Cd-F contribution whilst the second peak corresponds to the cation-cation contribution to the structure for CdF_2 (x = 0 mol % PbF_2). Both peaks (first and second) in Figure 5.10 tend to steadily go down with an increase in temperature (i.e. from 77 to 450 K). Comparatively, the first peak in the Cd-F RDFs for CdF_2 is sharper than for PbF_2 (x = 100 mol % PbF_2) in Figure 5.11. This implies that Cd adopts well-defined sites. Likewise for PbF_2, presented in Figure 5.11, a two-peak structure is observed with the second peak splitting into two and rapidly decreasing in amplitude with temperature increase until the structure ceases to exist at x = 60 mol % PbF_2. In short, the main difference between peaks for the Cd- and Pb- edges in the two binary compounds is on the magnitudes of the FT amplitudes and the rate of decrease with temperature (see Figures 5.10 and 5.11).

In the mixed crystals, i.e. for the composition range 0 mol %<x<100 mol % PbF_2, the two-peak structure is transformed into one peak for higher concentration x = 60 mol % PbF_2 and for higher temperatures (450 K and 500 K). This feature could be linked to destructive interference of amplitudes from Pb and Cd atoms. Hence, only a one-peak structure is observed for $x \approx$ 60 mol % PbF_2 (see Figures 5.10 and 5.11). The Fourier transform spectra for the Pb (L_3) edge show an increased broadening with temperature and peaks which progressively diminish over the given temperature range. This behaviour could represent a general phenomenon for mixed metal fluorites as a result of the extensive disorder in these materials (Cox et al. 1994).

174

5.4.6 Temperature effects on DW factors

Figure 5.12 shows the temperature dependence of the DW factors for Cd-F and Pb-F shells. Some of the main features shown in Figure 5.12 are: the values obtained for the solutions are larger than values obtained for pure compounds over the same temperature range and the plots in Figure 5.12 reveal that the DW factors increases linearly with temperature with the plot for the compound $x=60$ mol % PbF_2 showing large values for the DW factors in the Pb-F shells than in the Cd-F shells. This is in line with the discussion in section 5.4.3 on compositional dependence of the DW factors. In summary, the temperature dependence of the slopes of the DW factors for $x = 60$ mol % PbF_2 shows that there is a considerable thermal displacements within the Pb-F shell.

5.4.7   Temperature effects on bond-lengths

The temperature dependence of Cd-F and Pb-F bond-lengths for the compositions $x=0$ mol % PbF_2, $x=60$ mol % PbF_2 and $x=100$ mol % PbF_2 is shown in Figures 5.13 and 5.14. It is evident from Figures 5.13 and 5.14 that the positions of the various peaks vary with temperature. The general observation from the plots is that there is a reduction in cation-F separations in mixed solutions, which in turn is related to solution forming tendency. Thus, curves of the mixed crystals shift to shorter distances with increasing temperature. This is in line with the results from the work of Cox et al. (1994) on $PbSnF_4$. In addition, the Pb-F bond lengths are consistently longer than are Cd-F, i.e. the Cd-F bond lengths are consistently shorter than those for Pb-F distances. Hence, the first

175
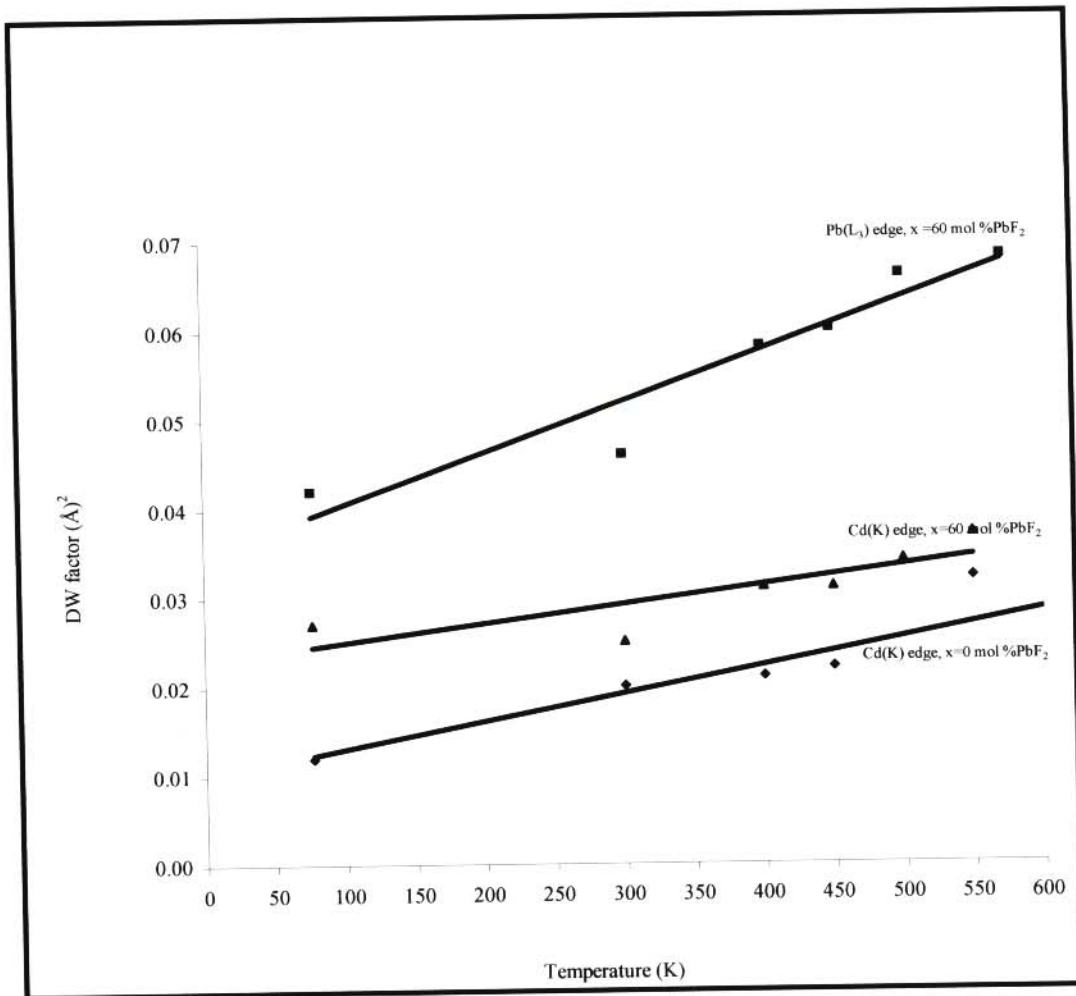
Figure 5.12 Variation of the DW factors for Cd-F and Pb-F as a function of temperature in $CdF_2(xPbF_2)$ mixed crystals.
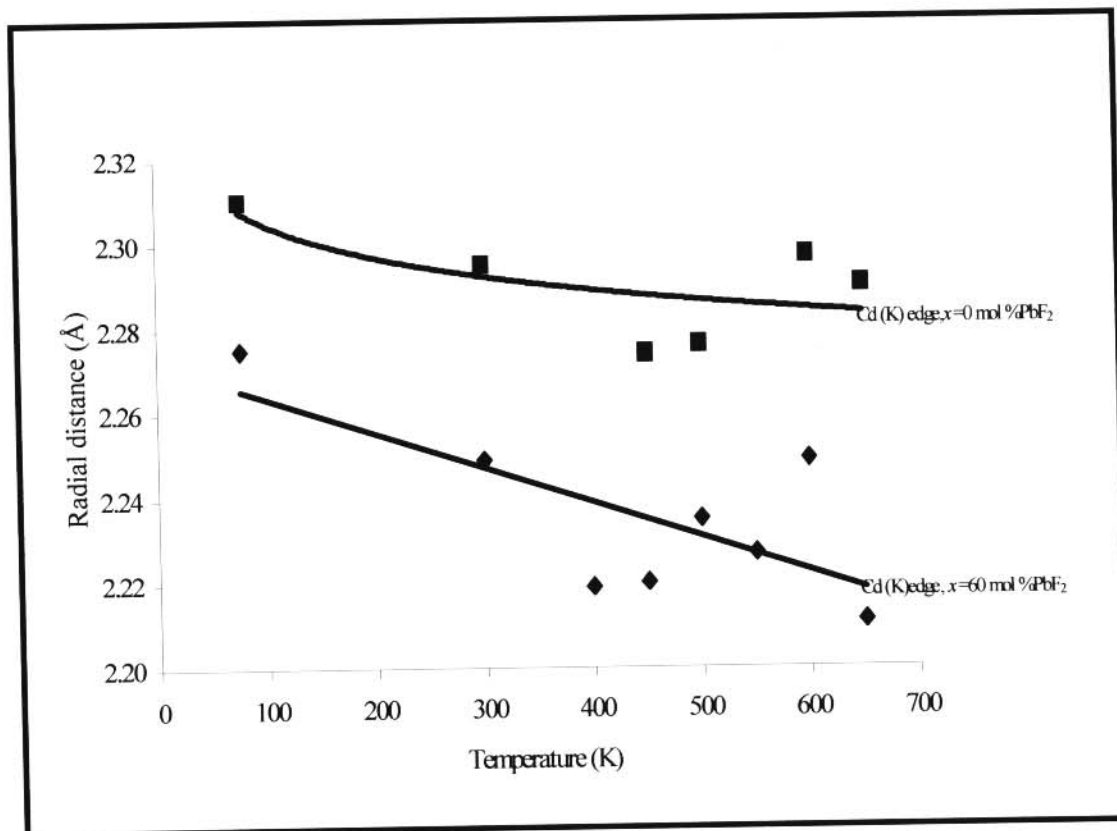
Figure 5.13 Temperature dependence of Cd-F bond lengths (r_{Cd-F}) in $CdF_2(xPbF_2)$ derived from the Cd K-edge.
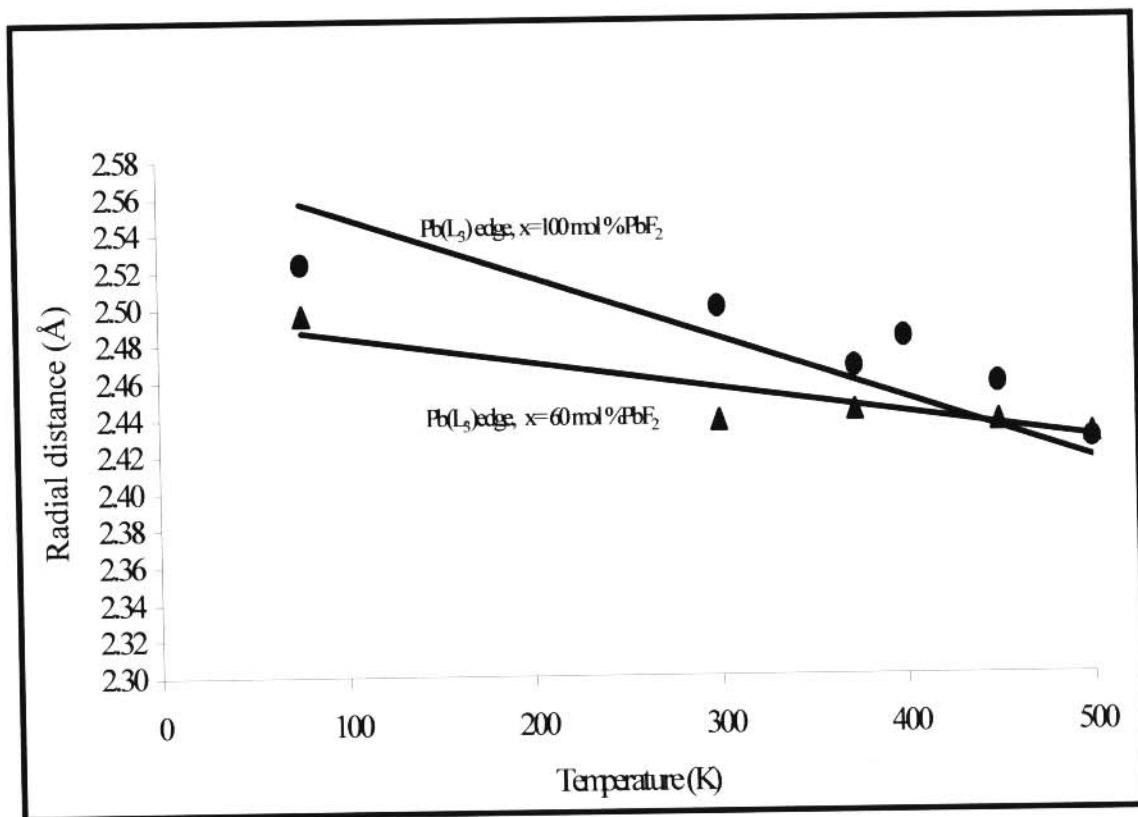
Figure 5.14 Temperature dependence of Pb-F bond lengths (r_{Pb-F}) in $CdF_2(xPbF_2)$ derived from the Pb L_3-edge.

neighbour distances correspond with the standard ionic radii. This phenomenon could be linked to the elastic and ion size arguments and the fact that both Cd and Pb (see Cox et al. 1994) share the same fluorine anion neighbours.

CHAPTER 6

COMPARISON OF THE EXPERIMENTAL AND SIMULATION

RESULTS

6.1   INTRODUCTION

The first part of this Chapter is devoted to the study of the local structures of the two cations (i.e. Cd and Pb ions) separately by means of EXAFS spectroscopy. Computer modelling technique is used to provide complimentary information on these features.

6.2   EFFECTS OF COMPOSITION AND TEMPERATURE ON THE PROFILES OF THE FOURIER TRANSFORMS/RADIAL DISTRIBUTION FUNCTIONS

Fourier transforming EXAFS data produces an approximate radial distribution function (RDF), in which features at low distances are more dominant (see Catlow et al. 1989). Figure 6.1 compares the calculated and experimental data for the Cd-F peaks in $CdF_2(xPbF_2)$ mixed solutions. However (as shown in the Figure), only selected peaks in the mixed solutions were monitored to ensure clarity in the presentation of the results. Moreover, the height of the Cd-F peak for the $x = 0$ mol % PbF_2 sample is far greater than peaks for other concentrations from calculations. Hence, the Cd-F peak

180

for the sample $x = 0$ mol % PbF_2 has been left out for clarity. As reported earlier (see sections 4.4.10 and 5.4.2), the first peak in the RDFs represents the cation-fluorine interaction. As may be seen from the two Figures, the calculated curves qualitatively reproduce the pattern of the FTs's variation with concentration x for the temperature $T = 77$ K. For short distances (less than 1.5 Å) the RDF is nearly zero. This is due to the strong repulsive forces (see discussion in Chapter 2). Furthermore, in all cases, it is clear that high (maximum) peaks at liquid nitrogen temperature (77 K) occur at lower values of the RDFs. Hence, there is no long-range order. This also indicates that the probability of finding two atoms (Cd^{2+} and F$^-$) within a distance r ~ 2.20 Å (or of finding F$^-$ atom/ion at a distance from the Cd atom) is high compared to the ideal gas distribution. It is quite gratifying to note that both experimental and modelling results reveal a minimum curve for the $x = 60$ mol % PbF_2 sample. This is in line with the results from the Raman scattering work of Kosacki et al. (1989). Furthermore, the present calculations of the conductivity have shown considerable enhancement in the ionic mobility on doping (i.e. when a cadmium ion is replaced by a lead ion of larger ionic radius) and a concomitant reduction of the activation energy for the conduction process for the $x = 60$ mol % sample in $CdF_2(xPbF_2)$ mixed crystals (see Chapter 4). The conductivity was shown to be anionic in nature. However, the experimental profiles are broader and less pronounced than those in the calculations. The explanation could be the polarization effects which were neglected in the calculations. Similarly, Figure 6.2 shows the concentration dependence of the Pb-F Fourier Transforms/RDFs (Figures 6.2(a) experimental and 6.2(b) computational results) for the various samples in $CdF_2(xPbF_2)$ mixed crystals. The Pb-F profiles vary with concentration x in a similar fashion as for the Cd-F profiles. Thus doping increases the disorder around both cations (i.e. Cd and Pb ions). However, the Pb-F profiles are broader than those for the Cd-F across the entire

181

Figure 6.1 The concentration dependence of the Cd-F RDFs at T = 77 K in CdF$_2$(xPbF$_2$) crystals. (a) present experimental work (b) present calculations. In (b), the Cd-F peak for the x = 0 mol % sample has been left out for clarity purposes since it is far greater than peaks for other concentrations from calculations.
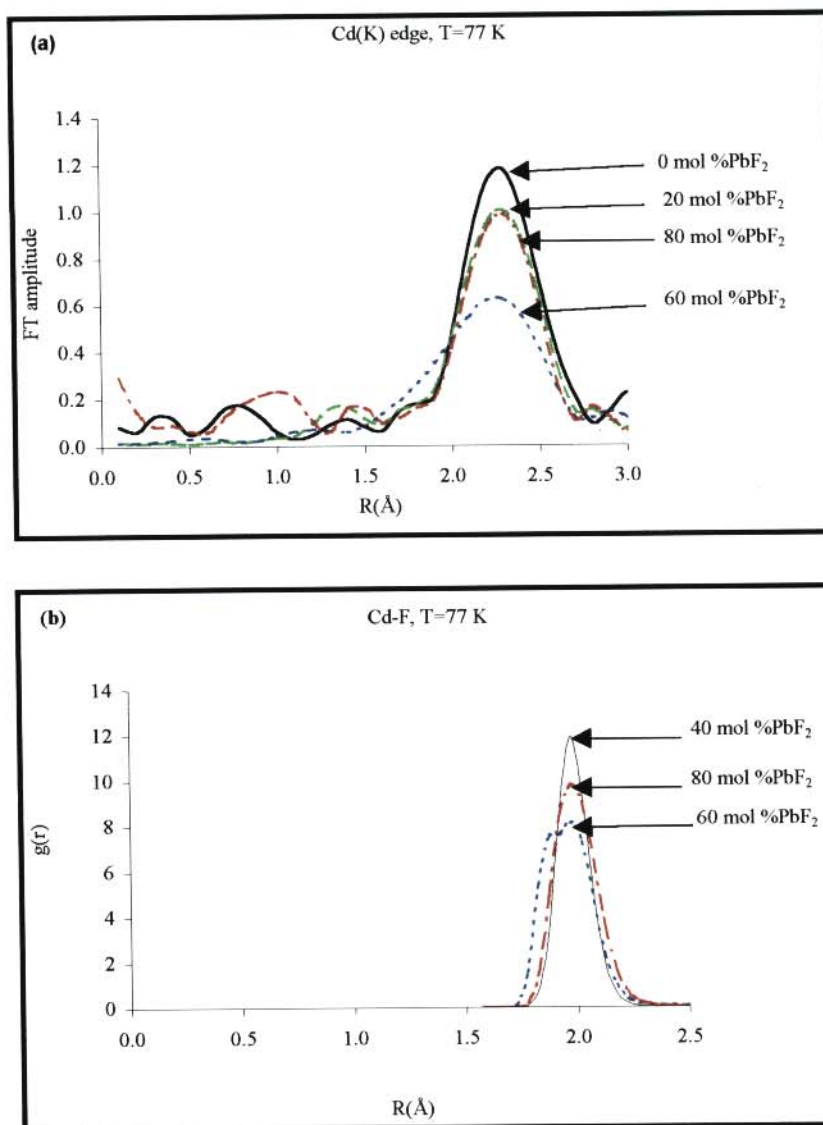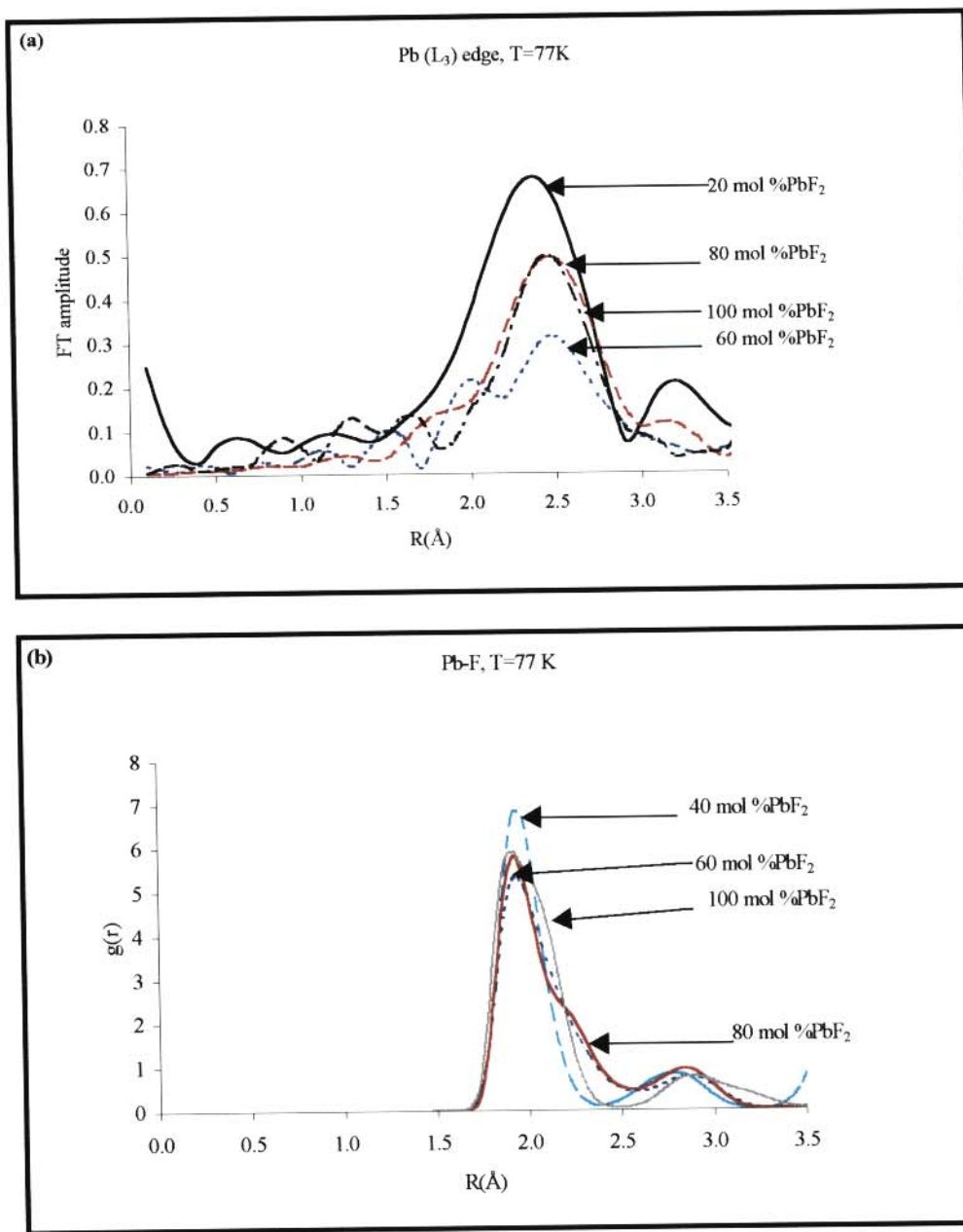
Figure 6.2 The concentration dependence of the Pb-F RDFs at T = 77 K in CdF$_2$(xPbF$_2$) crystals. (a) present experimental work (b) present calculations

composition. This suggests the predominance of static disorder in the Pb-F coordination shell, or simply stated, static disorder around the Pb ions is greater than around the Cd one. Hence, the neighbourhoods of the Cd and Pb ions are not the same. These features are quite consistent with earlier findings from Raman scattering spectroscopy studies of Kosacki et al. (1989). The experimental Fourier Transforms for the two-cation edges and their respective computational data indicate that the experimental Cd-F peaks are systematically higher than the calculated curves (see Figures 6.3a and 6.3b). Hence, the present calculations qualitatively describe the basic features of the real materials.

Figures 6.4 and 6.5 display reductions in the height of the first peaks of the Cd-F and Pb-F RDFs/FTs as the temperature increases. In all cases, there is good agreement between experimental and computational results and minor discrepancies are probable within the errors of the experimental results and the uncertainties in the calculations attributable to the quality of the interionic potentials. The significant broadening of the Pb-F peaks (see Figure 6.5) with an increase in temperature is ascribed to extra F^- vacancies which are present in interstitial sites. These features suggest that the local environment of Pb^{2+} ions is more disordered than that of the Cd^{2+} ions. A similar behaviour was noted by Cox et al. (1994) in their study on $PbSnF_4$. Consequently, more F^- vacancies are located around the Pb^{2+} cations in the fluorite structure of the CdF_2-PbF_2 systems than near the Cd^{2+} ions.
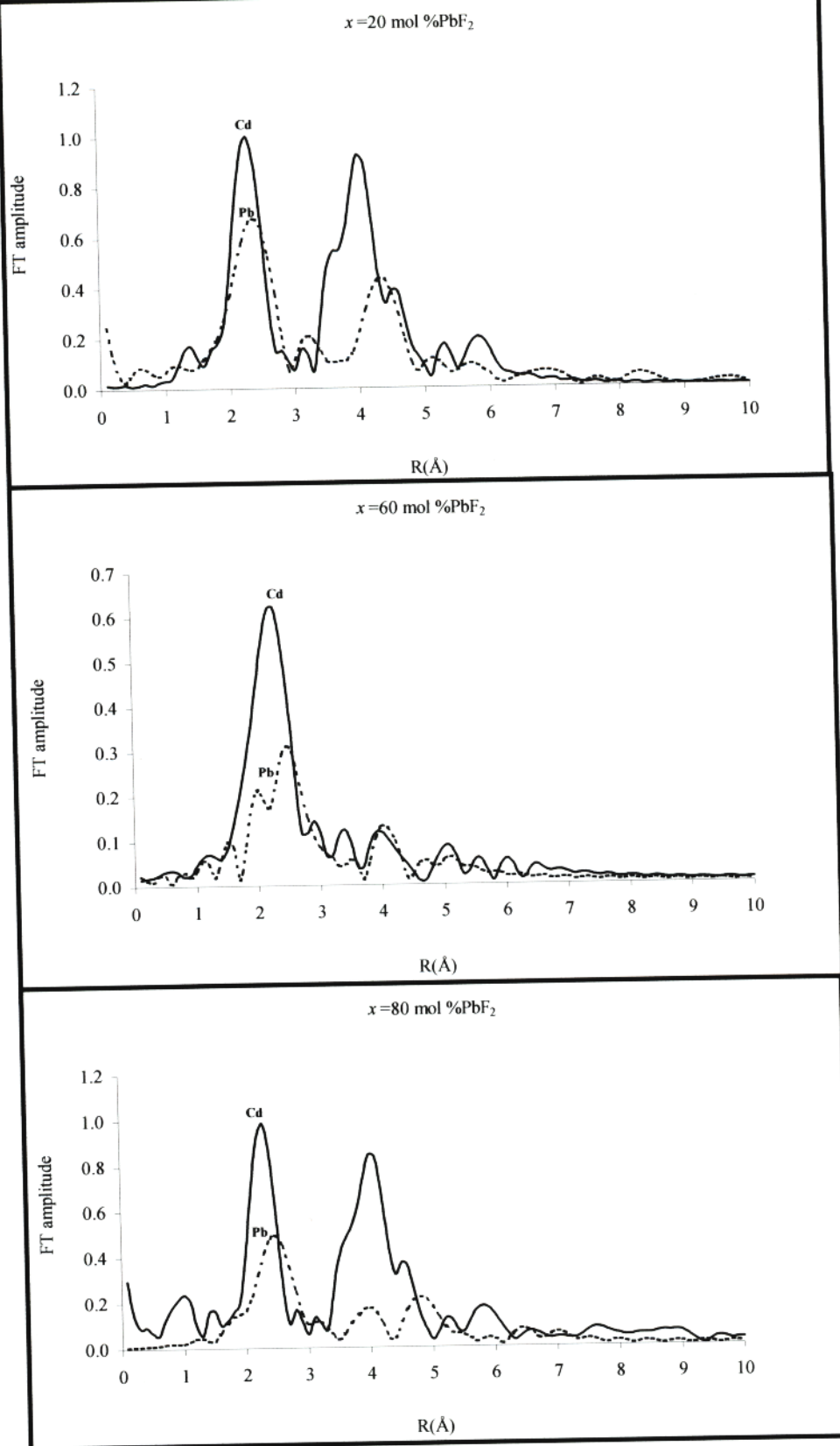
Figure 6.3a Comparison of the Cd-F and Pb-F radial distribution function (in CdF$_2$(xPbF$_2$) mixed solutions) from EXAFS at T=77 K.

185
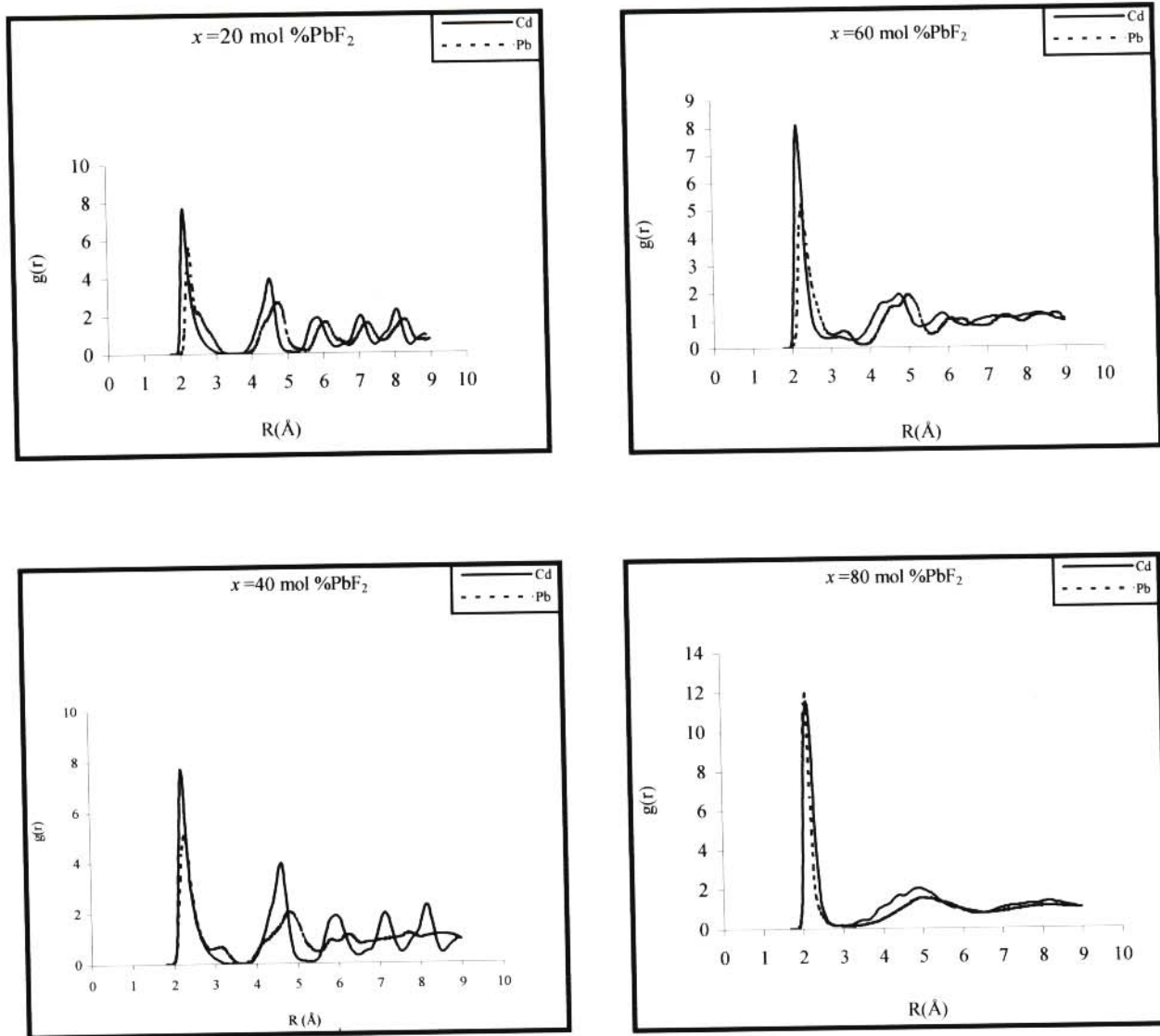
Figure 6.3b Comparison of the Cd-F and Pb-F radial distribution function (in $CdF_2(xPbF_2)$ mixed solutions) from calculations at T=77 K.
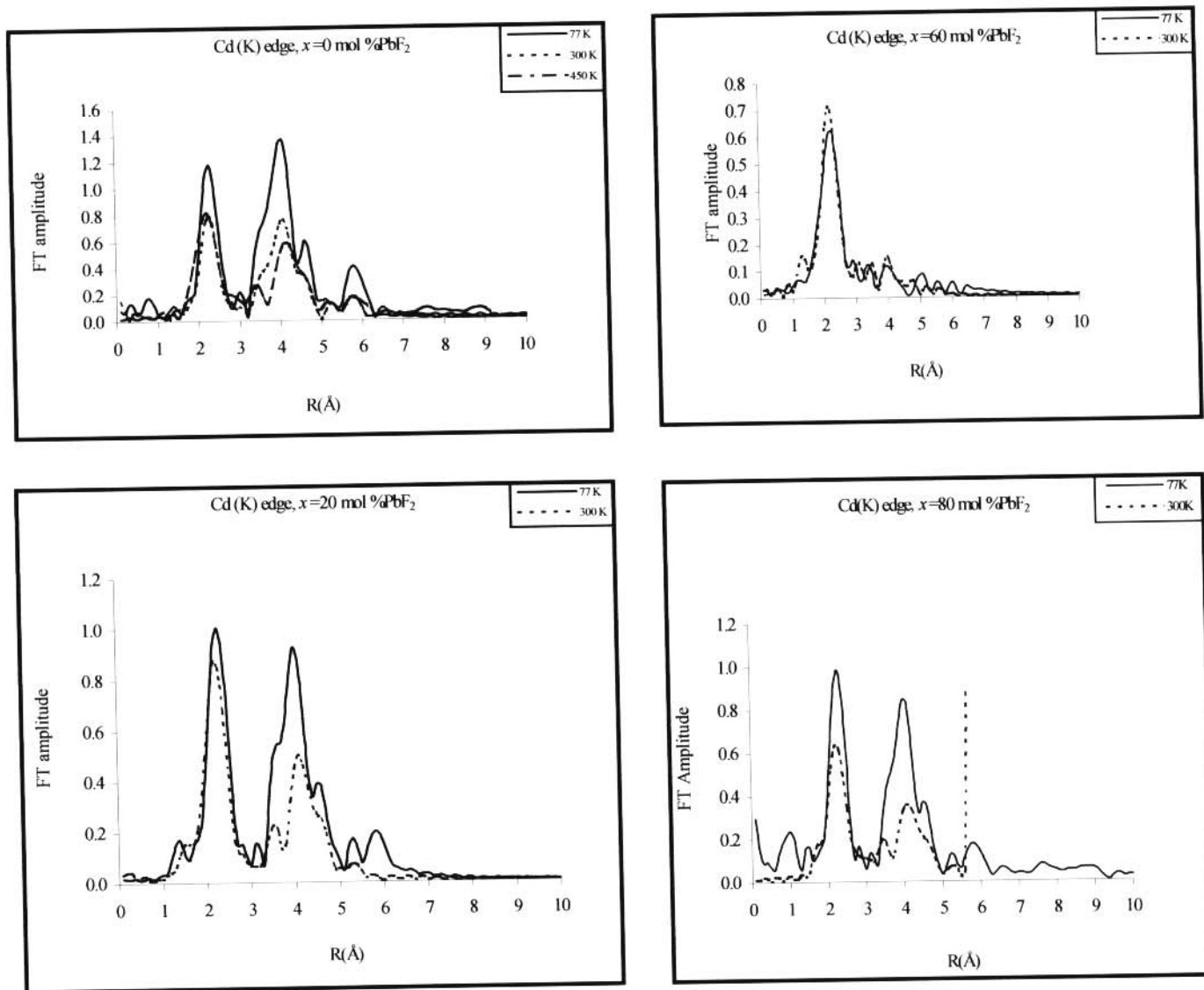
Figure 6.4a Cd-F experimental FTs for various samples at temperatures T = 77 and 300 K, respectively, in $CdF_2(xPbF_2)$.
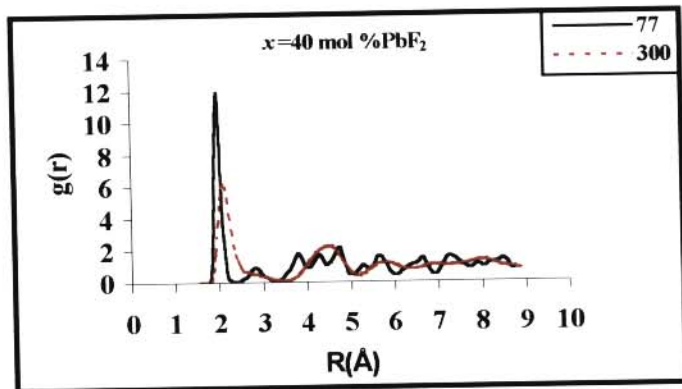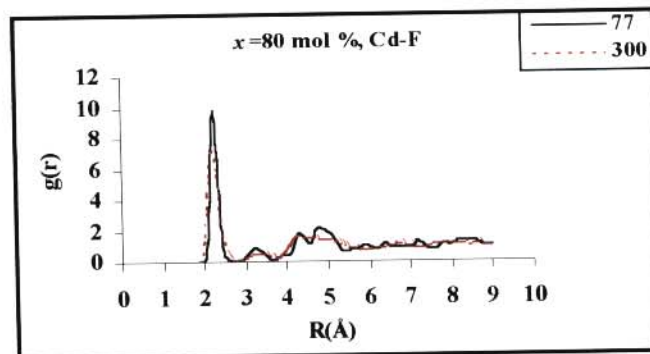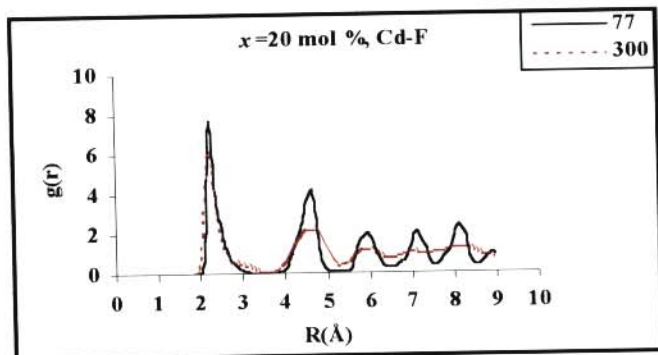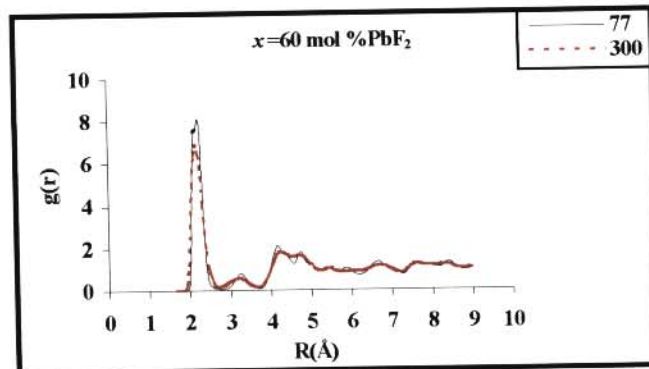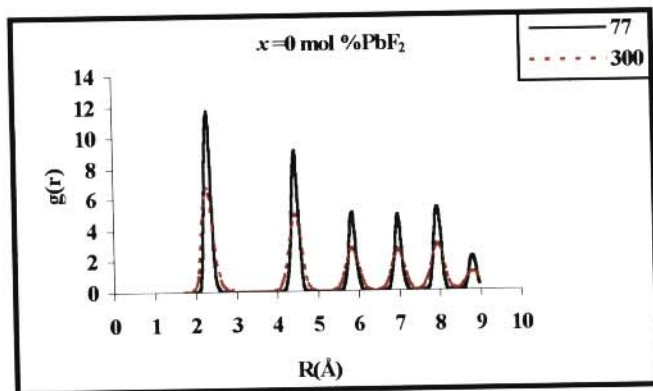
Figure 6.4b The calculated temperature dependence of the Cd-F RDFs at various concentrations x in CdF$_2$(xPbF$_2$).
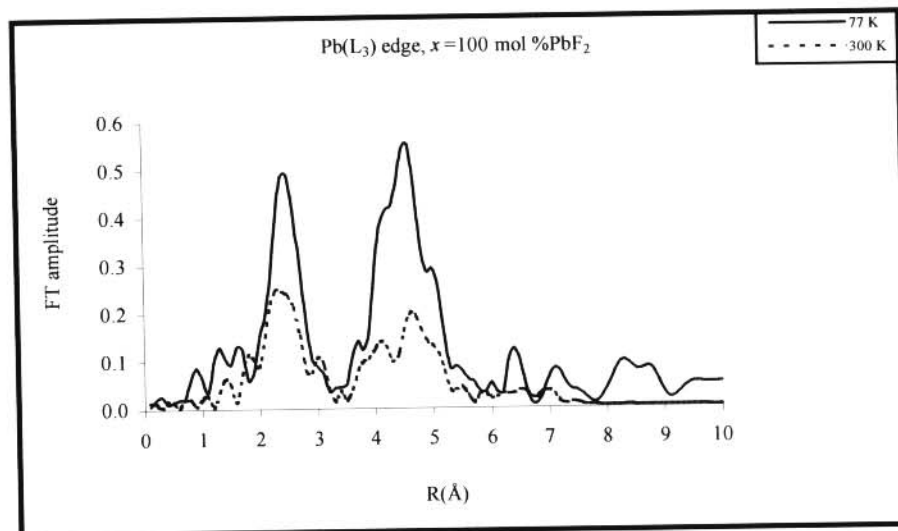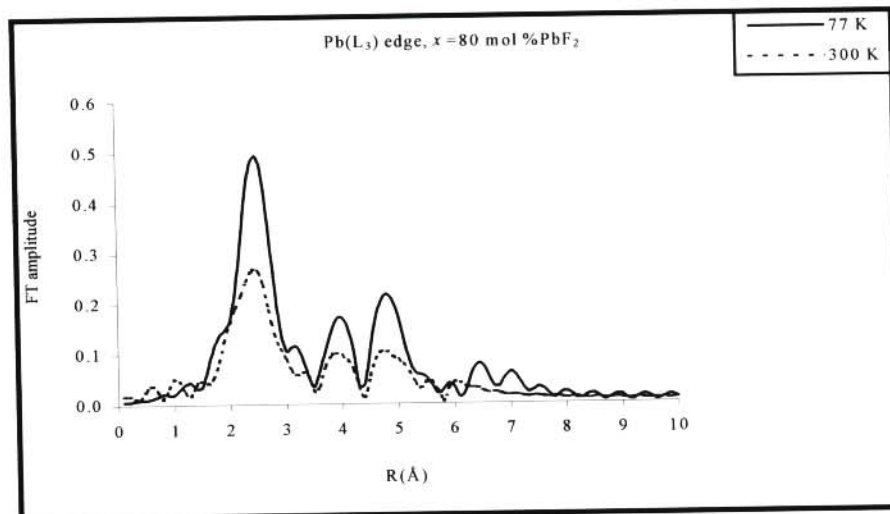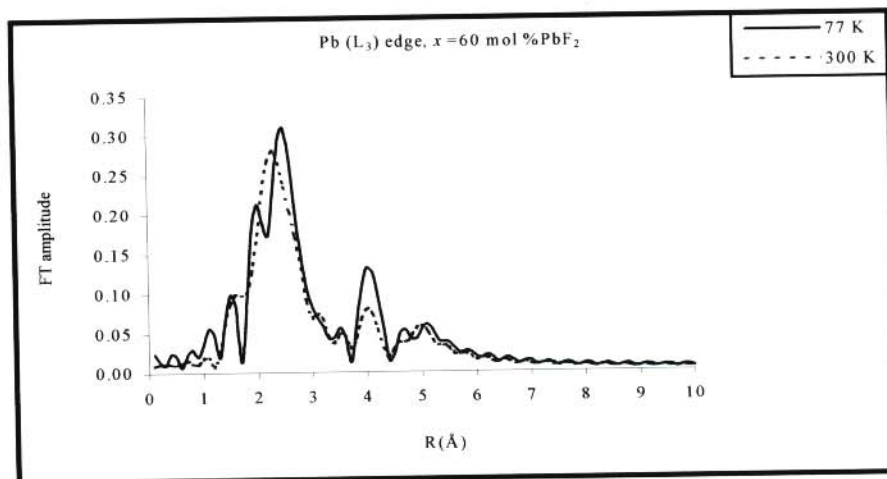
Figure 6.5a Experimental temperature dependence of the Pb-F FTs at various concentrations x in $CdF_2(xPbF_2)$.
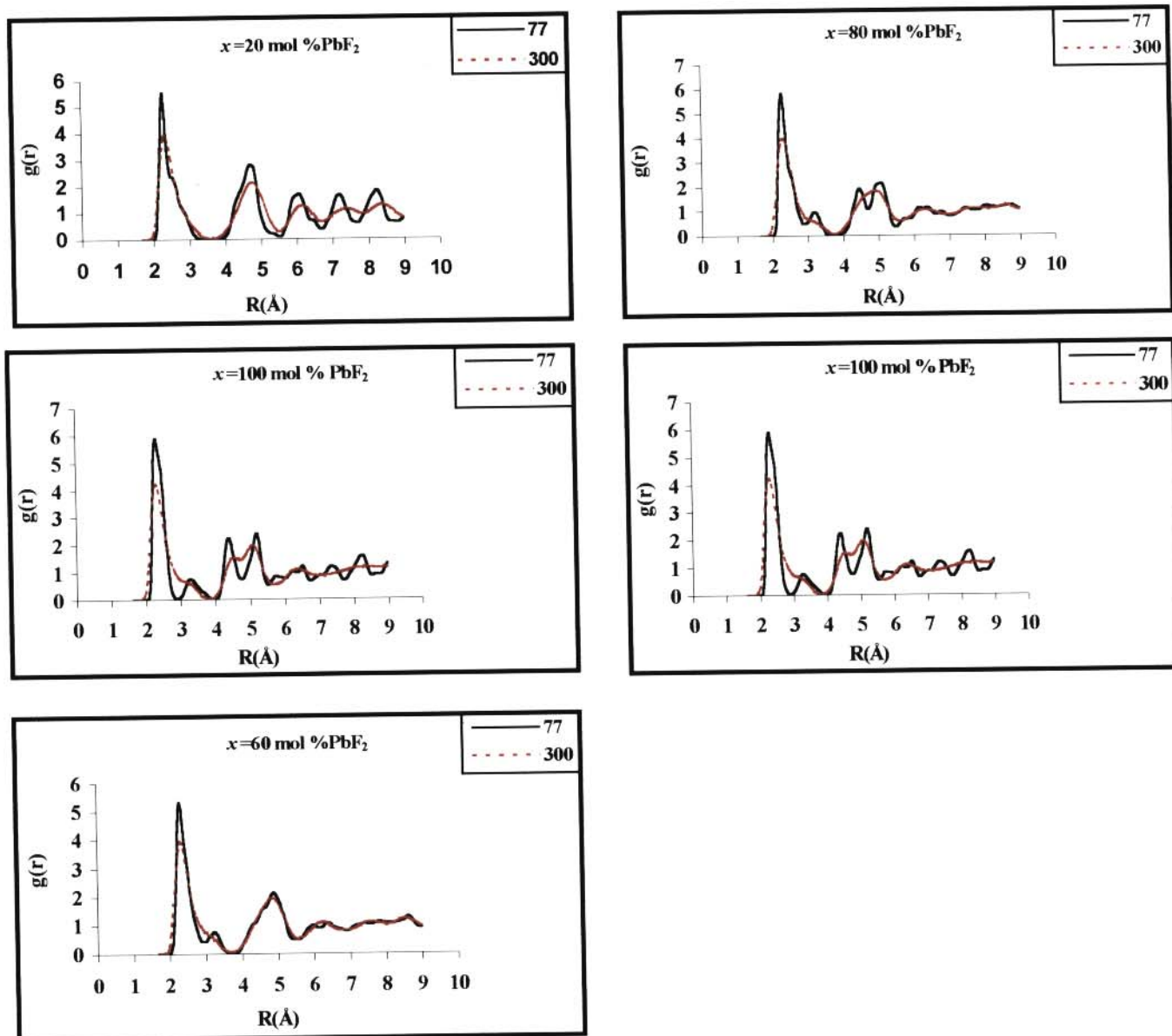
Figure 6.5b Calculated temperature dependence of the Pb-F RDFs at various concentrations x in

$CdF_2(xPbF_2)$.

6.3   THE F-F RADIAL DISTRIBUTION FUNCTIONS (RDFs) AND MEAN-SQUARE DISPLACEMENTS (MSDs) OF F- IONS IN CdF$_2$(xPbF$_2$) SYSTEMS

The temperature dependence of the MSDs curves in the CdF$_2$(xPbF$_2$) systems (shown in Figure 6.6) shows that the F$^-$ ion species are mobile at T = 700 K for systems x = 40 mol % - 100 mol % PbF$_2$. The transition temperatures T$_c$ to the fast-ion phase for pure CdF$_2$ and x = 20 mol % PbF$_2$ doped system are ~ 1000 K (see Figure 4.1(a)) and ~ 800 K (see Kosacki et al. 1989), respectively. It also appears from Figures 6.6. and 6.7 that diffusion in the 40 mol % - 100 mol % PbF$_2$ concentrations occurs at temperatures below and above T$_c$. Ngoepe and Catlow (1991) arrived at similar conclusions for CaF$_2$ (10 mol % LaF$_3$) doped fluorine ion conductors. In Table 6.1 we present details of the observed transition temperature T$_c$ in pure and doped samples of CdF$_2$(xPbF$_2$) (see Kosacki et al. 1989). It is clear from the Table that T$_c$ moves to lower temperatures with increasing doping until a 60 mol % PbF$_2$ dopant concentration (corresponding to T$_c$ = 485 K) is reached, beyond which an increase in T$_c$ is noted. The transition temperature marks the disappearance of long-range order, which is order over many interatomic distances.

The RDFs for the F-F interactions at T = 300 and 700 K are shown in Figure 6.8. These results complement those from the MSDs of the F$^-$ ion species in many respects: namely, at higher temperatures; the peaks become smaller in height and correspondingly broader as the amplitude of vibration of the ions around the lattice sites increases; the second shell/peak at a position between 3.0 and 4.0 Å disappears at concentrations beyond x = 40 mol % PbF$_2$. In addition, it is apparent from Figure 6.8 that the first peak becomes broader at concentration x = 60 mol % PbF$_2$. Hence, it suffices

191

to say that radial distribution function is a good qualitative indicator of atomic motion, for if rapid

diffusion is occuring on one sublattice (e.g. F⁻ in $CdF_2(xPbF_2)$), the self-correlation function, g(r),

indicates this by the presence of small and broad overlapping peaks.

Table 6.1 Transition temperatures for $x = 0$ to 100 mol % PbF_2 in $CdF_2(xPbF_2)$ systems.

Concentration, x (mol %)	Transition temperature, T_c (K)
0	1000
20	800
40	650
60	485
80	560
100	715
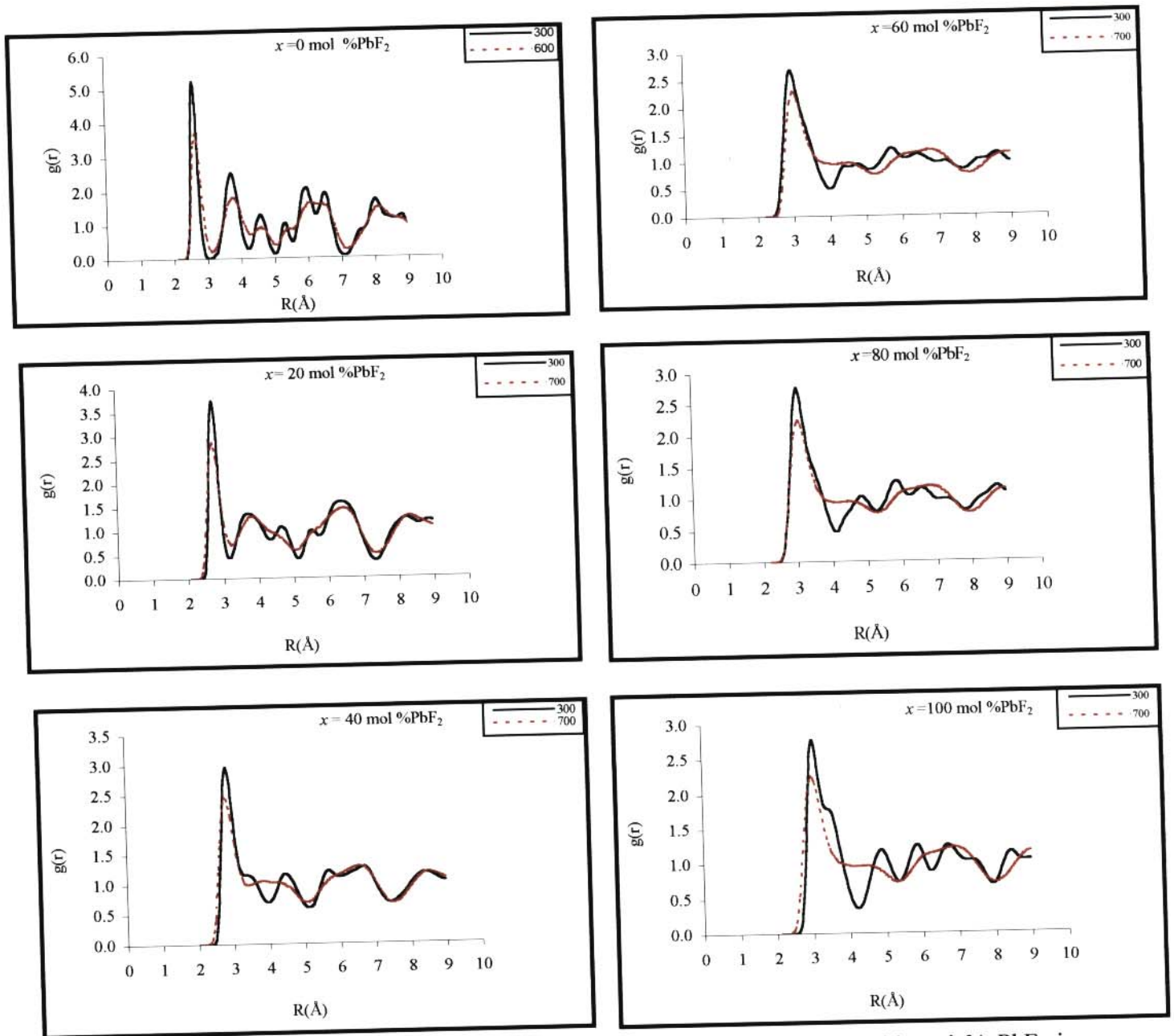
Figure 6.8 Radial distribution functions from F-F for samples $x = 0$ mol $- 100$ mol % PbF_2 in $CdF_2(xPbF_2)$ at various temperatures (T= 300 and T = 700 K)
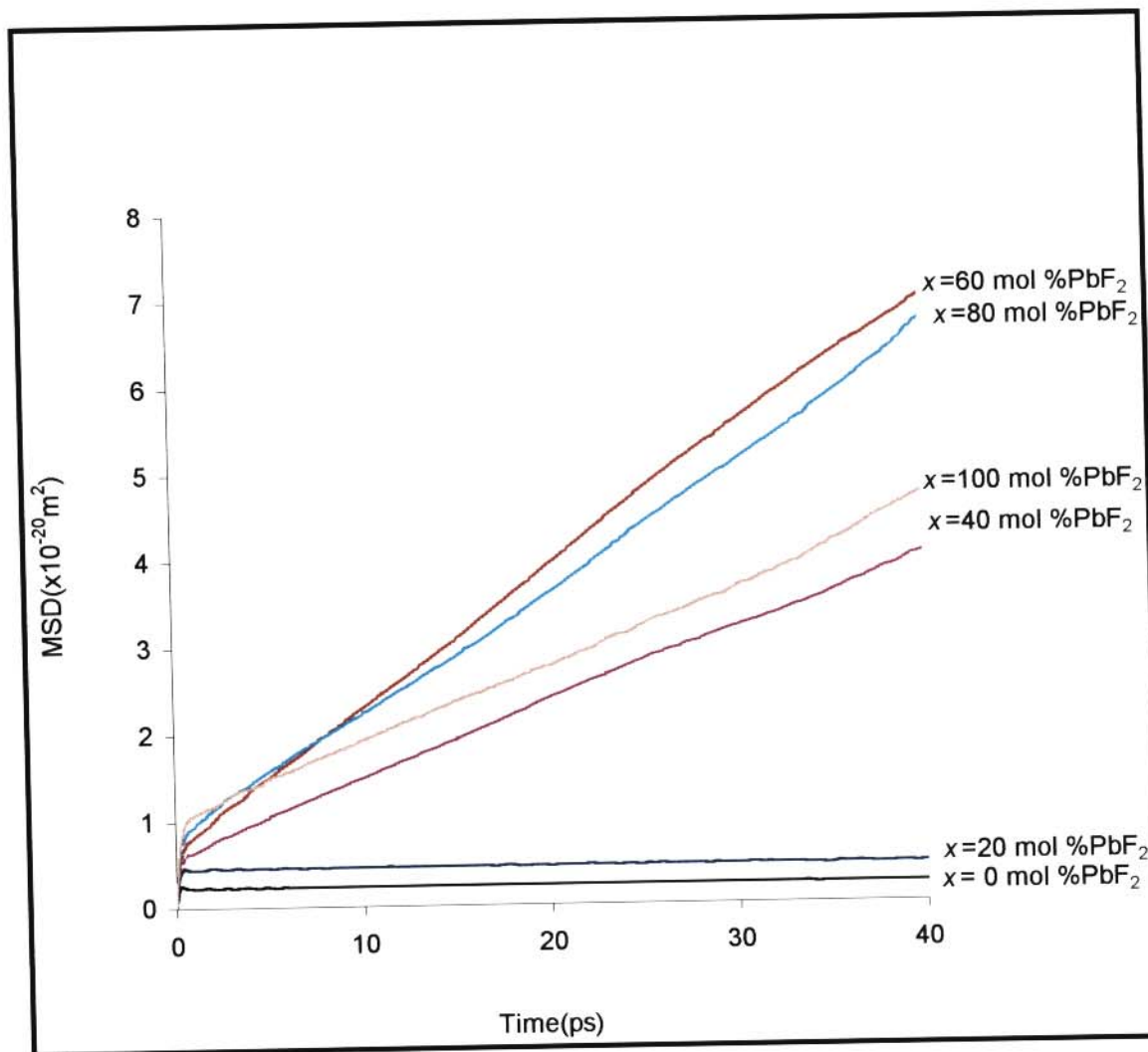
Figure 6.6 Mean square displacements of fluorine ions in various concentrations of PbF_2 in $CdF_2(xPbF_2)$ at T = 700 K.
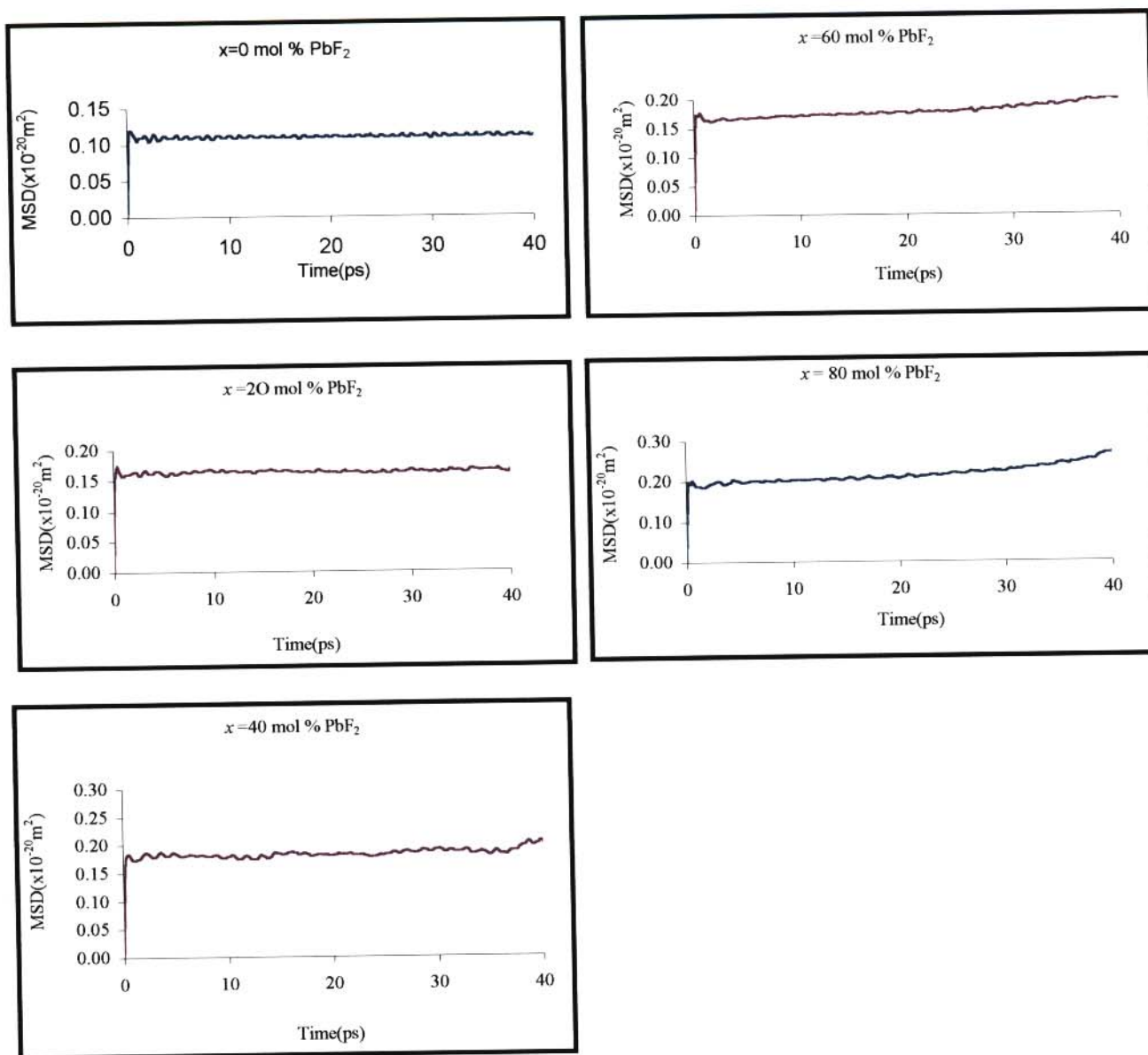
Figure 6.7   Mean square displacements of fluorine ions in various concentrations of   PbF$_2$ in

CdF$_2$(xPbF$_2$) at T = 300 K.

CHAPTER 7

CONCLUSIONS AND RECOMMENDATIONS

7.1   CONCLUSIONS

The work described in this thesis is the first EXAFS study of the $CdF_2(xPbF_2)$ mixed metal fluorites and provides an explanation of the ionic conductivity. The current study was mainly directed at a detailed understanding of structural and dynamical properties/features of mixed-metal fluorites in relation to high ionic conductivity. Hence, the investigation of the compositional and temperature dependence of the physical properties of $CdF_2(xPbF_2)$ solid solutions has been undertaken. Although (limited) information on the material under discussion is available, an important feature here has been the combined use of theory and experiment. The fair agreement between the molecular dynamics simulations RDFs and EXAFS results confirms the strong links between the simulations and experiment and adds confidence to the model structures. The poor agreement of the radial distribution distances with the results from EXAFS must be attributed to the failure of the model to account for thermal motions and polarisability in this material, in which the ions are particularly mobile, even at low temperatures.

The shortening of measured interatomic distances with increase in temperature in mixed solutions as noted in the current study, has already been encountered in other fluorite structured mixed cation

systems such as $PbSnF_4$. A possible explanation is that in these solutions the metal-fluorine bonds are less balanced by long-range order than they are in pure compounds.

The present model successfully allowed the identification of the mobile species and the nature of the conductivity. While these mixed metal fluorites are highly conducting at room temperature, they have considerably lower transition temperatures than those of their pure counterparts. Calculations of diffusion coefficients and RDFs obtained from the current MD simulations (modelled using rigid-ion potentials) confirm that the anions are the mobile species, whilst the cation sub-lattice remains essentially ordered. This is in line with the already recognised understanding that an ion (F^- ions are smaller than either Cd^{2+} or Pb^{2+} ions) hopping from one site to another must be small. Hence, we postulate that cations provide immobile 'lattice' through which the small (mobile) F^- ion can migrate. Furthermore, the present study shows that cations in mixed metal fluorites do not contribute to diffusion up to the highest temperature studied, $T = 700$ K. Hence, the calculated MSDs, diffusion coefficients and RDFs are generally in agreement with previous MD results on mixed metal fluorites such as $RbBiF_4$ (Catlow et al 1989), and perovskite-type oxides such as $LaMnO_3$ and $LaCoO_3$ (Islam 1996).

The ionic conductivity results from our MD calculations did allow the most important qualitative features of the experimental data (i.e., the observation of a maximum/peak in the σ vs. Pb content x curve) to be reproduced. The information on the activation energy (E_a) for conduction indicates the opposite trend, where the activation energy decreases with an increase in the dopant level. This tendency can be ascribed to the distribution of the conducting ions among the available interstitial

197

sites. Cox's (1994) and Matar et al.'s (1982) work on $RbBiF_4$ and $PbSnF_4$, respectively, found similar results. The resulting vacancies and the corresponding interstitials contribute to the enhanced ionic conductivity. Our computer modelling work predicts that 60 mol % PbF_2 doped CdF_2 crystals exhibit the lowest activation energy of conductivity in the class of $CdF_2(xPbF_2)$ crystals, in agreement with Raman scattering studies of Kosacki et al (1989). In addition, our calculations correctly predicted the maximum conductivity at $x = 60$ mol % PbF_2, which agrees with that of Kosacki et al. (1989). Hence, these crystals show the best fast-ionic properties than the other $CdF_2(xPbF_2)$ crystals. Thus, we have presented a qualitative picture of the ionic conductivity variations of a typical mixed metal fluorite.

The present work represents the first attempt to compute the complete set of elastic constants (C_{ij}) (which determine how a material responds to the application of external conditions such as stress, pressure, temperature, etc.) and their temperature dependences in $CdF_2(xPbF_2)$ mixed-metal-fluorites by means of computer modelling techniques. The calculations give C_{11} larger than C_{12} and C_{44}. This phenomenon is well known for pure fluorine ion conductors such as CaF_2, PbF_2, etc. The values of the elastic constants are compared with those from previous experiments (for the pure components of the alloy). They show a linear decrease in all the elastic properties with increasing Pb composition and the decrease is associated with the absence of phase transition/transformation since the mixture remains cubic (phase) for the whole composition range. Hence, the variation in elastic constants is only due to the composition change of the mixed systems. Perhaps the most significant result from the simulation is that all the elastic properties decrease with increasing bond-length (interatomic distances).

The temperature dependence of the second-order elastic constants (i.e. C_{11}, C_{12} and C_{44}) suggests that all three coefficients have the same characteristics as for the pure components of the $CdF_2(xPbF_2)$ mixed systems. This could be attributed to the similarity in the crystal structure in the entire crystal structure. Thus C_{11} is strongly dependent on temperature as opposed to C_{12} and C_{44} which are non-dependent. A feature to note is that doped crystals have smaller values of C_{ij} than in pure CdF_2. The dielectric constant ε_s increases when the mixed system changes from CdF_2 ($x = 0$ mol % PbF_2) to PbF_2 ($x = 100$ mol % PbF_2). This result is in excellent accord with the experiment. The plots reveal a steady increase in ε_s for $x<60$ mol % PbF_2 and a linear beond $x = 60$ mol % PbF_2. Thus the curvature on ε_s vs. x plot commences just below $x = 60$ mol % PbF_2. Calculations on defect properties of $CdF_2(xPbF_2)$ mixed systems have shown that Frenkel disorder is a more prevalent mode of transport in both CdF_2 and PbF_2, in accordance with experiments.

In general, the cation-cation RDFs consist of a series of sharp and well-separated (resolved) peaks corresponding to successive NN distances. Hence, cations are strongly localised on regular lattice sites. This is a normal trend for an ordered solid and is in agreement with MD studies on perovskite-type oxides (Islam et al. 1996) and yttria-stabilized-zirconia (YSZ) (Shimojo et al. 1992 and Chaba 2000). However, the F^--F^- peaks are broader with small maxima and for separations larger than NN (first peak) shells are barely resolved (i.e. they show featureless structure). This implies that the anions form a weakly correlated sub-system, which is indicative of the loss of long-range order on the mobile fluorine sub-lattice. Such disorder is expected for F^- ions, which are highly mobile on the molecular dynamics timescale. Furthermore, the Cd-Cd distances are shorter than those for Pb-Pb. The shorter Cd-Cd distances are due to strong Coulomb attraction between Cd ions and the fluorine

ion. Cd-F distances are also shorter than those for Pb-F in all cases. This implies that fluorine ion is shifted to the Cd ion from the normal fluorite position by the presence of the dopant Pb ion. Moreover, the Cd-F curves are sharper than the Pb-F curves, indicating that the local structural environment of Pb^{2+} ions is more disordered than of the Cd^{2+} ions. This could be linked to the disparity in the ionic radius/size between Cd^{2+} and Pb^{2+} ions. These differences are understandable if anion vacancies are sited adjacent to Pb than Cd with ensuring relaxations of ions in the vicinity of the vacancy increasing the degree of static disorder in the Pb coordination shells and maximising the proximity of the larger cation to its fluorine neighbours.

In addition, the Debye-Waller factors for the mixed metal fluorites are considerably greater than those for pure compounds. This is an indication of the presence of extensive short-range order in mixed metal fluorites. The relative lack of order can also be deduced from the loss of structural features over many interatomic distances, i.e. beyound the NN shells. Static disorder is the major contributor to the Debye-Waller factor in mixed systems.

Cationic properties that promote F^- ion vacancy creation and the correspoding interstitial in the mixed-metal fluorites (as reported by Cox e al. 1994) are:

(a) low ionic charge

(b) large ionic radius

(c) highly active lone pairs and

(d) strongly polarizable ions

The work described in this thesis has successfully shown the advantages of the combined use of EXAFS and computational approaches in synthesising fast-ion conductors with enhanced conductivities at a temperature as low as possible.

7.2   RECOMMENDATIONS

The study of mixed-metal fluorites has further enlarged our horizons by making it necessary to examine other questions, which play a more central role in the case of mixed-metal fluorites. Among these are the following:

- Clearly, further calculations remains to be done on these fascinating systems with the use of sophisticated potential models, larger numbers of particles (unit cells) for better statistics and longer simulations for MD. This would be possible on a TERAFLOP machine.

- Further experimental investigation with high-resolution NMR on these materials could contribute to the understanding of these complex and highly disordered materials.

- Measurements of elastic constants as a function of temperature can be compared with our predictions

- Other types of mixed-metal fluorites can be studied in a similar way, e.g. $[CaF_2 \, (xPbF_2)]$

CHAPTER 8

REFERENCES

Allnat A.R., Chadwick A.V. and Jacobs P.W.M., 1987, Proc. Roy. Soc. (London) A, **410**, 385.

Allen M.P. and Tildesley D.J., 1987, Computer Simulation of Liquids, Oxford University Press (OUP).

Andersen N.H., Clausen K., Kjems J.K. and Schoonman J., 1986a, J. Phys. C, **19**, 2377

Andersen N.H., Clausen K., Hacket M.A., Hayes W., Hutchings M.T., Macdonald J.E. and Osborn R., 1986b, Physica B, **136**, 315.

Aurora T.S., Pederson D.O. and Day, S.M., 1990, Phys. Rev. B, **41**, 9647

Azimi A., Carr V.M., Chadwick A.V., Kirkwood F.G. and Saghafian R., 1984, J. Phys. Chem, Solids, **45**, 23

Bhattacharyya A.J., Middya T.R., Tarafdar S., Phys. Rev. B, **6**(2), 909

Bendall P.J. and Catlow C.R.A., 1980, J. Phys. Colloq. (France), **41**, C6-61

Bendall P.J., Catlow C.R.A., Corish J. and Jacobs P.W.M., 1984, J. Solid State Chem., **51**, 159.

Benedek G.B. and Fritsch K, 1966, Phys. Rev., **149**, 647.

Bingham D., Cormark A.N. and Catlow C.R.A., 1989, J. Phys. C, **1**, 1205

Bingham D., Cormack A.N. and Catlow C.R.A., 1989, J. Phys., **1**, 1213

Binsted N., Campbell J.W., Gurman S.J. and Stephenson P.C., 1992, EXCURV92 Programme, SERC Daresbury Laboratory, Warrington, WA4 4AD, Ceshire, U.K.

Bonne R.W. and Schoonman J., 1977, J. Electrochem, Soc., **124**, 28

Born M. and Huang K., 1954, Dynamical Theory of Crystal Lattices, (Oxford University Press : Oxford).

Born M. and Wolf E., 1965, Principles of Optics, (Pergamon Press; Oxford), **p.665.**

Boyce J.B. and Huberman B.A., 1979, Phys. Rep., **51**, 189

Boyce J.B. and Hayes J.M. and Mikkelsen J.C. Jr., 1981, Phys. Rev. B. **23**, 2876.

Brass A.M., 1989, Phil. Mag. A, **59**, 483

Briozzo C.B., Budde C.E. and Ca´ceres M. O., 1989, Phys. Rev. A, **39**, 6010.

Buchrer W., Altorfer F., Mesot J., Bill H., Carron P and Smith H., 1991, J. Phys., **3**, 1055

Butler V., Catlow C.R.A. and Fender B.E.F., 1981, Solid State Ionics, **5**, 539

Butler V., Catlow C.R.A., Fender B.E.F. and Harding J.H., 1983, Solid State Ionics, **8**, 109.

Carr V.M., Chadwick A.V. and Figueroa D.R., 1976, J. Phys. (Paris), **37**, C7-337

Carr V.M., Chadwick A.V. and Saghafian R., 1978, J. Phys. C, **11**, L637

Carter R.E. and Roth W.L., 1963, General Electric Res. Rep., No. **63-RL-3479M**

Carter R.E. and Roth W.L, 1968, Eletromotive Force Measurements in High Temperature Systems, ed. Alcock C.R., (The Institute of Mining and Metallurgy : New York), **p. 125**

Catlow C.R.A., 1973, J. Phys. C, **6**, L64.

Catlow C.R.A. and Norgett M.J., 1973, J. Phys. C., **6**, 1325

Catlow C.R.A., 1976a, J. Phys. C, **9**, 1845

Catlow C.R.A., 1976b, J. Phys. C, **9**, 1859

Catlow C.R.A., Harley R.T. and Hayes W., 1977, J. Phys. C, **10**, L559

Catlow C.R.A., 1977, Proc. Roy, Soc. A, **353**, 533

Catlow C.R.A., Norgett M.J. and Ross T.A., 1977, J. Phys. C, **10**, 1063

Catlow C.R.A., Comins J.D., Germano F.A., Harley R.T. and Hayes W., 1978, J. Phys. C, **11**, 3197.

Catlow C.R.A., Mackrodt W.C., Norgett M.J., and Stoneham A.M., 1979, Phil. Mag. A, **40**, 161.

Catlow C.R.A., 1980, Comments Solid State Phys., **9**, 157.

Catlow C.R.A., Comins J.D., Germano F.A., Harley R.T., Hayes W. and Owens I.B., 1981, J. Phys.

C, **14**, 329.

Catlow C.R.A., Comins J.D., Germano F.A., Harley R.T. and Hayes W., 1978, **11**, 3197

Catlow C.R.A., Corish J., Jacobs P.W.M. and Lidiard A.B., 1981, J. Phys. C, **14**, L121.

Catlow C.R.A. and Hayes W., 1982, J. Phys. C, **15**, L9

Catlow C.R.A., James R., Mackrodt W.C., eds., 1982, Computer Simulation of Solids, Lecture notes in Physics no. 166, (Springer-Verlag : Berlin)

Catlow C.R.A. and Mackrodt W.C., 1982, Phys. Rev. R, **25**, 1006

Catlow C.R.A., 1983, Solid State Ionics, **8**, 89.

Catlow C.R.A., Chadwick A.V. and Corish J., 1983, J. Solid State Chem., **48**, 65.

Catlow C.R.A., Chadwick A.V., Greaves G.N. and Moroney L.M., 1984, Nature, **312**, 601.

Catlow C.R.A., Chadwick A.V., Greaves G.N. and Moroney L.M., 1985, Cryst. Latt. Def. and Amorph. Mater., **12**, 193.

Catlow C.R.A., 1986, Ann. Rev. Mater. Sci., **16**, 517

Catlow C.R.A., 1986, Swd. in Solids, (ed. Chadwick A.V., Terenzi M.), **269**

Catlow C.R.A., 'Computer Simulation Studies of Transport in Solids,' Ann. Rev. Mater. Sci., **16**, 517

Catlow C.R.A., 1987, Private Commun.

Catlow C.R.A., Cox P.A., Jackson R.A., Parker S.C., Price G.D., Tomlinson S.M. and Vetrivel R., 1989, Mol. Sim., **3**, 49

Catlow C.R.A., 1997, Computer Modelling in Inorganic Crystallography (Academic Press: London)

Catlow C.R.A. and Greaves G.N., Eds. (1990). 'Applications of Synchrotron Radiation', Blackie, Glasgow.

Chaba P.J. and Ngoepe P.E., 1998, Molecular Simulation, **21**, 161

Chaba P.J., M.Sc. Thesis, University of the North, 2000

Chadwick A.V., 1998, Molecular Simulation, **21**, 105

Chadwick A.V., Hope D.S., Jaroszkiewicz G, and Strange J.H., 1979, Fast ion transport in solids, (ed. Vashista P., Mundy J.N. and Senoy G.K.), p. **683.**

Chadwick A.V., Hope D.S., Jaroszkiewicz G. and Strange J.H., 1980b, AFOSR Report.

Chadwick A.V., Flack K.W., Strange J.H. and Harding J., 1988, Solid State Ionics, **28**, 185.

Chadwick A.V., Kirkwood F.G. and Saghafian R., 1980a, J. Phys. (Paris), **41**, C6-216.

Chadwick A.V., 1983, Solid State Ionics, **8**, 209.

Chadwick, 'EXAFS – An introductory guide for Chemistry students': Internal report, University of Kent at Canterbury, UK

Cheetham A.K., Fender B.E.F., Steele D., Taylor R.J. and Willis B.T.M., 1970, Solid State Commun., **8**, 171.

Cheetham A.K., Fender B.E.F. and Cooper M.J., 1971, J. Phys. C, **4**, 3107.

Cheetham A.K., Fender B.E.F., Fuess H and Wright A.F., 1976, Acta Crystallogr. B, **32**, 94.

Ciepielewski P. and Kosacki I., 1982, Solid State Commun., **44**, 417

Clausen K., Hayes W., Macdonald J.E. and Osborn R., 1984b, Phys. Rev. Lett., **52**, 1238.

Clausen K., Hayes W., Hutchings M.T., Macdonald J.E., Osborn R. and Schnabel P., 1984a, Rev. Phys. Appl., **19**, 719.

Clausen K., Hayes W., Hutchings M.T., Macdonald J.E., Kjems J.K. and Osborn R, 1985, High Temp. Sci., **19**, 189.

Comins J.D., Ngoepe P.E. and Catlow C.R.A., 1990, J. Chem. Soc. Faraday Trans., **86**, 183.

Corish J. and Jacobs P.W.M., 1975, Phys. Stat. Sol., **67**, 263.

Corish J., Catlow C.R.A., Jacobs P.W.M. and Ong S.H., 1982, Phys. Rev. B, **25**, 6425.

Cormack A.N., Catlow C.R.A. and Ling S., 1989, Phys. Rev. B, **40**, 3278.

Cox P.A., Ph.D. Thesis, University of Keele, 1988

Cox P.A., Catlow C.R.A. and Chadwick A.V., 1994, J. Master. Sci., **29**, 2725.

Cox P.A., Catlow C.R.A., Chadwick A.V. and Moroney L.M., To be published.

Derrington C.E. and O'Keefe M., 1973, Nature, **246**, 44

Derrington C.E., Lidner A. and O'Keeffe M., 1975, J. Solid State Chem., **15**, 171

Dick B.G. and Overhauser A.W., 1958, Phys. Rev., **112**, 90

Dickens M.T., 1976, J. Phys., **37**, 353

Dickens M.H. and Hutchings M.T., 1977, Proceedings of the International Symposium on Neutron Inelastic Scattering, Vienna

Dickens M.H. and Hutchings M.T., 1978, J. Phys. C, **11**, 461

Dickens M.H., Hayes W., Hutchings M.T. and Kleppman W.G., 1979, J. Phys. C, **12**, 17.

Dickens M.H., Hayes W., Smith C. and Hutchings M.T., 1979, Fast Ion Transport in Solids, (Ed. Vashishta P., Mundy J.N. and Shenoy G.K.), (North-Holland : Amsterdam), p. **225**

Dickens M.H., Hayes W., Schnabel P., Hutchings M.T., Lechner R.E. and Renker B., 1983, J. Phys. C, **16**, L1.

Dickens M.H., Hayes W., Hutchings M.T. and Smith C., 1982, J. Phys. C, **15**, 4043.

Dieterich W., Fulde P., Peschel I., 1980, Adv. Phys., **29**, 527.

Dieterich W. and Peschel I., 1983, J. Phys. C, **16**, 3841

Dil J.G., 1982, Rep. Prog. Phys., **45**, 285

Dixon M. and Sangster M.J.L., 1977, Phil. Mag., **35**, 1049

Dixon M. and Gillan M.J., 1978, J. Phys. C, **11**, L165

Dixon M. and Gillan M.J., 1980, J. Phys. C, **13**, 1919

Dwivedi A. and Cormack A.N., 1990, Phil. Mag. A, **61**, 1

Einstein A., Phys. Rev., **17**, 549, 1905

Elcombe M.M. and Pryor A.W., 1970, J. Phys. C, **3**, 492

Elcombe M.M., 1972, J. Phys. C., **5**, 2702

Elliott R.J. et al, 1978, Proc. Roy. Soc. A, **360**, 317

Elliott R.J., Hayes W., Kleppman W.G., Rushworth A.J. and Ryan J.F., 1978, Proc, Roy. Soc. A., **380**, 317

Evangelisti F., Proietti M.G., Balzarotti A., Comin F., Incoccia L., Mobilio S., 1981, Solid State Commun., **37**, 413

Every A.G., 1980, Phys. Rev. B, **22**, 1746

Farley T.W.D., Hayes W., Hull S., Hutchings M.T. and Vrtis M., 1991, J. Phys., **3**, 4761

Figueroa D.R., Chadwick A.V. and Strange J.H., 1978, J. Phys. C, **11**, 55.

Fitch A.N., Fender B.E. and Talbot J., 1984, J. Solid State Chem, **55**, 14

Forester T.R. and Smith W., 1993, DL_PLOY code, Daresbury Laboratory, UK

Gale, J.D., Catlow, C.R.A.and Mackrodt W.C., 1992, Modelling Simul. Mater. Sci. Engng., **1**, 73

Gale J.D., 1997, Chem. Soc., Faraday Trans., **93**(4), 629

Garber J.A. and Granato A.V., 1975, Phys. Rev. B, **11**, 3990

Garner and Halliwell, 1986

Gasanly N.M., Akinoglu, B.G. and Ellialtioglu S., 1993, Phys. Stat. Sol. (b), **177**, K59

Gillan M.J. and Dixon M., 1980a, J. Phys. C, **13**, 1901

Gillan M.J. and Dixon M., 1980b, J. Phys. C, **13**, L835

Gillan M.J., 1981, Phil. Mag., **43**, 301

Gillan M.J. and Dixon M., 1981, Solid State Ionics, **5**, 593

Gillan M.J. and Jacobs P.W.M., 1983, Phys. Rev. B, **28**, 759

Gillan M.J., 1985, Physica, **131B**, 157

Gillan M.J., 1986a, J. Phys. C, **19**, 3391

Gillan M.J., 1986b, J. Phys. C, **19**, 3517

Gillan M.J., Harding J.H. and Tarento R-J., 1987, J. Phys. C, **20**, 2331

Gillan M.J., Harding J.H. and Leslie M., 1988, J. Phys. C, **21**, 5465

Goff J.P., Hayes W., Hull S. And Hutchings M.T., 1991, J. Phys., **3**, 3677

Greaves G.N., in: Phillips J.C., Thorpe M.F. (Eds.), Phase Transitions and Self-Organisation in Electronic and Molecular Materials, Kluwer Academic/Plenum Publishers, New York, 2000, p. 225

Greaves G.N., in: H.D. Hochheimer (Ed.), Frontiers of High Pressure Research II, Application of High Pressure to Low Dimensional Electronic Materials, Kluwer Academic/Plenum Publishers, New York, 2001, p. 53

Grimes R.W., Catlow C.R.A. and Stoneham A.M., 1989, J. Phys., **1**, 7367

Grimes R.W., Miller R.H. and Catlow C.R.A., 1990, J. Nucl. Mater., **172**, 123

Harding J.H., 1979, J. Phys. C, **12**, 3931

Harding J.H., 1990, Rep. Prog. Phys., **53**, 1403

Harley R.T., Hayes W., Rushworth A.J. and Ryan J.F., 1975, J. Phys. C, **8**, L530

Harley R.T., Manning D.I. and Ryan J.F., 1978, J. Phys. E, **11**, 517

Hart S., 1970, Phys. D., **3**, 430

Hart S., 1971, Phys. Stat. Sol. (a), **5**, K95

Hart S., 1973, Phys. Stat. Sol., **17**, K107

Hart S., Wallis J. and Sigalas I., 1986, Physica, **139 & 140 B**, 183

Hayes T.M. and Boyce J.B., Solid State Physics, 1981, **37**, 173

Hayes T.L. and Boyce T.B., 1983, Solid State Physics, **37**, 173

Hayes W. and Stoneham A.M., 1974, Crystal with the fluorite structure, (Claredon Press, Oxford), p.**50**

Hayes W., Rushworth A.J., Ryan J.F., Elliot R.J. and Kleppman W.G., 1977, J. Phys. C, **10**, L111.

Hayes W. and Loudon R., 1978, Scattering of light by crystals

Hayes W., 1978, Contempt. Phys., **19**, 469.

Hayes W., 1981, J. Phys. C, **42**, 167

Hayes W. and Stoneham A.M., 1985, Defects and defects processes in non-metallic solids (Wiley : New York)

Hayes W., Contempt. Phys., **27**, 519

Hiki Y., Thomas J.F. and Granato A.V., 1967, Phys. Rev., **153**, 764

Huberman B.A., 1974, Phys. Rev. Lett., **32**, 1000

Hussain W. and Sirdeshmuckh D.B., 1987, J. Phys. C, **29**, 583

Hutchings M.T., Clausen K., Dickens M.H., Kjems J.K., Schnabel P.G. and Smith C., 1983, Harwell Report, AERE-R, **11127**

Ishigame M., Shin S. and Suemoto T., 1991, Solid State Ionics, **4848**.

Islam M.S., Cherry M. and Catlow C.R.A., J.Solid State Chem., 1996, **124**, 230

Jackson R.A., Murray A.D., Harding J.H. and Catlow C.R.A., 1986, Phil. Mag. A, **53**, 27

Jackson R.A.and Catlow C.R.A., (1988), Molecular Simulation, **1**, 207

Jacobs P.W.M., Sahni V.C. and Vempati C.S., 1984, Phil. Mag. A, **49**, 301

Jacobs P.W.M. and Rycerz, 1997 (ed. Catlow C.R.A., 1997, Computer Modelling in Inorganic Crystallography (Academic Press: London))

Kawamoto Y., Kanno R., Umetani Y., Tohji K. and Morikawa H., Solid State Ionics, 1991, **44**, 181

Kleppman W.G., 1978, J. Phys. C, **11**, L91

Kjems J.K., Andersen N.H. and Schoonman J., 1983, Physica **120B,** 357

Kolesik M., Tunega D. and Sobolev B.P., 1990, Phys. Stat. Sol. (b), **160**, 375

Kosacki I., Litvinchuk A.P., Tarasov J.J. and Valakh M. Ya, 1989, J. Phys. C, **1**, 929.

Kosacki I. and Dynowska E., 1980, J. Cryst. Growth, **50**, 575

Kosacki I., Walach Ya. M. and Litwinczuk A.P., 1985, Sol. Stat. Commun., **53**, 373

Kosacki I., Hibner K. and Stefanski T., 1987, Acta Physica Polonica A, **71**, 409.

Kosacki I. and Zalibowski K., 1988, Phys. Stat. Sol. (a), **108**, 765.

Kosacki I., Hibner K., Litvinchuk A.P., Valakh M. Ya., Solid State Commun., **57**, 729.

Kosacki I., Hibner K., Litvinchuk A.P., Valakh M. Ya., 1986, Phys. Stat. Sol., **134**, 495

Kosacki I., 1989, Appl. Phys. A, **49**, 413

Koto K., Schulz H. and Huggings R.A., 1980, Solid State Ionics, **1**, 355

Koto K. and Ito Y., 1983, Solid State Ionics, **9 - 10**, 527

Leach A.R., 1996, Molecular Modelling (Principles and applications), Addison Wesley Longman Limited

Lee P.A. and Pendry J.B., 1975, Phys. Rev. **B11**, 2795

Li X., Hafskijold B., 1995, J. Phys. C, **7**, 1255

Lidiard A.B and Norgett M.J., 1972, Computational Sol. Stat. Phys., (ed Herman F.).

Lindan P.J.D. and Gillian M.J., 1991, J. Phys., **3**, 3929

Lindan P.J.D. and Gillian M.J., 1993, J. Phys.C, **5**, 1019

Lindan P.J.D. and Gillian M.J., 1994, Phil. Mag. B, **69**(3), 535

Lindan P.J.D., 1995, Mol. Sim., **14**, 303

Mackrodt W.C. and Stewart R.F., 1979, J. Phys. C, **12**, 431

Mackrodt W.C. and Woodrow P.M., 1986, J. Am. Ceram. Soc., **69**, 277

Mahan G.D., 1976, In Superionic Conductors, (ed. Mahan G.D. and Roth W.)

Mahan G.D., 1976, Phys. Rev. B, **14**, 780

Mahan G.D., 1980, Solid State Ionics, **1**, 29

Manasreh M.O. and Pederson D.O., 1984, Phys. Rev. B, **30**, 3482

Manasreh M.O. and Pederson D.O., 1985, Phys, Rev. B, **31**, 3960

Manasreh M.O. and Pederson D.O., 1985, Phys, Rev. B, **31**, 8153

Manasreh M.O. and Pederson D.O., 1985, Solid State Ionics, **15**, 65

Matar S F, Catlow C.R.A., and Reau J.M, 1983, Solid State Ionics, **9 - 10**, 511

Matar S. and Reau J.M., 1982, C.R. Acad. Sci. Paris, **294**, 649

Mott N.F. and Littleton M.J., 1938, Trans. Faraday Soc., **34**, 485

Netshisaulu T.T., Ngoepe P.E., Comins J.D. and Catlow C.R.A., 1993, Proc. Int. Conf. Def. Ins. Mater., Eds. Spaeth J.M. and Kanet Z. (World Scientific Publishers), p. **979**

Netshisaulu T.T., Ngoepe P.E., Comins J.D. and Catlow C.R.A., 1995, Rad. Eff. and Def. in Solids, **134**, 111

Netshisaulu T.T., 1996, M.Sc. Thesis, University of the North, Sovenga, South Africa

Netshisaulu T.T., Ngoepe P.E. and Chadwick A.V., 1999, Molecular Simulation, **22**, 1

Netshisaulu T.T., M. Melle-Franco, Chadwick A.V. and Ngoepe P.E., 1999, Rad. Eff. and Def. in Solids, **149**, 243

Ngoepe P.E. and Comins J.D., 1986, J. Phys. C, **19**, L267

Ngoepe P.E. and Comins J.D., 1987, J. Phys. C, **20**, 2983

Ngoepe P.E. and Comins J.D., 1987, Cryst. Latt. Def. and Amorph. Mat., **15**, 317

Ngoepe P.E., Ph.D. Thesis, 1987, University of the Witwatersrand

Ngoepe P.E. and Comins J.D., 1988, Phys. Rev. Lett., **61**, 978

Ngoepe P.E., Jordan W.M. and Catlow C.R.A., 1990, Phys. Rev. B, **41**, 3815

Ngoepe P.E. and Catlow C.R.A., 1991, Rad. Eff. and Def. in Solids, **119**, 399

Norgett, M.J. and Fletcher, R., 1970, J. Phys. C, **3**, 163.

Norgett M.J., 1974, UKAEA Report AERE-R., **7650**

Nowick A.S., 1985, Cryst. Latt. Def. and Amorph. Mater., **12**, 3

Nye J.F., 1964, Physical properties of crystals (Oxford University Press).

O'Keeffe M. and Hyde B.G., 1976, Phil. Mag., **33**, 219

O'Keeffe M., 1977, Commun. Solid State Phys., 7, 163

O'Reilly M.B., 1978, Phys. Stat. Sol., **48**, 489

Osaka T and Shindo I., 1984, Solid State Commun., **51**, 421

Pederson D.O. and Brewer J.A., 1977, Phys. Rev. B., **16**, 4546

Petrolekas D.D., Metcalfe J.S. and Catal J., 1995, **152**, 147

Rahman A., 1976, J. Chem. Phys., **65**, 4845

Rammutla K.E., Comins J.D., Netshisaulu T.T., Ngoepe P.E. and Chadwick A.V., 2001, Rad. Eff. and Def. in Solids, **155**, 403

Rammutla K.E., Comins J.D., Erasmus R.M., Netshisaulu T.T., Ngoepe P.E. and Chadwick A.V., 2002, Rad. Eff. and Def. in Solids, **157**, 783

Rao K. J., Rao B.G. and Wong J., 1988, J. Chem. Soc., Faraday Trans. 1, **84(6)**, 1779

Reau J-M and Portier J., 1978, Solid Electrolytes, (ed Hagenmuller P. and Von Gool W.), (Academic Press : New York), **p.313**

Reau J-M Matar S., Villeneuve G. and Soubeyroux J-L, 1983, Solid State Ionics, **9 - 10**, 563.

Reau J-M, El Omari M., Senegas J. and Hagenmuller P., 1990, Solid State Ionics, **38**, 123.

Reau J-M, Wahbi M., Sénégas J. and Hagenmuller P., 1992, Phys. Stat. Sol., **169**, 331

Rice M.J., Strassler S. and Toombs G.A., 1974, Phys. Rev. Lett., **32**, 596

Robert R.B. and White G.K., 1986, J. Phys. C, **19**, 7167

Sahni V.C. and Jacobs P.W.M., 1983, J. Phys. C, **16.**, L241

Salamon M.B., 1977, Phys. Rev. B, **15**, 2236

Salamon M.B., 1979, Physics of Superionic Conductors, (ed. Salamon M.B.), (Springer-Verlag : Berlin), p. **175**

Samara G.A., 1978, Phys. Chem. Solids, **40**, 509

Sangster M.J.L and Dixon M., 1976, Adv. in Phys., **25**, 247

Sayle D.C., Catlow C.R.A., Perrin M.A., and Nortier P., 1995, J. Phys. Chem. Solids, **56**, 799.

Schoonman J., 1979, Fast ion transport in Solids, (ed. Vashishta P., Mundy J.N. and Shenoy G.K.), p. **631**

Schoonman J., 1980, Solid State Ionics, **1**, 123

Schoonman J., 1980, Solid State Ionics, **1**, 1221

212

Schoonman J., Oversluizen G. and Wapenaar K.E.D., 1980, Solid State Ionics, **1**, 211.

Schoonman J., 1981, Solid State Ionics, 5, 71

Schulz H., and Bachmann R, 1983, Solid State Ionics, **9 - 10**, 521.

Sekar P. and Haridasan T.M., 1989, Phil. Mag. A, **59**, 313

Shahi K., 1977, Phys. Stat. Sol. A, **41**, 11

Shapiro S.M., 1976, Superionic Conductors, (ed Mahan G.D. and Roth W.L.), p. **261**

Shapiro S.M. and Reidinger F., 1979, Phys. of Superionic Cond., (ed. Salamon M.B.), p.**56**

Shimojo F., Okabe T., Tachibana F., Kobayashi M. and Okazaki H., 1992, J. Phys. Soc. Jpn., **61**, 2848.

Shimojo F. and Okazaki H., 1992, J. Phys. Soc. Jpn., **61**, 4106.

Suemoto T. and Ishigame M., 1983, Solid State Commun., **45**, 641

Suemoto T. and Ishigane M., 1986, Phys Rev. B, **33**, 2757

Tan Y.N. and Kramp D., 1970, J. Chem. Phys., **53**, 3691

Teo B.K. and Joy D.C., Eds. (1980), 'EXAFS Spectroscopy, Techniques and Applications', Plenum Press, New York.

Uehara T., Koto K., Emura S. and Kanamaru F., 1987, Solid State Ionics, **23**, 331

Veal B.W., Mckale A.G., Paulikas A.P., Rothman S.J. and Nowick L.J., 1988, Physica B, **150**, 234

Voronin B.M., 1995, J. Phys. Chem. Solids, **56**, 839

Walker A.B., Dixon M. and Gillan M.J., 1982, J. Phys. C, **15**, 4061

Walker J.R., Springer Lecture Notes, 1982, (ed. Catlow C.R.A. and Mackrodt W.C.), 116

Walker J.R., 1982, Computer Simulation in the Physics and Chemistry of Solids, (ed. Catlow C.R.A. and Mackrodt W.C.), (Berlin : Springer-Verlag), p.**58**

Wang Y.R., Zu K.Q., Wang D.H., Wu Z.H. and Fang Z.Z., 1994, J. Phys. C, **6,** 633

Wang F. and Grey C.P., 1995, J. Am. Chem. Soc., **117**, 6637

Wang F. and Grey C.P., 1997, Chem. Mater., **9**, 1068

Watson G.W., Parker S.C. and Wall A., 1992, J. Phys., **4**, 2097

Wimmer E., 1996, Mater. Sci. Eng., **B37**, 72

Wolf M.L., Walker J.R. and Catlow C.R.A., 1984, J. Phys. C, **17**, 6623

Wolf M.L. and Catlow C.R.A., 1984, J. Phys. C., **17**, 6635

PUBLICATIONS AND CONFERENCE PRESENTATIONS

PUBLICATIONS

Netshisaulu T.T., M. Melle-Franco, Chadwick A.V. and Ngoepe P.E., 1999, Rad. Eff. and Def. in Solids, **149**, 243

Netshisaulu T.T., Ngoepe P.E , Catlow C.R.A. and Chadwick A.V., Computer Modelling of Elastic Properties of Mixed Cation Superionic Fluorites, Manuscript in preparation.

Netshisaulu T.T., Chadwick A.V., Ngoepe P.E and Catlow C.R.A., Spectroscopic and Computer Modelling Studies of Mixed-cation Superionic Fluorites, Manuscript in preparation.

CONFERENCE PRESENTATIONS

TT Netshisaulu, PE Ngoepe, AVC Chadwick, 'Computer Modelling and EXAFS studies of mixed metal fluorites', An International Material Modelling Meeting (4-5 May 1998, University of the North, South Africa)

TT Netshisaulu, M Melle-Franco, AVC Chadwick and PE Ngoepe, **'**Studies of disorder in mixed crystals', Eleventh International Europhysical Conference on Defects in Insulating Materials (July 1998, University of Keele, UK)

TT Netshisaulu, PE Ngoepe, CRA Catlow and AVC Chadwick, 'Computer modelling studies of $CdF_2(xPbF_2)$ mixed systems', An International Material Modelling Meeting (March, 1999, University of the North, South Africa)

TT Netshisaulu, 'Computer Modelling and EXAFS studies of mixed-metal fluorites', University of the North Foundation Year (UNIFY) Staff Development Session (May 2002, South Africa)

TT Netshisaulu, PE Ngoepe, CRA Catlow and AVC Chadwick, 'Computer Simulation and EXAFS studies of $CdF_2(xPbF_2)$ solid solutions', South African Institute of Physics (25-27 June 2003, University of Stellenbosch, South Africa)